DISSERTATION

submitted to the

Combined Faculty of Natural Sciences and Mathematics

of the Ruperto Carola University Heidelberg, Germany

for the degree of

Doctor of Natural Sciences

presented by

Eglė Maximowitsch, M.Sc.

born in Vilnius, Lithuania

Oral examination: 1 April 2019

Molecular mechanisms of spectral tuning and excited-state decay in phytochrome photoreceptors

Referees:

Prof. Dr. Frauke Gräter

Prof. Dr. Ilme Schlichting

Contents

Acknowledgements

I would like to acknowledge some people who were supporting me during my PhD work. Without their help during these years this work would not have been possible. I would like to thank…

… Tatiana Domratcheva for supervising me in my projects, introduction to quantum chemistry, giving me an opportunity to develop my skills, great support and advice, as well as discussions about science, career and life.

… Frauke Gräter for being first referee of my dissertation, for support and discussions broadening my knowledge.

… Ilme Schlichting for being second referee of my dissertation, giving me an opportunity to do a PhD in the department of Biomolecular Mechanisms, discussions and support on my career path.

… Andres Jäschke for being a member of my defence committee.

… Chris Roome for excellent IT support.

… Alex Granovsky for excellent support and personalized updates of Firefly software.

… Janne Ihalainen, Heli Lehtivuori, Heikki Takala and Nikolai Tkachenko for a long-lasting collaboration, discussions not only about science but also career and life.

… Evgeniy Gromov and Victor Beschastnov for sharing scientific knowledge, helping with technical questions and great discussions.

… Gabriela Nass Kovács, Sarah Duponchel, Kastė Jurgaitytė, Udo Heintz, Felix Schübel and Monica Chandra for sharing the office and being with me the most time during my work, for the support, discussions, laughs, sweets and plants.

… Andreas Dietl, Diana Born, Robert Lindner and Tiia Kittilä for the help and support during thesis writing, inspiring conversations and support in and outside the institute.

… Martina Blochmann for the support with all administrative issues during my PhD.

… all current and former members of the institute for creating a scientifically fruitful and friendly atmosphere, discussions and support on various issues.

… Max Planck Society for the opportunity to pursue my PhD at Max Planck Institute for Medical Research and for the great networking possibilities.

… Jülich Supercomputing Centre (JSC) for the computing time on the modular supercomputer JURECA.
… Heidelberg Biosciences International Graduate School for financial and non-material support.
… Graduate Academy of Heidelberg University for writing support services.
… my friends for the support and sharing great moments.
… my parents and sister for teaching me how to find my path, supporting throughout my way and never stopping believing in me.
… my husband Peter for love, philosophical and scientific discussions, for cheering me up, encouraging in taking challenges and supporting me no matter what.

Abstract

Most organisms on earth are able to sense light, to which they adapt their behavior by using photoreceptor proteins containing light-absorbing chromophores. Phytochrome photoreceptors contain a covalently-attached tetrapyrrole chromophore and switch between two thermally stable forms, a red-absorbing (Pr) and a far-red-absorbing (Pfr) state. Although phytochromes have been studied for more than fifty years, the molecular mechanisms defining their photoinduced properties are not fully understood, hampering the efficient engineering of phytochrome-based molecular tools. The computational study presented in this thesis combines quantum chemical calculations and molecular dynamics simulations in order to elucidate the molecular mechanisms of spectral tuning and excited-state decay in phytochromes. The calculations have demonstrated that the spectral red shift of the Pfr state is induced by the hydrogen bond formation between the chromophore and a highly conserved aspartate. Here it is also shown how the formation of this hydrogen bond is coupled to dynamics of other active-site interactions. In addition, the chromophore deprotonation by a protein residue is proposed to contribute to the absorption at the Q-band blue shoulder in the Pr-state spectrum. For the first time, the photoinduced electron transfer coupled to proton transfer was characterized in phytochromes. These charge transfer pathways may contribute to the excited-state decay by quenching fluorescence and influencing photoproduct formation. The discoveries provided in this thesis will facilitate further phytochrome investigations and the rational design of phytochrome-based fluorescent markers and optogenetic tools.

Zusammenfassung

Viele Organismen auf diesem Planeten können Licht wahrnehmen. Um ihr Verhalten daran anzupassen, nutzen sie Photorezeptor-Proteine, die Licht absorbierende Chromophore enthalten. Phytochrom-Photorezeptoren enthalten einen kovalentgebundenen Tetrapyrrol-Chromophor und wechseln zwischen zwei stabilen Formen, einer hellrot absorbierenden (Pr) und einer dunkelrot absorbierenden (Pfr) Form. Diese Art von Photorezeptoren wird seit mehr als fünfzig Jahren erforscht. Dennoch versteht man die molekularen Mechanismen, die ihre durch Licht induzierten Eigenschaften definieren, bisher nicht vollständig, was eine effiziente Entwicklung von Phytochrom-basierten molekularen Werkzeuge erschwert. Diese Computer-basierte Dissertation kombiniert quantenchemische Berechnungen und Molekulardynamik-Simulationen um die molekularen Mechanismen der spektralen Anpassung und des Zerfalls des angeregten Zustands der Phytochrome zu verstehen. Die Berechnungen ergaben, dass die spektrale Rotverschiebung des Pfr-Zustands durch die Bildung der Wasserstoffbrückenbindung zwischen Chromophor und hoch konserviertem Aspartat induziert wird. Die Entstehung der Wasserstoffbrückenbindung ist an die Dynamiken weiterer Interaktionen im aktiven Zentrum gekoppelt. Es wird hier vorgeschlagen, dass die Deprotonierung des Chromophors durch eine Aminosäure des Proteins zur Absorption an der blauen Schulter der Q-Bande im Pr-Zustandsspektrum beiträgt. Diese Dissertation charakterisiert erstmalig den an Protonentransfer gekoppelten, photoinduzierten Elektronentransfer in Phytochromen. Diese Art der Ladungsübertragung könnte zum Zerfall des angeregten Zustands durch Fluoreszenzlöschung und durch Einfluss auf die Bildung des Photoprodukts beitragen. Die Erkenntnisse dieser Dissertation ermöglichen die weitere Charakterisierung der Phytochrome und erleichtern das rationale Design Phytochrom-basierter Fluoreszenzmarker und optogenetischer Werkzeuge.

Publications

Major parts of this thesis will be published in peer-reviewed journals:

- Maximowitsch E and Domratcheva T. A hydrogen bond between tetrapyrrole and conserved aspartate causes far-red shifted absorption of phytochrome photoreceptors. *In preparation.*
- Maximowitsch E and Domratcheva T. Photoinduced charge transfer in phytochrome red-light receptor proteins. *In preparation.*
- Lehtivuori H*, Maximowitsch E*, Takala H, Kurkinen S, Tkachenko NV, Ihalainen JA, Domratcheva T. Charge transfer reactions of the red-light photoreceptors phytochromes. *In preparation.*

Additional articles in peer-reviewed journals, not within the scope of this thesis:

- Jian Y*, Maximowitsch E*, Liu D, Adhikari S, Domratcheva T, Li L. Indications of 5' to 3' Interbase Electron Transfer as the First Step of Pyrimidine Dimer Formation Probed by a Dinucleotide Analog. Chemistry. 2017;23(31):7526-37.
- Gromov E, Maximowitsch E, and Domratcheva T. Hydrogen bonds rule photochemistry of the PYP receptor protein. *In preparation.*

* - equal contribution

1 Introduction

Sun light is a primary source of energy for most ecosystems. Photon energy may be either converted by an organism to chemical energy serving as fuel or used to sense the environmental conditions and trigger physiological organism functions. Various organisms sense light to enable different functions such as vision, magnetoreception, organismal development, circadian rhythm and metabolism.

Depending on the environment by which organisms are surrounded, they are adapted to sense different ranges of visible light from blue to far-red by using different photoreceptor proteins. The wavelength of the absorbed light by the photoreceptor depends on the chromophore molecule, binding to the photoreceptor. Based on the chemical structure of the bound chromophore and protein structure, all known photoreceptors are classified into six distinct families: retinal-binding rhodopsins, bilin-binding phytochromes, p-coumaric acid binding xanthopsins, flavin-containing cryptochromes, LOV (light-oxygen-voltage) proteins and BLUF (sensors of blue-light using FAD) proteins (Figure 1.1) (1-3). More recently discovered photoreceptors include coenzyme B12-binding CarH-type photoreceptors (4-6), carotenoid-using OCP (orange carotenoid protein) (7), cofactor-independent UV receptor LITE-1 (8) and cofactor-independent UV-light-activatable photoreceptor UVR8 (ultraviolet resistance locus 8), which absorbs light by a tryptophan triad instead of the chromophore (9, 10).

The chromophore molecule of a photoreceptor possesses a π-conjugated system which enables electron delocalization and visible-light photon absorption. After photoexcitation, the π-conjugated system undergoes a distinct chemical reaction, a so-called photoreaction, and forms a photoproduct. Two main classes of chromophore photoreactions are observed in different photoreceptors: double-bond isomerization in rhodopsins, xanthopsins and phytochromes as well as charge transfer reactions in UVR8, flavin-binding and CarH-type photoreceptors (3, 5, 11). The phytochrome-bound bilin undergoes the photoinduced isomerization of the C15=C16 double bond (12). The photoproduct formation initiates structural changes of the photoreceptor which trigger physiological signal in the organism (3).

Phytochrome photoreceptors due to the large π-conjugated system of the bilin chromophore, which is a linear tetrapyrrole molecule, absorb the longest visible wavelength light, i. e. red to far-red. Such long-wavelength visible light is especially employed by organisms living under light-deprived conditions such as in the deep sea, soil or under the canopy. Phytochrome photoreceptors are present in wide range of organisms such as plants, bacteria, cyanobacteria, fungi and algae (12-15). They have different functions ranging from phototaxis, pigmentation in bacteria (14), developmental processes such as seed germination seedling maturation, flowering, shade-avoidance and temperature sensing in plants (16-18). Phytochrome modulates its activity depending on light conditions as it photoswitches between two functional states, a red-absorbing Pr and a far-red-absorbing Pfr state. Most phytochromes are canonical, with the Pr state as a dark state, whereas some are bathy, with the Pfr state as a dark state (19-21). Bathy phytochromes are beneficial for organisms living in environments such as soil, where light penetration is reduced especially of the shorter wavelength light (22). Phytochrome photoreceptors, due to their specific properties, are promising templates for engineering of various molecular tools for cell manipulation. They can be applied for multiple color imaging of deep tissues *in vivo*, as optogenetic tools or biomarkers (23-29). Therefore, deepening our knowledge of chemical and photophysical properties of phytochrome and its tetrapyrrole chromophore will not only broaden our understanding of photoreceptors but may also contribute to improved phytochrome application.

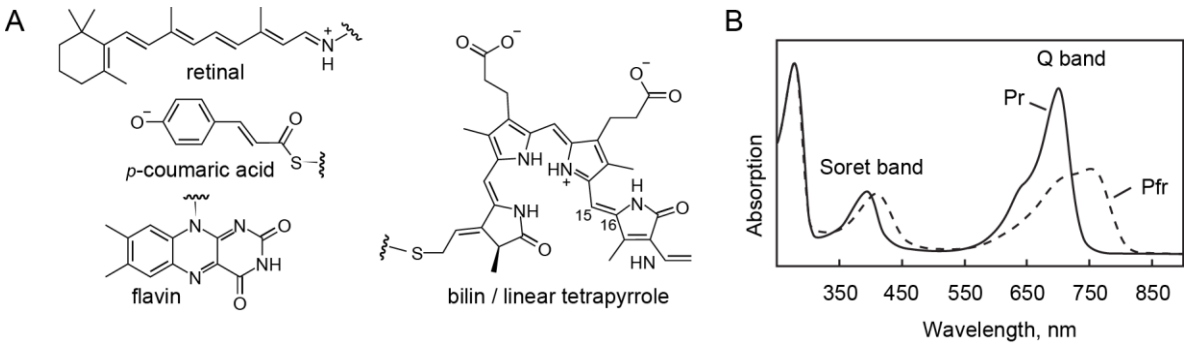

Figure 1.1. Visible light absorption by chromophore-binding photoreceptors. A) Chromophores in natural photoreceptor proteins: retinal, linear tetrapyrrole, p-coumaric acid, flavin derivatives. B) Spectrum of the DrBphP phytochrome, from the bacterium *Deinococcus radiodurans,* photoswitching between two states Pr and Pfr (adapted from Wagner et al. (30)). Q and Soret bands are indicated.

1.1 Phytochrome structural properties

1.1.1 Phytochrome domain architecture

Phytochrome photoreceptors have a modular structure which typically consists of the N-terminal photosensory core and the C-terminal regulatory output domain, which is usually a histidine kinase (12, 31). The photosensory core contains the CBD (chromophore binding domain) and PHY (phytochrome-specific) domains which is consistent for all phytochrome photoreceptors (12, 14, 31). The huge variety of phytochromes can be divided into five classes: bacterial (BphP), plant (Phy), cyanobacterial (Cph1), eukaryotic (Fph/Dph) and Synechocystis (Cph2) (Table 1.1). Phytochromes of all classes except Cph2 contain the PAS (Per/Arndt/Sim) and GAF (cGMP phosphodiesterase/adenyl cyclase/FhlA) domains to constitute their CBD, whereas in Cph2 the PAS domain is missing. The tetrapyrrole chromophore is covalently attached to a cysteine of the PAS or GAF domain and located in the cavity of the GAF domain with which it interacts non-covalently (12, 31-33). Plant phytochrome contains an extended regulatory output domain, as it contains two additional PAS domains between the photosensory core and the histidine kinase, whereas eukaryotic phytochrome contains a REC domain after the histidine kinase. Instead of the histidine kinase, the regulatory domain of Cph2 contains other domains such as GGDEF (a diguanylate cyclase with conserved residues GGDEF), EAL (a phosphodiesterase with conserved EAL residues) and GAF domains (12, 14, 31).

Table 1.1. Domain architecture in phytochrome photoreceptors.

Phytochrome	Abbreviation	Photosensory core	Regulatory output domain
plant	Phy	PAS-GAF*-PHY-	PAS-PAS - His kinase
cyanobacterial	Cph1	PAS-GAF*-PHY-	His kinase
bacterial	BphP	PAS*-GAF-PHY-	His kinase
eukaryotic	Fph/Dph	PAS*-GAF-PHY-	His kinase - REC domain
Synechocystis	Cph2	GAF*-PHY-	GGDEF-EAL-GAF*-GGDEF

* - binds tetrapyrrole chromophore

Changes of the quaternary structure during phytochrome activation occur only in the full photosensory core as was shown by small-angle X-ray scattering (SAXS) (34). Using SAXS analyses it was shown on multiple bacterial phytochromes that a dimer of the photosensory core undergoes opening at the PHY site while converting from the dark to the light state (35), Conversely, the photosensory core dimer undergoes a screw motion

and the output domains rotate in full-length phytochrome as shown by SAXS and single particle electron microscopy (EM) (36, 37). Single-particle EM helped to reveal protein structure changes during the photoreaction-induced photoactivation, in particular the perturbation of the helical spine along the photosensory core and the regulatory domain (38).

1.1.2 Interactions in the active site

Multiple high resolution X-ray crystal structures of various phytochromes enabled studying the structural arrangement of the domains and the active site (Figure 1.2 A). The first high resolution phytochrome structure (2.5 Å) was determined of the CBD domain of the bacterial phytochrome DrBphP from *Deinococcus radiodurans* in the Pr state (32). This structure was confirmed with subsequent even higher resolution structures (37, 39) and structures of the photosensory core of DrBphP (34, 37). The structural conservation of the active site was demonstrated by the structures of other phytochromes (33, 40-43). The PAS and GAF domains interact via a knot where 35 N-terminal residues pass through the loop between the PAS and GAF domains and likely stabilize the protein structure (32).

In the active site, the tetrapyrrole chromophore is autocatalytically (44) attached to a cysteine via a thioether linkage (32) and non-covalently interacts with the chromophore-binding site residues (Figure 1.2 B). Anionic propionates PropB and PropC, bound to the tetrapyrrole rings B and C, respectively, form salt bridges with the protein active site: PropB interact with arginine R254 (according to the numbering in DrBphP) and PropC interacts with serines S272 and S274 (32, 45). Tetrapyrrole rings A, B, C interact with the conserved water molecule (hereafter called "pyrrole water") that in turn interacts with the imidazole group of the highly conserved histidine H260. This residue belongs to an α-helix located above the biliverdin. Moreover, the pyrrole water molecule interacts with the backbone carbonyl oxygen of aspartate D207, which is part of the highly conserved Asp-Ile-Pro (DIP) motif located below the tetrapyrrole (32, 46). Tetrapyrrole ring D interacts with the conserved histidine H290 in the Pr-state phytochrome (12, 32, 45).

In the Pfr state, which can form only with the presence of the PHY domain (47, 48), the isomerized tetrapyrrole with its rotated ring D interacts with the carboxylate of the highly

conserved aspartate D207 (according to DrBphP sequence) (34, 40, 43) . The tetrapyrrole rings A, B, C, the pyrrole water, the imidazole group of histidine H260 and the backbone carbonyl of aspartate D207 form similar interactions as in the Pr state, whereas histidine H290 interacts with the propionate PropC instead of ring D. The propionate PropB interacts with another arginine (R222), and tyrosine Y176 is flipped out of the close proximity to ring D and interacts with PropC instead (12, 34, 38).

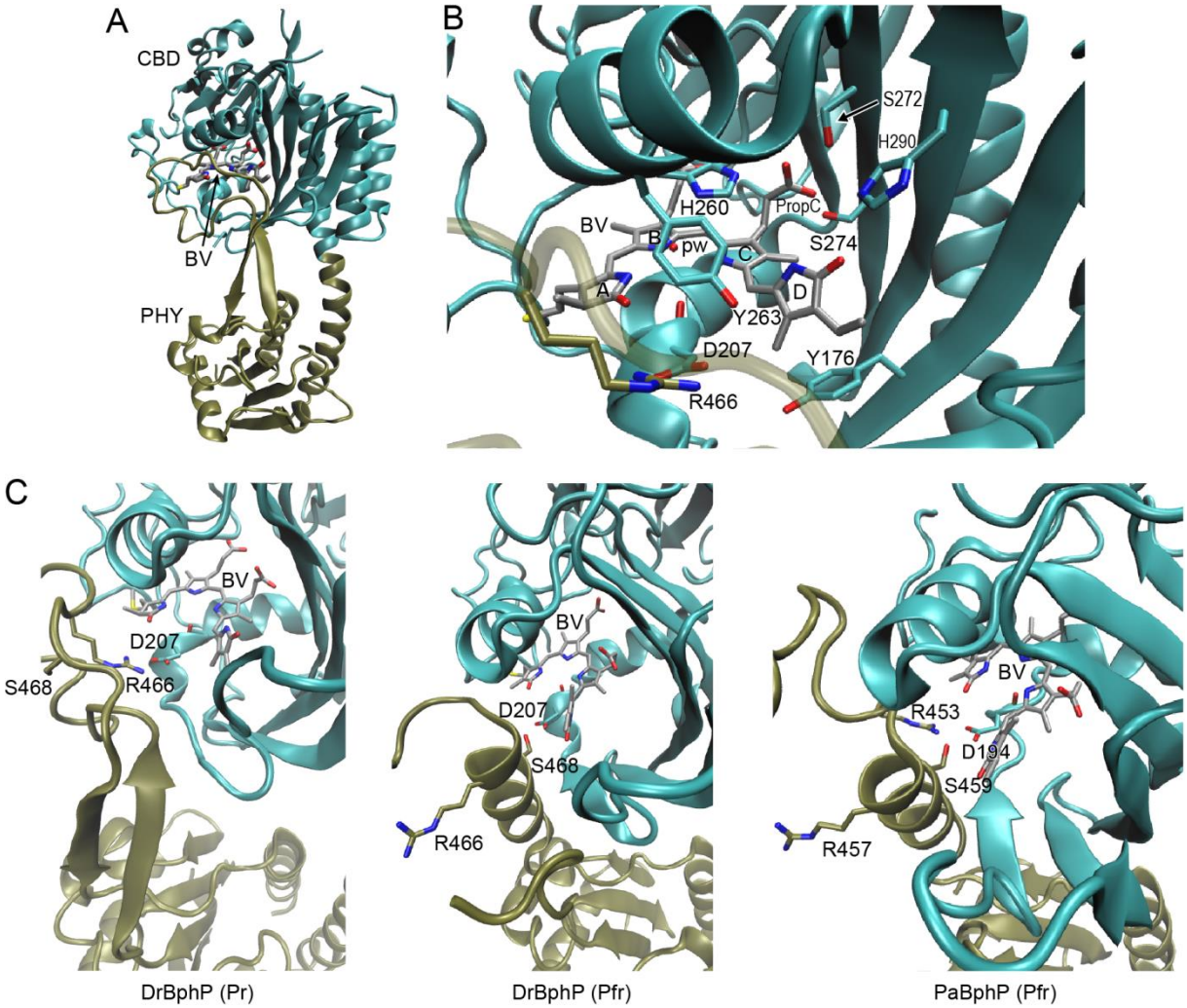

Figure 1.2. Phytochrome structure. A) Active site of bacterial phytochrome DrBphP in the Pr state. In the Pfr state biliverdin (BV) ring D is rotated and interacts with D207, which interacts with S468 instead of R466. B) Conformation of the PHY domain tongue and its interactions with CBD domain. Coordinates of Pr-state DrBphP, Pfr-state DrBphP, Pfr-state PaBphP were taken from PDBs 4q0j, 5c5k, 3c2w, respectively.

1.1.3 Interactions with the PHY domain

The presence of the PHY domain is crucial for the Pfr state formation (47, 48). The X-ray structures of the full photosensory core show that the highly conserved aspartate D207 interacts with the tongue of the PHY domain, structure of which changes between two

thermally stable Pr and Pfr states (34) (Figure 1.2 C). In the Pr state, the tongue appears as a β-sheet, as observed in the structures of DrBphP(34, 37), plant phytochrome AtPhyB from *Arabidopsis thaliana (33)*, cyanobacterial phytochrome Cph1 from *Synechocystis* PCC6803 (42) and SynCph2 (49). In the Pfr state, the tongue appears as an α-helix, as observed in the structures of DrBphP (34), bacterial bathy phytochromes PaBphP from *Pseudomonas aeruginosa* (40) and from *Rhodopseudomonas palustris* RpBphP1(43). The tongue of the PHY domain contains conserved arginine (R466 in DrBphP) and serine (S468 in DrBphP) that interact with the conserved aspartate D207 in the Pr and Pfr state, respectively (34, 37). While interactions with one residue, arginine or serine, are formed in the particular state, the other residue is rotated away from the interaction site with the D207 aspartate. In the Pfr state of bathy phytochromes, there is an additional interaction of the aspartate with a positively charged residue of the PHY domain: arginine in PaBphP or lysine in RpBphP1, whereas lysine interacts via water molecules as the residue is too far (~5 Å) to form a direct hydrogen bond (40, 43). If the conserved arginine or serine is mutated to alanine, the Pfr dark state of the bathy PaBphP phytochrome is disrupted (40). Whereas if the conserved aspartate (D207 in DrBphP) is mutated to alanine, phytochromes are not capable to form the Pfr state spectrum at all and do not undergo photoconversion (37, 40).

1.2 Tetrapyrrole chromophore absorbing light in phytochrome

1.2.1 π-conjugated system in different tetrapyrroles defines the phytochrome spectrum

All photochemical properties of phytochromes depend on the linear tetrapyrrole chromophore bound in the active site. A typical absorption spectrum of the linear tetrapyrrole chromophore bound to its phytochrome constitutes two bands, Soret and Q, with maxima at around 400 and 700 nm, respectively (Figure 1.1). The spectrum is qualitatively similar to the spectrum of porphyrins due to the π-conjugated system of the four pyrrole rings (50). In the absorption spectrum of tetrapyrrole in solution, the intensity of the Soret band is several times higher than of the Q band (51). In phytochrome proteins with their covalently and non-covalently bound tetrapyrrole chromophore, the intensity of the Q band is several times higher than of the Soret band (50). In the Sandercyanin protein with its non-covalently bound biliverdin tetrapyrrole,

the intensity of the Soret band is slightly larger than of the Q band in the absorption spectrum (51). The typical phytochrome spectrum is obtained only if tetrapyrrole is covalently and non-covalently bound to the protein (52).

Linear tetrapyrrole contains four pyrrole rings A-D linked by methine bridges AB, BC, CD and forms one of the largest π-conjugated systems among natural chromophores of photoreceptor proteins. The tetrapyrrole structure in the Pr-state phytochrome is ZZZssa (configuration: C5-Z, C10-Z, C15-Z; conformation: C5-syn, C10-syn, C15-anti) (32, 33, 39, 42, 49). The most common tetrapyrroles found as phytochrome chromophores are biliverdin, phytochromobilin and phycocyanobilin (Figure 1.3) which bind to bacterial, plant and cyanobacterial phytochromes, respectively (12, 14). The phytochrome's cysteine residue binds to the $C3^1$ atom of phytochromobilin or phycocyanobilin and the $C3^2$ atom of biliverdin (Figure 1.3) (31, 53). Two types of biliverdin addition are possible: 1,4-addition as in the phytochrome from *D. radiodurans* (39) and 1,2-addition as in the phytochrome from *A. fabrum* or *P. aeruginosa* (40, 54). These tetrapyrroles also vary in the number of double-bonds. Phytochromobilin with respect to biliverdin has one double-bond reduced at ring D, and phycocyanobilin with respect to phytochromobilin has a reduced bond at ring A. The reduced size of the π-conjugated system results in a blue-shifted absorption spectrum of plant phytochromes and even more blue-shifted spectra of cyanobacterial phytochromes. Cyanobacteriochromes are relatives of phytochromes but for their photoconversion only the GAF domain is sufficient (55-59). This domain may naturally bind phycocyanobilin, biliverdin or phycoviolobilin, with the reduced methine bridge AB, at the terminal ring and/or at the methine bridge, disrupting the π-conjugated system (55-59). Such a huge variety of the π-conjugated system sizes within different cyanobacteriochromes enables them to absorb light in a wide range, from blue to red (55, 60).

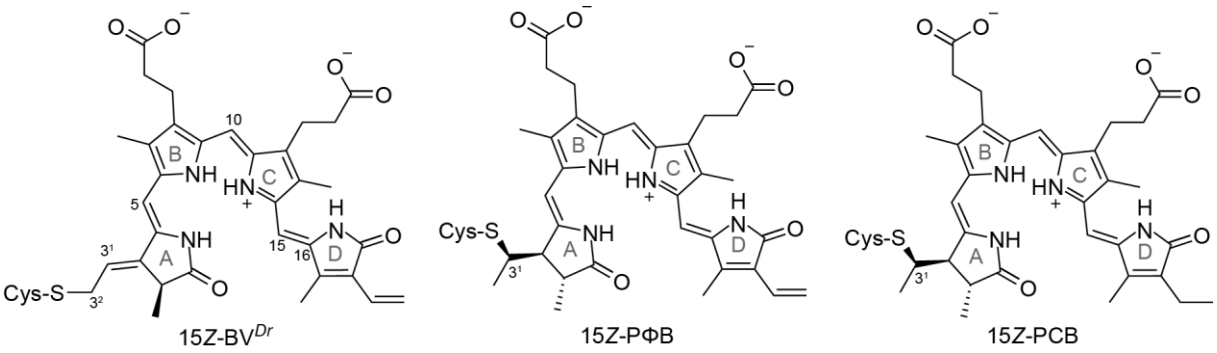

Figure 1.3. Chemical structure of biliverdin (BV), phytochromobilin (PΦB) and phycocyanobilin (PCB) tetrapyrrole chromophores (all in ZZZssa) bound to bacterial, plant, cyanobacterial phytochromes, respectively. Biliverdin is shown with its configuration of ring A as it binds to DrBphP phytochrome.

In the Pr state, phytochromes feature a spectrum with a shoulder on the blue edge of the Q band, the so-called blue shoulder. This shoulder is more pronounced in low temperature (-140°C) experiments (61, 62) and if a sterically locked tetrapyrrole in 15Z configuration is bound to the phytochrome (52, 63). The intensity at the shoulder decreases in microcrystals as compared to the protein in solution, whereas intensity of the Q band remains the same (64). Measurements in solution showed that at higher pH the intensity of the Q band and its blue shoulder decreases and the ratio between the blue-shoulder intensity and the Q-band maximum intensity increases (62, 65, 66). The decrease of the Q-band intensity was assigned to a tetrapyrrole deprotonation (62, 65, 66), however computations showed that the neutral deprotonated tetrapyrrole has a blue shift (67, 68). A blue shift of the absorption band upon pH increase was observed only in one study (69), which contradicts the previous findings where no spectral shift was observed (66). At higher temperature, the Q-band maximum blue-shifts and its intensity decreases, whereas intensity of the blue shoulder slightly increases (70). In some cyanobacterial phytochromes (e.g. SyB Cph1), there is almost no pronounced blue shoulder (71). The presence of the pronounced blue shoulder varies among cyanobacteriochromes and in the spectra of some proteins it is completely absent (72). The interpretation of the blue shoulder origin is not consistent in the literature. It was interpreted as a contribution of the 0-2 vibronic absorption of tetrapyrrole (73) as well as an evidence for the heterogeneity of the ground state in phytochromes (74-76). It was also suggested that phytochrome heterogeneity may be related to the different protonation states of

tetrapyrrole (66, 69) or of the highly conserved histidine (H260 in DrBphP) located above the tetrapyrrole (66).

1.2.2 Tetrapyrrole protonation

The protonation state of linear tetrapyrrole in solution and in phytochrome proteins was studied by experimental and computational methods. In solution, free tetrapyrroles are neutral in a neutral buffer and are protonated in an acidic buffer (77). In the literature there is a consensus that in the phytochrome protein all four pyrrole rings of tetrapyrrole are protonated under physiological conditions. Based on resonance Raman and Fourier-transform infrared spectroscopy it was proposed that tetrapyrrole is protonated (78, 79), however, it was noted that the signals can be interpreted differently (80). In later studies, the phytochrome spectral signatures obtained with Fourier-transform infrared spectroscopy (81) and resonance Raman spectroscopy (61, 82-84) were interpreted similarly, that tetrapyrrole is protonated. The protonated tetrapyrrole was also shown in NMR studies on different proteins such as cyanobacterial phytochrome Cph1 from *Synechocystis* PCC6803 and SyB-Cph1 from *Synechococcus* OSB' (84, 85).

Computationally the protonation state of tetrapyrrole was also addressed. A computational study showed that the C15=C16 isomerization of tetrapyrrole, as it occurs in phytochrome, is energetically more favorable in the protonated tetrapyrrole than in the neutral tetrapyrrole (86, 87), indicating that the photoreaction occurs with the protonated tetrapyrrole. As shown in several computational studies, the assignment of the positive charge on the tetrapyrrole skeleton can vary between four resonance structures (Figure 1.4) (67, 87, 88). The ground state geometry of tetrapyrrole is best described by resonance structures with a positive charge on rings B and C (89), which were shown to be the most acidic as computed for phytochromobilin (67). Computational studies also showed that neither isomerization at ring D nor excitation significantly changes the pKa of the tetrapyrrole (67, 90) which suggests that the observed changes in pKa are not determined by the properties of the tetrapyrrole but instead are rather induced by a protein (67). Computations also indicated that excitation energies of the neutral tetrapyrrole, in particular phytochromobilin, with one deprotonated ring A, B, C, or D are blue-shifted with respect to the fully protonated tetrapyrrole (67, 68).

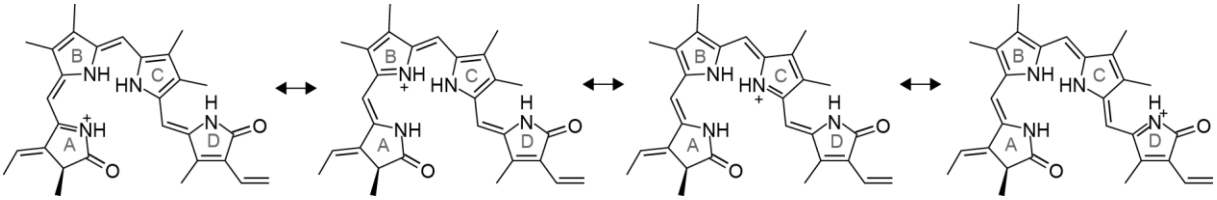

Figure 1.4. Chemical structure of the tetrapyrrole skeleton resonance structures.

The phytochrome spectrum is sensitive to pH as well as X-ray and light irradiation. UV/visible spectroscopy demonstrated that the pKa is increased by at least 3 units in the Pfr sate (pKa > 11) compared to the Pr state (pKa ~7.6) of the bacterial Agp2 phytochrome (65). The pH titration experiments showed that an increase in pH reduces the Q-band intensity, which was assigned to a tetrapyrrole deprotonation (62, 65, 91). However, the relative increase of the blue-shoulder intensity as compared to the Q-band maximum (62, 65, 66, 92) was not explained. X-ray radiation also reduces the absorption band intensity, which was explained as an X-ray-induced tetrapyrrole deprotonation (93). The photoreaction induces a tetrapyrrole deprotonation which is part of the phytochrome photoactivation mechanism (61).

Interactions in the active site of the phytochrome play a role on the tetrapyrrole protonation properties. Mutational analysis together with the UV/visible spectroscopy and resonance Raman spectroscopy demonstrated that the highly conserved histidine H260 (62, 66) and aspartate D207 (62) (DrBphP numbering) are important for stabilizing positive charge on the tetrapyrrole chromophore (62, 66). If one of these two residues are mutated to alanine, the intensity of the Q band is reduced and no Pfr spectra is formed as it has been shown for the bacterial Agp1 phytochrome (62).

1.2.3 Tetrapyrrole double-bond isomerization

The source of phytochrome photochromism is the double-bond isomerization of the linear tetrapyrrole chromophore. The 15Z/15E double-bond isomerization of tetrapyrrole (ZZZssa) as a photoreaction in phytochromes was indicated by the presence of the 15Z isomer in the Pr state and the 15E isomer in the Pfr state of phytochrome (Figure 1.5). The presence of such tetrapyrrole isomers in the Pr and Pfr states was indicated based on structures of the chromophores isolated from Pr- and Pfr-state phytochromes, NMR studies and resonance Raman spectroscopy (82, 94-99). The tetrapyrrole 15Z/15E isomerization and ring D rotation in phytochrome protein was later

confirmed by X-ray crystallography (34, 40, 41, 100) and NMR studies (101). In a single report it was suggested that ring A can rotate instead of ring D based on observations on the cyanobacterial phytochrome SyB-Cph1 from *Synechococcus* OSB' (102).

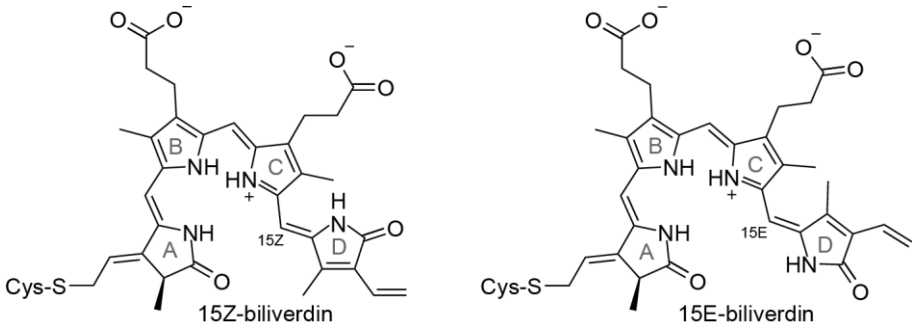

Figure 1.5. Chemical structure of tetrapyrrole with 15Z and 15E configuration.

The photochemical reactivity of the linear tetrapyrrole was extensively studied computationally. The computational study of the intrinsic chromophore properties indicated that rotation between ring B and C is energetically most favorable, whereas rotation of ring A or ring D is less favorable (87, 88). However, protein constrains and interactions in the active site restrict the rotation at the central methine bridge and favor the rotation of the terminal ring. The isomers and conformers with rotated ring A were computed, however only a change in the double-bond configuration does not provide a significant shift in the computed spectrum (103). The photoreactions for the ring D rotation by change of the configuration of the double bond (Z↔E) and the conformation of the single bond (s↔a) were computed and suggested that only the isomerization of the double bond occurs photochemically and switch in a conformation of the single bond is a thermal reaction(104, 105).

1.2.4 Computational studies of linear tetrapyrrole spectral properties

Large amounts of computational studies were performed to investigate the tetrapyrrole chromophore chemical structure in the phytochrome Pr and Pfr states and explain the spectral shift, especially before the X-ray and NMR structures became available and provided information about the tetrapyrrole structure in the phytochrome Pr and Pfr states. The computational studies addressed the absorption spectrum dependence on the conformation and configuration of the protonated tetrapyrrole. The accuracy of the methods used to compute excited-state energies was also addressed. Quantum chemical and QM/MM (quantum mechanics/molecular mechanics) calculations demonstrated that

computed spectra are in agreement with the experimental spectra (68, 106, 107). The excitation spectra were mostly computed with the TD-DFT (time-dependent density functional theory) method using different functionals. The computed spectra showed a systematic blue shift as compared to the experimental spectra, especially if a tetrapyrrole chromophore was considered for a so-called gas-phase computed spectrum (87, 105, 106). Depending on the used functional the blue shift varied: the smallest was with pure GGAs (Generalized Gradient Approximation), average – with hybrid GGAs (PBE0, B3LYP functionals) and the largest – with long-range-corrected hybrids (CAM-B3LYP, LC-ωPBE functionals) (87, 106). Increasing the size of the basis set may result in a slightly reduced blue shift (87, 105).

Quantum chemical calculations demonstrated that the spectral shifts are induced by the rotation of the terminal ring D but due to the change of a single-bond conformation (s↔a) rather than the change of the double-bond configuration (Z↔E) (104, 105, 108). The spectral blue shift was computed for the phycocyanobilin tetrapyrrole with a different conformation of ring A, ZZZasa as compared to ZZZssa (68). The latter was shown by crystallography and NMR studies to be present in the Cph1 phytochrome protein (42, 109). A similar spectral blue shift was also observed in the calculations of phytochromobilin with the respective conformations (107). On the contrary, a change of the conformation of ring D, from ZZZssa to ZZZsss in phytochromobilin, red-shifts the computed spectrum and changes the oscillator strength of the Q and Soret bands as such that the intensity of the Soret band exceeds the intensity of the Q band by several times (107). The computed spectral differences for the tetrapyrrole 15Z/E double-bond isomerization are much smaller than experimentally observed for the phytochrome Pr and Pfr states (104, 105, 108) and therefore do not explain the origin of the phytochrome Pr/Pfr spectral shift. It was even suggested that the spectral difference can be due to a change of the tetrapyrrole protonation state because a change from the deprotonated neutral tetrapyrrole to the protonated cationic or to the deprotonated anionic tetrapyrrole results in computed spectral red shift (110).

1.3 Excited-state decay in phytochrome

1.3.1 Photocycle and its intermediates

After photoexcitation, phytochrome undergoes a sequence of reactions which together make a photocycle (Figure 1.6 A). The intermediates formed during the photoreaction from Pr to Pfr were suggested based on stabilization at different temperatures (111) and on their different absorption (112, 113): first the Lumi-R intermediate is formed followed by the the meta-stable intermediates Meta-Ra and Meta-Rc. The primary reaction in the photocycle is the double-bond isomerization and Lumi-R formation shown by time-resolved UV/visual and resonance-Raman spectroscopy (80, 82, 95, 114). During the photoreaction from Pfr to Pr, first the Lumi-F intermediate is formed followed by the Meta-F intermediates (111). Time-resolved circular dichroism (CD) spectroscopy experiments showed that the intermediates have different CD spectra (113), indicating that during the photocycle phytochrome undergoes structural re-arrangements. Resonance Raman spectroscopy and transient UV/visible absorption spectroscopy combined with pH measurements indicated a proton release and uptake during the photocycle which were assigned to tetrapyrrole deprotonation and re-protonation (61, 82, 115). Ultrafast UV/visible spectroscopy demonstrated that photocycle kinetics depends on pH indicating rearrangement of the hydrogen-bonding network and proton transfer at the active site (91).

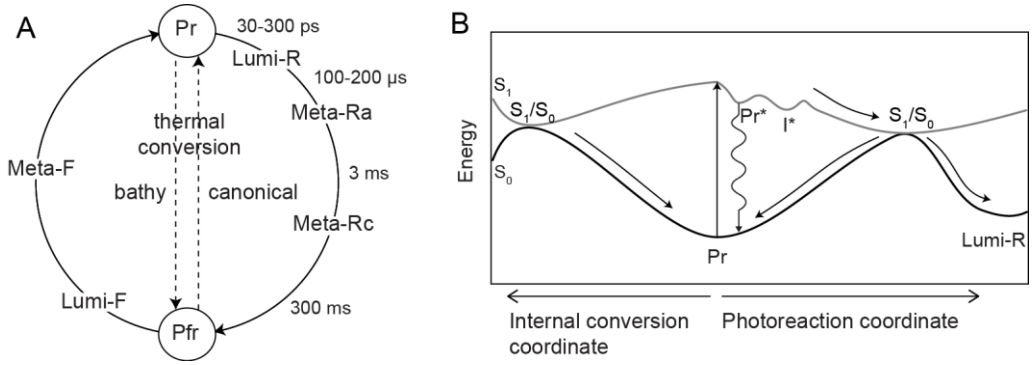

Figure 1.6. Photoreaction in phytochrome photoreceptors. A) Photocycle scheme (Adapted from Altoe et al. and Ihalainen et al. (116, 117). Canonical phytochromes undergo Pfr → Pr as a thermal reaction, whereas bathy phytochromes undergo Pr → Pfr. B) Excited-state decay: internal conversion, fluorescence, Lumi-R formation via intermediate I*.

1.3.2 Excited-state lifetime and Lumi-R photoproduct formation

Kinetics of the excited-state decay and photoproduct formation in phytochrome proteins was studied using ultrafast transient absorption and time-resolved fluorescence spectroscopy. The excited-state lifetime as well as the 15Z/15E double-bond isomerization reaction and the Lumi-R photoproduct formation varies depending on the chromophore nature and phytochrome. In plant and cyanobacterial phytochromes the Lumi-R formation is faster, about 30 ps (118-121), whereas in bacterial phytochrome it is usually slower, about 100-300 ps (47, 117, 122, 123). The longer excited-state lifetime correlates with the lower quantum yield of the Lumi-R formation (117, 122). Ultrafast UV/visible spectroscopy showed that there are other excited-state intermediates such as I*, formed on femtosecond-picosecond timescale before the Lumi-R formation (Figure 1.6 B); this can be interpreted as spectral heterogeneity (47) but might also indicate that the Lumi-R formation may be a multistep reaction (120, 122, 124, 125).

Mutations in the active site affect the excited-state lifetime and quantum yield of the Lumi-R intermediate formation. Destabilization of the hydrogen bonds between tetrapyrrole ring D and protein, e.g. by mutations of lysine and serine to methionine and alanine, respectively, reduces the excited-state lifetime and increases the Lumi-R quantum yield (47, 122). It was shown that mutations of H290 and Y263 in the DrBphP phytochrome (30), as well as a mutation of Y176 which is another tyrosine residue located next to the tetrapyrrole, in cyanobacterial and plant phytochromes increases fluorescence (126, 127). The D207A mutation or the truncation of the PHY domain increases the excited-state lifetime (47, 122, 128). The Y263F mutation increases the excited-state lifetime and decreases the Lumi-R quantum yield (128, 129). It was also shown that phytochrome kinetics is slower in D_2O, therefore the excited-state lifetime is longer and the Lumi-R quantum yield is raised (122). To explain the kinetic isotope effect it was suggested that phytochrome undergoes the excited-state proton transfer from the tetrapyrrole (122).

1.3.3 Excited-state reaction coordinates

After photoexcitation, excited-state decay includes not only the photoreaction leading to Lumi-R photoproduct formation (114) but also radiative decay (fluorescence) and unproductive radiationless internal conversion (117). CASPT2 calculations suggested that

in phytochrome there might be a reaction coordinate along the coordinate of the double-bond isomerization between tetrapyrrole rings B and C which is aborted and at the conical intersection results in a recovery of the ground state (Figure 1.6 B) (116). An excited-state proton transfer reaction was suggested as a possible pathway of an internal conversion reducing the excited-state lifetime (122). Time-resolved resonance Raman indicated that the branching along the photoreaction coordinate occurs after the photochemical Meta-R or Meta-F formation and results into ground-state recovery of 30-50 % of the population via a process called shunt reaction (130). Such internal conversion reactions can contribute to excited-state decay and reduce the excited-state lifetime as well as the Lumi-R photoproduct formation and the fluorescence quantum yield.

It was shown in different photoreceptors such as BLUF and cryptochromes that aromatic residues such as tyrosine or tryptophan located next to the chromophore can act as electron donors and participate in intermolecular charge transfer between the chromophore and protein residue (3). Although mutations of the tyrosine residues located next to the tetrapyrrole in the phytochrome active site increase its fluorescence (30, 126, 127), no charge transfer reactions were investigated or found so far in phytochromes.

To explain the complex excited-state decay in phytochromes, heterogeneity in the ground and excited states was suggested. Ultrafast transient absorption spectroscopy data were interpreted as excited-state heterogeneity in the excited state in Cph1, where the excited state can undergo photoreaction, radiative decay and internal conversion (69, 70, 124). It has been also suggested that the complexity of the excited-state dynamics is also contributed by the heterogeneity of the ground state. Based on time-resolved spectroscopy data the ground state was suggested to consist of two subpopulations: one with shorter excited-state lifetime resulting in photoproduct formation and another with longer excited-state lifetime and resulting in radiative decay and photoproduct formation (70, 131). Ground state heterogeneity was also supported by NMR studies and resonance-Raman spectroscopy (76, 101). There is no agreement on the ground-state heterogeneity and there are indications of the phytochrome homogeneity (73) or the heterogeneity which depends on the tetrapyrrole protonation state (66, 69).

1.4 Phytochrome application as molecular tools for cell and tissue studies

Phytochrome molecular properties make these proteins promising templates for engineering of various molecular tools for cell manipulation such as biomarkers, optogenetic tools and biosensors. Near-infrared absorption and emission of phytochromes is advantageous for imaging in deep tissues *in vivo* (23-25, 132, 133), because far-red light penetrates deep into tissue and shows lower light scattering by lipids as well as low absorption by water and other molecules such as hemoglobin and melanin which results in lower tissue autofluorescence (23, 134). Bacterial phytochromes are especially advantageous because mammalian cells produce the biliverdin chromophore endogenously and thus biliverdin addition prior to imaging is not needed (135). It was shown that engineered phytochrome variants can be used for photoacoustic imaging (136-139). Phytochrome-based fluorescent markers with a different color range of absorption and emission enable multiple color imaging (23, 25). The two templates used the most for phytochrome engineering as fluorescent tools are DrBphP and RpBphP1. So far, the engineered phytochrome variants with the largest fluorescence quantum yield (Φ) are IFP 2.0 (Φ = 8 %) and WiPhy2 (Φ = 9 %), based on the CBD of DrBphP phytochrome, and BphP1-FP (Φ = 13 %), based on the CBD of RpBphP1 phytochrome (140-142). One of the major limitations of phytochrome-based fluorescent markers is the low quantum yield of fluorescence which should be increased by blocking the radiationless excited-state energy dissipation pathways (23). The far-red-shifted Pfr-state phytochromes with good fluorescent properties may improve the signal to noise ratio and increase the color range of the fluorescent markers which is required for multicolor imaging (23).

Structural and spectral properties of phytochromes enable their application as optogenetic tools as well as biosensors. The photochromic property of the phytochrome is exploited by engineering them into optogenetic tools (26-28, 143, 144). Phytochromes can be engineered into biomarkers to sense protein-protein interactions (145-148), protease activity (147, 149) or heavy metals such as mercury (29). Phytochrome's involvement in heat tolerance in plants can be exploited for sensing temperature. Phytochromes which do not bind tetrapyrrole can have other functions such as redox sensing in bacteria (150).

1.5 Aims of this thesis

Phytochrome photoreceptors are not only used by multiple organisms to sense red light and regulate their physiological functions but can also be engineered as molecular tools. Despite the long history of phytochrome studies of over 50 years, the knowledge about the molecular mechanisms of spectral tuning, excited-state energy dissipation, and their detailed photoactivation mechanism is not complete. Although multiple X-ray crystal structures of both functional states, Pr and Pfr, are available and extensive mutagenesis analysis as well as computational studies have been performed, the molecular mechanism of the spectral red shift of the Pfr state is still not understood. The origin of the Q-band blue shoulder in the absorption spectrum and the reason for the changes in the absorption spectrum upon pH change are also unclear, although there are few suggestions. Since phytochromes might be engineered to fluorescent markers, it is important to study possible excited-state decay pathways of internal conversion which should be blocked in order to increase fluorescence quantum yield. Understanding how a phytochrome protein tunes quantum chemical properties of the tetrapyrrole chromophore will enable the rational-design of the phytochrome-based tools with improved properties and will advance their applications in cell and organismal biology and microscopy.

Tetrapyrrole is one of the largest chromophores present in natural photoreceptors. Its complex chemical structure is challenging not only by its size but also by a number of possible reactions. This thesis aims to answer fundamental questions about phytochromes:

i) What is the molecular mechanism of the spectral tuning between phytochrome Pr and Pfr states? If the spectral red shift originates from protein-chromophore interactions, how does protein dynamics influences these interactions?

ii) How tetrapyrrole deprotonation influences phytochrome spectrum and dynamics in the active site?

iii) Can charge transfer reactions contribute to the excited-state decay in phytochromes? Can the tyrosine and histidine residues located next to the tetrapyrrole chromophore act

as electron donors and take part in photoinduced charge transfer? How do manipulations of the newly-identified pathways may affect excited-state decay and dynamics in the active site? Which protein modifications should be done to shut down the newly-identified pathways in order to improve fluorescence properties of phytochrome-based fluorescent markers?

In this thesis the most extensively studied tetrapyrrole is biliverdin, the chromophore binding to bacterial phytochromes. Their spectra are the most red-shifted and the chromophore is naturally accessible in mammalian tissues, which makes these proteins the best templates for engineered phytochrome-based molecular tools. The canonical bacterial DrBphP phytochrome is one of the most extensively studied phytochromes; therefore, biliverdin which is present in the Pr state of this protein was studied and described in all three results parts. For studies of the Pfr-state properties, DrBphP and bathy PaBphP phytochromes were used. Plant phytochrome AtPhyB was studied in some results parts to make a comparison with bacterial phytochrome. In the AtPhyB phytochrome models, a spectral blue shift was expected, whereas other properties were expected to reproduce the results obtained for the bacterial phytochrome models.

2 Computational methods

2.1 Quantum chemical calculations

2.1.1 Software

The models for the quantum-chemistry calculations were prepared using the HyperChem software, release 8.0.8 for Windows (151) and the ChemCraft software, version 1.7 (152). If not stated otherwise, quantum chemical calculations were carried out using the Firefly (versions 8.1.0, 8.1.1, 8.2.0) package (153) which is partially based on the GAMESS US source code (154). Excited-state calculations with CAM-B3LYP functional were performed using Gaussian, version 09 (155). The computed spectra were plotted using the MATLAB software, version 2017a (156).

2.1.2 Composition of the models

Initial coordinates of all computed tetrapyrrole-cysteine adducts and active-site cluster models were prepared using coordinates from the X-ray crystal structures of phytochromes (PDB: 2o9c, 3s7o, 5c5k, 3c2w, 4our, 2vea (33, 38-40, 42, 133)). The adducts contain biliverdin (BV), phytochromobilin (PΦB) and phycocyanobilin (PCB) with 15Z and 15E configuration binding to bacterial (DrBphP or PaBphP), plant and cyanobacterial phytochromes, respectively (Figure 2.1). For the adduct geometry the propionates bound to rings B and C, PropB and PropC, were substituted by methyl groups, and of the Cys residue only the –S-CH_3 group was kept. The active-site cluster models contain the adduct and other residues.

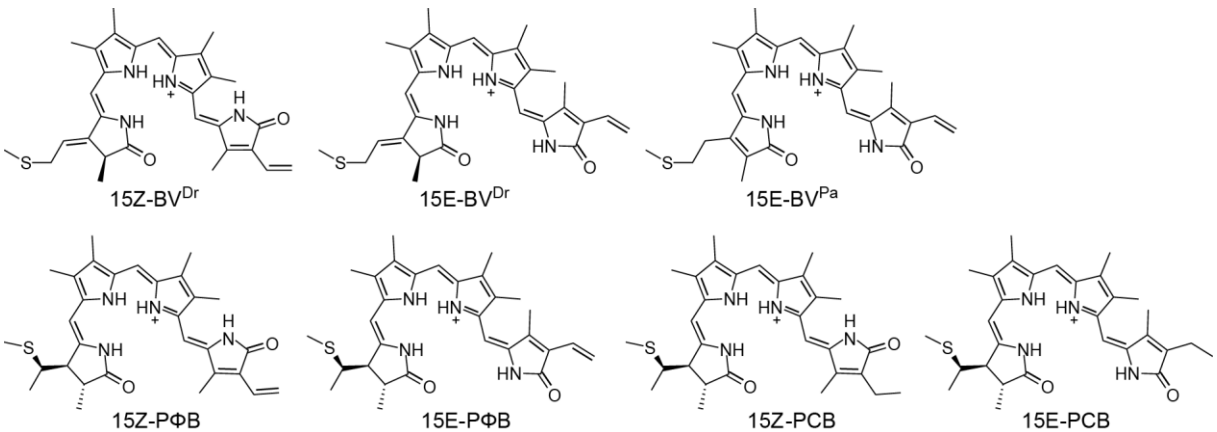

Figure 2.1. Chemical structures of the chromophores, tetrapyrrole-cysteine adducts, constituting the models of adduct or active-site cluster model.

Protonated tetrapyrrole-cysteine adducts (Sections 3.1.2-3.1.4, 3.2.2)

The adducts were prepared using X-ray crystal structures from the PDB: 2o9c, 3s7o, 5c5k, 3c2w, 4our, 2vea (Table 2.1). The adducts 15E-PΦB and 15E-PCB were prepared from crystal structures containing the 15Z-tetrapyrrole; therefore, ring D was manually rotated in order to obtain 15E configuration.

Table 2.1. Tetrapyrrole-cysteine adducts without propionates.

Adduct	PDB	Protein	State
15Z-BV^{Dr}	2o9c/3s7o*	DrBphP	Pr
15E-BV^{Dr}	5c5k	DrBphP	Pfr
15E-BV^{Pa}	3c2w	PaBphP	Pfr
15Z-PΦB	4our	AtPhyB	Pr
15E-PΦB	4our	AtPhyB	Pfr
15Z-PCB	2vea	Cph1	Pr
15E-PCB	2vea	Cph1	Pfr

*PDB 3s7o was used to get the geometry "fully optimized in intrinsic coordinates" which was used for benchmarking of XMCQDPT2 calculations (Section 3.1.2), whereas PDB 2o9c was used to get the geometry "fully optimized in Cartesian coordinates" which was used to compare the spectral shift between adducts (Sections 3.1.3 and 3.1.4) and to get the geometry "optimized in intrinsic coordinates with constrained six dihedrals" used to compare the spectral shift with deprotonated biliverdin adducts (Section 3.2.2).

Deprotonated tetrapyrrole-cysteine adducts (Section 3.2.2)

Adducts of deprotonated 15Z-BV^{Dr}, where one or two of rings A-D are deprotonated (Figure 2.2), were prepared from the crystal structure, PDB 2o9c. In total four singly-deprotonated biliverdin adducts and six doubly-deprotonated adducts were obtained.

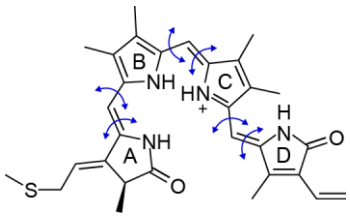

Figure 2.2. 15Z-BV^{Dr} with all four rings protonated. One or two shown protons were removed to get initial coordinates for the adducts with singly- or doubly-deprotonated tetrapyrroles. Blue arrows indicate frozen dihedrals during geometry optimization (in intrinsic coordinates) of protonated, singly- or doubly-deprotonated biliverdin.

Active-site cluster models (all models in Sections 3.1.5-3.1.6, At-Pr model at D_0-min in Section 3.3.3, Dr-Pr, Dr-Pfr, Pa-Pfr in Section 3.3.4)

The models Dr-Pr, Dr-Pfr, Pa-Pfr, At-Pr, At-Pfr representing the active site of bacterial DrBphP in Pr and Pfr state, PaBphP in Pfr state and plant AtPhyB in Pr and Pfr state,

respectively were prepared using crystal structures from the PDB: 2o9c, 4o0p, 5c5k, 3c2w, 4our. The At-Pfr model was prepared from the crystal structure of AtPhyB in Pr state, with analogy to Dr-Pfr and Pa-Pfr, by rotating tetrapyrrole ring D to acquire 15E configuration because the crystal structure of AtPhyB in Pfr state is unknown. The five main models contain protonated biliverdin with anionic propionates PropB and PropC, cationic Arg, anionic Asp and all histidines in neutral (Nε-H) protonation states (Table 2.2). In additional models the protonation state of H290 (according to the numbering in DrBphP) was varied or one of the side chains (H290 or D207) were removed (Table 2.3). In the models without H290, none of His atoms were left, whereas in the models without D207, the D207A substitution was performed.

Table 2.2. Five main active-site cluster models. In these models the protonation state of H260 (in Dr-Pr, Dr-Pfr), H277 (in Pa-Pfr), H403 (in At-Pr, At-Pfr) is neutral (Nε-H). Total charge, number of atoms and basis functions (BF) are indicated.

Model	Composition	Charge	Atoms	BF	PDB
Dr-Pr	protonated biliverdin, residues C24, D207, Y216, R254, H260, S272, S274, Y263, H290, R466, pyrrole water, two water molecules (330 and 331) between PropC and serines	0	214	2114	2o9c/ 4o0p*
Dr-Pfr	protonated biliverdin, residues C24, Y176, H201, D207, R222, H260, S272, Y263, H290, S468 and pyrrole water	-1	201	2019	5c5k
Pa-Pfr	protonated biliverdin, residues C12, Y163, D194, R209, H247, Y250, S259, S275, H277, R453, S459, pyrrole water and a water molecule (905) between PropC and H247	0	220	2164	3c2w
At-Pr	protonated phycocyanobilin, residues C357, D307, R322, R352, H358, Y361, H403, R582, pyrrole water and a water molecule between PropC and H358	1	195	1929	4our
At-Pfr	protonated phycocyanobilin, residues C357, D307 (D207 in Dr), R322, R352, H358, Y361, pyrrole water and a water molecule between PropC and H359	0	167	1669	4our

* - all residues except R466 were taken from PDB 209c

Table 2.3. Variants of active-site cluster models. Models contain H290 in different protonation states, or are without H290 or D207 (according to the numbering in DrBphP).

Variants	Dr-Pr	Dr-Pfr	Pa-Pfr	At-Pr	At-Pfr
neutral H290 (Nε-H)	+	+	+	+	+
neutral H290 (Nδ-H)	+	-	-	-	-
protonated H290	+	+	+	+	-
w/o H290	+	-	-	+	-
w/o D207*	+	+	+	+	+

* - neutral H290 (Nε-H) was present

Reduced-size active-site cluster models (Sections 3.2.3 and 3.3.2)

The models of wild-type and D207H mutant of bacterial DrBphP in Pr state were prepared using crystal structures 2o9c and 3s7o, respectively. The models contain protonated biliverdin with protonated PropB and anionic PropC, residues C24, D207 or H207, H260, S272, S274, Y263 and the pyrrole water. The main models contain neutral H260 and all possible protonation states for D207 or H207 (Table 2.4). Additionally, the model containing protonated H260 and deprotonated D207 was also prepared. One model containing deprotonated biliverdin (at ring C) with anionic PropB and PropC was prepared with neutral H260 (Nε-H) and deprotonated D207.

Table 2.4. Protonation state in reduced-size active-site cluster models. All models contain protonated biliverdin except the neutrBV-protH260 model, which contains neutral biliverdin deprotonated at ring C.

Model	H260	D207	H207	Charge
D207*	neutral (Nε-H)	deprotonated	-	-1
D207(H)	neutral (Nε-H)	protonated	-	0
H207(ε)	neutral (Nε-H)	-	neutral (Nε-H)	0
H207(δ)	neutral (Nε-H)	-	neutral (Nδ-H)	0
H207(H)	neutral (Nε-H)	-	protonated	+1
H260(H)-D207	protonated	deprotonated	-	+1
neutrBV-protH260	protonated	deprotonated	-	+1

* - model name "protBV-neutrH260" is used in Section 3.2.3

Increased-size active-site cluster models for computation of CT states (At-Pr model in Section 3.3.4)

The active-site model of AtPhyB in the Pr state was prepared using X-ray structure 4our. The composition of the model is protonated phytochromobilin with anionic PropB and PropC, Y104, Y276, E296, P297, Y298, Y303, anionic D307, I308, R322,R352, H355, G356, C357, H358, S359, Q360, Y361, M362, A363, N364, M365, G366, S367, I368, A369, S370, H403, R578, M579, H580, P581, R582, pyrrole water and three water molecules next to phytochromobilin ring D (Figure 3.47). Additionally, two water molecules were added: between PropC and S370 as well as between D307 and Y276. In the model all His are neutral (Nε-H), all Asp are anionic and all Arg – protonated, although only the backbone of R358 was taken.

In order to compute spectra, several different fragments of the optimized model were cut out: 1a (the largest), 1b and 1c (the smallest). Their composition is shown in Table 2.5 and Figure 3.48.

Table 2.5. Increased-size At-Pr model. Composition during model optimization and model fragments used to compute spectra.

Model/fragment	Composition
Fragments A, B, C	Phytochromobilin, Y276, Y303, D307, I308, R322, R352, C357, H358, S367, S370, H403, R582, PW, 3 water molecules
Fragments A, B	Y104, H355, R578, M579,
Fragment A	E296, P297, Y298,
only during optimization	G356, S359, Q360, Y361, M362, A363, N364, M365, G366, I368, A369, H580, P581,

2.1.3 Geometry optimization

Geometry optimization of the adduct and cluster models was conducted with density functional theory corrected for dispersion (DFT-D) (157). The optimization was done in Cartesian coordinates using the PBE0 functional and the standard cc-PVDZ basis set (158) was used, if not stated otherwise. In few calculation the B3LYP (159, 160) functional and 6-31G* basis set were used as described below. The geometry optimizations in Cartesian coordinates were performed using second-order optimization (METHOD=GDIIS). For the increased-sized cluster model of AtPhyB, the optimization of 10 steps using the Hartree-Fock (HF) method was done prior the PBE0 optimization. The adducts were fully optimized, whereas for the cluster models the particular number of optimization steps was performed.

Ground (S_0) state

The ground-state geometries (S_0-min) of all models were obtained by geometry optimization with the restricted R-DFT geometry optimization.

Tetrapyrrole-cysteine adducts for the benchmark calculations of XMCQDPT2 were fully optimized in intrinsic coordinates (Section 3.1.2). Phytochromobilin-cysteine adducts used to study the effect of the geometry optimization procedure on the excited-state energies were optimized in intrinsic and Cartesian coordinates (Section 3.1.3). Additional geometries for the phytochromobilin-cysteine adducts in Section 3.1.3 were obtained by the optimization with PBE0/6-31G*, B3LYP/cc-PVDZ, B3LYP/6-31G* in Cartesian

coordinates. Adducts used for spectral shift calculations were optimized in Cartesian coordinates (Section 3.1.4). Adducts with protonated, singly- and doubly-deprotonated biliverdin discussed in Section 3.2.2. were optimized in intrinsic coordinates with frozen six dihedral angles between adjacent rings as shown in Figure 2.2.

The majority of the cluster models was optimized for 120 steps. During the first 20 steps of optimization, the coordinates of the H−N groups in the histidine side chains were frozen. During the following 100 steps, the coordinates of all atoms of the cluster model were optimized. The Dr-Pr, Dr-Pfr, Pa-Pfr, At-Pr, At-Pfr models without D207 or H290 (according to the numbering in DrBphP) as shown in Table 2.3 (results with these geometries are described in Section 3.1.6, Table 3.7) were optimized for 20 steps starting from the corresponding wild-type models with all residues present and the same protonation state of the histidines. For the increased-sized cluster model of AtPhyB in Pr state (Table 2.5), an optimization of 10 steps using the HF method was done prior the 100 steps of PBE0/6-31G* optimization.

Duplet ground (D_0) state

The duplet-ground-state geometry (D_0-min) of the At-Pr models was obtained by geometry optimization with the unrestricted U-DFT geometry optimization (an additional electron was added to the system). The D_0 state corresponds to the CT_0 state where an additional electron is localized on the tetrapyrrole. During the first 20 steps of optimization, the coordinates of the H−N groups in the histidine side chains were frozen. During the following 100 steps, the coordinates of all atoms of the cluster model were optimized.

Excited (S_1) state

Tetrapyrrole-cysteine adducts with protonated or singly-deprotonated biliverdin, discussed in Section 3.2.2., were optimized with the TD-DFT method in intrinsic coordinates with frozen six dihedral angles between adjacent rings as shown in Figure 2.2. Coordinates of the crystal structure (PDB 2o9c) were taken as starting geometries.

The excited-state geometries (S_1-min) of all models (D207/protBV-neutrH260, H207ε, neutrBV-protH260) were obtained by geometry optimization with the TD-DFT method

starting from the S0–min geometry. 30 steps of optimization in Cartesian coordinates were performed on models with some atoms changed and constraints to ensure that the S_1 state and not CT_0 is the first excited state in the TD-DFT calculation and optimization proceeds in the correct state. For the D207 and neutrBV-protH260 models, the OH fragment of Y263 was replaced by an H atom and the carboxylate of D207 was protonated. For the D207 model, the carboxylate of PropC was also protonated. All three models were optimized with all fragments of the amino acid residues including C24, the carboxylates of PropB and PropC and the pyrrole water being constrained. After geometry optimization, the particular atoms of Y263 and the carboxylates (PropC or D207) were changed back and this final geometry was considered as S_1-min geometry.

The S_1'-min geometry of the H207ε model was obtained by geometry optimization with the R-DFT and TD-DFT methods starting from the CT_0H-min geometry. At the CT_0H-min geometry, the first excited state computed with the TD-DFT method corresponds to the CT_0H state and not to the S_1 state. In order to obtain a starting geometry with an increased energy of the CT_0H state, the neutral H260 was extracted, fully optimized in the S_0 state with the R-DFT method in Cartesian coordinates with frozen coordinates of the CD2, CE1, CB atoms and then inserted back to the CT_0H-min geometry. This was followed by model optimization in the S_1 state with the TD-DFT method for 30 steps in Cartesian coordinates with all fragments of the amino acid residues including C24, the carboxylates of PropB and PropC the and pyrrole water being constrained. During the optimization, PropC was protonated, afterwards the proton was removed to constitute S_1'-min geometry.

Excited (CT_0) state

The radical-pair geometries CT_0Y-min of the D207 model and CT_0H-min of the H207ε model were obtained by geometry optimization with the TD-DFT and U-DFT method, starting from the S_0–min geometry. Optimization was performed with some atoms changed and constraints to ensure that the particular CT_0 state is optimized.

For the D207 model, during the initial 50 steps of optimization with the TD-DFT method in the CT_0Y state, the coordinates of the green- and black- coloured atoms were frozen (Figure 2.3). Then, the hydrogen atom of the OH group of Y263 was manually

moved toward the COO group of D207 which resulted in crossing of the CT_0Y and S_0 states. Geometry optimization was continued in the triplet radical-pair CT_0Y state with the U-DFT method for 200 steps with the coordinates of the black-coloured atoms frozen to prevent large movements of the S274 side chain and D207 backbone.

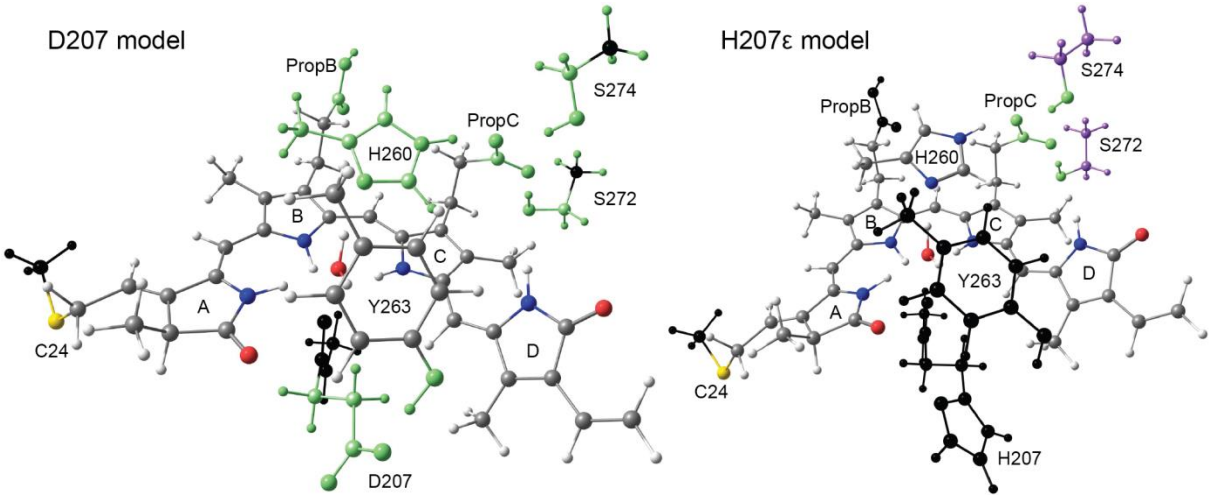

Figure 2.3. Constraints used for geometry optimization in the excited state. Atoms shown in black, green and purple were frozen during some steps of optimization in order to obtain CT_0Y-min geometry of the D207 model, CT_0H-min and S_1'-min geometries of the H207ε model.

For the H207ε model, the Hε atom of H260 was manually moved toward the carboxylate group of PropC in order to lower the CT_0H-state energy and simultaneously increase the S_1-state energy, followed by proceeding the optimization with the TD-DFT method in the CT_0H state. During the initial 50 steps of optimization, the coordinates of the green-, purple- and black-coloured atoms were frozen (Figure 2.3). During the following 100 steps of optimization, the coordinates of the purple- and black-coloured atoms were frozen. During the final 140 steps of optimization, the coordinates of the black-coloured atoms were frozen. Constraining the black-coloured atoms was necessary to avoid the CT_0H/CT_0Y state crossing during geometry optimization, after which the optimization would continue in the CT_0Y state instead of the CT_0H state.

2.1.4 Excited-state energy calculations at the optimized geometry

XMCQDPT2-SAN-CASSCF(M,L)

At the optimized geometry, the energies were computed with the HF/cc-PVDZ method. The molecular orbitals (MOs) obtained from the HF calculations were used for the complete-active-space self-consistent-field (CASSCF) calculations with equal state

averaging (SA). The zeroth-order wave function SA*N*-CASSCF(*M,L*), containing the active space of *M* electrons, *L* MOs and *N* number of states used in energy averaging, was used for the multireference multiconfigurational perturbation theory method to the second order XMCQDPT2, implemented in the Firefly software (161). The XMCQDPT2 energies were computed with the modified zeroth-order Hamiltonian (IFITD=5) and the intruder-state avoidance shift (EDSHFT=0.02) if not indicated otherwise.

For the benchmark of the CASSCF calculations using tetrapyrrole-cysteine adducts, different active spaces were compared. SA7-CASSCF(6,5) was the mostly used active space (containing tetrapyrrole MOs) for the active-site cluster models. In Section 3.3 also other active spaces including MOs of the electron donor residues were used.

TD-PBE0, TD-CAM-B3LYP, CIS

At the optimized geometries (S0-min) of Dr-Pr, Dr-Pfr, Pa-Pfr, At-Pr, At-Pfr models, the energies were computed with time-dependent DFT using PBE0 and CAM-B3LYP (162) functionals and with CIS (configuration interaction singles) method (163). Ten states were computed with each method. For the TD-CAM-B3LYP calculations the Gaussian software was used.

2.1.5 Evaluation of absorption and emission properties

To evaluate probability of absorption or emission, oscillator strengths f_{ij} were calculated from the energy gap ΔE of the corresponding transition and the transition dipole moment μ between ground ψ_i and first excited ψ_j state wave functions, using the formula

$$f_{ij} = \frac{2}{3} < \psi_i |\mu| \psi_j >^2 \Delta E \qquad (2.1)$$

where μ and ΔE are in atomic units.

The excited-state energies and the oscillator strengths *f*ij, computed with XMCQDPT2-SAN-CASSCF(M,L), were convoluted to excitation spectra: absorption spectra at the S_0-min, S_1-min, D_0-min, CT_0-min geometries and emission spectra at the S_1-min geometry. The spectra were convoluted by applying Gaussian broadening according to the formula

$$g(x) = f_{ij} e^{-(\frac{x-E}{\sigma})^2} \qquad (2.2)$$

where E is the excitation energy of the state and σ^2 is the variance. Most spectra were plotted in eV, with a variance of 0.0175 eV. However, a spectrum in Figure 3.46 in Section 3.3.3 was plotted in nm, therefore here a variance of 150 nm was used.

The radiative lifetime τ_{rad} was calculated from the energy difference ΔE between two states computed at the S_1-min geometry and μ between these two states, using the formula

$$\frac{1}{\tau_{rad}} = 2.14205 \cdot 10^{10} < \phi_i|\mu|\phi_j >^2 \Delta E^3 \quad (2.3)$$

where τ_{rad} is in seconds, μ and ΔE are in atomic units.

2.1.6 Electron-transfer theory

In order to evaluate charge transfer (electron transfer coupled to proton transfer) rates from the excited-state energies, the adiabatic Marcus theory and the generalized Mulliken-Hush scheme (164-166) were applied. The energies were computed with the XMCQDPT2-CASSCF(6,5)7 method in reduced-size active-site cluster models D207 and H207ε. Parabolic shapes of the potential energy surfaces (PES) for the S_1 and CT_0 states along the charge transfer reaction coordinate x (Figure 2.4) are assumed:

$$E_{S1}(x) = x^2 \quad (2.4)$$

$$E_{CT0}(x) = \frac{\lambda_{CT0}}{\lambda_{S1}}(x - \sqrt{\lambda_{S1}})^2 + \Delta E \quad (2.5)$$

λ_{S1} and λ_{CT0} are the reorganization energies of the S_1 and CT_0 sates, respectively. The reaction energy ΔE is represented by the difference of the two minima. The crossing of the parabolas defines the activation energy $E^{\#}$, required for the transition from S_1 to CT_0:

$$E^{\#} = E_{S1}(x) = E_{CT0}(x) \quad (2.6)$$

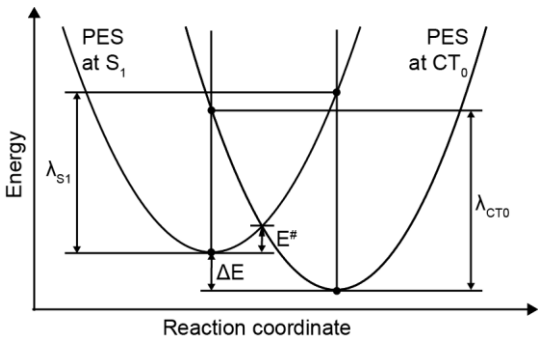

Figure 2.4. Potential energy surfaces (PESs) along the charge transfer reaction coordinate. Parabolic PES of the S_1 and CT_0 states were used for charge transfer energies calculations.

The electronic coupling V_{el} determines the strength of the interaction between two states and is calculated according to the generalized Mulliken-Hush scheme (166):

$$V_{el} = \mu \frac{\lambda_{CT0} - \Delta E}{\sqrt{\mathbf{d}_{12}^2 + 4\mu^2}} \quad (2.7)$$

where μ is the transition dipole moment and $\mathbf{d}_{12}$ is the difference of the dipole moments of the two states.

The charge transfer rate constant k_{CT} was calculated from $E^{\#}$ and V using formula:

$$k_{CT} = \frac{2\pi}{\hbar\sqrt{4\pi\lambda k_b T}} V_{el}^2 \cdot \exp\left(-\frac{E^{\#}}{k_b T}\right) \quad (2.8)$$

where k_b, ħ, T are Boltzmann constant, reduced Planck constant and standard ambient temperature (298.15 K), respectively; λ_{S1} and λ_{CT0} were used for the rate calculations of $S_1 \rightarrow CT_0$ and $CT_0 \rightarrow S_1$ reactions, respectively.

2.2 Molecular dynamics (MD) simulations

2.2.1 Software

Protein models for the MD simulations were prepared using the HyperChem software (151) and the VMD software, version 1.9.2 (167). MD simulations were performed using the NAMD software, version 2.11 (168) on the JURECA supercomputer (169). Analysis of the MD trajectories was done using the VMD analysis tools (RMSD Trajectory Tool) and MATLAB, version 2017a (156).

2.2.2 Biliverdin parameters

The published CHARMM22 force field parameters for the protonated biliverdin (170, 171) were used in all protein models, where biliverdin is protonated and in 15Z configuration with DrBphP cysteine attachment (protonated biliverdin in DrBphP-Pr). Based on these parameters, modifications were done to prepare parameters for protonated biliverdin in 15E configuration with any cysteine attachment (protonated biliverdin in Pfr state phytochrome including DrBphP-Pfr and PaBphP-Pfr) (Table 2.6). Additional modifications were done to encounter modified attachment of protonated biliverdin to cysteine in the PaBphP protein (protonated biliverdin in PaBphP) (Table 2.7). The H2C atom, bound to the C2C atom, was removed, and the HBC atom, bound to CAC, was added (Figure 2.5).

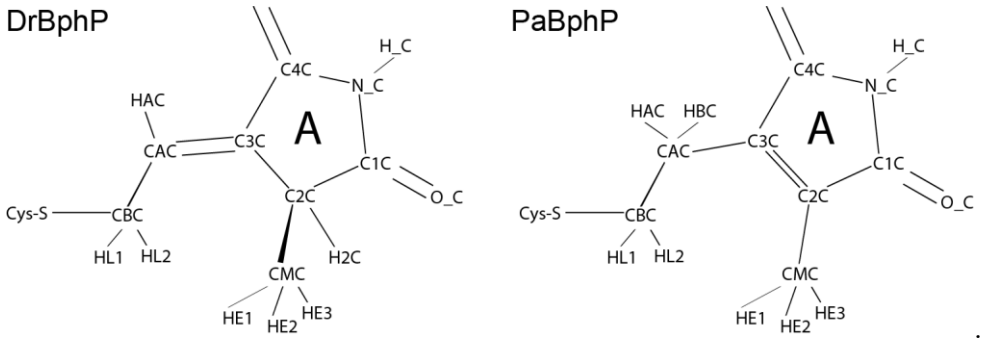

Figure 2.5. Atom names in the ring A of biliverdin bound to DrBphP and PaBphP protein used for force field parameters preparation.

For the neutral biliverdin (deprotonated at ring C) with DrBphP cysteine attachment, the charges on the atoms were modified, whereas parameters defining bonds, angles, dihedral angles and impropers were used the same as for the protonated biliverdin. The charges assigned to 15Z and 15E chromophores are the same. Four parameter sets with different charges were prepared: "a", "b", "c" and "d", (Table 2.8). All four were used to simulate neutral biliverdin in DrBphP-Pr but only parameter "a" was used to simulate DrBphP-Pfr. Usually parameter set "a" was used for the DrBphP-Pr models, unless specified otherwise. In all four parameter sets, the H atom of the ring C was removed and only charges on the tetrapyrrole system atoms were changed, whereas charges on PropB and PropC were kept as in protonated biliverdin. In the set "a", charge on rings A-D and the methine bridge BC was reduced, whereas on methine bridges AB and CD it was increased in order to smoothen differences between positive and negative parts of the tetrapyrrole. H atoms on the methyl groups of rings A and B and all atoms except N on ring C were kept with unchanged charges. Charge on the N atom of ring A was unchanged, on ring B increased by 0.1, on rings C and D decreased by 0.05 and 0.03, respectively. Charges on the other atoms were reduced by maximum 0.035 or increased by maximum 0.015 atomic charges. In the parameter set "b", charge on all atoms was reduced by 0.011, but on N atoms of rings A, B, D by 0.013, of ring C by 0.012. In the parameter set "c", charge on all atoms was reduced by 0.012, but on the N atoms of rings A, B, D by 0.014, of ring C by 0.015, however atoms on vinyl group of ring D were unchanged. In the parameter set "d", charge on all atoms was reduced by 0.0175, but on the N atoms of rings ring C by 0.015, however atoms on vinyl group of ring D and all methyl groups were unchanged.

Table 2.6. Force field parameters (dihedral angle) for protonated biliverdin in 15E configuration in MD simulations. Parameters for all phytochrome models in Pfr form (DrBphP and PaBphP).

Atom types	Dihedral angle, degree	Multiplicity	Force constant, kcal/mol
CPA CPY2 CA CPY5	180.00	1	11.80

Table 2.7. Force field parameters for protonated biliverdin in PaBphP in MD simulations. Parameters, modified for the PaBphP cysteine attachment to protonated biliverdin.

Atomic charges:

Atom name	Atom type	Atomic charge
CAC	CT2	0.018
HAC	HA	0.090
HBC	HA	0.090
C2C	CA	0.215

Bonds:

Atom types	Distance, Å	Force constant, kcal/mol/Å^2
CT2 CPY1	1.4900	230.00
CPM C	1.4711	250.00
CPM CT3	1.4850	230.00

Angles:

Atom types	Angle, degree	Force constant, kcal/mol/rad^2
HA CT2 CPY1	109.50	50.00
CT2 CT2 CPY1	113.00	70.00
CT2 CPY1 CA	124.10	61.60
CT2 CPY1 CPM	126.74	70.00
CA CPY1 CPM	116.00	52.00
CPY1 CPM C	116.50	40.00
CPY1 CPM CT3	122.30	45.80
CT2 CT2 SE	114.50	58.00
CT3 CPM C	115.90	45.80
CPM C O	121.00	80.00
CPM C NR1	109.50	20.00
CPM CT3 HA *	33.43	110.10

* Urey-Bradley parameters: constant 22.53 kcal/mol/Å^2, Urey-Bradley 2.1790 Å.

Dihedral angles:

Atom types	Angle, degree	Multiplicity	Force constant, kcal/mol
HA CT2 CPY1 CA	0.00	3	0.00
HA CT2 CPY1 CPM	0.00	3	0.00
CT2 CT2 CPY1 CA	0.00	3	0.00
CT2 CT2 CPY1 CPM	0.00	3	0.00
SE CT2 CT2 CPY1	45.00	2	1.40
HA CT2 CT2 CPY1	0.00	3	0.00
CT2 CPY1 CA CPY3	180.00	2	3.10
CT2 CPY1 CA NR1	180.00	2	3.00

CT2 CPY1 CPM C	0.00	3	3.00
CT2 CPY1 CPM CT3	180.00	2	3.10
CA CPY1 CA CPY3	180.00	2	3.10
CA CPY1 CA NR1	0.00	3	0.19
C CA CPY1 CA	0.00	3	0.04
CT3 CA CPY1 CA	180.00	2	3.10
CPY1 CPM C NR1	0.00	1	0.00
CPY1 CPM C O	180.00	1	1.40
CT2 SE CT2 CT2	10.00	3	0.70
CT2 SE CT2 CT2	88.00	1	1.10
C CPM CPY1 CA	0.00	3	0.04
CA CPY1 CPM CT3	180.00	2	3.10
CPY1 CPM CT3 HA	0.00	3	0.20
CT3 CPM C NR1	0.00	1	0.00
CT3 CPM C O	180.00	2	3.10
HA CT3 CPM C	0.00	3	0.20
CPM C NR1 H	180.00	2	2.50
CPM C NR1 CA	180.00	2	2.75

Impropers:

Atom types	Angle, degree	Force constant, kcal/mol/rad^2
CPY1 CPM CA CT2	0	0
CPY1 CT2 CT2 HA	180	29.4

Table 2.8. Force field parameters for neutral biliverdin (deprotonated at ring C) in DrBphP in MD simulations. Four parameter sets "a" – "d" with different atomic charges were used for DrBphP-Pr and one set "a" was used for DrBphP-Pfr.

Atom name	Atom type	Atomic Charges in parameter sets			
		"a"	"b"	"c"	"d"
CAC	CPM	-0.107	-0.093	-0.094	-0.0995
HAC	HA	0.098	0.112	0.111	0.1055
C1C	C	0.264	0.278	0.277	0.2715
H2C	HA	0.032	0.046	0.045	0.0395
N_C	NR1	-0.505	-0.568	-0.569	-0.5725
H_C	H	0.307	0.321	0.32	0.3145
C4C	CA	0.287	0.301	0.3	0.2945
C3C	CPY1	-0.185	-0.171	-0.172	-0.1775
C2C	CT1	0.29	0.304	0.303	0.2975
O_C	O	-0.47	-0.456	-0.457	-0.4625
CHD	CPY3	-0.351	-0.512	-0.513	-0.5185
HHD	HA	0.264	0.203	0.202	0.1965
C1D	CPA	0.275	0.364	0.363	0.3575
N_D	NR1	-0.443	-0.556	-0.557	-0.5605
H_D	H	0.271	0.295	0.294	0.2885
C4D	CPA	0.264	0.353	0.352	0.3465
C3D	CPB	-0.121	-0.102	-0.103	-0.1085

C2D	CPB	-0.061	-0.042	-0.043	-0.0485
CHA	CPM	-0.061	-0.122	-0.123	-0.1285
HHA	HA	0.219	0.308	0.307	0.3015
C1A	CPA	0.119	0.108	0.107	0.1015
N_A	NR1	-0.704	-0.666	-0.669	-0.669
C2A	CPY4	-0.038	-0.049	-0.05	-0.0555
C3A	CPB	-0.155	-0.166	-0.167	-0.1725
C4A	CPA	0.487	0.476	0.475	0.4695
C4B	C	0.446	0.465	0.464	0.4585
N_B	NR1	-0.51	-0.573	-0.574	-0.5775
H_B	H	0.395	0.414	0.413	0.4075
C1B	CA	0.422	0.441	0.44	0.4345
C2B	CPY5	-0.145	-0.126	-0.127	-0.1325
C3B	CPY6	-0.121	-0.102	-0.103	-0.1085
O_B	O	-0.437	-0.418	-0.419	-0.4245
CHB	CPY2	-0.398	-0.459	-0.46	-0.4655
HHB	HA	0.219	0.208	0.207	0.2015
CAB	CE1	-0.362	-0.343	-0.332	-0.332
HAB	HE1	0.277	0.296	0.307	0.307
CBB	CE2	-0.299	-0.280	-0.269	-0.269
HV1	HE2	0.159	0.178	0.189	0.189
HV2	HE2	0.123	0.142	0.153	0.153
CBC	CT2	0.018	0.032	0.031	0.0255
HL1	HA	0.048	0.047	0.046	0.0405
HL2	HA	0.048	0.047	0.046	0.0405
CMC	CT3	-0.144	-0.130	-0.131	-0.119
HE1	HA	0.038	0.027	0.026	0.038
HE2	HA	0.038	0.027	0.026	0.038
HE3	HA	0.038	0.027	0.026	0.038
CMD	CT3	-0.054	-0.035	-0.036	-0.024
HD1	HA	0.022	0.011	0.01	0.022
HD2	HA	0.022	0.011	0.01	0.022
HD3	HA	0.022	0.011	0.01	0.022
CMA	T3	-0.075	-0.086	-0.087	-0.075
HA1	HA	0.05	0.039	0.038	0.05
HA2	HA	0.05	0.039	0.038	0.05
HA3	HA	0.05	0.039	0.038	0.05
CMB	CT3	-0.048	-0.029	-0.03	-0.018
HB1	HA	0.044	0.038	0.037	0.049
HB2	HA	0.044	0.038	0.037	0.049
HB3	HA	0.044	0.038	0.037	0.049
CBD	CT2	-0.28	-0.28	-0.28	-0.28
HO3	HA	0.09	0.09	0.09	0.09
HO4	HA	0.09	0.09	0.09	0.09
CGD	CC	0.62	0.62	0.62	0.62
O2D	OC	-0.76	-0.76	-0.76	-0.76

O1D	OC	-0.76	-0.76	-0.76	-0.76
CBA	CT2	-0.28	-0.28	-0.28	-0.28
HO1	HA	0.09	0.09	0.09	0.09
HO2	HA	0.09	0.09	0.09	0.09
CGA	CC	0.62	0.62	0.62	0.62
O2A	OC	-0.76	-0.76	-0.76	-0.76
O1A	OC	-0.76	-0.76	-0.76	-0.76
CAA	CT2	-0.18	-0.18	-0.18	-0.18
HO5	HA	0.09	0.09	0.09	0.09
HO6	HA	0.09	0.09	0.09	0.09
CAD	CT2	-0.18	-0.18	-0.18	-0.18
HO7	HA	0.09	0.09	0.09	0.09
HO8	HA	0.09	0.09	0.09	0.09

2.2.3 Model preparation

The initial atomic coordinates for the protein models were taken from the crystal structures from the PDB database: 2o9c (CBD domain of DrBphP-Pr), 4o0p (CBD-PHY domains of DrBphP-Pr), 5c5k (CBD-PHY domains of DrBphP-Pfr with the F459W mutation), 3c2w (CBD-PHY domains of PaBphP-Pfr), 4cqh (fluorescent variant IFP2.0, engineered from CBD domain of DrBphP) (34, 38-40, 142). If multiple chains were present in the crystal structure, only chain A was used. Crystallographic water molecules were kept for protein model preparation. The pyrrole water molecule and two water molecules, located between biliverdin ring D, PropC and H290 were added to the 4o0p structure from the 2o9c structure after aligning both structures. The CBD domain was considered as residues 1-321 in DrBphP (and its engineered fluorescent variant IFP2.0) and as residues 1-308 in PaBphP. Missing atoms of the residues which were not resolved in the crystal structures, consisting of protein backbone and side chains, (Table 2.9) were added using the protein-building module of the HyperChem software. Missing atoms of poorly resolved side chains and hydrogen atoms were added using the VMD software. The protonation state of the titratable residues were standard (corresponding to protonation at pH=7): lysine and arginine – protonated, aspartate and glutamate – deprotonated, histidine except H260 and H290 (DrBphP numbering) – neutral. These two histidines are at the tetrapyrrole binding site, therefore various protonation states were assigned as described below. The biliverdin was "protonated" with a total charge of -1 because of the positively charged four-pyrrole-ring system (+1) and two negatively protonated propionates, if not stated that biliverdin was "neutral", where the total charge

is -2 because of the neutral four-pyrrole-ring system (0) and two negatively charged propionates.

To prepare the protein model from the crystal structure, the protein was solvated in a cubic water box with periodic boundary conditions using the *solvate* package within the VMD software. The cubic water box was created with a 15 Å layer of TIP3P water molecules around the protein. 150 mM sodium cations and an appropriate amount of chloride anions were added to neutralize the system. Few specific protein models were prepared from already simulated protein models as specified below.

Wild-type protein models

Wild-type models of DrBphP-Pr, DrBphP-Pfr and PaBphP-Pfr with protonated biliverdin are specified in Table 2.10. These models were prepared with initial coordinates taken from the PDB structures.

Special wild-type models with protonated biliverdin 15E configuration but with different conformations of the CBD and PHY domains of DrBphP were prepared differently (Table 2.11). 15E-CBD-Pr-PHY-Pr models were prepared from Dr-Pr-CBDPHY models with corresponding protonation states of H290, coordinates after 5 ns of equilibration taking as initial coordinates and then manually rotating ring D of the biliverdin. In contrast to the other models, these two were not equilibrated before the production run. For 15E-CBDPr models, the coordinates of the CBD domain and solvent (water and ions) atoms within 4 Å were taken after 5 ns of equilibration of Dr-Pr-CBDPHY models with corresponding protonation states of H290, then biliverdin ring D was rotates and the protein was additionally solvated and ionized (periodic cubic water box with a 15 Å layer of water, 150 mM sodium cations and an appropriate amount of chloride anions). To prepare 15E-CBDPr-PHYPfr model, the coordinates of the Dr-Pr-CBDPHY model with corresponding protonation state of H260 and H290 after 5ns of equilibration (for the CBD domain coordinates) and the 5c5k structure was aligned (for the PHY domain coordinates) and appropriate coordinates were used. The biliverdin ring D was rotated and the protein was solvated and ionized (periodic cubic water box with a 15 Å layer of water, 150 mM sodium cations and an appropriate amount of chloride anions). For the 15E-CBDPfr-PHYPr model, 5c5k (for the CBD domain coordinates) and 4o0p (for the

PHY domain coordinates) were aligned and then appropriate coordinates were used. The protein was solvated and ionized (periodic cubic water box with a 15 Å layer of water, 150 mM sodium cations and an appropriate amount of chloride anions).

Wild-type models of DrBphP-Pr and DrBphP-Pfr with neutral biliverdin were prepared with initial coordinates taken from the PDB structures are specified in Table 2.12.

IFP2.0 and PaBphP and their mutants

For the study of electron donor mutations, IFP2.0, PaBphP-Pfr (CBD-PHY) and their mutants were simulated Table 2.13. Wild-type and mutant models of IFP2.0 contained neutral (Nε-H) H260 and H290. Wild-type and mutant models of PaBphP contained neutral (Nε-H) H247 and protonated H277. Both wild-type models, IFP2.0 and PaBphP, were prepared from the crystal structures and solvated as indicated above (periodic cubic water box with a 15 Å layer of water, 150 mM sodium cations and an appropriate amount of chloride anions). For the initial coordinates of the mutant model, the coordinates of the wild-type model were taken after 10 ns or 30 ns of production run of IFP2.0 or PaBphP model, respectively. To prepare the mutant model, introduction of the mutation and removing one sodium ion in case of residue protonation state increase was done. In contrast to the wild-type models, all mutant models were not equilibrated before the production run. The length of the production runs for both wild-type models and all mutant models was 100 ns.

Table 2.9. X-ray crystal structures used to prepare protein models. Missing atoms of the residues which were not resolved in the X-ray crystal structures were added using HyperChem.

Structure (PDB)	Resolution	Protein	Missing residues
2o9c	1.45	DrBphP-Pr (only CBD)	-
4o0p	3.80	DrBphP-Pr	107-109,132-137, 401, 431-433, 458-462,*
5c5k	3.31	DrBphP-Pfr	454-459
3c2w	2.90	PaBphP-Pfr	396-407
4cqh	1.14	IFP2.0	130-137

*the pyrrole water molecule and the two water molecules between ring D, PropC and H290 were added from 2o9c X-ray crystal structure after aligning.

Table 2.10. Wild-type models with protonated biliverdin. Models were prepared from the X-ray crystal structures (PDB coordinates) taken as initial coordinates. All prepared models were minimized for 20000 steps and equilibrated for 5 ns. These models contain "protBV" in their name when they are compared to phytochrome with neutral biliverdin in the Results chapter. If the protonation state of H260 and H290 (according to the numbering in DrBphP) is other than neutral (Nε-H) and protonated, respectively, it is always indicated in the Results chapter.

Model name	Protein	State	Domains	Protonation state H260***	Protonation state H290***	PDB	Production run, ns
Dr-Pr-CBD[a]	DrBphP	Pr	CBD	neutral (Nε-H)	neutral (Nε-H)	2o9c	80
Dr-Pr-CBD[b]	DrBphP	Pr	CBD	neutral (Nε-H)	protonated	2o9c	80
Dr-Pr-CBD	DrBphP	Pr	CBD	neutral (Nε-H)	neutral (Nε-H)**	2o9c	0
Dr-Pr-CBD	DrBphP	Pr	CBD	protonated	neutral (Nε-H)	2o9c	20
Dr-Pfr-CBD	DrBphP	Pfr	CBD	neutral (Nε-H)	protonated	5c5k	80
Pa-Pfr-CBD	PaBphP	Pfr	CBD	neutral (Nε-H)	protonated	3c2w	80
Dr-Pr-CBDPHY	DrBphP	Pr	CBD-PHY	protonated	neutral (Nε-H)	4o0p	20
Dr-Pr-CBDPHY	DrBphP	Pr	CBD-PHY	protonated	protonated	4o0p	20
Dr-Pr-CBDPHY	DrBphP	Pr	CBD-PHY	neutral (Nε-H)	neutral (Nε-H)	4o0p	80
Dr-Pr-CBDPHY	DrBphP	Pr	CBD-PHY	neutral (Nε-H)	neutral (Nδ-H)	4o0p	80
Dr-Pr-CBDPHY[c]	DrBphP	Pr	CBD-PHY	neutral (Nε-H)	protonated	4o0p	430
Dr-Pfr-CBDPHY	DrBphP	Pfr	CBD-PHY	neutral (Nε-H)	neutral (Nε-H)	5c5k	80
Dr-Pfr-CBDPHY[d]	DrBphP	Pfr	CBD-PHY	neutral (Nε-H)	protonated	5c5k	80
Pa-Pfr-CBDPHY	PaBphP	Pfr	CBD-PHY	protonated	neutral (Nε-H)	3c2w	20
Pa-Pfr-CBDPHY	PaBphP	Pfr	CBD-PHY	protonated	protonated	3c2w	20
Pa-Pfr-CBDPHY	PaBphP	Pfr	CBD-PHY	neutral (Nε-H)	neutral (Nε-H)	3c2w	80
Pa-Pfr-CBDPHY	PaBphP	Pfr	CBD-PHY	neutral (Nε-H)	protonated	3c2w	80

*** - according to the numbering in DrBphP sequence (H247 and H277 in PaBphP);
** - histidine residue was rotated in comparison to the X-ray crystal structure; during equilibration run, rotates back, so production run was not conducted; stopped at equilibration run at step 64000;
a-c - alternative names in Section 3.2.4. are CBD-protBV-(εε), CBD-protBV-(εP), DrPr-protBV- (εP);
d - alternative names are 15E-CBD(Pfr)-PHY(Pfr) in Section 3.1.8 and DrPfr-protBV- (εP) in Section 3.2.5.

Table 2.11. DrBphP models with protonated 15E-biliverdin, neutral (Nε-H) H260 and different conformation of the CBD and PHY domains. Models were prepared from the coordinates of the other models after their equilibration or from the X-ray crystal structures (PDB coordinates) taken as initial coordinates. of DrBphP**.** All prepared models were minimized for 20000 steps and equilibrated for 0 or 5 ns.

Model name	Domains	H290	PDB	Equilibration run, ns	Production run, ns
15E-CBD(Pr)-PHY(Pr)	CBD-PHY	protonated	4o0p	0	80
15E-CBD(Pr)	CBD	protonated	4o0p	5	80
15E-CBD(Pr)-PHY(Pfr)	CBD-PHY	protonated	4o0p(CBD)/ 5c5k(PHY)	5	80
15E-CBD(Pfr)-PHY(Pr)	CBD-PHY	protonated	5c5k(CBD)/ 4o0p(PHY)	5	80

Table 2.12. DrBphP models with neutral biliverdin. Models were prepared from the X-ray crystal structures (PDB coordinates) taken as initial coordinates. All prepared models were minimized for 20000 steps and equilibrated for 5 ns. Force field parameters of neutral biliverdin (FF) are indicated. If FF is other than "a", it is always indicated in Results Sections 3.2.4 and 3.2.5.

Model name	State	Domains	Protonation state		PDB	FF	Prod. run, ns
			H260*	H290*			
CBD-neutrBV-(εε)	Pr	CBD	neutral (Nε-H)	neutral (Nε-H)	2o9c	a	100
CBD-neutrBV-(Pε)	Pr	CBD	protonated	neutral (Nε-H)	2o9c	a	100
CBD-neutrBV-(Pε)	Pr	CBD	protonated	protonated	2o9c	a	100
DrPr-neutrBV-(εε)	Pr	CBD-PHY	neutral (Nε-H)	neutral (Nε-H)	4o0p	a	100
DrPr-neutrBV-(εP)	Pr	CBD-PHY	neutral (Nε-H)	protonated	4o0p	a	100
DrPr-neutrBV-(εδ)	Pr	CBD-PHY	neutral (Nε-H)	neutral (Nδ-H)	4o0p	a	100
DrPr-neutrBV-(Pε)	Pr	CBD-PHY	protonated	neutral (Nε-H)	4o0p	a	100
DrPr-neutrBV-(PP)	Pr	CBD-PHY	protonated	protonated	4o0p	a	150
DrPr-neutrBV-(Pδ)	Pr	CBD-PHY	protonated	neutral (Nδ-H)	4o0p	a	100
DrPr-neutrBV-(PP)	Pr	CBD-PHY	protonated	protonated	4o0p	b	100
DrPr-neutrBV-(PP)	Pr	CBD-PHY	protonated	protonated	4o0p	c	100
DrPr-neutrBV-(PP)	Pr	CBD-PHY	protonated	protonated	4o0p	d	300
DrPfr-neutrBV-(Pε)	Pfr	CBD-PHY	protonated	neutral (Nε-H)	5c5k	a	100
DrPfr-neutrBV-(Pε)	Pfr	CBD-PHY	protonated	neutral (Nε-H)	5c5k	d	100
DrPfr-neutrBV-(PP)	Pfr	CBD-PHY	protonated	protonated	5c5k	a	100
DrPfr-neutrBV-(PP)	Pfr	CBD-PHY	protonated	protonated	5c5k	d	100
DrPr-neutrBV-(εδ→PP)	Pr	CBD-PHY	protonated**	protonated**	4o0p	d	200

* - according to the numbering in DrBphP sequence (H247 and H277 in PaBphP).

** - initial coordinates taken from DrPr-CBDPHY (neutral biliverdin, neutral (Nε-H) H260, neutral (Nδ-H) H290, force field parameters for neutral biliverdin "a") after 100 ns of production run, then subjected to 20000 minimization steps and then production run directly.

Table 2.13. IFP2.0 and PaBphP mutant models. The initial coordinates of mutant models were taken from the coordinates of the wild-type model after 10 ns (IFP2.0) or 30 ns (PaBphP) of production run. All prepared mutant models were minimized for 20000 steps and equilibrated for 0 ns.

Nr.	IFP2.0	PaBphP
1	Y216Q	Y163Q
2	Y216F	Y163F
3	Y216R	H247Q
4	Y216S	Y250F
5	H260Q	Y250Q
6	Y263F	H277R
7	Y263Q	H277K
8	Y263T	Y190F
9	H290Q	Y203F
10	Y198F	Y203R
11	Y198Q	Y185F
12	Y198T	Y185Q
13	Y176F	
14	Y176Q	

15 Y263F-H290Q
16 H260Q-Y263F-H290Q ("3-mutant")
17 Y176F-Y198F-Y216F-H260Q-Y263F-H290Q ("6-mut(Y176F)")
18 Y176Q-Y198F-Y216F-H260Q-Y263F-H290Q ("6-mut(Y176Q)")

2.2.4 Simulation details

For atoms of all proteins the CHARMM22 force field parameters were used, and water molecules were described with TIP3P parameters (172). For the prepared models (in a periodic cubic water box with a 15 Å layer of water, 150 mM sodium cations and an appropriate amount of chloride anions) energy minimization was done for 20000 steps. If not specified otherwise in the previous section (Section 2.2.3), this was followed by water box equilibration at 300 K, for total 5 ns with 2 fs integration step. The simulation was performed in the isobaric-isothermal (NPT) ensemble using a combination of Langevin dynamics (173) and Nosé-Hoover thermostat (174). During the equilibration run selected atoms of the protein (backbone atoms resolved crystallographically) and the oxygen atom of the pyrrole water were constrained by harmonic potential restrains, described with a quadratic potential energy function. After water box equilibration, the production run was performed for 20-430 ns (as indicated in Tables 2.10-2.13) with 2 fs integration step in isobaric-isothermal (NPT) ensemble at 300 K.

To study the dynamics of phytochrome with protonated and neutral biliverdin over longer period of time, production runs of 300-430 ns were performed.

2.2.5 Observables from MD simulations

Root-mean-square deviations (RMSDs) for the whole protein, its backbone or the chromophore were computed after the alignment of protein atoms coordinates on the first frame of the production run.

For the statistics of the distances and dihedral angles presented in the Results chapter, the Kernel smoothening (https://de.mathworks.com/help/stats/kernel-distribution-1.html) was performed to plot the Kernel distribution, which is a non-parametric representation of the probability density function and used to estimate univariate and bivariate data.

3 Results

In this study, the excited-state decay pathways and spectroscopic properties of phytochrome proteins were investigated. The following results obtained from quantum chemical calculations and MD simulations were divided into three parts. The first part addresses the molecular mechanism of the spectral red shift between thermally stable Pr and Pfr forms. In the second part, the properties of the chromophore deprotonation in the active site are presented and the origin of the Q-band blue shoulder in the experimental spectrum of the Pr-state phytochrome is proposed. The last chapter presents the existence of the charge transfer states, their contribution to the excited-state decay, fluorescence quenching and photoproduct formation, as well as suggestions for the strategies to increase fluorescence in phytochrome-based markers.

The numbers of the phytochrome residues are indicated in the text according to the DrBphP sequence, if not specified otherwise, and the atom names of the tetrapyrrole and phytochrome residues are as shown in Appendix A.

3.1 Red to far-red spectral tuning between Pr and Pfr form

3.1.1 Background and overview

The phytochrome protein photoswitches between structurally and spectrally different Pr and Pfr states by undergoing double bond isomerization of the linear tetrapyrrole chromophore bound to a cysteine residue. The red-shifted spectrum of the Pfr state ensures the light-induced switch of the protein function. Computational studies demonstrated that there is no significant spectral shift due to the tetrapyrrole isomerization (104, 105, 108), hinting that the origin of the red shift is not the isomerization of the chromophore but rather other factors present in the active site of the Pfr-state phytochrome. The red-shifted Pfr-state spectrum can be formed only in the complete photosensory module of phytochromes (47, 48), which is comprised of the CBD and PHY domains, and on a much longer timescale than the double-bond isomerization (117). The interactions causing the spectral-shift should be related to the conformational changes in phytochromes and linked to phytochrome signaling. However,

the molecular mechanism of spectral tuning in phytochromes remains unknown yet but is of high interest not only for fundamental understanding of the phytochrome function but also for rational design of phytochrome-based molecular tools.

Here, quantum chemical calculations were performed to compute the spectra of the Pr- and Pfr-state phytochrome models and elucidate the molecular origin of the red shift. For computations of excited-state energies, the XMCQDPT2 method (161) was used. Firstly, the selection of the active space, required by this method, was studied in tetrapyrrole-cysteine adducts. Then, it was investigated how the tetrapyrrole geometry optimization in Cartesian and intrinsic coordinates affects the excitation energies. The calculations with the best-performing active space and geometry optimization protocol were performed on the active-site cluster models representing bacterial and plant phytochromes in the Pr and Pfr states. Analyzing the molecular orbital energies, tetrapyrrole geometry and charge distribution enabled unraveling the electronic-structure origin of the spectral red shift. To study how the formation of the revealed red-shifting bond correlates with other hydrogen-bonding interactions in the active site and how this depends on the protein conformation, an MD study of bacterial phytochromes was performed. First of all, it was investigated how the active-site dynamics depends on the protonation state of conserved histidines surrounding the tetrapyrrole, and then how dynamics in the active site changes depending on the presence of the PHY domain and the conformation of the CBD and PHY domains.

The majority of results presented in this part will be published in the following peer-reviewed article:

Maximowitsch E and Domratcheva T. A hydrogen bond between tetrapyrrole and conserved aspartate causes far-red shifted absorption of phytochrome photoreceptors. *In preparation.*

3.1.2 Active space selection for calculations of biliverdin-cysteine adducts

To select the method for the excited-state calculations of the active-site models, first, the calculations on the tetrapyrrole-cysteine adducts were performed. The electronic state energies and state properties were computed with the multi-reference multi-configurational perturbation theory method to the second order (XMCQDPT2) (161) with the zeroth-order complete-active-space self-consistent-field (CASSCF) wave function SA*N*-CASSCF(*M,L*) where *N* is the number of states used in energy averaging, *M* and *L* are the number of electrons and molecular orbitals (MOs) in the active space. The selection of the active space in CASSCF calculations requires defining the number of states as well as choosing the active occupied and unoccupied MOs among the starting orbitals. Linear tetrapyrroles are large molecules featuring up to twelve double bonds. Including the entire π-electron system of such size in the active space is computationally not feasible. Instead, the frontier π-MOs can be selected to account for the static correlation, and subsequent XMCQDPT2 calculations would account for the dynamic correlation. To study how the active space selection influences the excited-state energies, the tetrapyrrole-cysteine adducts as shown in Figure 3.1 were calculated. The adducts were prepared from biliverdin (BV), phytochromobilin (PΦB) and phycocyanobilin (PCB) chromophores in 15Z and 15E configurations by removing propionates PropB and PropC and were optimized in the intrinsic coordinates.

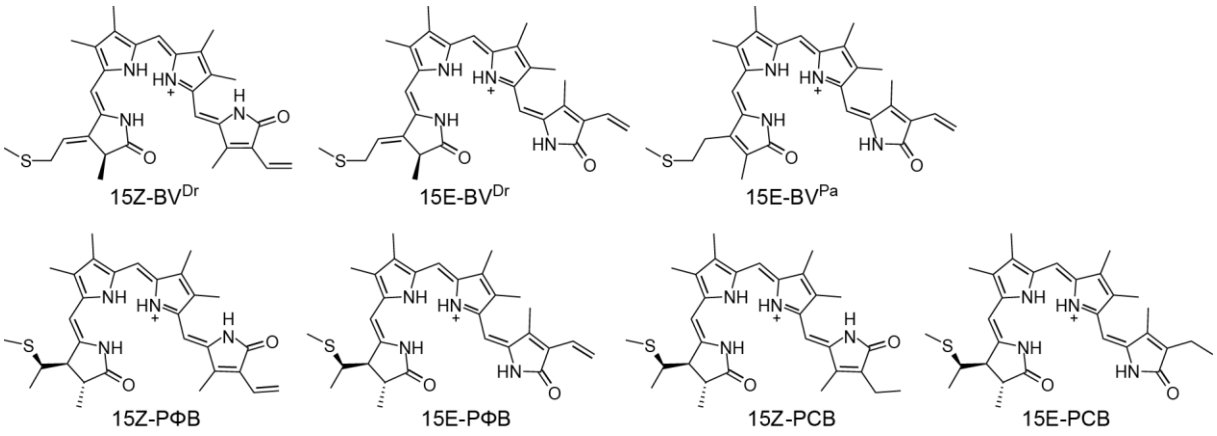

Figure 3.1. Chemical structures of tetrapyrrole-cysteine adducts used in the calculations. The adducts represent biliverdin (BV), phytochromobilin (PΦB) and phycocyanobilin (PCB) chromophores binding to bacterial, plant and cyanobacterial phytochromes, respectively. BV^{Dr} and BV^{Pa} represent the chromophore attachment to cysteine as it is found in DrBphP and PaBphP.

First, the 15Z-BV^{Dr} biliverdin-cysteine adduct was used to evaluate the effect of the active-space selection on the excitation energies and oscillator strengths. The calculations were performed with different numbers of occupied (1-6) and unoccupied (1-3) MOs in the active space and different numbers of states (3-18) (Figure 3.2 A). Among the computed states, there are three excited states with considerably large oscillator strength, at the energies around 1.7, 3.0 and 3.8 eV. The first two energies correspond to the energies of the Q and Soret bands in the experimental absorption spectrum. The S_1 state corresponding to the Q band is dominated by the single-electron excitation from the HOMO to the LUMO (HOMO→LUMO), whereas the state corresponding to the Soret band originates from a mixture of different single-electron (HOMO-1 → LUMO, HOMO → LUMO+1), double-electron (HOMO → LUMO/LUMO+1) and other excitations. This structure of the excited states identifies CASSCF(4,4) as a minimal size active space.

In case when only one unoccupied MO or only one occupied MO was present in the active space, the energy corresponding to the Soret band was reduced in comparison to the energies obtained when the active space contained at least two occupied and two unoccupied MOs. The minimal number of computed states is four for CASSCF(4,4) and six for CASSCF(6,5) otherwise the Soret band is blue-shifted. For the active spaces SA5-CASSCF(4,4), SA6-CASSCF(6,5), SA8-CASSCF(6,5) but not SA7-CASSCF(6,5) different composition of the active space was obtained depending on the selection of starting MOs (Figures 3.2 B and 3.3). This shows that in order to save computational time SA5-CASSCF(4,4) can be used, whereas SA7-CASSCF(6,5) would give reproducible result independently on the selected starting MOs. The excited-state calculations were used to simulate absorption spectra: the energy defines the position of the band, and the corresponding oscillator strength defines the intensity of the band. Spectra computed with SA5-CASSCF(4,4) and SA7-CASSCF(6,5) active spaces reproduce the general shape of the experimentally obtained spectra of a phytochrome (Figure 3.4 and Figure 1.1).

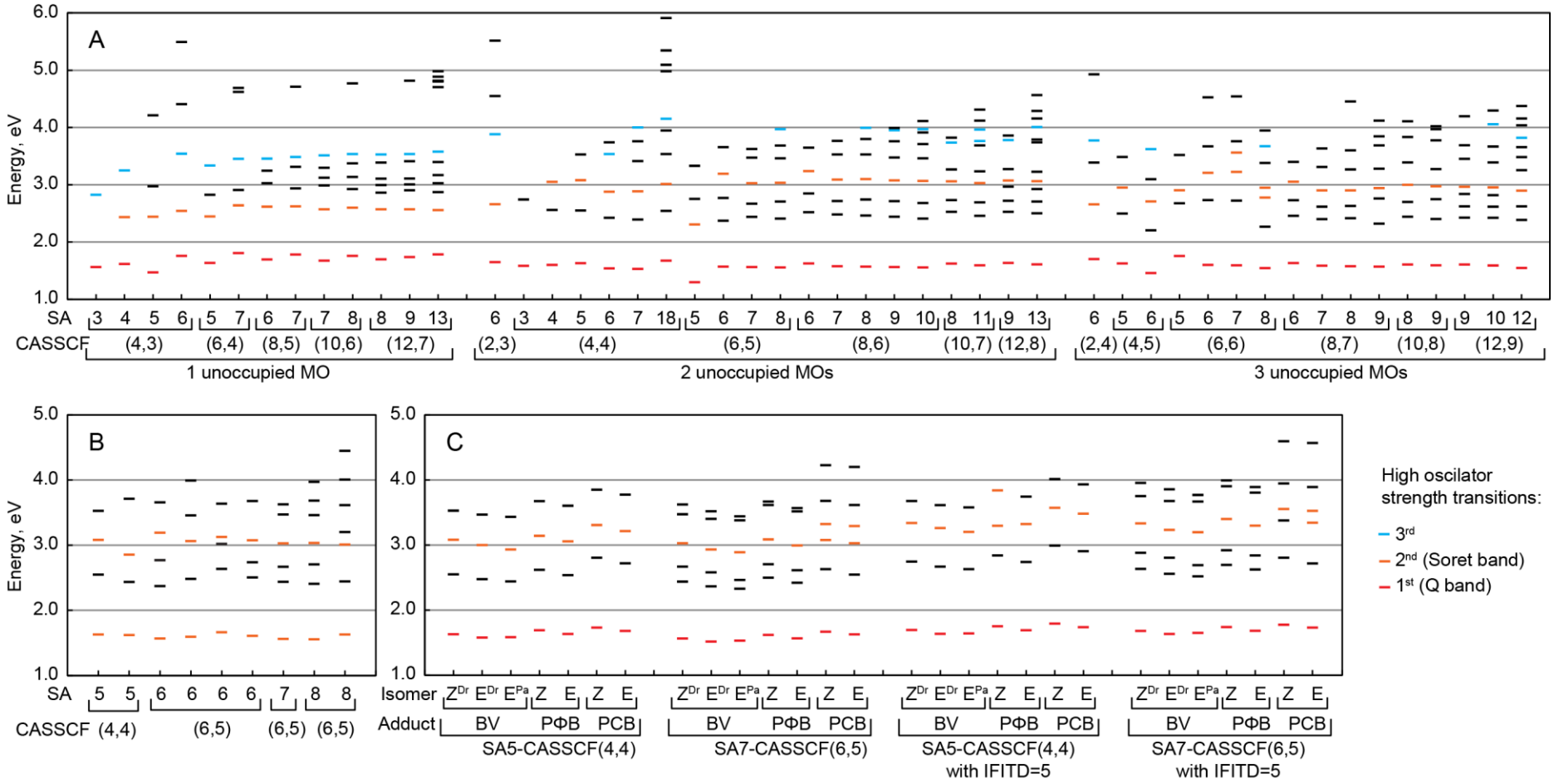

Figure 3.2. Excited-state energies (with respect to the ground state) of tetrapyrrole-cysteine adducts computed with XMCQDPT2-SA*N*-CASSCF(*M*,*L*). Active space in CASSCF: *M* electrons, *L* MOs, *N* states. A) Energies of the 15Z-BV^{Dr} adduct. B) Energies of the 15Z-BV^{Dr} adduct, where selection of different starting MOs in the same size active space converged to different solutions, with active MOs as shown in Figure 3.3. C) Energies of tetrapyrrole adducts with 15Z and 15E configurations. (A-C) XMCQDPT2 energies were computed with (in panel C) and without (in panels A, B, C) the density modification, specified as IFITD=5 and described in Methods Section 2.1.4. Adducts were optimized in intrinsic coordinates.

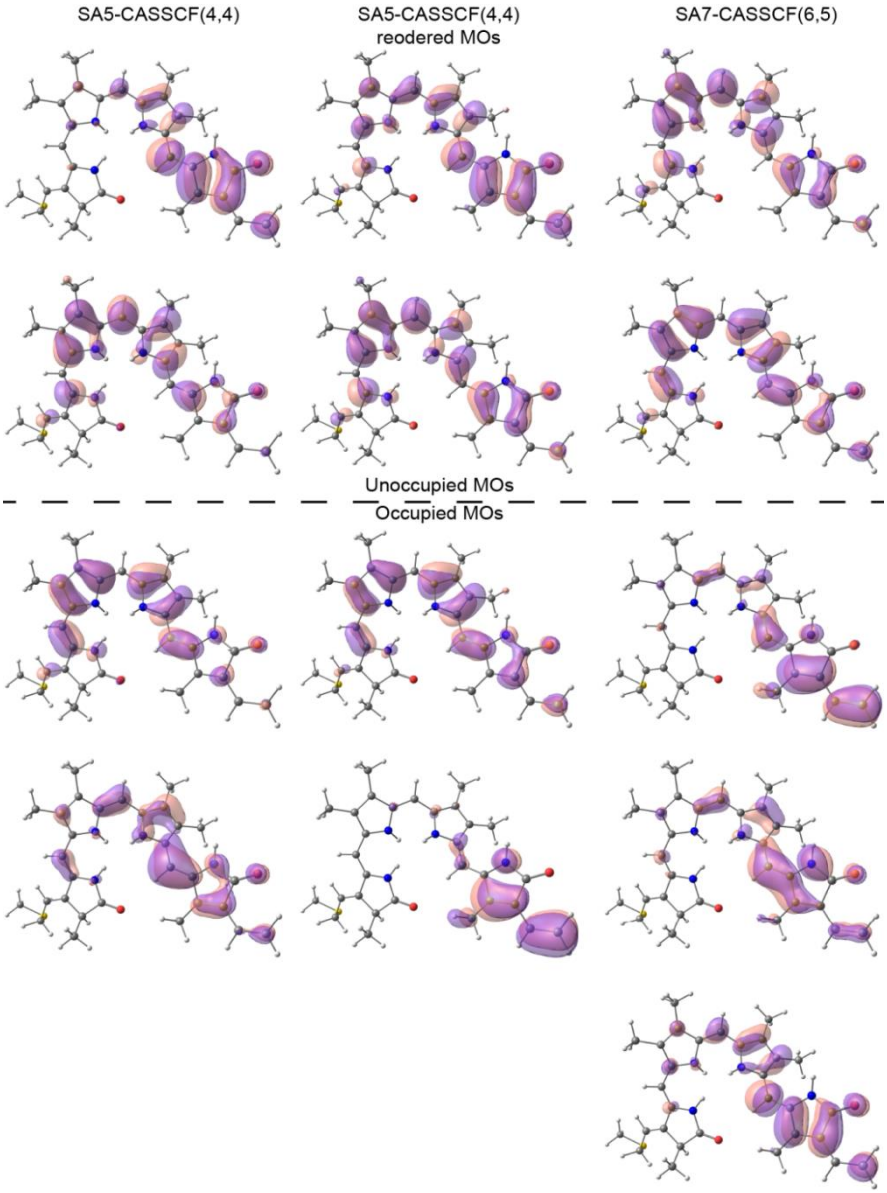

Figure 3.3. MOs in different active spaces of CASSCF calculations. The SA5-CASSCF(4,4) calculations with different starting MOs were always converging to the same active space (left column), except one calculation which resulted in different active space (middle column). The SA7-CASSCF(6,5) calculations were always converging to the same active space (right column) independently on the set of starting MOs.

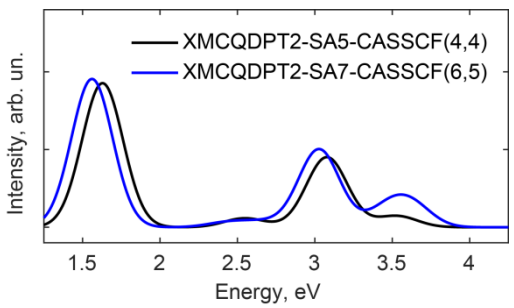

Figure 3.4. Spectra simulated from the XMCQDPT2 calculations of the 15Z-BV^{Dr} adduct. XMCQDPT2 energies were computed without density modification IFITD=5.

Further, it was studied how the solutions of the CASSCF calculations depend on the size of the π-electron system in tetrapyrrole and the double-bond configuration, 15Z and 15E. The SA5-CASSCF(4,4) and SA7-CASSCF(6,5) calculations (Figure 3.2 C) were performed for different isomers of biliverdin, phytochromobilin and phycocyanobilin (adducts shown in Figure 3.1). The solutions did not change for the studied adducts when 15Z and 15E isomers were considered. The energy of the first excitation (S_0-S_1 transition) corresponding to the Q band in the absorption spectrum was compared among all isomers: there was a blue shift (energy increase) upon reducing the π-electron system of the tetrapyrrole and a slight red shift (energy decrease) upon isomerization from 15Z to 15E. However, some excited-state calculations of phycocyanobilin, especially with the active space of SA7-CASSCF(6,5), converged to a solution with two states which have considerable oscillator strength and correspond to the Soret band. Therefore, the calculations with the active space of SA5-CASSCF(4,4) would be preferred for phycocyanobilin. There were also two states corresponding to the Soret band in one calculation of phytochromobilin computed with the active space of SA5-CASSCF(4,4), therefore the larger active space, SA7-CASSCF(6,5), is preferred for this chromophore. In further calculations of biliverdin and phytochromobilin chromophores as well as active-site cluster models of bacterial and plant phytochromes the active space of SA7-CASSCF(6,5) was used, where only two states have considerable oscillator strength and correspond to the energies of Q and Soret bands in the absorption spectrum.

3.1.3 Effect of geometry optimization procedure on the excited-state energies

The excited-state energies depend on the chromophore geometry which is obtained with a specific geometry optimization method. Conventionally, the geometry of a molecule is optimized in the intrinsic coordinates as it is a fast method to reach the minimum on the potential energy surface (PES). However, the tetrapyrrole molecule is complex and may have different minima on the PES. The geometry optimization in Cartesian coordinates usually finds the closest minimum, similar to the starting geometry which is often taken from the X-ray crystal structure. On the contrary, optimization in intrinsic coordinates may lead to a farther minimum on the PES with a less similar geometry. The optimization of the phytochromobilin isomers, 15Z and 15E, in intrinsic coordinates resulted in geometries with distorted orientation of the pyrrole ring A as compared to the X-ray

crystal structure (Figure 3.5). Such conformation of the tetrapyrrole is unlikely in the phytochrome due to the hydrogen-bonding network in the active site which restricts the tetrapyrrole conformation. At these two distorted geometries, the S_0-S_1 energy wass considerably smaller in 15E-phytochromobilin than in 15Z; the red shift between these two isomers was equal to 0.11 eV. In contrast, optimization in Cartesian coordinates resulted in geometries close to the crystal structure and the red shift between these two isomers was only 0.06 eV.

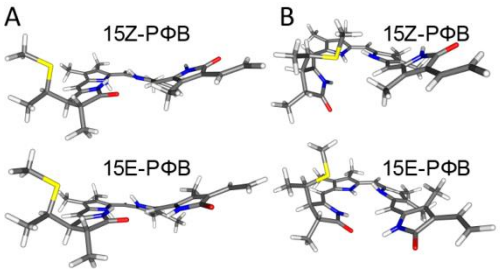

C

Adduct	Cart.C.	Intr.C.
15Z-PΦB	1.739	1.833
15E-PΦB	1.681	1.719

Figure 3.5. Conformations of phytochromobilin dependent on geometry optimization procedure. All geometries were optimized with the PBE0/cc-PVDZ method. A) Geometries, optimized in Cartesian coordinates, are similar to the protein X-ray crystal structure (PDB code: 4our). B) Geometries, optimized in intrinsic coordinates, are different from the ones found in the protein X-ray crystal structure. C) S_0-S_1 energies, computed with XMCQDPT2-SA7-CASSCF(6,5), at geometries optimized in Cartesian (Cart. C.) and intrinsic (Intr. C.) coordinates.

It was studied how the geometry and excited-state energies depend on the DFT functional and basis set used for the geometry optimization in Cartesian coordinates (Table 3.1). In addition to the previously used PBE0 functional of DFT and cc-PVDZ basis set, the B3LYP functional and 6-31G* basis set were also tested for the biliverdin geometry optimization. The optimized geometries were similar and the energy difference between the first excited state in the 15Z- and 15E-biliverdin isomers did not depend on the tested DFT functional or basis set. In addition, it was tested how the starting geometry (PDB 3c2w or 3nhq used for biliverdin 15E-BV^{Pa}) may influence the geometry; however, no significant changes were found (Table 3.1). To sum up, the tetrapyrrole geometry optimization can be done with different DFT functional or basis set but in Cartesian coordinates in order to avoid conformations which are not possible in the phytochrome protein. Results in the following sections were obtained by the geometry optimizations performed in Cartesian coordinates with the PBE0/cc-PVDZ method.

Table 3.1. S_0-S_1 energies (in eV) in biliverdin-cysteine adducts computed with XMCQDPT2-SA7-CASSCF(6,5). PDBs of the X-ray crystal structures, used to prepare initial coordinates for the adduct geometry optimization, are indicated. The adducts were optimized in Cartesian coordinates with the PBE0 or B3LYP functional and the cc-PVDZ or 6-31G* basis set.

Adduct	PDB	PBE0/cc-PVDZ	B3LYP/cc-PVDZ	PBE0/6-31G*	B3LYP/6-31G*
15Z-BV^{Dr}	2o9c	1.68	1.64	1.72	1.69
15E-BV^{Pa}	3c2w	1.66	1.63	1.70	1.68
15E-BV^{Pa}	3nhq	1.64	1.63	1.70	1.68

3.1.4 Spectral shift in tetrapyrrole-cysteine adduct isomers

After the clarification that geometry optimization should be done in Cartesian coordinates to preserve the geometries closest to the ones found in proteins and that the XMCQDPT2-SA7-CASSCF(6,5) calculations produce a consistent active space, the spectral shifts between the 15Z- and 15E-tetrapyrrole isomers were evaluated. The 15Z-tetrapyrrole represents the geometry in the Pr-state phytochrome and the 15E-tetrapyrrole represents the geometry in the Pfr-state phytochrome. The tetrapyrrole-cysteine adducts, in particular 15Z-BV^{Dr}, 15E-BV^{Dr}, 15E-BV^{Pa}, 15Z-PΦB, 15Z-PΦB (chemical structures are shown in Figure 3.1) were prepared from the X-ray crystal structures of bacterial and plant phytochromes (the same coordinates were used for the preparation of the active-site cluster model presented in the following Sections 3.1.5-3.1.6) by optimization in the Cartesian coordinates. The bond lengths of the optimized tetrapyrroles as well as dihedral angles between pyrrole rings are listed in Appendix Table B.1.

The excited-state energies computed with the XMCQDPT2-SA7-CASSCF(6,5) method for the optimized geometries of the tetrapyrrole isomers are listed in Table 3.2. The S_0-S_1 energy in 15E-BV^{Dr} and 15E-BV^{Pa} decreased by 0.04 and 0.02 eV, respectively, as compared to the energy in 15Z-BV^{Dr}. The red shift due to configuration change in tetrapyrrole was not larger than 0.04 eV in biliverdin and 0.06 eV in phytochromobilin, whereas in experimental spectra of the Pr- and Pfr-state phytochromes the shift is about 0.12 eV (30, 33, 41). These results indicate that the spectral change upon the C15=C16 double-bond isomerization is relatively small and there must be other factors (such as active site interactions) which induce the full red shift of the phytochrome Pfr state as compared to the Pr state.

Table 3.2. XMCQDPT2-SA7-CASSCF(6,5) excitation energies (in eV) and oscillator strengths (in parentheses) of tetrapyrrole-cysteine adducts. Excitations corresponding to the Q and Soret bands are shown in bold.

Transition	15Z-BV^{Dr}	15E-BV^{Dr}	15E-BV^{Pa}	15Z-PΦB	15E-PΦB
S_0-S_1	**1.68 (1.042)**	**1.64 (1.006)**	**1.66 (0.908)**	**1.74 (1.079)**	**1.68 (1.012)**
S_0-S_2	2.64 (0.062)	2.58 (0.052)	2.53 (0.050)	2.69 (0.056)	2.62 (0.041)
S_0-S_3	2.88 (0.035)	2.84 (0.046)	2.70 (0.065)	2.92 (0.043)	2.84 (0.058)
S_0-S_4	**3.33 (0.529)**	**3.25 (0.557)**	**3.20 (0.616)**	**3.40 (0.516)**	**3.30 (0.567)**
S_0-S_5	3.74 (0.156)	3.68 (0.089)	3.68 (0.105)	3.90 (0.125)	3.81 (0.056)
S_0-S_6	3.95 (0.107)	3.88 (0.103)	3.78 (0.057)	3.99 (0.119)	3.89 (0.144)

3.1.5 Spectral shift in bacterial and plant phytochrome models

The quantum chemical calculations on cluster models of the phytochrome active site were performed to investigate how the active-site hydrogen-bonding network influences the phytochrome absorption spectra. The five main models Dr-Pr, Dr-Pfr, Pa-Pfr, At-Pr, At-Pfr represent the active site of bacterial DrBphP in the Pr and Pfr state, PaBphP in the Pfr state and plant AtPhyB in the Pr and Pfr state, respectively (Figure 3.6). All models except At-Pfr were prepared from the respective crystal structures, whereas At-Pfr was modeled based on the similarities of bacterial and plant phytochromes. In all computed models the protonated tetrapyrrole rings A-C interacts with the structurally conserved pyrrole water. In the Pr-state models the ring D of the 15Z-tetrapyrrole interacts with histidine H290 (according to the numbering in DrBphP), whereas in the Pfr-state models the rotated ring D of the 15E-tetrapyrrole interacts with aspartate D207 (Figure 3.7). In the five main models, the protonation state of all histidines, was considered as neutral (Nε-H) with a hydrogen attached to the Nε atom. This choice is supported by previous quantum chemical calculations where models with protonated H260 demonstrated weakened interactions of rings B and C with the pyrrole water (175), therefore here only models with neutral (Nε-H) H260 were considered. Different protonation states of H290 were tested for some models; however there was no significant difference found in the structure or excitation energies as it will be discussed below. Therefore, throughout this and next sections (Sections 3.1.5-3.1.6) the results will be discussed for the five main models, containing only neutral (Nε-H) histidines, if not stated otherwise.

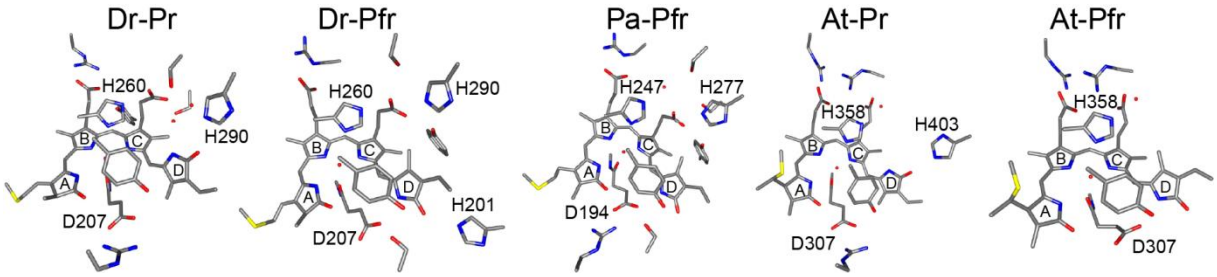

Figure 3.6. Cluster models of the active site in bacterial and plant phytochromes. All residues of each model are shown; the numbering is according to the protein sequence. In five main models all histidines were neutral (Nε-H).

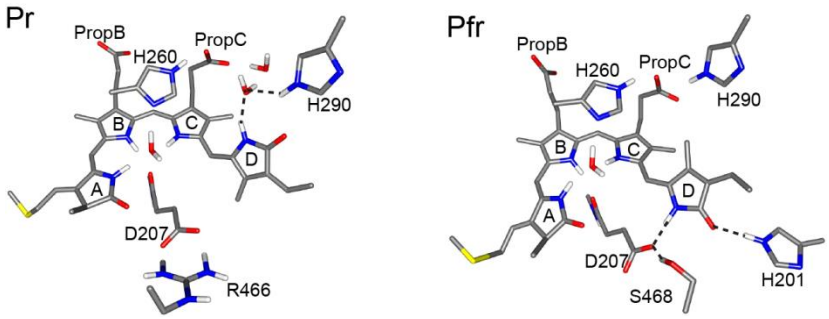

Figure 3.7. Tetrapyrrole interactions in the Pr- and Pfr-state phytochrome models. Fragments from the active-site cluster models of DrBphP phytochrome are shown; histidine protonation states are the same in five main models.

At the optimized geometries of the active-site models, the excitation spectra were computed with the XMCQDPT2-SA7-CASSCF(6,5) method (Table 3.3). The computed spectra (Figure 3.8), simulated from the excited-state energies and oscillator strengths, represent the general shape of the experimental spectrum (Figure 1.1). The computed energies correlate with the maxima of the Q and Soret bands in the experimental spectrum (Figure 3.9). The S_0-S_1 energy corresponding to the Q band decreased in the Pfr-state models by 0.16, 0.11 and 0.26 eV as compared to the respective Pr-state models (the Pa-Pfr model is compared with the Dr-Pr model); the excited-state energy difference corresponding to the Soret band was 0.26, 0.28 and 0.34 eV. The computed models predict the red shift of the Q and Soret band maxima in the Pfr state of both bacterial and plant phytochromes. Additionally, the blue shift of the plant phytochrome models as compared to the bacterial phytochrome models is also predicted. Plant phytochromes contain phytochromobilin which has a smaller π-electron system than biliverdin, which is present in bacterial phytochromes. The computed spectrum of Pa-Pfr is blue-shifted as compared to Dr-Pfr, probably due to an additional interaction between arginine and aspartate next to tetrapyrrole ring D.

Table 3.3. XMCQDPT2-SA7-CASSCF(6,5) excitation energies (in eV) and oscillator strengths *f* of the active-site cluster models. Five main models contain neutral (Nε-H) histidines. Some additional models contain neutral (Nδ-H) or protonated H290, all indicated in parentheses as δ or H, respectively. Excitations corresponding to the Q and Soret bands are shown in bold.

Tran-sition	Dr-Pr		Dr-Pfr		Pa-Pfr		At-Pr		At-Pfr	
	E, eV	*f*	E, eV	*f*	E, eV	*f*	E, eV	*f*	E, eV	*f*
S_0-S_1	**1.78**	**1.323**	**1.62**	**1.214**	**1.67**	**1.091**	**1.97**	**1.243**	**1.71**	**1.360**
S_0-S_2	2.74	0.022	2.53	0.036	2.51	0.016	2.98	0.005	2.59	0.034
S_0-S_3	3.00	0.038	2.61	0.067	2.66	0.082	**3.50**	**0.701**	2.80	0.071
S_0-S_4	**3.25**	**0.487**	**2.99**	**0.380**	**2.97**	**0.461**	3.67	0.074	**3.16**	**0.330**
S_0-S_5	3.71	0.044	3.61	0.043	3.57	0.071	4.29	0.054	3.65	0.006
S_0-S_6	4.09	0.096	3.80	0.097	3.80	0.074	4.43	0.288	3.93	0.135
Q*	1.77*		1.65*		1.65*		1.87*		1.71*	
Soret*	3.09*		3.03*		3.01*		3.24*		3.09*	

Tran-sition	Dr-Pr(H)		Dr-Pr(δ)		Dr-Pfr(H)		Pa-Pfr(H)		At-Pr(H)	
	E, eV	*f*	E, eV	*f*	E, eV	*f*	E, eV	*f*	E, eV	*f*
S_0-S_1	**1.77**	**1.286**	**1.76**	**1.335**	**1.56**	**1.176**	**1.62**	**1.094**	**2.06**	**1.199**
S_0-S_2	2.76	0.000	2.71	0.046	2.46	0.040	2.49	0.025	2.87	0.097
S_0-S_3	3.20	0.036	**3.13**	**0.432**	2.75	0.093	2.73	0.061	**3.39**	**0.549**
S_0-S_4	**3.35**	**0.684**	3.65	0.113	**3.09**	**0.342**	**3.03**	**0.466**	3.75	0.117
S_0-S_5	3.66	0.001	4.08	0.004	3.45	0.017	3.52	0.050	4.25	0.211
S_0-S_6	4.09	0.116	4.38	0.043	3.94	0.111	3.90	0.084	4.48	0.026

* - maxima of the Q (<2 eV) and Soret (>3 eV) bands in experimental spectra of DrBphP in Pr and Pfr states, PaBphP in Pr state, AtPhyB in Pr and Pfr (30, 33, 41).

The excited-state energies were also computed for the models with a different protonation state of H290: neutral (Nδ-H) and protonated. Even though there was a small red shift in the Dr-Pfr and Pa-Pfr models with protonated H290 and a blue shift in the At-Pr models with protonated H290 in comparison to the respective models with neutral H290, the protonation state of H290 did not have a significant effect on the excitation spectra (Table 3.3). There is still a significant red shift in the Pfr-state models as compared to the Pr-state models independently on the protonation state of H290. The protonation state of this highly conserved histidine was addressed in several previous experimental and computational studies and it was shown that the protonation state of the histidines in the active site may vary depending on the protein and of the state (66, 176-179). There are indications that in multiple canonical phytochromes in the Pr state (bacterial, plant cyanobacterial) histidine H290 is neutral (66, 176-178), whereas in the bathy phytochromes this histidine may be also protonated and was suggested to be

involved in the chromophore keto-enol tautomerization resulting in thermal conversion of the phytochrome (179). Since the excited-state energies are similar for the models with neutral and protonated histidines, only the models with neutral histidines were considered in further analyses.

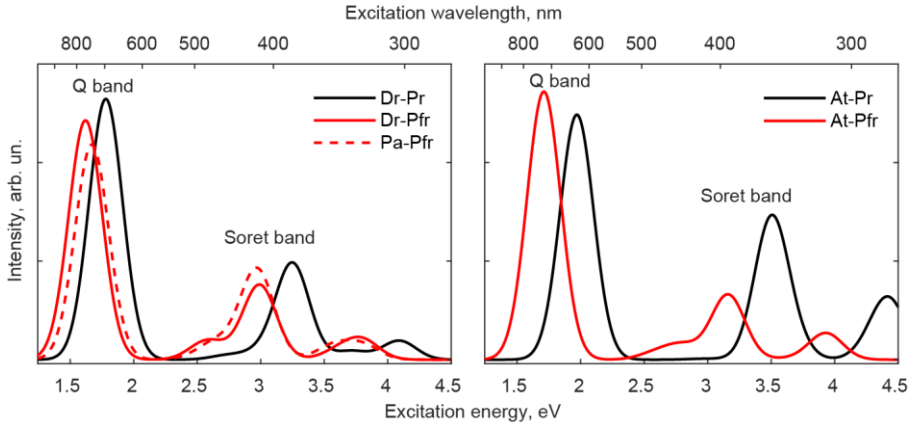

Figure 3.8. Computed spectra of active-site cluster models representing Pr- and Pfr-state phytochromes. Excited-state properties were taken from the XMCQDPT2-SA7-CASSCF(6,5) calculations (Table 3.3) of five main models containing neutral (Nε-H) histidines (Figure 3.6).

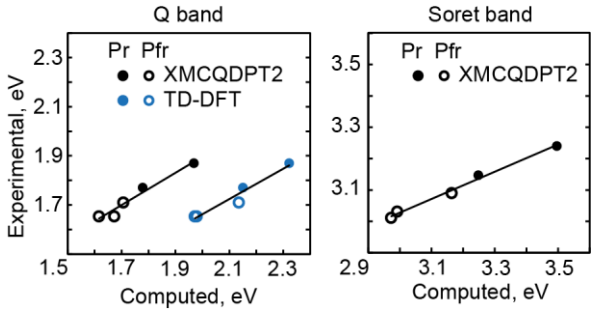

Figure 3.9. Correlation between computed and experimental phytochrome spectra. Spectra were computed with the XMCQDPT2-SA7-CASSCF(6,5) method and the TD-DFT (CAM-B3LYP functional) method for five main active-site cluster models containing neutral (Nε-H) histidines (Figure 3.6). Computed values (S_0-S_1 energies for the Q band, S_0-S_3 or S_0-S_4 for the Soret band) were taken from Tables 3.3 and 3.4 and experimental values were taken from the literature (30, 33, 41).

The excitation spectra for the main five active-site models were also computed with the widely-used TD-DFT method (Table 3.4). In contrast to the XMCQDPT2 calculations, which may dependent on the active space selection, the TD-DFT method does not require a definition of the active space. The TD-DFT calculations, performed with the CAM-B3LYP functional also showed the red shift of the S_0-S_1 energy, corresponding to the Q band, in the Pfr-state models as compared to the Pr-state models: 0.17, 0.18 and 0.18 eV in the Dr-Pfr, Pa-Pfr and At-Pfr models, respectively (Figure 3.9). There are several excited states above 3 eV with considerable oscillator strength therefore it is hard

to identify which state corresponds to the Soret band. The origin of the Soret band cannot be described by only single-electron excitations meaning that the TD-DFT method is inappropriate for evaluation of the energy corresponding to the Soret band. The TD-DFT energies of the Q band are systematically blue-shifted in comparison to the XMCQDPT2 energies, but nonetheless predict the red shift in the Pfr-state models as compared to the Pr-state models.

Table 3.4. TD-CAM-B3LYP excitation energies E and oscillator strengths *f* (with respect to the ground state) of the active-site cluster models. Calculations of five main models containing neutral (Nε-H) histidines. Excited-state energies corresponding to the Q band are shown in bold.

Excited state	Dr-Pr		Dr-Pfr		Pa-Pfr		At-Pr		At-Pfr	
	E, eV	*f*	E, eV	*f*	E, eV	*f*	E, eV	*f*	E, eV	*f*
1	**2.15**	**0.975**	**1.98**	**0.845**	**1.97**	**0.622**	**2.32**	**0.883**	**2.14**	**0.883**
2	3.05	0.001	2.55	0.049	2.44	0.000	3.26	0.002	2.54	0.051
3	3.25	0.025	3.18	0.016	2.81	0.016	3.26	0.001	3.35	0.131
4	3.35	0.192	3.21	0.019	2.92	0.002	3.51	0.124	3.40	0.086
5	3.53	0.129	3.27	0.384	3.18	0.075	3.70	0.548	3.47	0.087
6	3.57	0.067	3.42	0.009	3.29	0.054	3.71	0.011	3.59	0.037
7	3.61	0.242	3.47	0.028	3.36	0.879	3.78	0.038	3.62	0.239
8	3.64	0.047	3.48	0.365	3.49	0.015	3.93	0.194	3.77	0.013
9	3.67	0.255	3.56	0.000	3.54	0.043	4.01	0.003	3.78	0.028
10	3.96	0.013	3.65	0.061	3.72	0.030	4.14	0.014	3.83	0.081

Table 3.5. CIS excitation energies E and oscillator strengths *f* (with respect to the ground state) of the active-site cluster models. Calculations of the main models containing neutral (Nε-H) histidines. Excited-state energies corresponding to the Q band are shown in bold.

Excited state	Dr-Pr		Dr-Pfr		Pa-Pfr	
	E, eV	*f*	E, eV	*f*	E, eV	*f*
1	**2.62**	**1.321**	**2.48**	**1.225**	**2.45**	**0.891**
2	4.40	1.455	4.23	1.482	4.17	1.854
3	4.81	0.013	4.43	0.064	4.46	0.093
4	4.84	0.224	4.56	0.034	4.67	0.031
5	5.01	0.020	4.82	0.010	4.71	0.003
6	5.19	0.062	4.90	0.081	4.72	0.079
7	5.28	0.074	5.11	0.096	4.85	0.009
8	5.39	0.002	5.34	0.022	5.18	0.287
9	5.42	0.014	5.47	0.000	5.23	0.002
10	5.47	0.049	5.51	0.094	5.32	0.009

The excitation spectra of the models representing bacterial phytochromes were also computed with the CIS method. The S_0-S_1 energy, representing the Q band, was red-shifted in the Pfr-state models (0.14 eV for Dr-Pfr, 0.17 eV for Pa-Pfr) as compared to

the Pr-state model (Table 3.5). This is in agreement with the red shift observed for the Pfr-state phytochrome even though the CIS energies are systematically blue-shifted.

3.1.6 Origin of the spectral shift in bacterial and plant phytochromes

The properties of the Pr- and Pfr-state active-site cluster models were analyzed to understand the origin of the spectral difference between the Pr and Pfr states in phytochrome. The cysteine-tetrapyrrole adducts were extracted from the five main models (models are shown in Figure 3.6) and chromophore's propionate groups PropB and PropC were substituted with methyl groups. The prepared adducts were used for the XMCQDPT2 calculations (Table 3.6). The S_0-S_1 energies were red-shifted in adducts extracted from the Pfr-state models as compared to the energies of the adducts extracted from the Pr-state models. This indicates that the observed spectral shift in the cluster models is related to the chromophore geometry changes induced by different interactions in the active site of the Pr- and Pfr-state phytochrome.

Table 3.6. XMCQDPT2-SA7-CASSCF(6,5) excitation energies E and oscillator strengths *f* of the cysteine-tetrapyrrole adducts, without propionates, extracted from five main active-site cluster models. Five main models are shown in Figure 3.6.

Transition	Dr-Pr 15Z-BV^{Dr}		Dr-Pfr 15E-BV^{Dr}		Pa-Pfr 15E-BV^{Pa}		At-Pr 15Z-PΦB		At-Pfr 15E-PΦB	
	E, eV	*f*	E, eV	*f*	E, eV	*f*	E, eV	*f*	E, eV	*f*
S_0-S_1	1.85	1.368	1.73	1.237	1.73	1.119	2.02	1.312	1.87	1.367
S_0-S_2	2.73	0.040	2.51	0.017	2.48	0.020	2.91	0.039	2.66	0.008
S_0-S_3	3.06	0.044	2.95	0.064	2.83	0.070	3.38	0.071	3.04	0.084
S_0-S_4	3.43	0.480	3.26	0.555	3.20	0.586	3.69	0.573	3.35	0.420
S_0-S_5	3.89	0.075	3.80	0.031	3.76	0.047	4.29	0.062	3.93	0.044
S_0-S_6	4.03	0.093	3.96	0.084	3.83	0.064	4.39	0.418	4.01	0.138

The red shift of the Pfr-state spectrum with respect to the Pr-state spectrum is an effect of the tetrapyrrole hydrogen bonds and could be explained as a blue shift of the Pr state due to the ring D interactions with H290, as a red shift of the Pfr state due to the ring D interactions with D207 or both. To study this, the respective side chains, H290 or D207 (its carboxylate), were removed from the active-site models. The modified models were re-optimized and used for the XMCQDPT2 calculations (Table 3.7). The removal of H290 in the Pr-state models did not induce a change in the excitation spectra, whereas the removal of D207 in the Pfr-state models significantly increased the S_0-S_1 energy. In

comparison, removal of the D207 in the Pr-state models only slightly changed the S_0-S_1 energy. The red shift between respective wild-type Pr- and Pfr-state models was larger by 0.09-0.25 eV than the shift in the respective Pr- and Pfr-state models without D207. In an additional, reduced-size active-site model where ring D was rotated as in the Pfr state but did not form a hydrogen bond with D207 (Appendix Figure C.1), the full spectral red shift was not formed since the S_0-S_1 energy (1.68 eV) of this model was larger (by 0.06 eV) than in the Dr-Pfr model (Table 3.3) and similar to the Dr-Pfr w/o D207 model (Table 3.7). Based on the excited-state energies, such a model with the rotated ring D but not yet forming a ring D-D207 interaction might correspond to the Lumi-R intermediate, which has an absorption maximum at around 1.70 eV (47, 122). The computed energies indicate that the red shift of the Pfr-state spectrum originates from the tetrapyrrole ring D–D207 hydrogen bond in the Pfr state. Without this hydrogen bond the full spectral shift cannot form.

Table 3.7. XMCQDPT2-SA7-CASSCF(6,5) excitation energies E and oscillator strengths *f* of the active-site cluster models without (w/o) H290 or D207 (according to the numbering in DrBphP). Models were prepared from five main models containing neutral (Nε-H) histidines as described in Sections 2.1.2-2.1.3.

Transition	Dr-Pr w/o H290		At-Pr w/o H290	
	E, eV	*f*	E, eV	*f*
S_0-S_1	1.79	1.341	1.95	1.244
S_0-S_2	2.72	0.026	2.99	0.005
S_0-S_3	2.95	0.042	3.52	0.573
S_0-S_4	3.24	0.468	3.64	0.152
S_0-S_5	3.74	0.047	4.28	0.005
S_0-S_6	4.08	0.101	4.42	0.409

Transition	Dr-Pr w/o D207		Dr-Pfr w/o D207		Pa-Pfr w/o D207		At-Pr w/o D207		At-Pfr w/o D207	
	E, eV	*f*	E, eV	*f*	E, eV	*f*	E, eV	*f*	E, eV	*f*
S_0-S_1	1.77	1.224	1.70	1.188	1.75	1.028	1.93	1.254	1.92	1.297
S_0-S_2	2.62	0.005	2.57	0.007	2.51	0.018	2.86	0.006	2.82	0.009
S_0-S_3	2.84	0.007	3.10	0.151	3.12	0.453	3.11	0.239	3.46	0.668
S_0-S_4	3.31	0.483	3.26	0.497	3.35	0.489	3.43	0.347	3.54	0.059
S_0-S_5	3.62	0.028	3.63	0.031	3.87	0.028	3.91	0.011	4.18	0.128
S_0-S_6	4.08	0.000	4.09	0.080	4.12	0.051	4.25	0.015	4.39	0.149

The Pr- and Pfr-state models were analyzed to understand the correlation between spectral properties and electronic effects. The excitation corresponding to the Q band is

the local excitation from the HOMO to the LUMO according to the CASSCF solution, used for the XMCQDPT2 calculations. The calculations of all computed cluster models, including those with a different protonation state of H290 and those with removed H290 or D207, demonstrate that the XMCQDPT2 energies of the S_0-S_1 transition correlate with the HOMO-LUMO energy computed with the single-reference method e.g. HF or DFT (with PBE0 functional) (Figure 3.10 A and Appendix Table B.2). The red shift of the excitation energy and the decrease of the HOMO-LUMO energy can be related to the increase of the HOMO energy or decrease of the LUMO energy. The trend lines in the plot (Figure 3.10 A) indicate that the energies of both the HOMO and the LUMO increase, especially of the HOMO energy, meaning that the HOMO-LUMO energy gap reduction (in the Pfr-state models) correlates with the HOMO destabilization. The HOMO and LUMO are mostly localized on the tetrapyrrole rings B and C with a small component on ring D which is larger in the Pfr-state models as compared to the Pr-state models (Figure 3.10 B). This links the red shift of the S_0-S_1 energy to the larger localization of the HOMO on ring D.

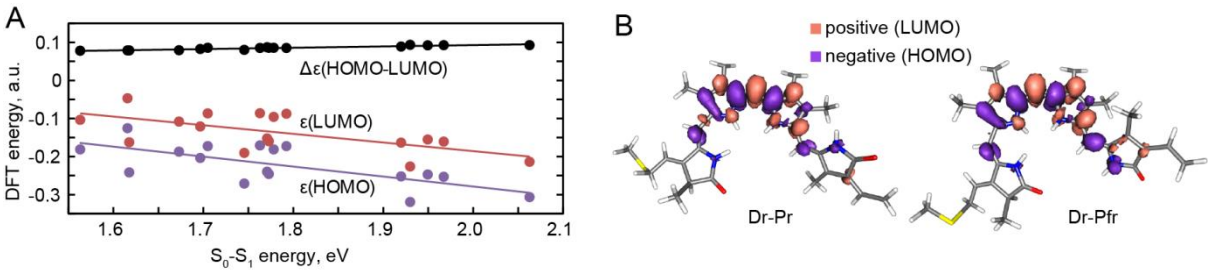

Figure 3.10. HOMO and LUMO properties causing the red shift in Pfr-state phytochromes. A) Correlations between the XMCQDPT2 energies of the S_0-S_1 transition and the DFT (PBE0 functional) energies of HOMO, LUMO and HOMO-LUMO difference in all computed cluster models. Energies are shown in Appendix Table B.2 B) Electronic density of the S_0-S_1 transition in the active-site cluster models (only tetrapyrrole adducts without propionates are shown for clarity).

The active-site models of the Pr and Pfr states were compared to illustrate how the electronic effects lead to changes of the chromophore geometry and charge re-distribution. The bond length alternation, describing a difference between lengths of single and double bonds, changed in tetrapyrrole of the Pfr-state models as compared to the Pr-state models. The change was localized mostly on ring D and the methine bridge between rings C and D (Figure 3.11 A, Appendix Figure C.2 and Table B.3). In the tetrapyrrole of the Pfr-state models, single bonds C14-C15 and C16-N^D extended, whereas bond N^D-H and double bond C15=C16 shortened. Such geometry differences

disappeared in the models without D207 (Table 3.8), indicating a crucial role of D207 in changing electronic properties of the tetrapyrrole. In the active-site models, the difference between the lengths of single bond C14-C15 and double bond C15=C16 correlates with the XMCQDPT2 energy of the first excitation (S_0-S_1) (Figure 3.11 B). The models without D207 and the optimized tetrapyrrole-chromophore adducts (adducts presented in Section 3.1.4) also show this trend. The positive charge decreased on rings A-B-C and increased on ring D in the Pfr-state models while the negative charge on the N atom of ring C increased (Figure 3.11 C and Appendix Table B.4). The changes in the geometry and charge distribution can be explained by different contributions of two resonance structures (Figure 3.11 D). The contribution of the tetrapyrrole resonance structure with the positive charge on ring D and the double bond C14=C15 increases in the Pfr-state models as compared to the Pr-state models. In the At-Pr and At-Pfr models the positive charge on ring D is larger as in the Dr-Pr and Dr-Pfr models indicating a larger contribution of the resonance structure with the positive charge on ring D. To conclude with, D207 interacts with the tetrapyrrole ring D in the Pfr state and induces changes of the tetrapyrrole electronic structure. Increased localization of the HOMO on ring D increases the HOMO energy and decreased the excitation energy that is observed as a spectral red shift of the Pfr state in phytochromes.

Table 3.8. Bond lengths (Å) in tetrapyrrole in Pr- and Pfr-state active-site cluster models and models without (w/o) D207. Five main models containing neutral (Nε-H) histidines are shown in Figure 3.6.

Model	C15-C16	C16-C17	C16-N^D	N^D-H
Dr-Pr	1.3662	1.4699	1.3727	1.0342
Dr-Pfr	1.3764	1.4694	1.3700	1.0666
Pa-Pfr	1.3745	1.4664	1.3681	1.0310
At-Pr	1.3592	1.4640	1.3856	1.0074
At-Pfr	1.3753	1.4726	1.3660	1.0482
Dr-Pr w/o D207	1.3672	1.4694	1.3719	1.0406
Dr-Pfr w/o D207	1.3645	1.4599	1.3905	1.0063
Pa-Pfr w/o D207	1.3640	1.4558	1.4016	1.0144
At-Pr w/o D207	1.3571	1.4613	1.3831	1.0125
At-Pfr w/o D207	1.3682	1.4660	1.3782	1.0084

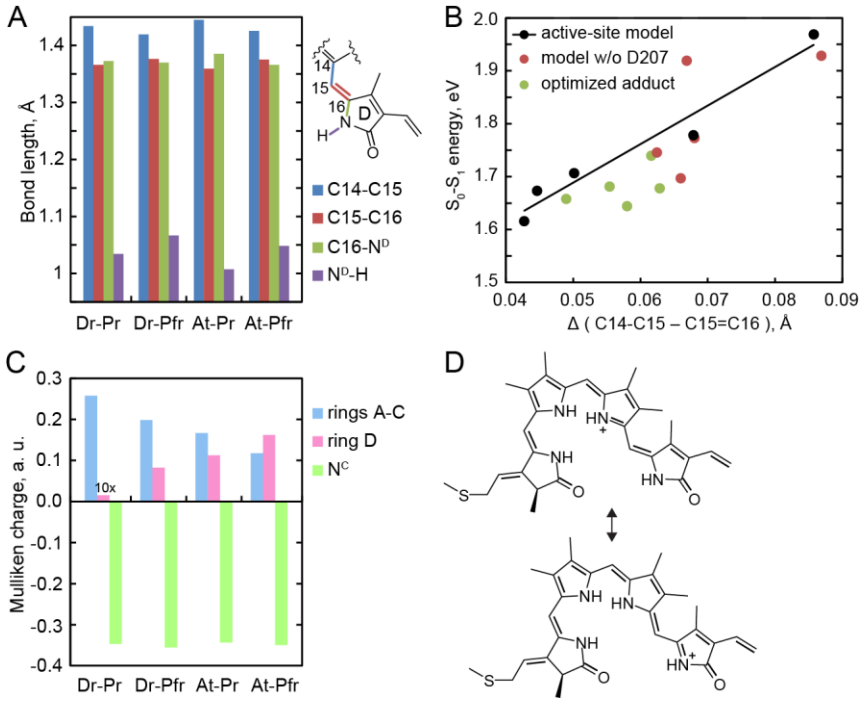

Figure 3.11. Changes in tetrapyrrole geometry and charge distributions causing the red shift in Pfr-state phytochromes. A) Bond length alternations in Pr- and Pfr-state active-site cluster models; values are shown in Appendix Table B.3. B) Correlation between the XMCQDPT2 energies of the S_0-S_1 transition and the difference of the C14-C15 and C15=C16 bond lengths. Values in the five main active-site models containing neutral (Nε-H) histidines, the models without D207 and the optimized adducts are compared. Energies are shown in Tables 3.2, 3.3 and 3.7 and bond lengths in Appendix Tables B.1 and B.3. C) Charge distribution in Pr- and Pfr-state active-site models; values are shown in Appendix Table B.4. D) Resonance structures of the 15E-tetrapyrrole in Pfr-state phytochromes.

3.1.7 Histidine protonation state in phytochrome models in MD simulations

In order to investigate the relation between the red-shifting aspartate-ring D interactions and other interactions in the phytochrome active site, first the assignment of the titratable groups (histidines) was addressed in phytochrome MD simulations. All simulations were done using the CHARMM force field. The protonated tetrapyrrole chromophore is integrated via a hydrogen bonding network in the phytochrome active site. Tetrapyrrole interacts with histidines H260 and H290 side chains (the DrBphP numbering is used in the following text to refer to residues in both DrBphP and PaBphP), which can be either protonated or neutral. The dependence of the active-site dynamics on the protonation state of two histidine residues was simulated (for 20-430 ns) for the CBD domain of DrBphP in the Pr state and then for the CBD-PHY domains of DrBphP in the Pr and Pfr states and of PaBphP in the Pfr state.

The conserved H260 is stacked with the biliverdin rings B and C and interacts with the pyrrole water and with PropC. These interactions are structurally conserved (12, 32) and indicate that H260 must possess a proton bound to the Nε atom in order to form a hydrogen bond with the anionic PropC. In the Dr-Pr-CBD models with various protonation states of H260 and H290, the chromophore-binding pocket was accessible to water leading to an exchange of the pyrrole water molecule by solvent water molecules, similarly as reported for the phytochrome variants consisting of the CBD domain (180). In the Dr-Pr-CBD model with protonated H260, the hydrogen bonds between the pyrrole water and biliverdin rings B and C became destabilized. In addition to the pyrrole water exchange in this model, multiple water molecules were entering the active site between biliverdin and the above-located α-helix, especially above ring A (Figure 3.12). In the Dr-Pr-CBD model with protonated H290, water molecules were entering the active site between biliverdin and the above-located α-helix, especially above the ring D. In the model with both H260 and H290 being neutral (Nε-H), the solvent water molecules did not enter between biliverdin and the above-located α-helix, neither above ring A nor ring D, and hydrogen bonds of tetrapyrrole and the surrounding side chains were stable in the active site during the whole simulation time of 100 ns (Appendix Figure C.3). This indicates that for the MD simulations of the stable hydrogen-bonding network in the active site of the Dr-Pr-CBD model, both H260 and H290 should be neutral (Nε-H).

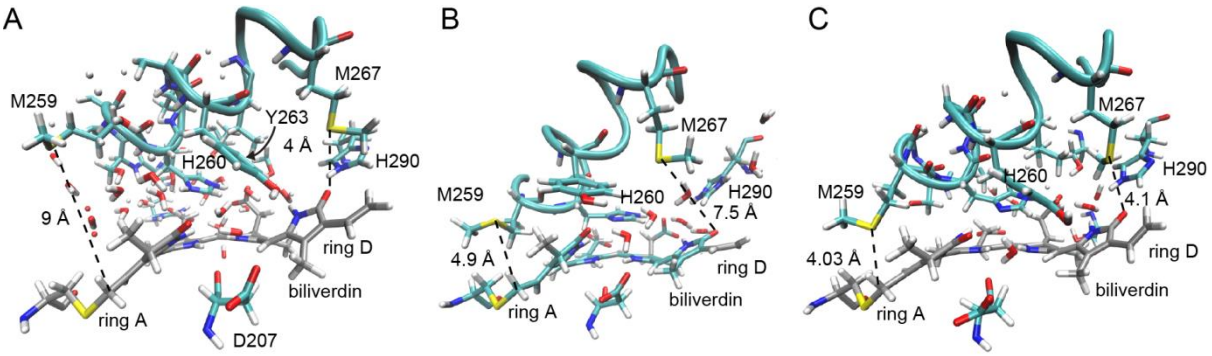

Figure 3.12. Chromophore environment in Dr-Pr-CBD models during MD simulations. Models containing protonated biliverdin, protonated H260 and neutral (Nε-H) H290 after 15 ns of simulation (A), neutral (Nε-H) H260 and protonated H290 after 20 ns of simulation (B), both neutral (Nε-H) H260 and H290 after 20 ns of simulation (C). Distances biliverdin ring A ($C3^2$)–M259 (S) and biliverdin ring D (O^D)–M267(S) were measured.

Further, the protonation states of H260 and H290 were tested for the Dr-Pr, Dr-Pfr, Pa-Pfr models containing CBD-PHY domains. Similarly as it was already observed for the Dr-Pr-CBD model, when H260 was protonated, the hydrogen bonding network in the active site, especially with the pyrrole water, became destabilized (Figure 3.13) in both the Dr-Pr-CBDPHY and Pa-Pfr-CBDPHY models. In the models with neutral (Nε-H) H260 and protonated H290, these bonds were stable over the simulation of 80 ns, although PropC rotated leading to a hydrogen bond with one of its two oxygens with H260. Therefore, H260 cannot be protonated but should be neutral in phytochrome models of both the Pr and Pfr states to preserve stable active-site interactions. While the interactions of H260 in the active site are conserved in the Pr and Pfr states, the interactions of H290 are different in each state. In the Pr state, H290 interacts with biliverdin ring D but is also solvent-exposed and a part of the cavity filled with water (Figure 3.14 A), whereas in the Pfr state H290 interacts with PropC and stays buried from the solvent by the protein residues. In the Pfr-state models with neutral (Nε-H) H290, the hydrogen bond H290-PropC became destabilized (Figure 3.15), H290 flipped out, became solvent-exposed and reached towards the water-filled cavity as shown in Figure 3.14 A. In contrast, in the models with protonated H290, this cationic histidine formed hydrogen bonds with the anionic PropC (Figure 3.15) and other hydrogen bonds in the active site also remained stable. This implies that in the MD simulations of the Pfr-state phytochrome, H290 should be protonated in order to interact with PropC electrostatically. As H290 is solvent-exposed in the Pr state, its protonation state influences the hydrogen-bonding network in the active site to a lesser extent. However, in the models with neutral (Nε-H or Nδ-H) H290, the hydrogen bond D207-Y263 was unstable, but in the model with protonated H290 this bond was stable over the whole trajectory of 80 ns (Figure 3.14 B). In order to have a stable hydrogen-bonding network in the active site, CBDPHY models of both the Pr and Pfr states should contain neutral (Nε-H) H260 and protonated H290.

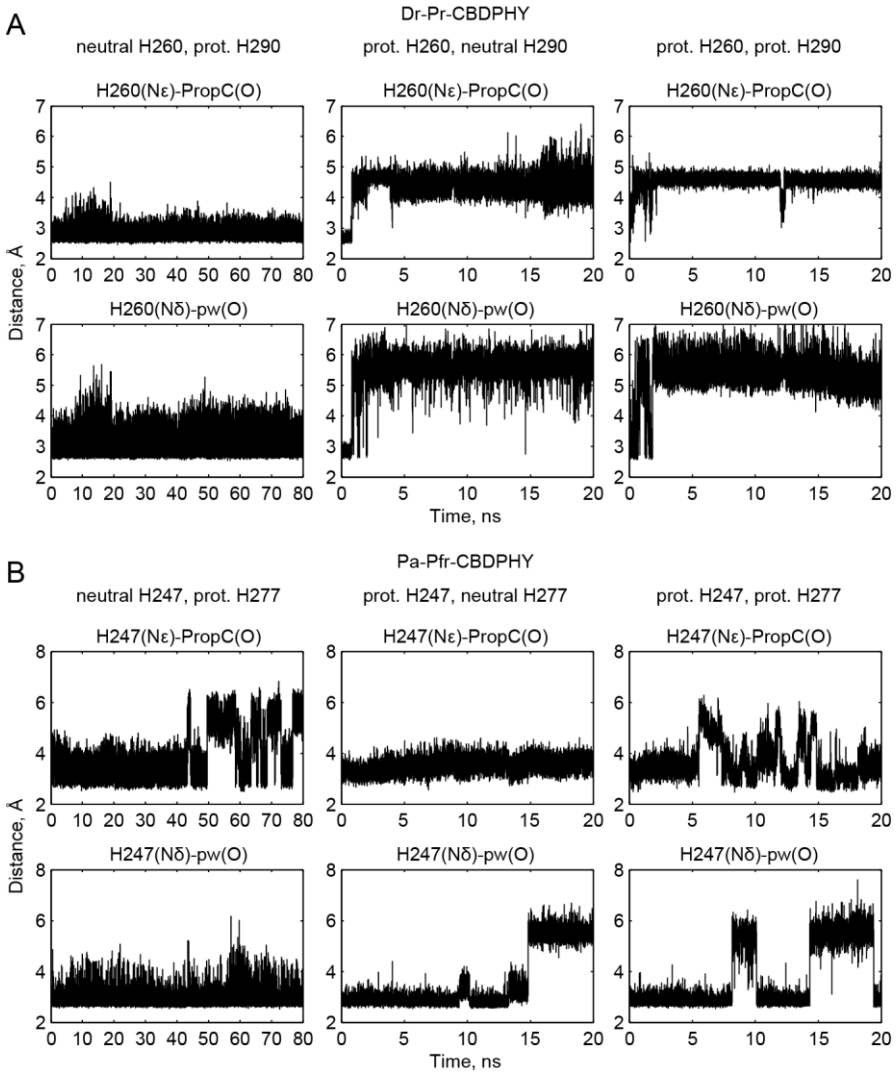

Figure 3.13. Unstable interactions in phytochrome CBDPHY models with protonated H260. Interactions of H260 (H247 in Pa-Pfr), PropC and pyrrole water (pw) measured for Dr-Pr-CBDPHY (A) and Pa-Pfr-CBDPHY (B) with protonated or neutral (Nε-H) H290 (H247 in Pa-Pfr).

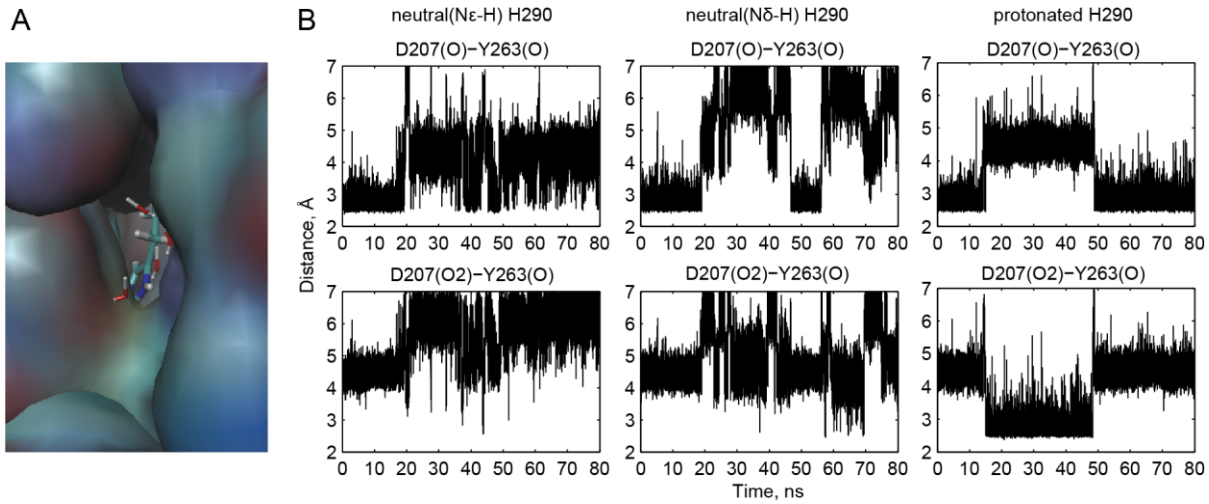

Figure 3.14. Interactions in Dr-Pr-CBDPHY models with neutral (Nε-H) H260 and different protonation states of H290. A) Solvent-exposed H290 in the model with protonated H290 after 0 ns of production run. B) Distance between Y263 and one of the carboxyl oxygens of D207 in the models with different protonation state of H290.

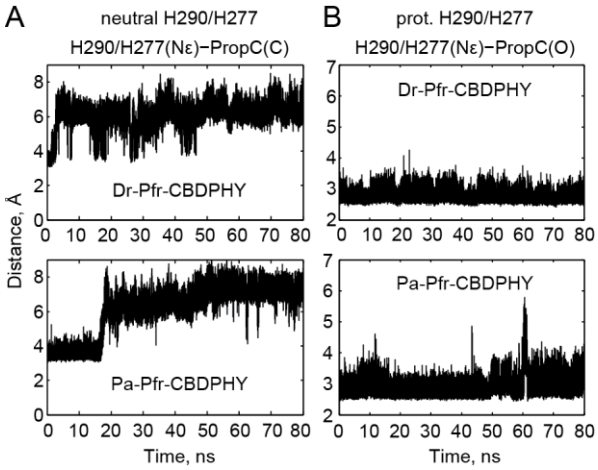

Figure 3.15. Interactions in phytochrome Pfr-state CBD-PHY models with neutral (Nε-H) H260/H247 and different protonation states of H290/H277. H290-PropC (H277-PropC in Pa-Pfr) distances in Dr-Pfr-CBDPHY and Pa-Pfr-CBDPHY models with neutral (Nε-H) (A) and protonated (B) H290/H277.

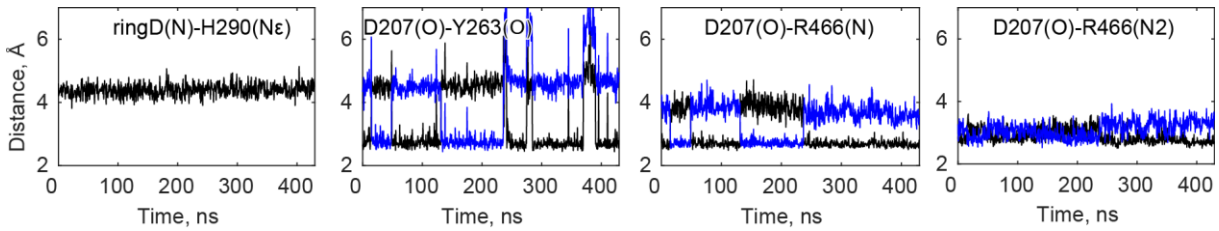

Figure 3.16. Dynamics of Dr-Pr-CBDPHY model during 430 ns simulation. Model with neutral (Nε-H) H260 and protonated H290. Distributions of the distances characterizing hydrogen-bond interactions in the active site: two different colors indicate distances to the O and O2 atoms of the D207 carboxylate.

For the trajectories of the Dr-Pr, Dr-Pfr and Pa-Pfr models containing the CBD-PHY domains with neutral (Nε-H) H260 and protonated H290, the average RMSD for all non-hydrogen atoms of the protein was 2.8±0.4 Å, 2.8±0.5 Å and 3.4±0.5 Å over 80 ns trajectories (Appendix Figure C.4). The distances corresponding to the hydrogen bonds in the active site, including interactions of the pyrrole water, biliverdin ring D, PropC, D207, H260, H290, R466 and S468 side chains, were similar to the respective distances between atoms in the crystal structures and were stable during the simulation time of 80 ns (Appendix Figures C.5-C.7). To test whether the hydrogen-bonding network in the active site and the whole model stays stable during longer trajectories, Dr-Pr was simulated for 430 ns. The average RMSD is 3.2±0.5 Å for all non-hydrogen atoms of the protein, the pyrrole water in the active site exchanged once, and the interactions in the active site were stable during the whole simulation time (Figure 3.16 and Appendix Figure C.8). Therefore, for the following analysis of the dynamics of the red-shifting aspartate-ring D

interactions, the models with neutral (Nε-H) H260 and protonated H290 were considered.

3.1.8 Dynamics of conserved aspartate-ring D interactions causing the red shift

Phytochrome's inability to undergo the full Pfr-state red shift in the absence of the PHY domain (47, 48) indicates that active-site interactions with this domain may play a role in developing the spectral shift. The MD simulations of bacterial phytochromes DrBphP and PaBphP were employed to study how the formation of the red-shifting aspartate-ring D interactions depends on other interactions in the phytochrome active site. Upon tetrapyrrole double-bond isomerization the interactions of ring D change, whereas conformational change from the Pr to the Pfr state results in changes of other interactions including tetrapyrrole-CBD domain interactions and CBD-PHY domain interactions in the active site. All models, discussed in this section, contained protonated biliverdin, neutral (Nε-H) H260 and protonated H290, according to the analysis of the previous Section 3.1.7.

The dependence of the active-site dynamics on the presence of the PHY domain was studied in the phytochrome CBDPHY and CBD models (Figure 3.17). The interactions in the active site were more stable in the CBDPHY models than in the CBD models during 80 ns of simulations. The pyrrole water was constantly exchanging in the CBD models but not in the CBDPHY models. In the CBD models of the DrBphP phytochrome, the D207 interactions with Y263 or ring D were not stable, independently on the interaction partner (Y263 in Pr state or ring D in Pfr state), as D207 rotated and its interactions became destabilized. In the Pfr-state CBD models, the H290-PropC interactions were unstable, especially of the DrBphP model. The D207-ring D interactions were also less stable due to rotation of the carboxylic group, in particular D207 rotated several times in the PaBphP model or more frequently in the DrBphP model after 15 ns of simulation leading to two peaks at the distributions. However, in the CBDPHY model of DrBphP in the Pr state, there are also two peaks for the D207 interactions as D207 rotated twice during the 80 ns trajectory. The comparison of the CBD and CBDPHY models (as presented in Figure 3.17) shows that interactions between the CBD and PHY domains, including hydrogen bonds between D207of the CBD domain and R466 or S468 of the PHY domain, may contribute to the stabilization of the active site.

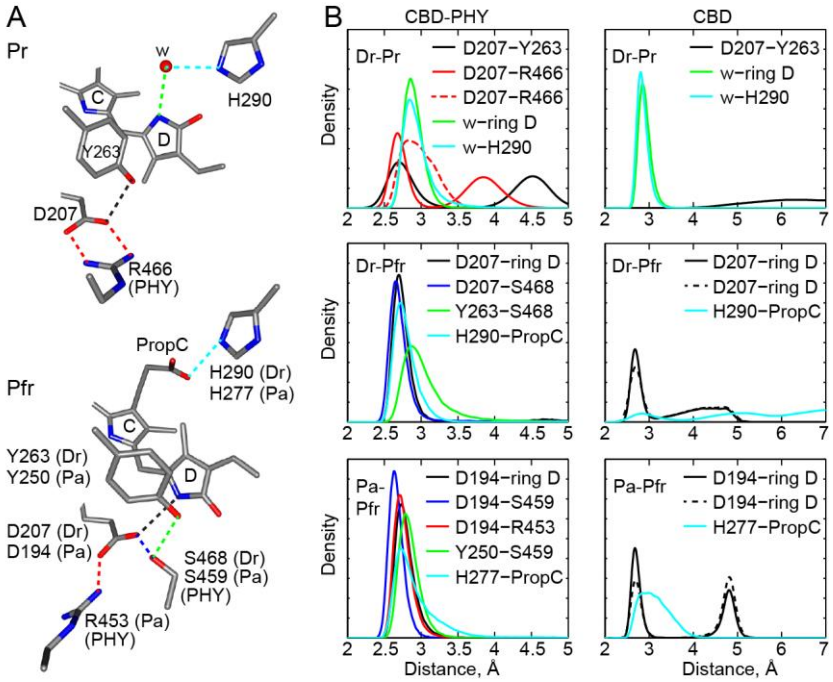

Figure 3.17. Dynamics of the active site in the Pr- and Pfr-state DrBphP (Dr) and PaBphP (Pa) phytochrome models. Models with neutral (Nε-H) H260/H247 and protonated H290/H277. The residue numbering is according to the specific protein sequence. A) Key hydrogen-bond interactions in the Pr- and Pfr-state active site. B) Distributions of the distances characterizing hydrogen-bond interactions in CBD and CBD-PHY containing models. Distributions of the distances from the last 70 ns of the 80 ns simulation. Distances over time are shown in Appendix Figures C.5-C.7, C.9-C.11.

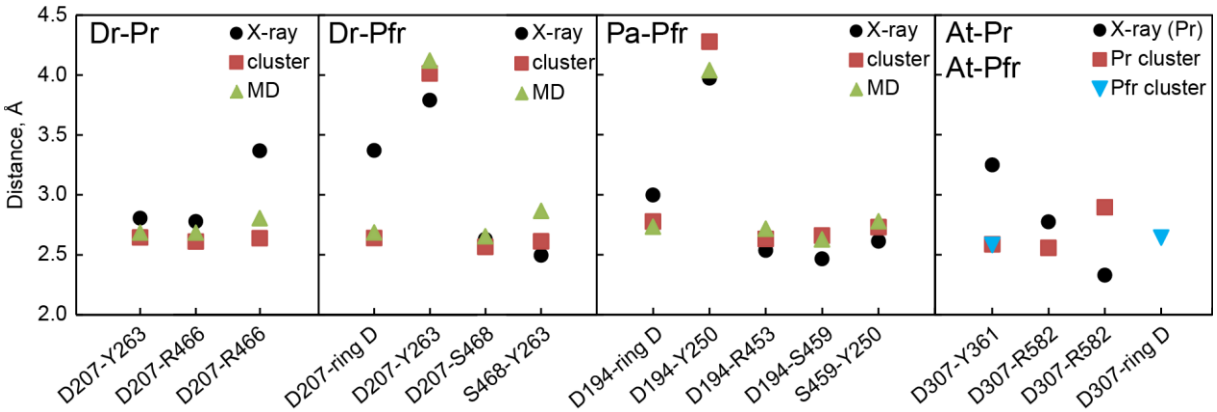

Figure 3.18. Hydrogen-bonding distances in the active site of phytochrome models. Comparison of the average distances in the CBDPHY models (MD simulation models), five main active-site cluster models (presented in Sections 3.1.5-3.1.6, Figure 3.6), X-ray crystal structures (Dr-Pr: PDB code 2o9c for CBD domain distance D207-Y263, 4o0p for CBD-PHY domains distance D207-R466; Dr-Pfr: 5c5k; Pa-Pfr: 3c2w; At-Pr: 4our). Distribution maxima of the bonds from the entire 80 ns MD simulations are plotted. Residue numbering is according to specific protein sequence: residues D194, Y250, R457, S459 of PaBphP and residues D307, Y361, R582, S584 of AtPhyB correspond to residues D207, Y263, R466, S458 of the DrBphP phytochrome.

The hydrogen-bonding interactions in the active site were compared among the simulated CBDPHY models and the X-ray crystal structures. The maxima of the distance

distributions obtained by analyzing the entire 80 ns trajectories of the MD models as well as the active-site cluster models (presented in Section 3.1.5-3.1.6) are in good agreement with the respective distances of the crystal structures (Figure 3.18). However, the D207-ring D distance in the computed and simulated Pfr-state models is shorter than in the crystal structures and corresponds to a strong hydrogen-bond. In the simulated CBDPHY models this distance became shorter already during the first steps of the energy minimization.

To characterize the formation of the hydrogen bond between D207 and ring D after the tetrapyrrole double-bond isomerization along the Pr → Pfr conversion, the DrBphP variants consisting of the CBD and PHY domains in the Pr or Pfr conformation were simulated with bound 15E-biliverdin (Figure 3.19). Conformational changes in the PHY and CBD domains together with changes of local hydrogen-bonding network induced gradual formation of the D207-ring D interactions in the investigated models. The protein dynamics showed that while the CBD and PHY domains were still in the Pr conformation with already isomerized 15E-tetrapyrrole, the D207-ring D interactions did not form during simulation of 80 ns. Typical Pr-state interactions between D207 and Y263 or R466 as well as between Y176 and ring D were stable (Appendix Figure C.12). Removing PHY domain or changing its conformation to that of the Pfr state, which in both cases removed D207-R466 interactions, led to formation of typical Pfr-state interactions such as D207-ring D and H290-PropC as well as destabilization of typical Pr-state interactions such as D207-Y263 (Figures 3.19, 3.20 A and Appendix Figures C.13-C.14). In the model containing only the Pr-state CBD domain, Y176 dissociated from ring D to interact with PropC (Figure 3.20 B), whereas in the CBD(Pr)-PHY(Pfr) model Y176 dissociated from ring D but did not form interactions with PropC during entire 80 ns of simulation. In the Pfr-state model, comprised of both the CBD and PHY domains, the D207-ring D interactions were stable among the others in the active site as shown in Figures 3.17 B and 3.19. Thence, the analysis of the MD simulations shows that the formation of the D207-ring D hydrogen bond depends on the other hydrogen-bonding interactions in the active site and on the conformation of both the CBD and PHY domains.

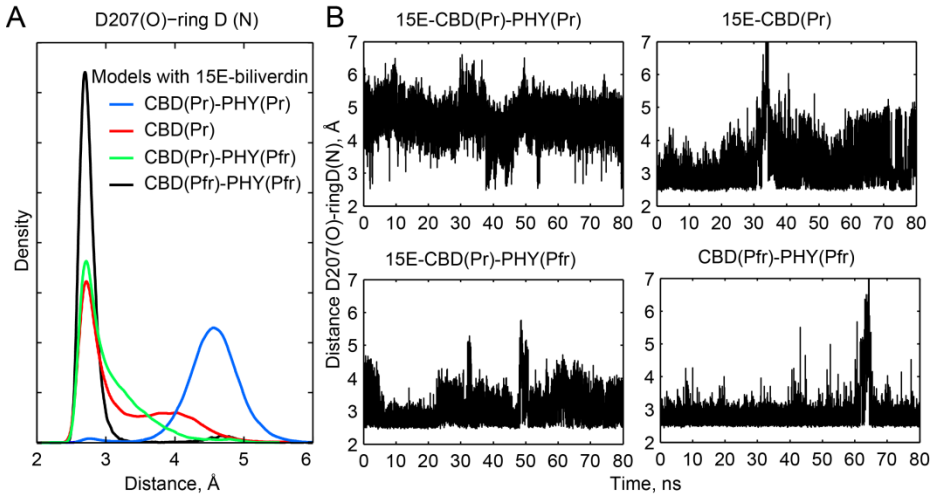

Figure 3.19. D207–ring D bond formation in MD simulations of different DrBphP phytochrome models with 15E-biliverdin. Distances are shown for models with neutral (Nε-H) H260 and protonated H290. A) D207–ring bond distribution from the last 70 ns of the 80 ns simulation. B) D207–ring D bond distance along the MD trajectory.

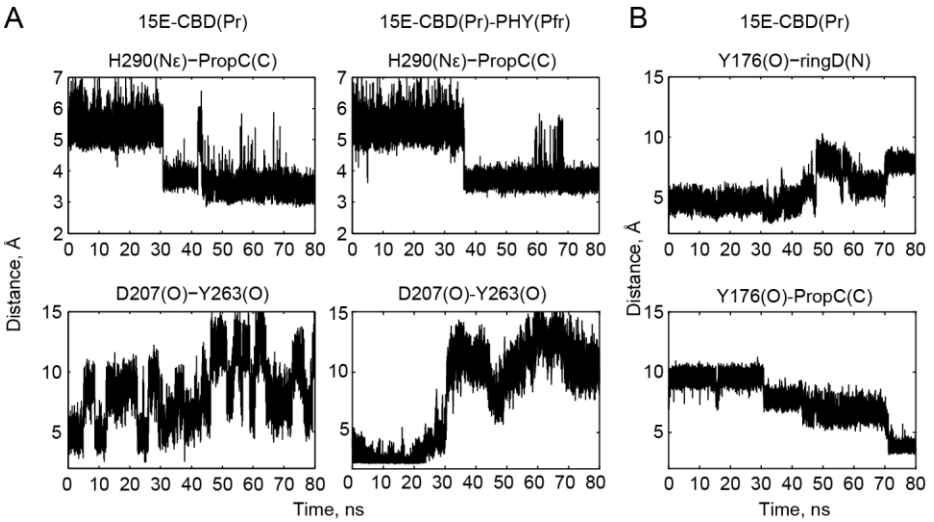

Figure 3.20. Change of the hydrogen-bonding network during MD simulations of DrBphP models with 15E-biliverdin. Distances over time are shown for models with neutral (Nε-H) H260 and protonated H290. A) H290-PropC bond formation and D207-Y263 bond dissociation in 15E-CBD(Pr) and 15E-CBD(Pr)-PHY(Pfr) models. B) Change of the Y176 interactions from ring D to PropC. For measuring distances including D207 and PropC only atom C or two different oxygen atoms of the carboxylate were selected.

To study the hydrogen-bonding network in the CBD domain of the Pfr state, the models comprised of the Pfr-state CBD domain with or without Pr-state PHY domain were simulated and compared (Figure 3.21 and Appendix Figures C.10 and C.15). In both the CBD(Pfr) and CBD(Pfr)-PHY(Pr) models the D207-ring D interactions remained present, although became less stable than in the CBD(Pfr)-PHY(Pfr) model (Figure 3.19 B). Whereas the carboxyl group of D207 rotated in the CBD(Pfr) model frequently, which is consistent with the destabilized D207-ring D interactions. In both

models, CBD(Pfr) and CBD(Pfr)-PHY(Pr), typical Pfr-state interactions between PropC and H290 or Y176 became destabilized over time and Y263 moved away from D207 and S468 indicating that the absence of the PHY domain or its presence in the Pr conformation destabilizes typical Pfr-state interactions in the CBD domain. In CBD(Pfr)-PHY(Pr) model, Y176 moved towards ring D and started interacting with it after 10 ns of the simulation indicating that the presence of the PHY domain in the Pr state induces typical Pr-state interactions (Y176-ring D) in the CBD domain. These results illustrate that typical interactions of the CBD domain in the Pfr state are destabilized in the absence of the PHY domain, and that typical interactions of the CBD domain in the Pr state are formed in the presence of the PHY domain in the Pr state.

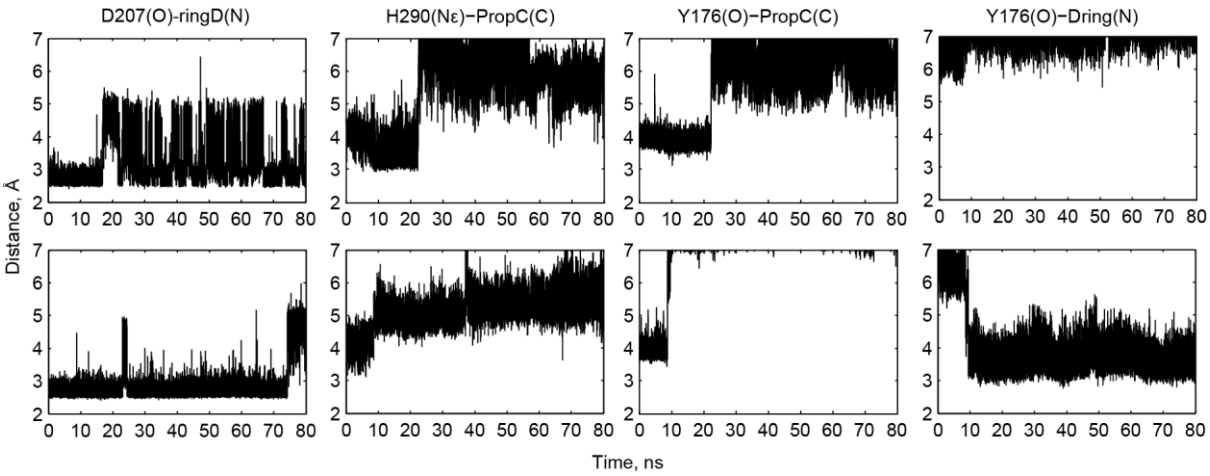

Figure 3.21. Hydrogen-bonding network change in Pfr-state CBD domain during MD simulation. CBD(Pfr) (top) and CBD(Pfr)-PHY(Pr) (bottom) models with neutral (Nε-H) H260 and protonated H290.

The MD simulations show that the interactions between the CBD and PHY domains regulate interactions in the active site and therefore the spectral properties of phytochromes. After the tetrapyrrole isomerization from 15Z to 15E, the CBD-PHY domain interactions such as D207-R466 should break in order to induce the Pfr-state interactions in the CBD domain including the D207-ring D hydrogen bond. The formation of the red-shift inducing D207-ring D hydrogen bond after the phytochrome conformational switch might be a crucial property of the phytochrome photoreception which may ensure that the phytochrome spectrum does not change before the conformational and functional switch takes place.

3.2 Protonation states of biliverdin in the phytochrome active site

3.2.1 Background and overview

Under certain conditions phytochromes can undergo deprotonation of the bound linear tetrapyrrole chromophore. Absorption spectroscopy combined with pH titrations demonstrated that the intensity of the Q band, its maximum and the blue shoulder, in the phytochrome absorption spectrum (Figure 1.1) decrease at high pH, which was assigned to tetrapyrrole deprotonation (62, 65, 66, 92). Additionally, these studies observed that the intensity ratio between the blue shoulder and the Q-band maximum increases. However, computational studies have shown that tetrapyrrole deprotonation should result in a blue-shifted spectrum (62, 65, 66), which indicates that the tetrapyrrole deprotonation as such does not necessarily lead to the decrease of the Q band intensity. The blue shift of the Q band and its blue shoulder at higher pH were demonstrated only in one spectroscopic study (69), which contradicts the previous studies, where no spectral shift was detected at higher pH, neither for the same protein (66) nor for other phytochrome proteins (62, 65, 92). In order to clarify the origin of the spectroscopic signals and their shifts, more knowledge about energetic and spectral properties of tetrapyrrole deprotonation in phytochromes is needed.

This results part presents a mechanism of tetrapyrrole deprotonation and how it influences the phytochrome spectrum and dynamics in the active site. First of all, the protonated and deprotonated biliverdin-cysteine adducts were computed to compare their energies and spectral properties as well as to evaluate spectral shifts induced upon biliverdin deprotonation. In the active site, the biliverdin can potentially donate its proton to a histidine (H260 in DrBphP) via the pyrrole water molecule. The active-site cluster models of the Pr-state phytochrome with protonated and neutral biliverdin (deprotonated at ring C) were computed to compare contributions of the proton transfer to the phytochrome absorption spectrum and to suggest an explanation for the Q-band blue shoulder. The active-site models were also used to study how the proton transfer influences emission and radiative decay kinetics. In addition to the quantum-chemical calculations, an MD study was performed on the DrBphP protein by simulating the CBD and CBD-PHY domain models to investigate how the transfer of the positive charge from biliverdin influences the dynamics of the phytochrome active site. The dynamics in

the models with protonated and neutral biliverdin was compared to evaluate changes in the hydrogen-bonding network due to proton transfer from the biliverdin to the histidine.

3.2.2 Energies and spectral shifts of deprotonated biliverdin-cysteine adduct

The biliverdin deprotonation and its spectral properties were studied on the biliverdin-cysteine adducts with different protonation states of the pyrrole rings A-D. The biliverdin-cysteine adduct without propionates was deprotonated at none, one or two of the pyrrole rings (Figure 3.22 A). The geometries of the adducts were optimized in the ground (S_0) state with constrained dihedral angles between the adjacent pyrrole rings (total six angles) with the PBE0/cc-PVDZ method. At the optimized S_0-min geometries of the biliverdin-cysteine adducts with different rings being deprotonated, the PBE0 energies were compared (Figure 3.22). The singly-deprotonated adducts had lower energy when one of the rings A, B or C was deprotonated as compared to the adduct deprotonated at ring D; this indicates that deprotonation at rings A, B or C is energetically more favorable. The doubly-deprotonated adducts had lower energy when two of the rings A, B, or C were deprotonated as compared to the adducts deprotonated at ring D and one of rings A, B or C. These results suggest that if biliverdin undergoes deprotonation, first it happens rather to rings A, B or C than ring D.

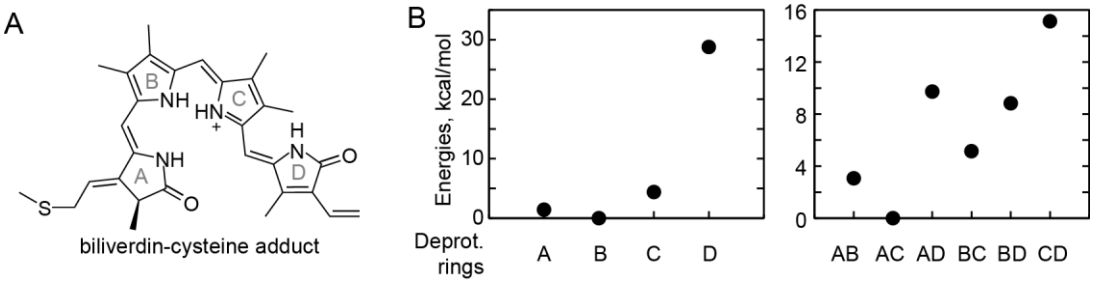

Figure 3.22. Deprotonation of biliverdin-cysteine adducts. A) Chemical structure of the protonated biliverdin-cysteine adduct. B) Energies of singly-deprotonated (neutral) and doubly-deprotonated (anionic) biliverdin-cysteine adducts computed with the PBE0/cc-PVDZ method.

The excited-state energies, computed with the XMCQDPT2-CASSCF method at the optimized geometries, were compared between the protonated, singly- and doubly-deprotonated biliverdin-cysteine adducts (Figure 3.23). The SA7-CASSCF(6,5) and SA5-CASSCF(4,4) active spaces for the CASSCF calculations were selected based on the previous results (Section 3.1.2) which indicated that these both active spaces give comparative energies. The transition energies between ground and first excited states

(S_0-S_1) computed with both active spaces were similar for the same adduct. The singly-deprotonated adducts had higher S_0-S_1 energies than the protonated adduct. The doubly-deprotonated adducts had similar or slightly increased S_0-S_1 energies as compared to the protonated adduct. The oscillator strength of the S_0-S_1 transition was similar in all adducts (protonated and variously deprotonated), except for the adducts with both rings A-B or C-D being deprotonated (Table 3.9). In these two adducts, the oscillator strength of the S_0-S_1 transition was significantly reduced. This indicates that upon biliverdin deprotonation no significant reduction of the absorption intensity is expected. All S_0-S_n transition energies were increased in the singly-deprotonated adducts (except S_0-S_4 energy in the adduct with deprotonated ring A) as compared to the protonated adduct. However, in the doubly-deprotonated adducts the energies were rather similar as in the protonated adduct. These results predict that both the Q and Soret bands in the spectra of a singly-deprotonated biliverdin is blue-shifted as compared to the spectrum of the protonated biliverdin. By contrast, a doubly-deprotonated biliverdin is expected to have a similar or slightly blue-shifted spectrum as compared to the protonated biliverdin. Interestingly, subtraction of a single proton from the biliverdin induces a blue shift, whereas subtraction of a second proton induces a red shift of the excitation corresponding to the Q band.

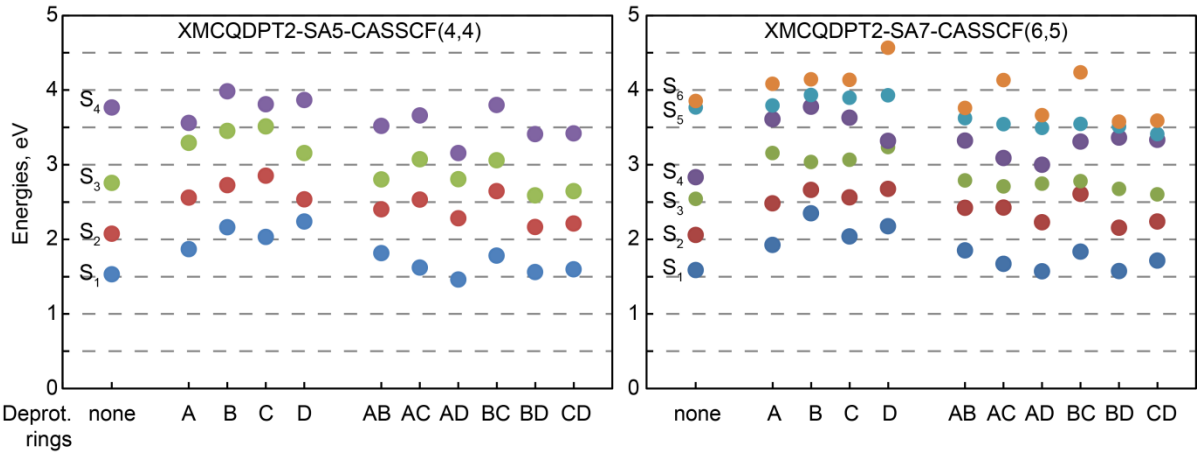

Figure 3.23. Excitation energies of biliverdin-cysteine adducts computed at S_0-min geometries. Energies of protonated, singly-deprotonated (neutral) and doubly-deprotonated (anionic) biliverdin adducts were taken from Table 3.9.

The emission properties were further studied in protonated and singly-deprotonated biliverdin-cysteine adducts. Biliverdin deprotonation at ring C was addressed based on the phytochrome active site structure, suggesting that the highly conserved histidine H260

could potentially deprotonate biliverdin via the pyrrole water molecule. The protonated and deprotonated biliverdin-cysteine adducts were optimized in the S_1 state with the TD-PBE0/cc-PVDZ method with constrained six dihedral angles. At the optimized S_1-min geometries, the excited-state energies were computed with the XMCQDPT2 method (Figure 3.24). Depending on the active space in the CASSCF calculations, the Stokes shifts were 0.06-0.013 and 0.27-0.29 eV in the protonated and deprotonated adducts, respectively (Tables 3.9 and 3.10). At the S_1-min geometries the excitation energies differed in both adducts more as compared to the energies at the S_0-min geometries (Figure 3.24). These results show that the biliverdin deprotonation at ring C leads to a larger blue shift in the absorption spectrum than in the emission spectrum and that the Stokes shift increases upon the biliverdin deprotonation.

Table 3.9. Excitation energies (in eV) and oscillator strengths (in parentheses) of biliverdin-cysteine adducts at S_0-min geometries. The protonation state of pyrrole rings is indicated.

Transition	prot.	deprot. A	deprot. B	deprot. C	deprot.D	
			XMCQDPT2-SA5-CASSCF(4,4)			
S_0-S_1	1.53 (0.908)	1.87 (0.878)	2.16 (1.049)	2.03 0.968)	2.24 (0.894)	
S_0-S_2	2.08 (0.016)	2.56 (0.021)	2.73 (0.026)	2.85 (0.004)	2.53 (0.029)	
S_0-S_3	2.75 (0.645)	3.29 (0.545)	3.45 (0.708)	3.51 (0.620)	3.16 (1.020)	
S_0-S_4	3.76 (0.596)	3.56 (0.404)	3.98 (0.170)	3.81 (0.097)	3.87 (0.120)	
			XMCQDPT2-SA7-CASSCF(6,5)			
S_0-S_1	1.59 (1.015)	1.92 (0.834)	2.35 (1.083)	2.04 (1.012)	2.17 (0.911)	
S_0-S_2	2.06 (0.028)	2.48 (0.044)	2.66 (0.030)	2.56 (0.015)	2.67 (0.122)	
S_0-S_3	2.54 (0.053)	3.15 (1.185)	3.03 (0.356)	3.06 (0.015)	3.24 (0.351)	
S_0-S_4	2.83 (0.839)	3.61 (0.059)	3.77 (0.166)	3.63 (0.514)	3.32 (0.150)	
S_0-S_5	3.77 (0.439)	3.79 (0.052)	3.93 (0.119)	3.89 (0.134)	3.93 (0.061)	
S_0-S_6	3.85 (0.242)	4.08 (0.008)	4.14 (0.026)	4.14 (0.087)	4.57 (0.116)	
Transition	deprot. AB	deprot. AC	deprot. AD	deprot. BC	deprot. BD	deprot. CD
			XMCQDPT2-SA5-CASSCF(4,4)			
S_0-S_1	1.81 (0.365)	1.62 (0.944)	1.46 (1.057)	1.78 (0.966)	1.56 (0.908)	1.60 (0.512)
S_0-S_2	2.40 (0.204)	2.53 (0.116)	2.28 (0.056)	2.65 (0.180)	2.17 (0.160)	2.21 (0.334)
S_0-S_3	2.80 (1.379)	3.07 (0.321)	2.80 (0.330)	3.06 (0.548)	2.59 (0.754)	2.64 (0.861)
S_0-S_4	3.52 (0.132)	3.66 (0.056)	3.16 (0.059)	3.80 (0.073)	3.41 (0.112)	3.42 (0.356)
			XMCQDPT2-SA7-CASSCF(6,5)			
S_0-S_1	1.85 (0.356)	1.67 (0.992)	1.57 (1.099)	1.83 (1.187)	1.57 (0.874)	1.71 (0.508)
S_0-S_2	2.42 (0.196)	2.42 (0.010)	2.23 (0.100)	2.61 (0.052)	2.15 (0.126)	2.24 (0.243)
S_0-S_3	2.79 (1.091)	2.71 (0.290)	2.74 (0.110)	2.78 (0.290)	2.67 (0.681)	2.60 (0.480)
S_0-S_4	3.32 (0.178)	3.09 (0.271)	3.00 (0.161)	3.31 (0.152)	3.36 (0.015)	3.33 (0.135)
S_0-S_5	3.62 (0.096)	3.54 (0.333)	3.49 (0.118)	3.55 (0.377)	3.51 (0.259)	3.41 (0.559)
S_0-S_6	3.76 (0.051)	4.13 (0.018)	3.66 (0.251)	4.24 (0.003)	3.58 (0.106)	3.59 (0.027)

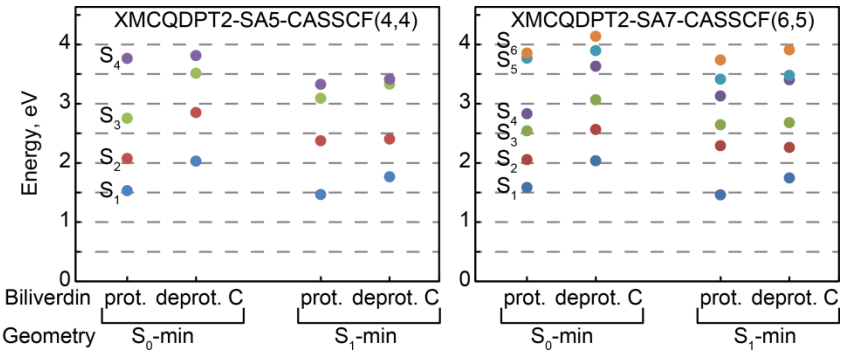

Figure 3.24. Excitation energies of the protonated and deprotonated (at ring C) biliverdin-cysteine adducts. Energies corresponding to the computed absorption and emission spectra at S_0-min and S_1-min geometries, respectively, are shown in Tables 3.9 and 3.10.

Table 3.10. Excitation energies (in eV) and oscillator strengths (in parentheses) of the protonated and deprotonated (at ring C) biliverdin-cysteine adducts at the S_1-min geometry.

Transition	XMCQDPT2-SA5-CASSCF(4,4)		XMCQDPT2-SA7-CASSCF(6,5)	
	prot.	deprot. C	prot.	deprot. C
S_0-S_1	1.47 (0.904)	1.76 (0.895)	1.46 (0.945)	1.75 (0.947)
S_0-S_2	2.37 (0.043)	2.40 (0.021)	2.29 (0.033)	2.26 (0.008)
S_0-S_3	3.09 (0.561)	3.33 (0.633)	2.64 (0.074)	2.68 (0.046)
S_0-S_4	3.33 (0.143)	3.41 (0.124)	3.13 (0.503)	3.40 (0.576)
S_0-S_5			3.41 (0.230)	3.48 (0.088)
S_0-S_6			3.74 (0.133)	3.91 (0.057)

3.2.3 Spectral blue shift due to proton transfer between biliverdin and H260

The proton transfer between biliverdin and protein and how this affects the phytochrome spectral signatures was studied by employing the cluster models representing the active site of the DrBphP phytochrome in the Pr state. In the phytochrome protein, biliverdin can be potentially deprotonated by the highly conserved H260 which is located above biliverdin rings B and C, especially ring C, and interacts with biliverdin rings A-B-C via a pyrrole water molecule and with the anionic PropC. Therefore, H260 can be a good proton acceptor. Here, biliverdin deprotonation was considered only at ring C. The reduced-size active-site cluster models were prepared with protonated and neutral (deprotonated at ring C) biliverdin as described in Methods Section 2.1.2 and are shown in Figure 3.25 A. The protBV-neutrH260 model contained protonated biliverdin and neutral (Nε-H) H260 in addition to other residues. The neutrBV-protH260 model was prepared with the same composition of residues but containing neutral biliverdin and protonated H260, where the proton was transferred from the N atom of ring C to the Nδ atom of H260 via the pyrrole water molecule. Both models were optimized in the ground state with the PBE0/cc-PVDZ method to obtain the S_0-min geometry. During the

geometry optimization of the neutrBV-protH260 model, the proton from the Nε atom of H260 moved to the anionic PropC and resulted in neutralizing the charges in the model (Figure 3.25 A).

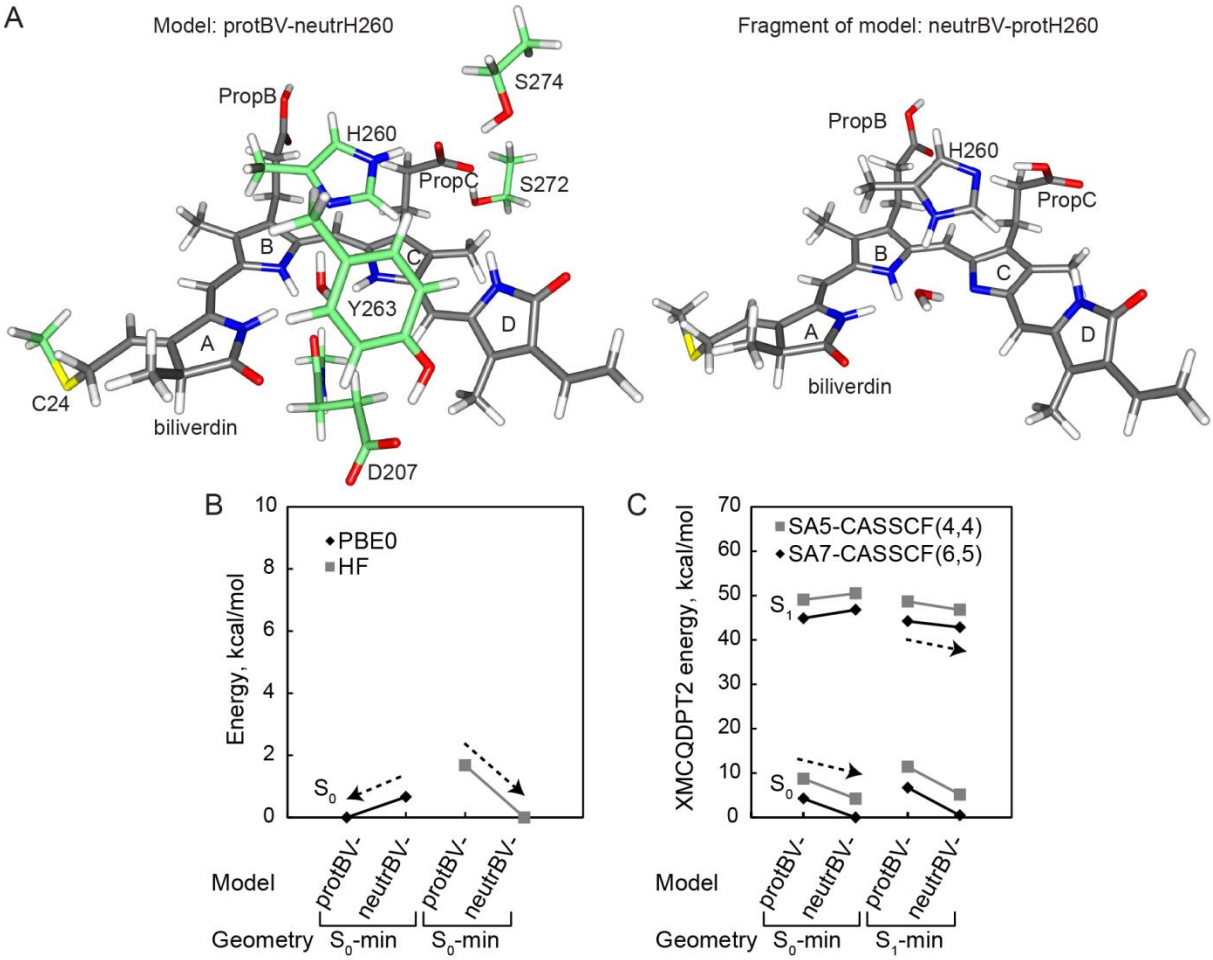

Figure 3.25. Biliverdin deprotonation by H260 in the active site of DrBphP phytochrome. A) The active-site cluster model with protonated biliverdin (left) and the fragment of the model with neutral biliverdin (right), where only residues with changed protonation state are shown. B) Proton transfer in the ground (S_0) state computed with the PBE0 and HF methods. C) Proton transfer in the ground (S_0) and excited (S_1) states computed with the XMCQDPT2-SA7-CASSCF(6,5) and XMCQDPT2-SA5-CASSCF(4,4) methods. In panels B and C the names of protBV-neutrH260 and neutrBV-protH260 were abbreviated as protBV- and neutrBV-, respectively; arrows indicate the proton transfer direction.

The ground-state energies of the active-site models with protonated and neutral biliverdin were compared. At the S_0-min geometries, the energy computed with PBE0/cc-PVDZ, the same method as used for the geometry optimization, was lower for the model with protonated biliverdin, indicating that the biliverdin protonation in the ground state is energetically favorable (Figure 3.25 B). The energy difference upon the biliverdin deprotonation is small (0.67 kcal/mol) indicating that the phytochrome might be present

in both states of biliverdin protonation. The energies computed with a less accurate but also a single-reference method, the HF method, were lower for the model with neutral biliverdin, however the energy difference of -1.68 kcal/mol was also relatively small. These results show that the change of the ground-state energy upon the biliverdin deprotonation is small and suggest an energetically-favorable proton transfer between biliverdin ring C and H260 in phytochrome.

Table 3.11. Excited-state energies (in eV) and oscillator strengths (in parentheses) of the active-site cluster models with protonated or neutral biliverdin.

Transition	protBV-neutrH260		neutrBV-protH260	
	S_0-min	S_1-min	S_0-min	S_1-min
	XMCQDPT2-SA5-CASSCF(4,4)			
S_0-S_1	1.75 (1.267)	1.61 (1.243)	2.00 (1.231)	1.80 (1.200)
S_0-S_2	2.84 (0.034)	2.56 (0.014)	3.09 (0.042)	2.68 (0.019)
S_0-S_3	3.31 (0.339)	3.14 (0.391)	3.51 (0.359)	3.24 (0.453)
S_0-S_4	3.71 (0.056)	3.43 (0.076)	3.87 (0.066)	3.49 (0.073)
	XMCQDPT2-SA7-CASSCF(6,5)			
S_0-S_1	1.76 (1.385)	1.63 (1.365)	2.03 (1.358)	1.84 (1.337)
S_0-S_2	2.71 (0.025)	2.47 (0.010)	2.94 (0.031)	2.60 (0.009)
S_0-S_3	3.00 (0.047)	2.87 (0.056)	3.28 (0.028)	3.04 (0.044)
S_0-S_4	3.28 (0.465)	3.16 (0.478)	3.47 (0.558)	3.27 (0.611)
S_0-S_5	3.73 (0.070)	3.47 (0.100)	3.90 (0.048)	3.57 (0.061)
S_0-S_6	4.09 (0.106)	3.92 (0.119)	4.32 (0.094)	4.07 (0.093)

To evaluate the effect of the proton transfer between biliverdin and H260 on the S_0-S_1 energies, the following calculations were done using the active-site models. Starting from the S_0-min geometries of the active-site models, biliverdin atoms were optimized in the first excited state with the TD-PBE0/cc-PVDZ method to obtain the S_1-min geometry. The excited-state energies were calculated at the S_0-min and S_1-min geometries of both models using the XMCQDPT2-SA5-CASSCF(4,4) and XMCQDPT2-SA7-CASSCF(6,5) methods (Figure 3.25 C). Depending on the active space in the CASSCF calculations, the S_0-S_1 energy upon the biliverdin deprotonation decreased by 0.25-0.27 eV at the optimized S_0-min geometries and by 0.19-0.21 eV at the optimized S_1-min geometries (Table 3.11), indicating a larger blue shift in the absorption than emission spectrum. The blue-shifted S_0-S_1 energy at the S_0-min geometry of the model with neutral biliverdin in comparison to the model with protonated biliverdin suggests that the origin of the Q-band blue shoulder in the Pr-state phytochrome absorption may be assigned to the phytochrome with bound neutral biliverdin (Figure 3.26). The Stokes shifts were larger

for the model with neutral biliverdin as compared to the model with protonated biliverdin (Table 3.12) which is in line with results obtained for the biliverdin-cysteine adducts (Figure 3.24). Altogether, the calculations show that the biliverdin deprotonation by H260 in phytochrome leads to a larger Stokes shift and induce a larger blue shift of the absorption than emission spectrum and that the biliverdin deprotonation might contribute to the Q-band blue shoulder in the Pr-state phytochrome absorption.

Table 3.12. Properties of the active-site cluster models with protonated or neutral biliverdin computed with the XMCQDPT2-SA5-CASSCF(4,4) (left value) and XMCQDPT2-SA7-CASSCF(6,5) (right value) methods.

Property	protBV-neutrH260	neutrBV-protH260
τ_{rad}, ns	7.11/6.38	5.90/5.11
Stokes shift, eV	0.134/0.136	0.201/0.193
ΔS0 in S_0-min, eV	-4.50*/-4.27*	
ΔS1 in S_1-min, eV	-1.87**/-1.38**	

* - average of both values computed with the XMCQDPT2 methods is -4.38 kcal/mol. ΔS0 value computed with the PBE0 and HF methods is 0.67 and -1.68 kcal/mol , respectivelly.
** - average of both values computed with the XMCQDPT2 methods is -1.63 kcal/mol.

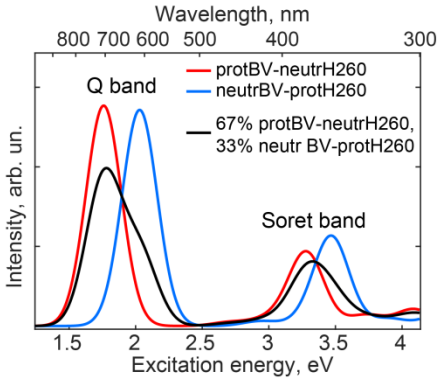

Figure 3.26. Computed absorption spectrum of the active-site cluster models with protonated or neutral biliverdin. Excitation energies, computed with XMCQDPT2-SA7-CASSCF(6,5) at S_0-min geometries, were taken from Table 3.11. The Q band is only contributed by the S_0-S_1 transition. Combined spectrum of both models with different occupancies (black line) corresponds to the experimental spectrum shown in (Figure 1.1).

The proton transfer between biliverdin and H260 in the excited (S_1) state was evaluated based on the XMCQDPT2 energies in the active-site models. Comparing the energies at the optimized S_1-min geometries showed that the S_1 energy was lower by -1.63 kcal/mol in the model with neutral biliverdin than in the model with protonated biliverdin (Table 3.12) indicating that the biliverdin deprotonation in the excited state is energetically favorable. The radiative decay lifetime τ_{rad} was estimated in the models with protonated and neutral biliverdin. Depending on the active space in the CASSCF calculations, τ_{rad}

decreased from 6.7±0.04 ns to 5.5±0.4 ns upon the biliverdin deprotonation (Table 3.12), indicating shorter radiative lifetime in the model with neutral biliverdin. The oscillator strength of the S_1-S_0 transition at the S_1-min geometries decreased upon the biliverdin deprotonation (from 1.243 to 1.200 or from 1.365 to 1.337 depending on the active space in the CASSCF calculations as shown in Table 3.11). Such a decrease indicates lower fluorescence intensity in the model with neutral biliverdin. These results show that the biliverdin deprotonation by H260 in phytochrome may be energetically favorable in the excited state and lead to a lower fluorescence intensity and shorter radiative decay lifetime.

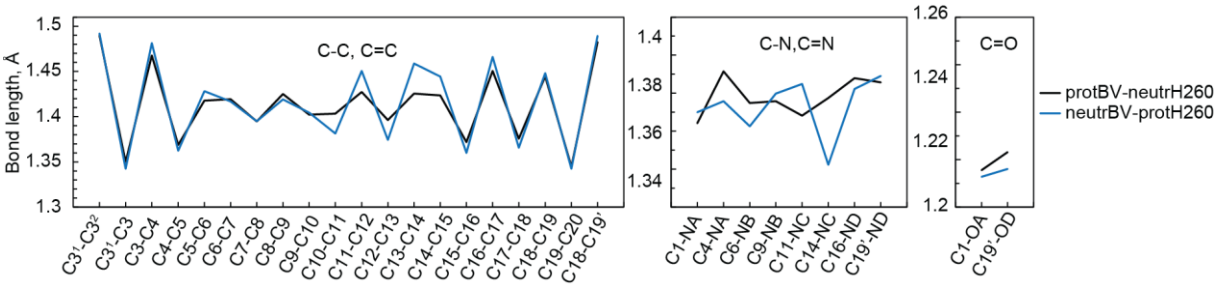

Figure 3.27. Bond lengths in the biliverdin from the active-site cluster models with protonated or neutral biliverdin at S_0-min geometries.

The bond lengths and charges in the biliverdin were compared between the active-site models containing protonated and neutral biliverdin. The geometry of the protonated and neutral biliverdin at the S_0-min geometries differs mostly for ring C and methine bridges BC and CD (Figure 3.27). The C-C single bonds became longer and the C=C double bonds became shorter in the neutral biliverdin as compared to the protonated one. The change of bond length alternations upon the biliverdin deprotonation indicates weaker π-conjugation in the neutral biliverdin which correlates with an increased excitation energy and corresponds to the Q-band blue shoulder in the Pr-state phytochrome spectrum. Interestingly, in the literature one of the explanations for the blue shoulder was suggested to be a vibronic transition, contributed by the C=C, C-C, C-N stretches (73), which points out to similar electronic effects. Upon the deprotonation, the charge on all pyrrole rings decreased, especially on ring C (by -0.484 a. u.), the negative charge on the N atom of ring C decreased by -0.229 a. u. (Table 3.13). The charges on methine bridges AB and CD almost did not change, whereas they decreased on bridge BC by -0.076 a. u. These results suggest that changes in bond length and charge distribution upon biliverdin (de)protonation in the phytochrome active site may induce a change of the π-system

conjugation which might lead to differences of the absorption and emission spectra and be linked to the presence of the Q-band blue shoulder in the Pr-state phytochrome spectrum.

Table 3.13. Mulliken charges (in a. u.) computed for the S_0 state with the XMCQDPT2-SA7-CASSCF(6,5) method at S_0-min geometries of the active-site cluster models with protonated and neutral biliverdin.

	Ring				Methine bridge			Atom*		
Model	A	B	C	D	AB	BC	CD	N^C	H^C	C10
protBV-neutrH260	0.167	0.090	0.151	0.089	-0.131	0.074	-0.047	-0.349	0.215	0.048
neutrBV-protH260	0.151	0.003	-0.332	0.031	-0.130	-0.002	-0.051	-0.577	n/a	-0.011
difference	-0.016	-0.086	-0.484	-0.058	0.002	-0.076	-0.004	-0.229	n/a	-0.059

* charge on other atoms changes not more than 0.030 a. u. H^C atom is bound to N^C, C10 is the atom of BC bridge. n/a – not applicable.

3.2.4 Dynamics of phytochrome CBD domain with neutral biliverdin

The influence of the biliverdin deprotonation on the dynamics in the phytochrome active site was studied in the DrBphP phytochrome models containing protonated and neutral (deprotonated at ring C) biliverdin. To simulate models with neutral biliverdin, the force field parameters for the neutral biliverdin were prepared based on the parameters for the protonated biliverdin published by Kaminski and co-workers (170, 171). The H atom (with a charge of 0.355 a. u.) of ring C was removed and only charges on the tetrapyrrole atoms were changed, whereas charges on PropB and PropC were kept as in the protonated biliverdin (Table 3.14). The charge on rings A-D and methine bridge BC was reduced, whereas on methine bridges AB and CD it was increased in order to smoothen differences between positive and negative parts of the biliverdin, similarly as it was observed in the quantum chemical calculations of the active-site model with neutral biliverdin (Table 3.13). H atoms on the methyl groups of rings A and B as well as all atoms except N on ring C were kept with unchanged charges. The charge on the N atom of rings A, B and D was increased by 0.05, 0.1 and 0.05 a. u., respectively, and was decreased on ring C was by 0.05 a. u. Charges on the other atoms were reduced by a maximum of 0.035 a. u. or increased by a maximum of 0.015 a. u. as specified in the Methods Section 2.2.2. The prepared set of the force field parameters for the neutral (deprotonated at ring C) biliverdin (referred as parameter set "a") was used to simulate all models with neutral biliverdin presented in this section.

Table 3.14. Comparison of charges (in a. u.) in CHARMM force field for protonated and neutral biliverdin (BV). Parameter set "a" is indicated for neutral biliverdin deprotonated at ring C.

	Ring				Bridge		
BV	A	B	C	D	AB	BC	CD
prot.	0.340	0.422	0.189	0.357	-0.287	0.208	-0.229
neutr.	0.095	0.197	-0.216	0.032	-0.087	0.158	-0.179
difference	-0.245	-0.225	-0.405	-0.325	0.200	-0.050	0.050

	Atom*							
BV	N^A	N^B	N^C	N^D	H^A	H^C	H^B	H^D
prot.	-0.555	-0.543	-0.654	-0.56	0.332	0.355	0.306	0.425
neutr.	-0.505	-0.443	-0.704	-0.51	0.307	n/a	0.271	0.395
difference	0.050	0.100	-0.050	0.050	-0.025	n/a	-0.035	-0.030

* H^A, H^B, H^C, H^D atoms are bound to N^A, N^B, N^C , N^D atoms, respectively. n/a – not applicable.

To study dynamics in the active site of the DrBphP phytochrome in the Pr state, the CBD domain models containing protonated and neutral (deprotonated at ring C) biliverdin were used. The models, containing neutral or protonated histidines H260 and H290, were named by indicating ε or P, corresponding to neutral (Nε-H) or protonated form, first for H260 and then for H290. Models CBD-neutrBV-(Pε) and CBD-neutrBV-(PP) were compared with CBD-neutrBV-(εε) as a negative control and with models CBD-protBV-(εε) and CBD-protBV-(εP) as positive controls. According to the above-described proton transfer mechanism between ring C and H260, the phytochrome active-site interactions are expected to be stable when biliverdin is protonated and H260 is neutral and *vice versa*. The RMSDs of the protein, its backbone and the chromophore were similar among all models (Appendix Figure C.16). As for the majority of the models the RMSDs increased during the initial 30 ns, only the last 70 ns out of total 100 ns were used for the plotted distributions.

The stability of the hydrogen bonds between biliverdin ring C and H260 was analyzed to evaluate the proton transfer via the pyrrole water (pw) molecule. The ring C-pw-H260 interactions are the key interactions in the above-described biliverdin (de)protonation mechanism. The pyrrole water, serving as a bridge for the ring C-H260 interactions, was exchanged by bulk water after 5-15 ns in all models (Appendix Figure C.17). However, the distance between the N atom of ring C and the Nδ atom of H260 were stable in all models except CBD-neutrBV-(PP), where this distance was longer due to the repulsive electrostatic forces between the positively charged protonated biliverdin and H260

(Figure 3.28). This indicates that the change in the protonation state of biliverdin and H260 i.e. protonated biliverdin/neutral H260 or neutral biliverdin/protonated H260 does not affect the hydrogen-bonding interactions between these two residues significantly.

Hydrogen-bonding interactions in the active site, especially of PropC and H290, were analyzed to evaluate how the change in protonation state of biliverdin, H260 and H290 affects neighboring hydrogen bonds in the active site (Figure 3.28). It was observed that protonated H260 interacted more with the second oxygen of the PropC carboxyl group in the CBD-neutrBV-(Pε) model after 65 ns of the simulation, whereas in all other models as well as in the crystal structure it interacted with only one PropC oxygen. Interactions between S272 and PropC were stable in all models, however in the CBD-neutrBV-(Pε) model the interactions were slightly weaker as they were destabilized for about 15 ns and then formed again. The interactions between S274 and PropC were destabilized in the CBD-neutrBV-(Pε) model after 60 ns of simulation (a water molecule entered between S274 and PropC), whereas in the CBD-neutrBV-(PP) model these interactions were rather instable during almost the entire trajectory. H290 interacted with the biliverdin ring D via a water molecule in all models, but in the models with protonated H290 it moved closer to PropC independently on the biliverdin protonation state. H290 interacted with PropC in the CBD-neutrBV-(Pε) model for less than 20 ns, whereas in the CBD-neutrBV-(PP) model these interactions were constantly forming and breaking during the entire length of the trajectory.

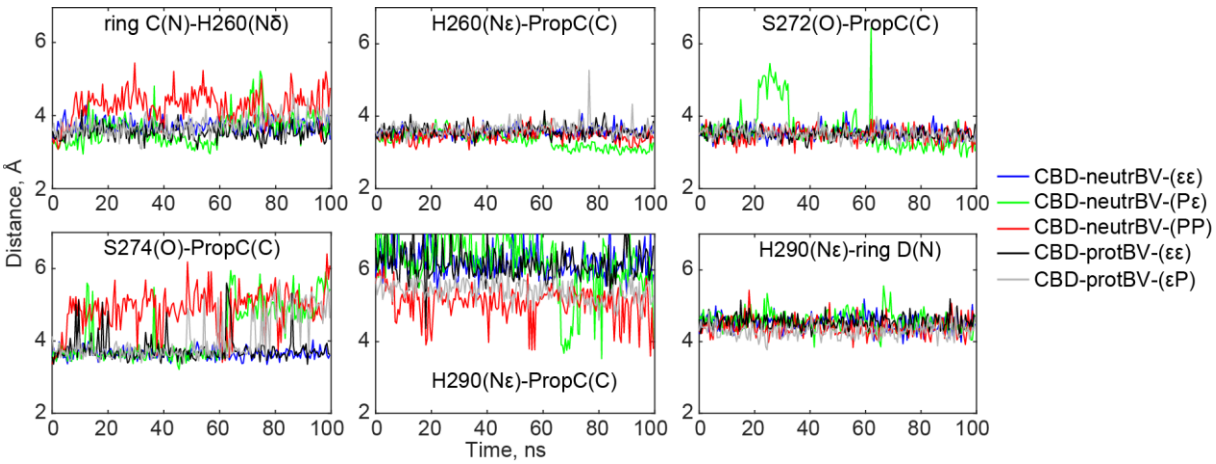

Figure 3.28. Active-site hydrogen-bonding interactions in CBD models of the Pr-state DrBphP phytochrome. Interacting residues are shown in Figure 1.2.

The protonation state of H260 influences the stability of the hydrogen bonds in the active site as it was observed in the models containing neutral as well as protonated biliverdin. In the models with neutral H260, independent of the biliverdin protonation state, the negatively charged PropC could form hydrogen bonds with neutral H260, S272 and S274. In the models with protonated H260 and neutral biliverdin, due to the salt bridge between cationic H260 and anionic PropC, the PropC carboxylate formed less stable hydrogen bonds with the neutral serine side chains (S274 or both S272 and S274) and stronger hydrogen bonds with the protonated histidines (H290 or both H260 and H290). PropC interacted stronger with H260 in the CBD-neutrBV-(Pε) model and with H290 in the CBD-neutrBV-(PP) model.

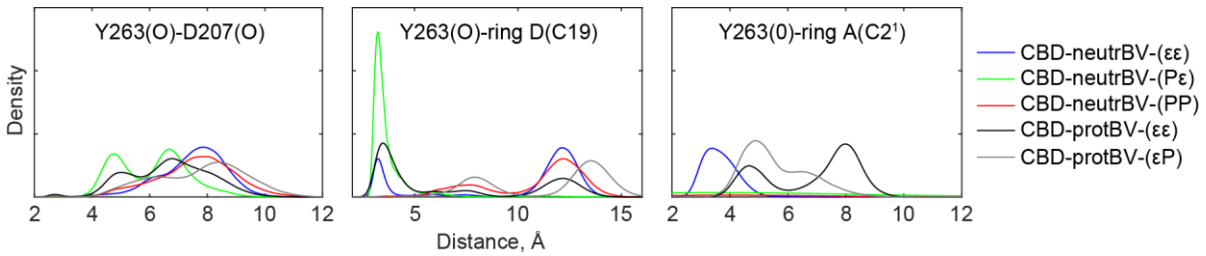

Figure 3.29. Y263 interactions with D207 and biliverdin rings A and D in CBD models of the Pr-state DrBphP phytochrome. Distributions of the distances from the last 70 ns of the 100 ns simulation.

Interactions of the highly conserved aspartate Y263 in the active site were analyzed in the models with neutral and protonated biliverdin (Figure 3.29). In the crystal structure Y263 interacts with D207, however the Y263-D207 interactions were not stable in the MD trajectories of the CBD models independent of the biliverdin protonation state. A poor stability of the Y263-D207 interactions in the MD simulations of the CBD domain with protonated biliverdin was indicated in Section 3.1.7 and was already reported by Field and co-workers for the phytochrome variants consisting of a CBD domain (180). Since Y263 is solvent-exposed, it interacted with the bulk water or moved above biliverdin ring D or ring A in all models. In some models, the OH group of Y263 interacted with the vinyl group of the biliverdin ring D or the methyl group of ring A. In the models with neutral H290, ring D interacted with the OH group of Y263, whereas in the models with protonated H290 these interactions were absent. Despite the observations that the stability of the ring D-H290 interactions does not depend on the protonation state of

H290 (Figure 3.28), the presence or absence of ring D-Y263 interactions depends on the protonation state of H290.

The distance distributions characterizing interactions in the MD simulations reflect on the importance of the electrostatic forces that depend on the atomic charges. PropC interacts with protonated H290 because of the increase of the positive charge on the protonated H290 as compared to the neutral one. The interactions between the O atom (charge -0.76) of PropC and the histidine are stronger with protonated than neutral histidine since the charges on the Hε atom (connected to Nε) are 0.44 and 0.32 a. u., respectively. The difference in the Hε atom charge in the histidine also indicates that when H260 is protonated, PropC interacts with it more strongly as compared when H260 is neutral. The PropC interactions with serines S272 and S274 (H atom of OH group with charge 0.43) are weaker when H260 is protonated because the competition between serines' H atoms and the protonated H260's H atom for the interactions with PropC is larger than the competition between serines' H atoms and the neutral H260's H atom. Further, Y263 (H atom of the OH group with charge 0.43) can interact with ring D simultaneously with its interactions with neutral H290 (Hε atom with charge 0.32), but Y263 cannot interact with ring D simultaneously with its interactions with protonated H290 (Hε atom with charge 0.44) due to the larger repulsive electrostatic forces between Y263 and H290 when H290 is protonated. The hydrogen bond analysis illustrates that the stability of the hydrogen bonds in the active site depends rather on the histidine protonation states than on the biliverdin protonation state.

How the charge distribution in the active site influences the biliverdin geometry dynamics was studied in the models with differently protonated biliverdin, H260 and H290. Distributions of the six dihedral angles between the adjacent rings in biliverdin are shown in Figure 3.30. Shapes of the particular dihedral angles were similar in all models, the least spread was the AB1 and the most spread was the CD1 dihedral angle, indicating similar rigidity of the specific angle. The distribution maxima were compared between the models with the same protonation state of H290: the maxima of the dihedral angle distributions were most spread in the model with neutral biliverdin, H260 and H260 indicating larger biliverdin geometry flexibility and lower biliverdin planarity in the models with neutral residues. The maxima of the dihedral angle distributions were spread more in the models

with neutral biliverdin and protonated H260 than in the models with protonated biliverdin and neutral H260, independent of the protonation state of H290. In the models with neutral biliverdin the distribution maxima of the angles between rings B and C are smaller whereas between rings C and D are larger than in the respective models with protonated biliverdin. The results show that upon proton transfer from biliverdin to H260 the biliverdin geometry slightly changes, the biliverdin becomes more planar between rings B and C whereas ring D becomes more out-of-plane.

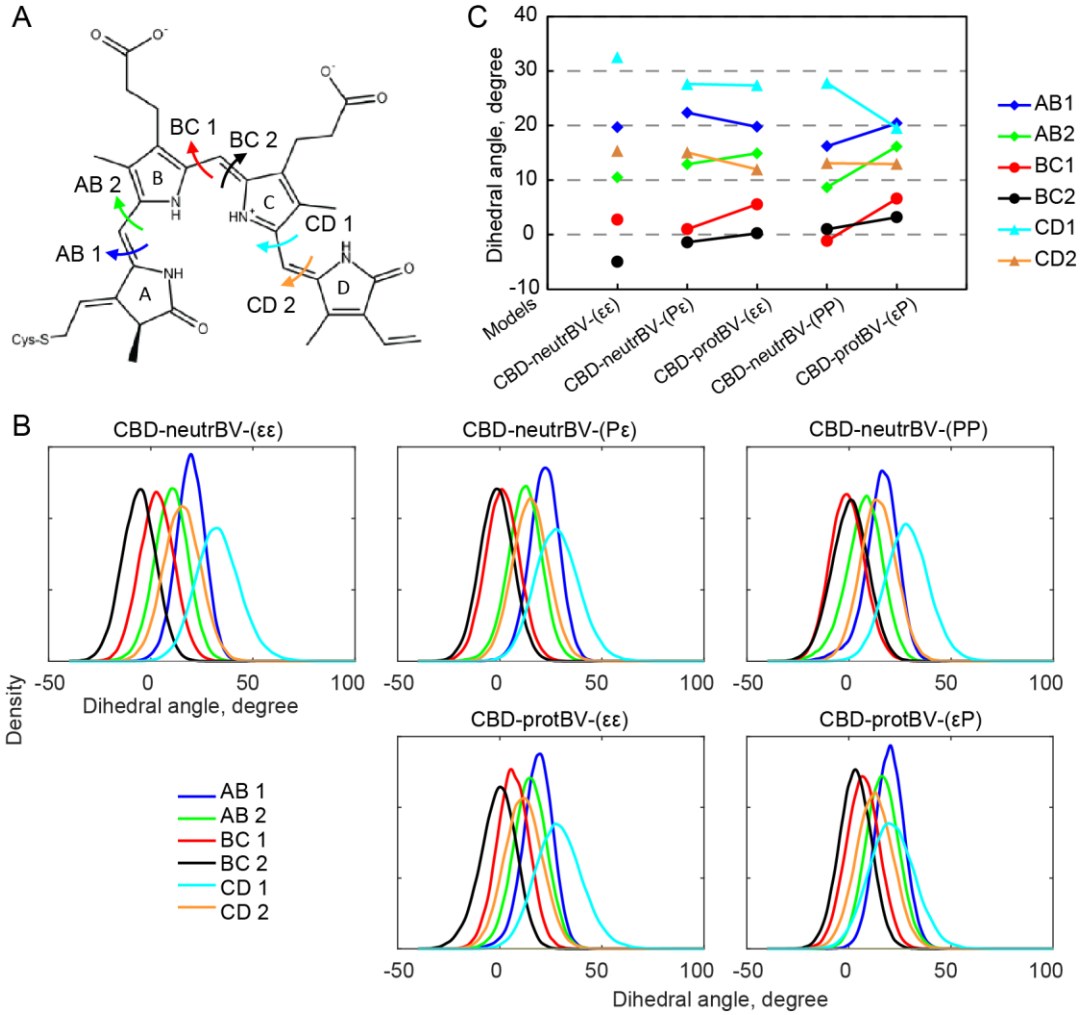

Figure 3.30. Dihedral angles of the methine bridges between two adjacent pyrrole rings of the biliverdin in the CBD models of the Pr-state DrBphP phytochrome. A) Measured dihedral angles in biliverdin. B) Distributions of the dihedral angles from the last 70 ns of the 100 ns simulation. C) Maxima of the dihedral angle distributions. Dihedral angles between rings A and B (angles AB1, AB2), rings B and C (angles BC1, BC2), rings C and D (angles CD1, CD2) measured by defining atoms N-C-C-C, except CD1 angle which was measured by defining atoms N-C-C-H.

3.2.5 Dynamics of phytochrome CBD-PHY domains with neutral biliverdin

The influence of the biliverdin deprotonation (at ring C) on the active-site dynamics was studied in the models composed of the CBD-PHY domains, constituting the

photosensory module of the DrBphP phytochrome. The following section addressed the biliverdin deprotonation in the Pr state, and only in the last paragraph of the section the active site dynamics in the Pfr-state models with neutral biliverdin is presented. The models with neutral biliverdin and different protonation states of histidines H260 and H290 were compared to the model with protonated biliverdin. Models with neutral (Nε-H or Nδ-H) or protonated histidines were named by indicating ε, δ or P, respectively, first for H260 and then for H290. The force field parameters used for neutral biliverdin are as described earlier (Table 3.14).

It was analyzed how the dynamics of the hydrogen-bonding network in the active site depends on the protonation states of both histidines H260 and H290 in the models with neutral biliverdin (Figure 3.31). The RMSDs of the protein, its backbone and the chromophore were compared among the Dr-Pr models with neutral and protonated biliverdin, simulated for 100 ns (Appendix Figure C.18). The RMSDs for some models increased at the beginning of the trajectories, therefore the initial 30 ns were excluded from the total trajectory length in the statistical distribution analysis described in the following section. The dynamics dependence on the protonation states of histidines H260 and H290 was shown for the models with protonated biliverdin in Section 3.1.7; the model with protonated biliverdin, neutral H260 and protonated H290 named as DrPr-protBV-(εP) is used in the current section and positive control. In the crystal structure and the DrPr-protBV-(εP) model, the PropC carboxylate forms hydrogen bonds with H260, S272, S274 but not with H290, which interacts with the biliverdin ring D via a water molecule. D207 forms two hydrogen bonds with R466 and a hydrogen bond with Y263 as shown in Figure 3.32 A. The same interactions were preserved in the model with neutral biliverdin and both protonated H260 and H290. Conversely, in the models with other protonation states of these histidines, the Y263-D207 interactions became destabilized and the Y263-ring D and Y263-R466 interactions formed as shown in Figure 3.32 B. Additionally, other interactions such as PropC-H260 were destabilized. The analysis shows that the hydrogen bond stability in the models with neutral biliverdin indeed depends on the protonation states of the histidines H260 and H290 and that the most stable interactions are obtained in the model with both H260 and H290 being protonated.

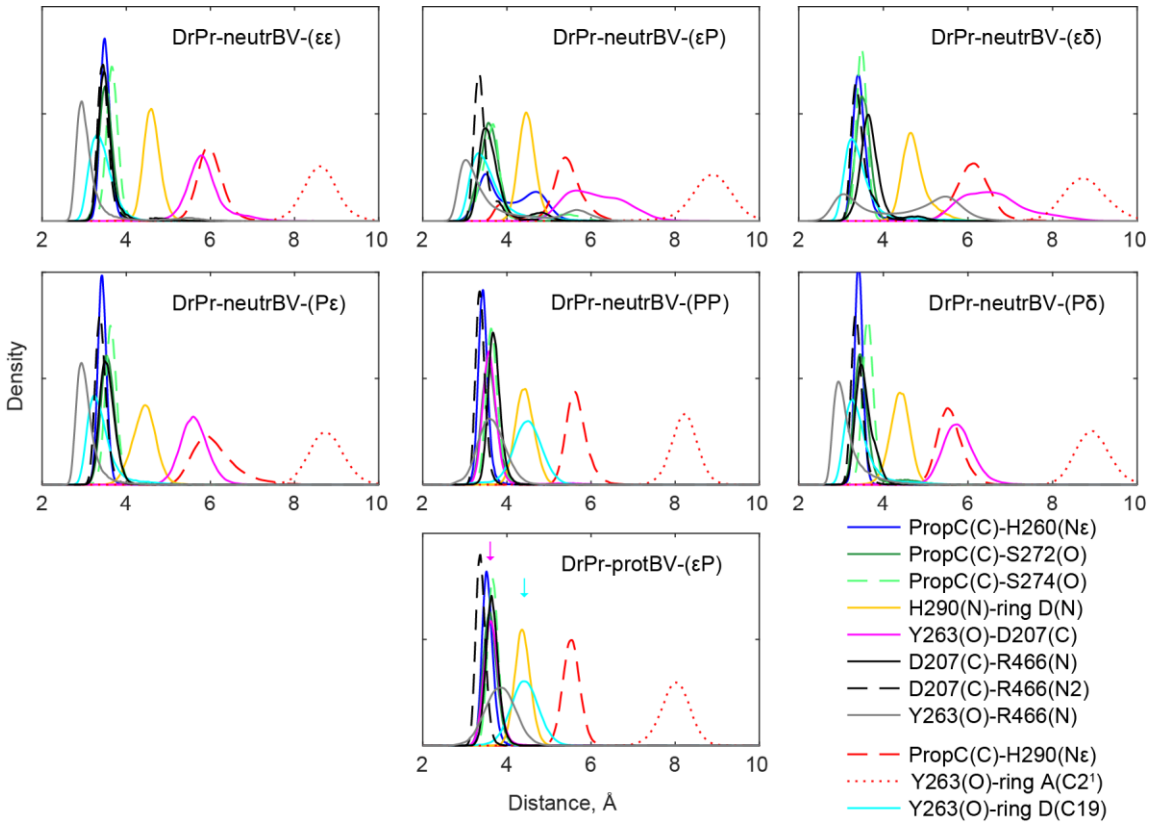

Figure 3.31. Distances in the active site of DrPr models consisting of CBD-PHY domains and containing different protonation state of biliverdin, H260 and H290. Distributions of the bonds from the last 70 ns of the 100 ns simulation. For the DrPr-protBV-(εP) model arrows indicate maxima of two distributions. Force field parameter set "a" was used for the neutral biliverdin. Interacting residues are shown in Figure 1.2.

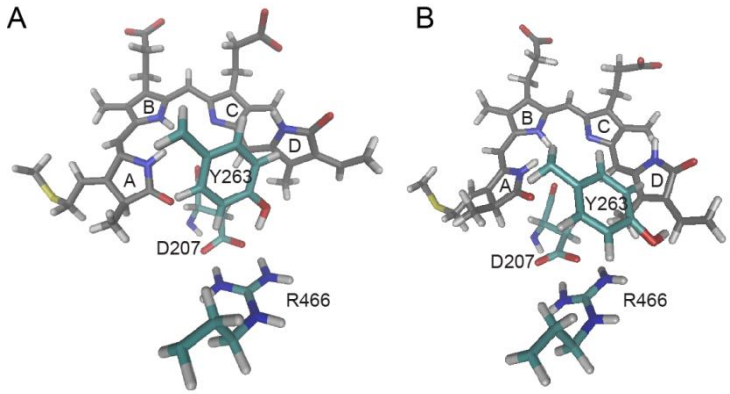

Figure 3.32. Interactions of Y263 in DrPr models consisting of CBD-PHY domains. A) Initial Y263-D207 interactions as found in the X-ray crystal structure (PDB 4o0p); B) Y263 interactions with ring D and R466 as found in DrPr-neutrBV-(Pε) after 100 ns and other models.

The model with neutral biliverdin and protonated both H260 and H290, named as DrPr-neutrBV-(PP), was considered as a model representing phytochrome after the proton transfer from biliverdin to H260 and was compared to the DrPr-protBV-(εP) model containing protonated biliverdin. The interactions of the biliverdin ring C and H260 via the pyrrole water molecule were stable during the entire length of the

trajectories, 150 ns and 430 ns for the models with neutral and protonated biliverdin, respectively (Figure 3.33). In the DrPr-neutrBV-(PP) model, the Y263-D207 interactions became destabilized and Y263 started to interact with ring D of the neutral biliverdin at ~130 ns of the trajectory (Figure 3.34), whereas in the model with protonated biliverdin the Y263-D207 interactions remained stable during the entire trajectory (Appendix Figure C.8). The results show that despite the slight change of the Y263 interactions in the model with neutral biliverdin, the biliverdin ring C-pw-H260 hydrogen bonds, which play a key role in the above-described biliverdin (de)protonation mechanism, are stable in the models representing phytochrome with protonated and neutral biliverdin.

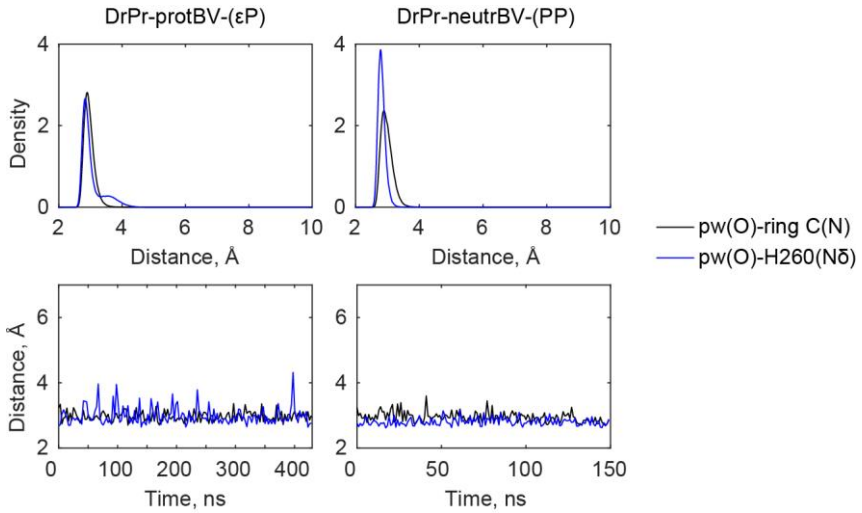

Figure 3.33. Interactions between biliverdin ring C and H260 via the pyrrole water (pw) molecule in DrPr models consisting of CBD-PHY domains with protonated or neutral biliverdin. Distributions of the bonds from the last 400 ns or 120 ns of the 430 ns or 150 simulation, respectively. Force field parameter set "a" was used for neutral biliverdin.

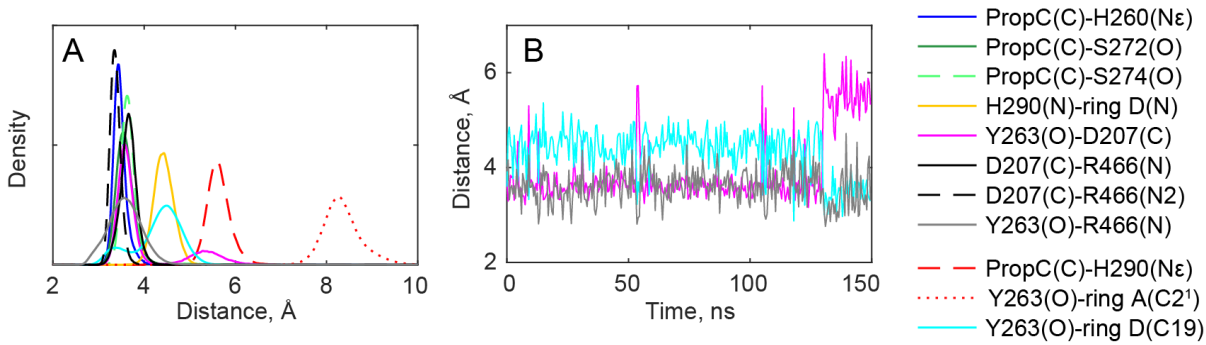

Figure 3.34. Interactions in the active site of the DrPr-neutrBV-(PP) model consisting of CBD-PHY domains during the first 150 ns. Force field parameters set "a" was used for neutral biliverdin. A) Distributions of the bonds from the last 120 ns of the 150 ns simulation. B) Y263 interactions with D207, ring D and R466.

Different force field parameter sets for the neutral biliverdin were prepared in order to study how the active-site dynamics depends on the charge distribution in the neutral biliverdin. In addition to the above-described and used parameters set "a" (Section 3.2.4), three additional sets "b", "c" and "d" with different charge distribution on neutral biliverdin were prepared. In set "a", the charges were changed with respect to the charges in the protonated biliverdin by reducing the positive charge on rings A-D and methine bridge BC and by reducing the negative charge on methine bridges AB and CD; whereas in sets "b"-"d" the charges were reduced on all rings and bridges including all methyl and vinyl groups ("b"), or excluding methyl groups on all rings ("c"), or excluding methyl and vinyl groups ("d") (Table 3.15). In the particular set "b", "c", or "d" the charge was reduced on all atoms by the same amount with an exception of the N atoms, where the charge was reduced by a slightly different amount (Table 3.16). The prepared parameter sets "b"-"d" for neutral biliverdin, in addition to set "a", were used to simulate the DrPr-neutrBV-(PP) model.

Table 3.15. Comparison of charges in force field (FF) sets for protonated and neutral biliverdin (BV). Parameter sets "a"-"d" are indicated for neutral biliverdin, deprotonated at ring C.

BV/ FF set	Ring				Bridge			Atom*			
	A	B	C	D	AB	BC	CD	N^C	C17	C18	C19
prot.	0.340	0.422	0.189	0.357	-0.287	0.208	-0.229	-0.654	-0.115	-0.091	-0.332
neutr."a"	0.095	0.197	-0.216	0.032	-0.087	0.158	-0.179	-0.704	-0.145	-0.121	-0.362
neutr."b"	0.151	0.310	-0.266	0.179	-0.309	0.186	-0.251	-0.666	-0.126	-0.102	-0.343
neutr."c"	0.134	0.300	-0.277	0.223	-0.311	0.184	-0.253	-0.669	-0.127	-0.103	-0.332
neutr."d"	0.113	0.317	-0.251	0.235	-0.322	0.173	-0.264	-0.669	-0.133	-0.109	-0.332

Table 3.16. Charge reduction for atoms of neutral biliverdin, deprotonated at ring C, in force field parameter sets "b"-"d".

set	N^C	N^A, N^B, N^D	other
"b"	0.012	0.013	0.011
"c"	0.015	0.014	0.012
"d"	0.015	0.0175	0.0175

The MD trajectories of the DrPr-neutrBV-(PP) model with parameter sets "a"-"d" for the neutral biliverdin were simulated for 100 ns and distances between residues in the active site were analyzed to investigate how the charge distribution on the neutral biliverdin influence the active-site dynamics (Figure 3.35). In comparison to the model with protonated biliverdin, the most changes in distance distributions were present in the models simulated with parameter sets "b" and "c". In the trajectory with parameter set

"b" the PropC-H260 interactions were weakened. In the trajectories simulated with parameter sets "b" and "c", the interactions of Y263 with D207 were weakened but with biliverdin ring D and R466 became stronger (Figure 3.36). During these two trajectories, the D207-Y263 hydrogen bond was disrupted and the D207-R466-Y263 hydrogen bonds were formed as shown in Figure 3.32, whereas in the models simulated with parameter sets "a" and "d" the Y263-D207 hydrogen bond remained stable as well as in the model with protonated biliverdin. The reason for the presence of the strong Y263-D207 interactions and the absence of the strong Y263-ring D and Y263-R466 interactions during the first 100 ns of the trajectories in the models simulated with parameter sets "a" and "d" may be larger repulsive electrostatic forces between the O atom (charge -0.54) of the OH group in Y263 and the C17 and C18 atoms of ring D, whose charge is more negative in sets "a" and "d" as compared to sets "b" and "c" (Table 3.16). This indicates that charge distribution in sets "a" and "d" facilitates more stable active-site interactions involving Y263. However, longer trajectories simulated with parameters sets "a" and "d" showed that after the initial ~130 ns and ~180 ns of simulation, respectively, the Y263 interactions with D207 became destabilized and with ring D and R466 became stronger (Figure 3.34 and 3.37). These results indicate that the Y263-D207 interactions are sensitive to the charge distribution in the active site and become weaker in the model with neutral biliverdin as compared to the model with protonated biliverdin, although among the model with neutral biliverdin these interactions stay stable for the longest time (~180 ns) when the model is simulated using the force field parameters set "d". However, the stability of the ring C-pw and pw-H260 interactions was similar in the model with protonated biliverdin and in the models simulated parameters sets "a" and "d" during the entire trajectories (Appendix Figure C.19) The significant changes of interactions in the active site other than of Y263 were not observed in the models with neutral biliverdin simulated with the best-performing sets "a" and "d" for 150 ns and 300 ns, respectively. This indicates that both parameter sets "a" and "d" , especially the set "d", may be used to simulate neutral biliverdin in phytochrome models and result in comparably stable active-site interactions. Despite the slight changes of the Y263 interactions, the hydrogen-bonding network in the active site of the model with neutral biliverdin and protonated H260 and H290 stays similar as in the model with protonated biliverdin and in the crystal structure.

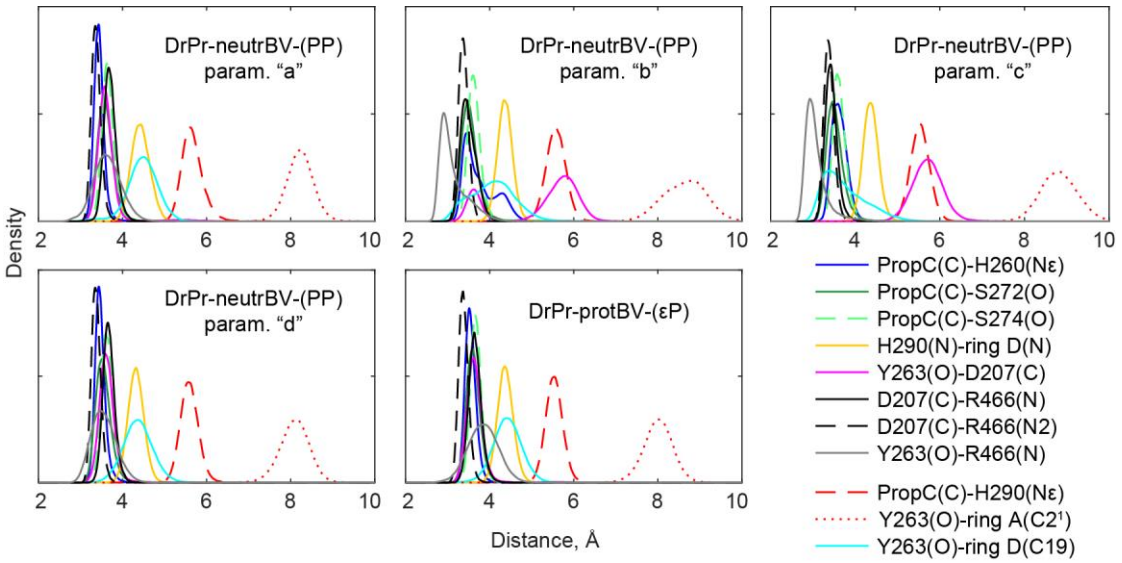

Figure 3.35. Distances in the active site of the DrPr-neutrBV-(PP) model consisting of CBD-PHY domains, simulated with different force field parameters ("a"-"d") of neutral biliverdin. The DrPr-protBV-(εP) model is shown for comparison. Distributions of the bonds from the last 70 ns of the 100 ns simulation.

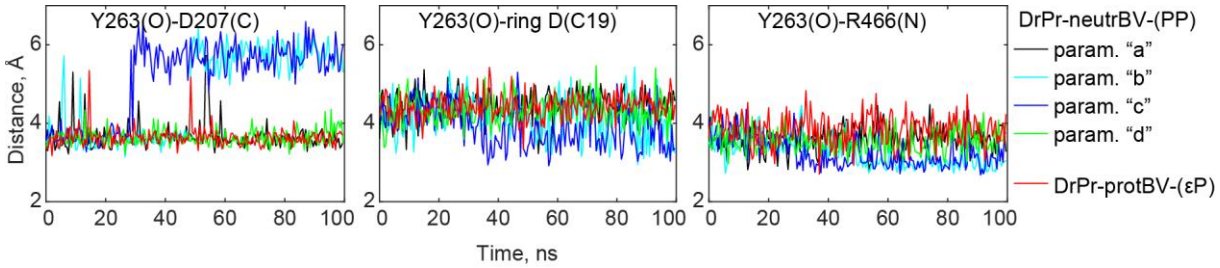

Figure 3.36. Y263 interactions in the active site of the DrPr-neutrBV-(PP) model consisting of CBD-PHY domains, simulated with different force field parameters ("a"-"d") of neutral biliverdin. The DrPr-protBV-(εP) model is shown for comparison.

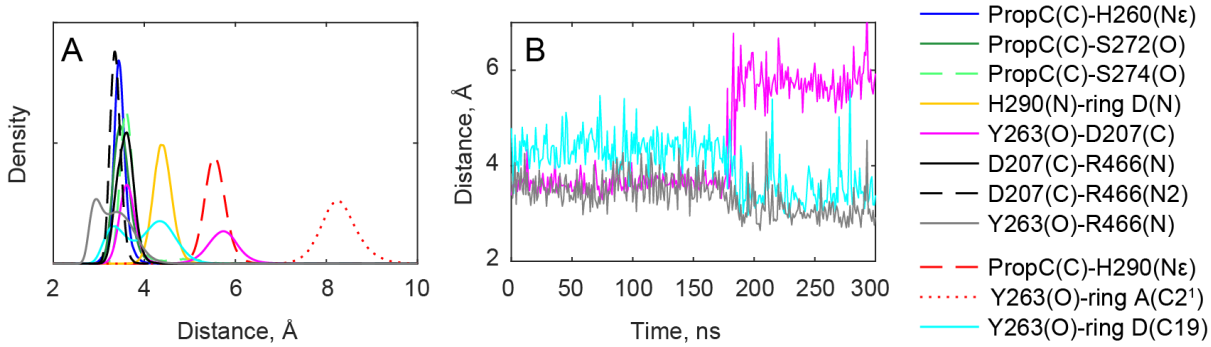

Figure 3.37. Interactions in the active site of the DrPr-neutrBV-(PP) model consisting of CBD-PHY domains, simulated with force field parameters set "d" for neutral biliverdin. A) Distributions of the bonds from the last 270 ns of the 300 ns simulation. B) Y263 interactions with D207, ring D and R466.

A model containing neutral biliverdin and with changed protonation states of H260 and H290 was simulated to further investigate how the hydrogen-bonding interactions depend on the charge distribution in the active site. The DrPr-neutrBV-(εδ→PP) model was prepared from the snapshot of the DrPr-neutrBV-(εδ) model after 100 ns (active-site interactions are shown in Figure 3.31, top right panel) by modifying protonation states of both H260 and H290 from neutral to protonated and then simulated for 200 ns (Figure 3.38). The crystal-structure interactions were less preserved in the DrPr-neutrBV-(εδ) model compared to the DrPr-neutrBV-(PP) model, whereas the DrPr-neutrBV-(εδ→PP) model showed formation of some crystal-structure interactions. The active-site distances in the model with modified histidine charges changed during the initial 10 ns of the simulation. The interactions of Y263 with biliverdin ring D were weakened and with R466 were enhanced. The PropC-H290 hydrogen bond was more rigid in the DrPr-neutrBV-(εδ→PP) model as compared to the DrPr-neutrBV-(εδ) model. The observed dynamics indicates that the active-site interactions, destabilized by the specific selection of the histidine protonation states, can be restored after the protonation states are modified.

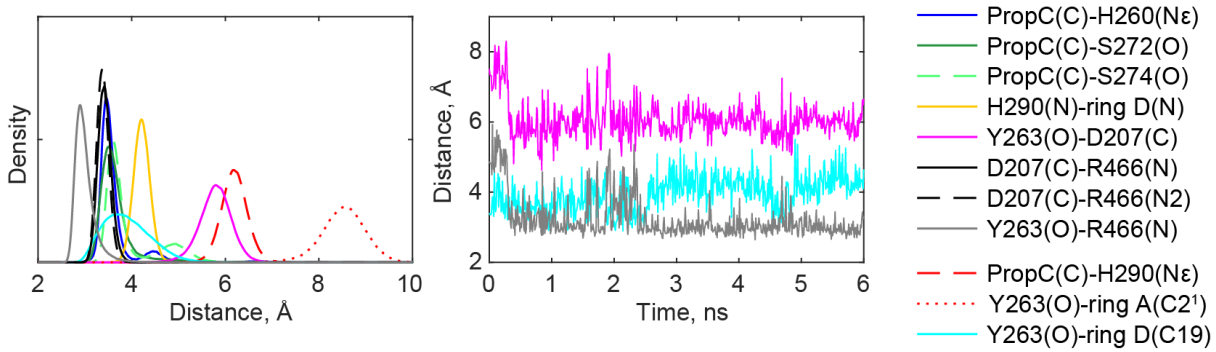

Figure 3.38. Interactions in the active site of the DrPr-neutrBV-(εδ→PP) model consisting of CBD-PHY domains after the change of charge distribution. As initial coordinates model DrPr-neutrBV-(εδ) after 100 ns simulation was used, protonation state of H260 and H290 were changed to protonated, force field parameters of neutral biliverdin changed from "a" to "d". Distribution of the bonds from the last 180 ns of the 200 ns simulation (left) and Y263 interactions over first 6 ns of the MD simulation (middle) are shown.

Although the above-described calculations addressed the proton transfer from biliverdin only in the Pr state, the MD simulations with neutral biliverdin (deprotonated at ring C) were also performed for the models of the Pfr state. The active-site dynamics of the DrPfr models with protonated and neutral biliverdin is compared in Figure 3.39; the models with neutral biliverdin contained protonated H260 and protonated or neutral

H290 and were simulated with parameter sets "a" and "d". Similarly to the simulations of the models with protonated biliverdin (Section for 3.1.7), in the model with neutral biliverdin and neutral H290 (Figure 3.39 A), interactions between neutral H290 and PropC were not stable independently on the charge distribution on the biliverdin atoms. In the models with neutral biliverdin and protonated H260 and H290 (Figure 3.39 B), the active site interactions were stable for a longer time when parameter set "a" was used. However, Y263 flipped out of the active site and became solvent-exposed after 90 ns, which led to the destabilization of the Y263-S468 and other interactions. In the model simulated with parameter set "d", D207 flipped out of the active site and became solvent-exposed after 35 ns, which followed by the changes of the Y263 interactions, specifically Y263 flipped out and became solvent-exposed. Neither in the models simulated with parameter set "a" nor with "d", the active-site interactions stayed stable for at least 100 ns. The results show that the hydrogen-bonding network in the active site is preserved only in the Pr-state models (with slight changes of the Y263 interactions) but not in the Pfr-state models which indicates that the active-site interactions are more sensitive to the biliverdin deprotonation in the Pfr state as compared to the Pr state.

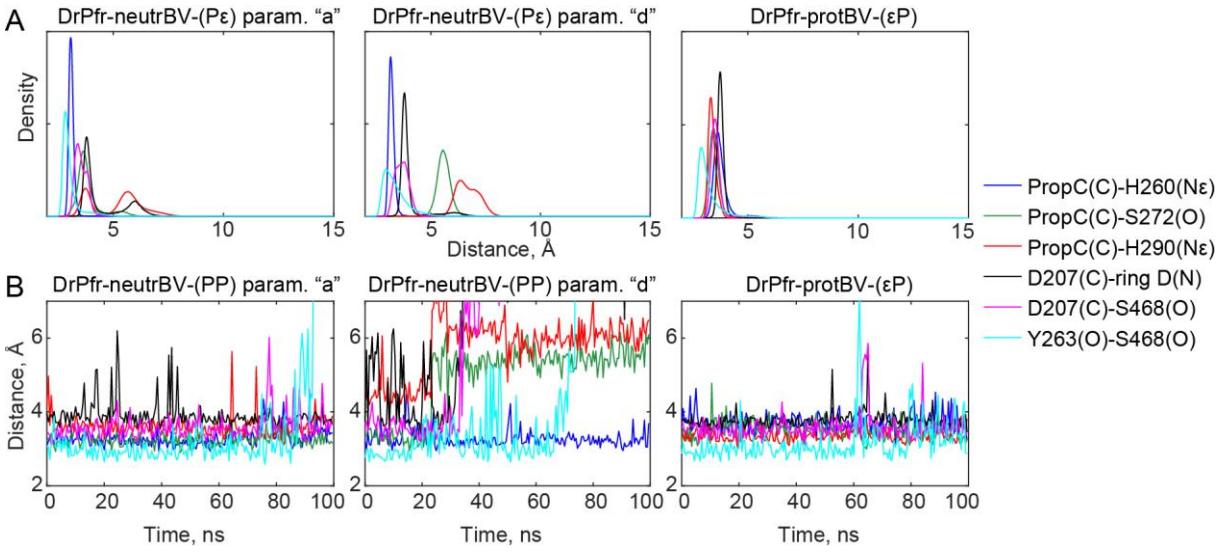

Figure 3.39. Interactions in the active site of the DrPfr model consisting of CBD-PHY domains, simulated with force field parameters set "a" or "d" for neutral biliverdin. The DrPfr-protBV-(εP) model is shown for comparison. A) Unstable interactions in models with neutral H290. Distributions of the bonds from the last 70 ns of the 100 ns simulation. B) Interactions in models with protonated H290.

3.3 Charge transfer states contributing to the excited-state decay

3.3.1 Background and overview

The ability of phytochromes to absorb red to far-red light together with their modular protein structure were exploited to engineer fluorescent proteins which can be used as markers (23). Increased fluorescence quantum yield of mutated phytochromes as compared to the wild-type phytochromes was previously achieved by mutating different residues including the highly conserved Y263, D207 and H290 (DrBphP numbering) (30). However, there is a high demand for improving properties of phytochrome-based fluorescent tools because the fluorescence quantum yield of the current mutants does not exceed 15 % (23). To improve fluorescence of phytochrome-based tools by rational molecular engineering approaches, the excited-state decay pathways that quench fluorescence should be identified. So far it is known that fluorescence, which is a radiative decay, competes with radiationless decay pathways such as internal conversion from the conical intersection of tetrapyrrole isomerization (122).

In this results part, by employing quantum chemical calculations it was studied whether the charge transfer reactions, in particular electron transfer coupled to proton transfer, may take place in phytochromes. The active-site cluster models representing the DrBphP phytochrome in the Pr state were used to compute the excited-state energies and to investigate whether the highly conserved tyrosine Y263 and histidine H260 can act as electron donors and donate an electron to the protonated tetrapyrrole. The charge transfer states (CT states) were found to be low in energy which suggests that the photoinduced charge transfer reactions may occur in phytochromes. The charge transfer process, depending on its rate, may quench fluorescence. Therefore, properties of the CT states were characterized, the forward and backward charge-transfer reaction coordinates were predicted and the charge transfer rates were calculated. The results suggest that Y263 and H260 can act as electron donors and induce the formation of the charge transfer intermediate – a tetrapyrrole radical. Thus, the excitation spectrum of the tetrapyrrole radical was computed to predict its spectral signatures.

The finding that the charge transfer reactions mediate the excited-state energy dissipation may open new directions for rational engineering of phytochromes. Mutations of the

electron donors or proton acceptors might be employed as a strategy to increase fluorescence quantum yield in phytochrome variants. In the phytochrome active site, the tetrapyrrole is surrounded by multiple tyrosine and histidine residues which might be potential electron donors. To characterize the electron donor properties of these residues, the excited states were computed and charge transfer rates were evaluated in the active-site cluster models of bacterial (DrBphP, PaBphP) and plant (AtPhyB) phytochromes using quantum chemical methods. To study how mutations of potential electron donors, tyrosine and histidine, influence the protein dynamics in the active site, an MD study on two templates IFP2.0 and PaBphP as well as their mutants was performed. IFP2.0, engineered from the CBD domain of the DrBphP phytochrome (142), is small in size and has increased fluorescence quantum yield, therefore improving its properties even further is desirable. PaBphP phytochrome adopts the Pfr state as its ground state, and improving its fluorescence properties might enable its application as the protein with the most red-shifted spectrum. Therefore, the active-site dynamics was compared between the template protein and its mutants to predict the mutations which could be performed for a particular phytochrome variant without destabilizing its active site.

The majority of results presented in this part will be published in the following peer-reviewed article:

Maximowitsch E and Domratcheva T. Photoinduced charge transfer in phytochrome red-light receptor proteins. *In preparation.*

Lehtivuori H*, Maximowitsch E*, Takala H, Kurkinen S, Tkachenko NV, Ihalainen JA, Domratcheva T. Charge transfer reactions of the red-light photoreceptors phytochromes. *In preparation.*

* - equal contribution

3.3.2 Characterization of conserved tyrosine and histidine as electron donors in phytochromes

3.3.2.1 Energies of charge transfer states involving tyrosine and histidine

In the phytochrome active site, the protonated tetrapyrrole chromophore is surrounded by residues which are known to act as electron donors in other systems. In order to investigate whether Y263 and H260 can act as electron donors and participate in the intermolecular charge transfer in phytochromes, quantum chemical calculations were performed on the models representing the Pr-state DrBphP phytochrome containing these both residues. The charge transfer is described by the CT state featuring an electron transferred from the donor's MO to the acceptor's MO and resulting in a radical pair: a biliverdin radical and a radical of the electron donor (Y263 or H260). The environment of the electron donor residues may influence their properties, therefore it was evaluated how a change of charge next to the Y263 donor affect its properties. For that the reduced-size active-site cluster models (as described in Methods Section 2.1.2) were prepared with all possible protonation states of residue D207 or H207, which is next to Y263, and optimized in the ground state to obtain the S_0-min geometry of each model (Figure 3.40 A). The S_0-min geometries of the models were similar to the X-ray crystal structures, in particular the hydrogen-bond distances for the pyrrole water molecule and PropC (Figure 3.40 B). The protonation state of H260 was also addressed by preparing a model with protonated H260. During the geometry optimization of such a model the hydrogen bonds as found in the crystal structure were not preserved, e.g. the bonds between the biliverdin rings and the pyrrole water molecule became significantly weaker. In addition to that, the protonated histidine cannot act as an electron donor, therefore in further studies only the models with neural H260 were considered as the main models.

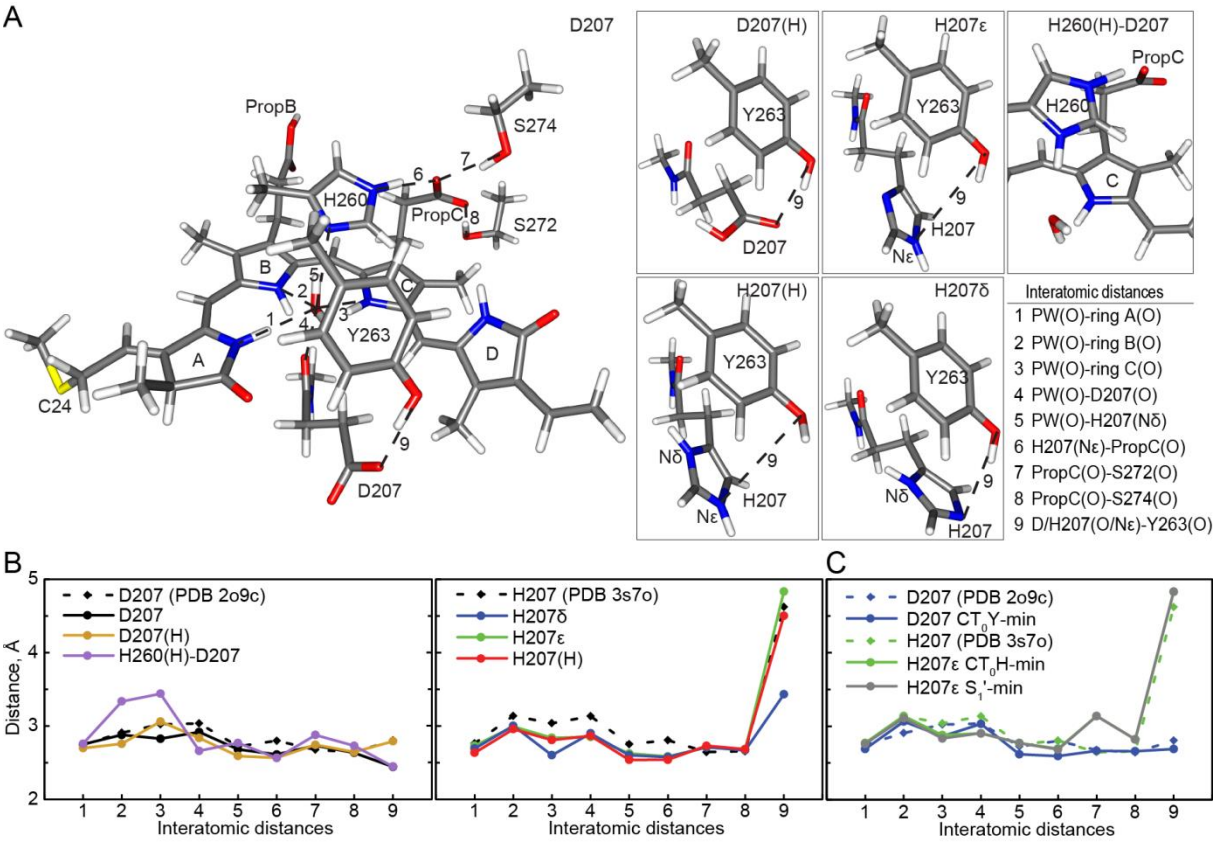

Figure 3.40. Active-site cluster models containing Y263 and H260 and representing the Pr-state DrBphP phytochrome. A) D207 model and fragments of other models in which either residue 207 or the protonation state of H260 are changed. B) Comparison of the interatomic distances at S_0-min geometries and X-ray crystal structures. C) Comparison of the interatomic distances at CT_0-min or S_1'-min geometries and X-ray crystal structures.

The excited-state energies at the S_0-min geometries of the main cluster models were computed with the XMCQDPT2-SA9-CASSCF(8,6) method where the active space included biliverdin MOs and electron donor MOs (Figure 3.41). The active space consisted of four occupied (two biliverdin, one H260, one Y263 MOs) and two unoccupied (biliverdin) MOs (biliverdin MOs are as shown in Figure 3.3) with an exception for the H207(H) model where a biliverdin MO was present instead of the Y263 MO. Among the nine computed low-lying energy states, not only locally excited (S_1-S_6) states but also the charge transfer (CT_0-CT_3) states are present and correspond to the electron transfer from Y263 (CT_0Y state) or H260 (CT_0H state) to the protonated biliverdin.

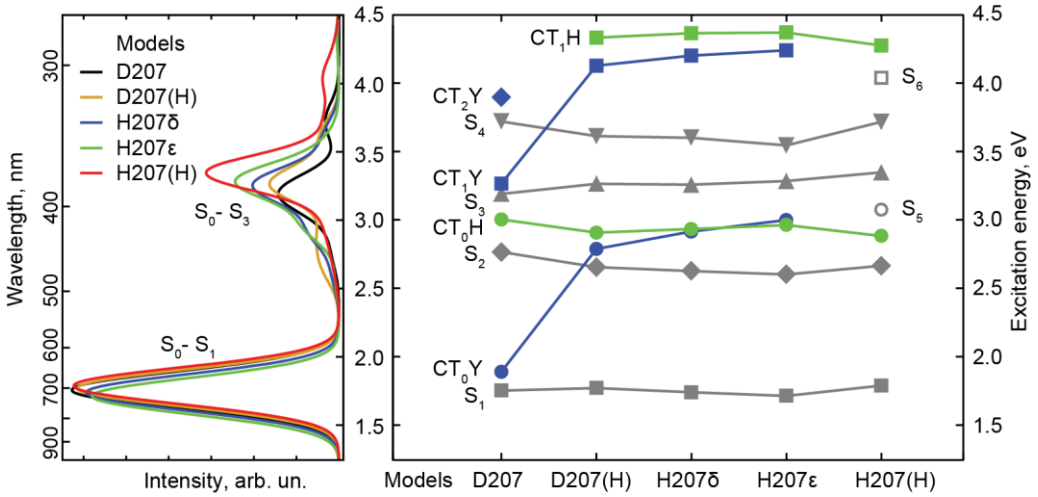

Figure 3.41. Excited-state energies and their properties in the active-site cluster models at S_0-min geometries. Energies computed with the XMCQDPT2-SA9-CASSCF(8,6) method, where active space consists of four occupied (two biliverdin, one H260, one Y263 MOs) and two unoccupied (biliverdin) MOs with exception for the H207(H) model where the biliverdin MO is present instead of the H260 MO. Values of excited states with respect to the S_0 state were taken from Table 3.17.

The energies of the CT states depend on the protonation state of the neighboring residues next to the electron donor. The energy of the CT_0Y state differs in the models depending on the protonation state of residue D207 or H207. In the D207 model the carboxylate of D207 is anionic and serves as a good proton acceptor, therefore states CT_0Y, CT_1Y and CT_2Y are lower in energy for about 1 eV when compared with the models D207(H), H207δ, H207ε, where D207 or H207 is neutral. In the H207(H) model, the protonated imidazole of H207 cannot act as a proton acceptor and thus impairs the electron donor properties of Y263 and increases the energy of the CT_0Y state considerably such that it is not among the low-lying excited-states manifold. The energies of the CT_0H and CT_1H states are similar in all models because the interactions of H260 do not change. The energies of the CT states can also be tuned by deprotonating biliverdin, which results in increased CT state energies by ~0.5 eV (Appendix Figure C.20), as neutral biliverdin is a weaker electron acceptor.

Oscillator strengths of the computed transitions were analyzed. The local excitations, especially the transitions from the S_0 state to the S_1 and S_3 states, carry considerable oscillator strength and correspond to the Q and Soret bands in the experimental spectrum, respectively (Table 3.17). In contrast, pure transitions from the S_0 state to the CT states have negligible oscillator strengths, since in the excitation participating MOs do

not overlap. In some models (H207δ, H207ε), the CT_0H and S_3 states mix and both computed states thus have considerable oscillator strength originating from the S_3 state. The reason for such mixing can be that the biliverdin MO and the H260 MO interact in the π-π stacking and both CT_0H and S_3 states are very close in energy and become degenerate. The CT_0Y state is close in energy to the S_1 state, which defines the Q band, but these states do not mix and the oscillator strength of the S_0-CT_0Y transition is negligible. Although the low-lying CT states do not contribute to the absorption spectrum, their properties were further analyzed to study changes in the active site upon population of the CT states.

Table 3.17. XMCQDPT2-SA9-CASSCF(8,6) excitation energies (in eV) and oscillator strengths (in parentheses) of the active-site cluster models at S_0-min geometries.

Transition	D207	D207(H)	H207δ	H207ε	H207(H)
$S_0 \rightarrow S_1$	1.75 (1.207)	1.77 (1.230)	1.74 (1.188)	1.71 (1.161)	1.79 (1.247)
$S_0 \rightarrow S_2$	2.77 (0.029)	2.65 (0.062)	2.63 (0.031)	2.60 (0.017)	2.66 (0.019)
$S_0 \rightarrow S_3$	3.19 (0.228)	3.26 (0.322)	3.26 (0.397)	3.28 (0.470)	3.35 (0.616)
$S_0 \rightarrow S_4$	3.72 (0.063)	3.61 (0.083)	3.60 (0.071)	3.54 (0.054)	3.72 (0.066)
$S_0 \rightarrow CT_0Y$	1.89 (0.080)	2.79 (0.015)	2.91 (0.005)	3.00 (0.025)	
$S_0 \rightarrow CT_1Y$	3.27 (0.050)	4.13 (0.001)	4.20 (0.001)	4.24 (0.002)	
$S_0 \rightarrow CT_0H$	3.00 (0.039)	2.91 (0.076)	2.93 (0.129)	2.96 (0.133)	2.88 (0.038)
$S_0 \rightarrow CT_1H$		4.33 (0.005)	4.37 (0.007)	4.37 (0.009)	4.27 (0.015)
$S_0 \rightarrow S_5$					3.07 (0.054)
$S_0 \rightarrow S_6$					4.04 (0.070)
$S_0 \rightarrow CT_2Y$	3.90 (0.002)				

The charge transfer character of the excited states is defined by the localization of the MOs which participate in the transition. The transition electron densities and molecular electrostatic potentials between states are shown in Figure 3.42. In the CT_0 states the negative charge is transferred from the electron donor to the protonated biliverdin and there is a change in dipole moment and angle (Tables 3.18 and 3.19). In contrast, locally excited states of biliverdin have a negligible charge transfer character.

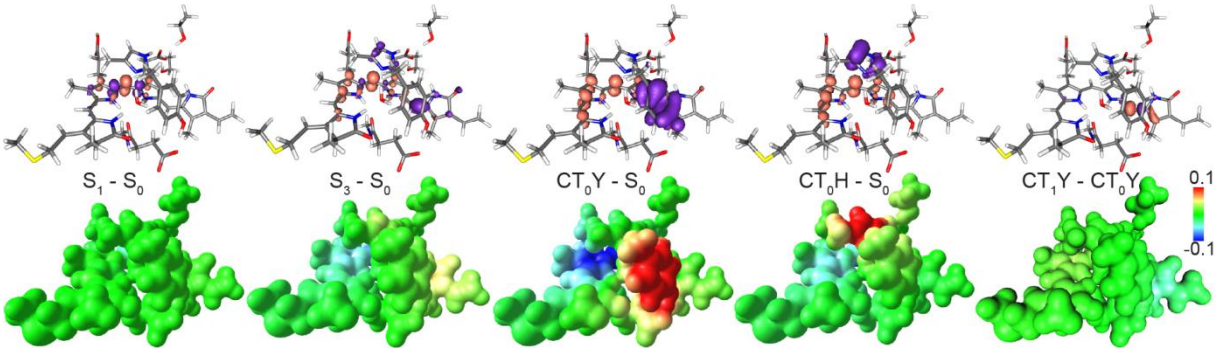

Figure 3.42. Electronic properties of transitions between computed states in the D207 model. Transition electron densities (top) and difference molecular electrostatic potentials (bottom) computed with XMCQDPT2-SA9-CASSCF(8,6) at the S_0-min geometry.

Table 3.18. Dipole moments (in Debye) of ground S_0 and excited states computed with XMCQDPT2-SA9-CASSCF(8,6) in the active-site cluster models at S_0-min geometries.

State	D207	D207(H)	H207δ	H207ε	H207(H)
S_0	28.4	27.8	26.8	27.8	39.4
S_1	26.8	28.2	27.2	27.7	40.9
S_2	26.3	24.6	26.6	27.7	39.0
S_3	19.8	21.5	20.9	23.5	39.4
S_4	25.8	26.6	26.6	27.8	39.8
CT_0Y	21.4	28.6	24.4	35.2	
CT_1Y	23.8	32.2	34.5	35.9	
CT_0H	29.5	25.8	33.3	22.3	34.5
CT_1H		28.7	29.1	25.5	34.8
S_5					40.2
S_6					41.9
CT_2Y	25.6				

Table 3.19. Angles (degrees) between dipoles of ground S_0 and excited states computed with XMCQDPT2-SA9-CASSCF(8,6) in the active-site cluster model D207 at the S_0-min geometry.

S_1	CT_0Y	S_2	CT_0H	S_3	CT_1Y	S_4	CT_2Y
4.2	51.3	1.6	29.9	11.0	39.8	3.9	47.5

3.3.2.2 Charge transfer reaction coordinate

Competing excited-state decay pathways were studied: radiative decay or so-called emission from the S_1 state and the radiationless decay via the CT states where either the Y263 or the H260 electron donor is involved. Whether the CT states can be populated from the S_1 state, depends on how the protein can stabilize the CT states. This can be evaluated by computing the relaxation in the S_1 and CT_0 states. Therefore, models were optimized in the S_1 and CT_0 states and excited-state energies were computed at the optimized geometries. In particular the D207 and H207ε models were used to characterize the charge transfer involving Y263 and H260 as electron donors, respectively

(Figure 3.43). Both models have a reduced energy gap between the S_0 and S_1 states at the S_1-min geometry as compared to the S_0-min geometry. The reduction of the energy gap, the so-called Stokes shift, equals to 0.12 and 0.14 eV in the D207 and H207ε models, respectively.

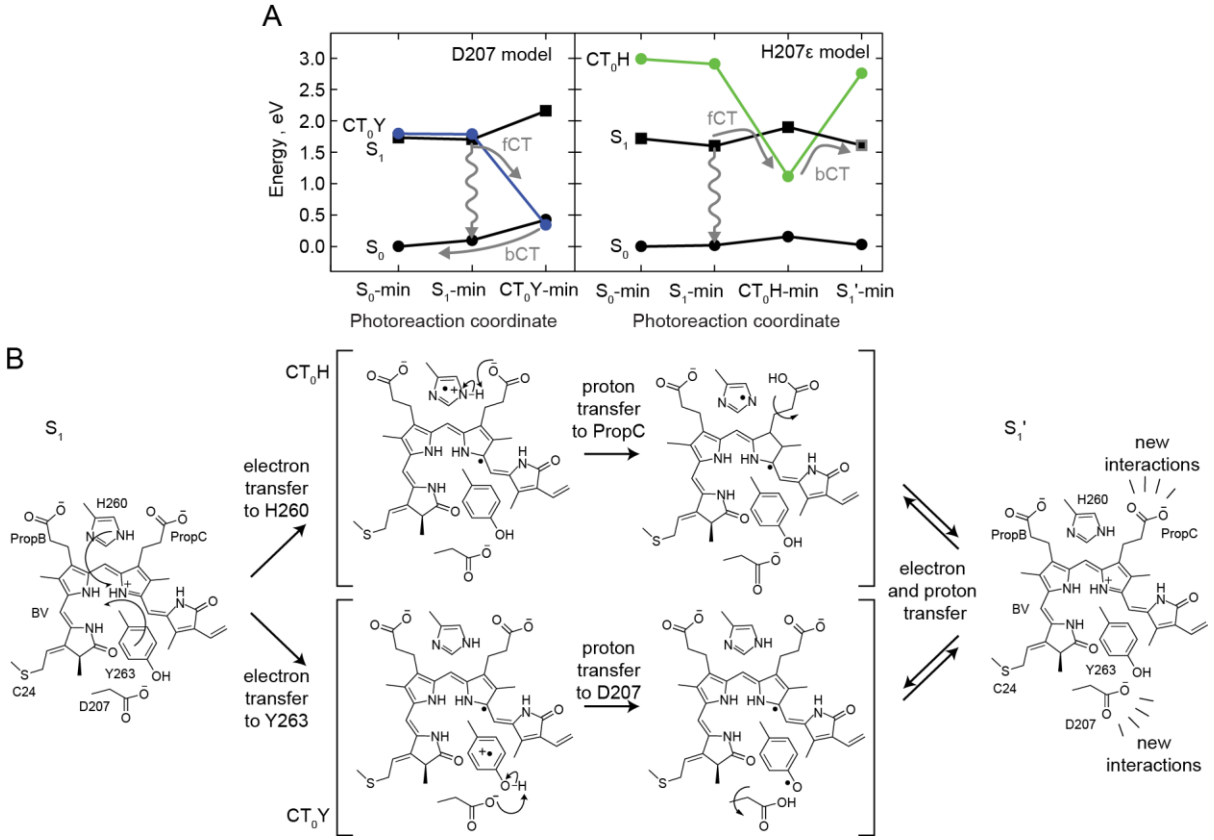

Figure 3.43. Charge transfer reactions contributing to the excited-state decay. A) Excitation energies of models D207 and H207ε at optimized geometries along the charge transfer photoreaction coordinate. Energies ware taken from Table 3.20 and are indicated with respect to the S_0 energy at the S_0-min geometry of each model. Curly arrows indicate emission and curved arrows – forward (fCT) and backward (bCT) charge transfer. B) Chemical structures of the molecular complex participating in the charge transfer.

The computed energies at the optimized geometries indicate that the charge transfer process is indeed possible. The crossing of the S_1 and CT_0 states along the charge transfer reaction coordinate corresponds to the electron transfer coupled to proton transfer. The drastic energy decrease during the optimization in the CT_0 state is due to the proton transfer which stabilizes the electron donor radical. In the D207 model when Y263 donates an electron to the biliverdin, the proton from the protonated Y263 radical is donated to the anionic D207 carboxylate, whereas in the H207ε model when H260 donates an electron to the biliverdin, the proton from the protonated H260 radical is donated to the anionic PropC carboxylate. Thais results in the formation of a radical pair

consisting of two neutral radicals: biliverdin and electron donor Y263 or H260. The neutralization of the chemical entities which were previously charged may result in the carboxylate rotation or the changes of interactions.

The charge transfer process induces changes in the active site interactions which can be studied by comparing the models at the S_0-min and CT_0-min geometries (Figure 3.44). The hydrogen bonds between the electron donor and the carboxylate were weakened in the radical pair. The hydrogen bond between the OH group of Y263 and a carboxyl oxygen of D207 elongated from 2.44 to 2.69 Å. Similarly, the hydrogen bond between the Nε-H group of H260 and a carboxyl oxygen of PropC elongated from 2.59 to 2.69 Å. Weakened interactions between H260 and PropC led to changes of PropC interactions with serines at the CT_0H-min geometry. The hydrogen bond between serine S274 and the carboxyl group of PropC elongated from 2.68 to 2.82 Å. The serine S272 changed its interactions with PropC by interacting with both oxygen atoms of the carboxyl group instead of one O atom, therefore hydrogen-bonding distances changed from 2.71 and 3.70 Å to 3.14 and 3.07 Å. This suggests that due to the charge transfer reactions and charge redistribution in the active site, the hydrogen bonds may weaken.

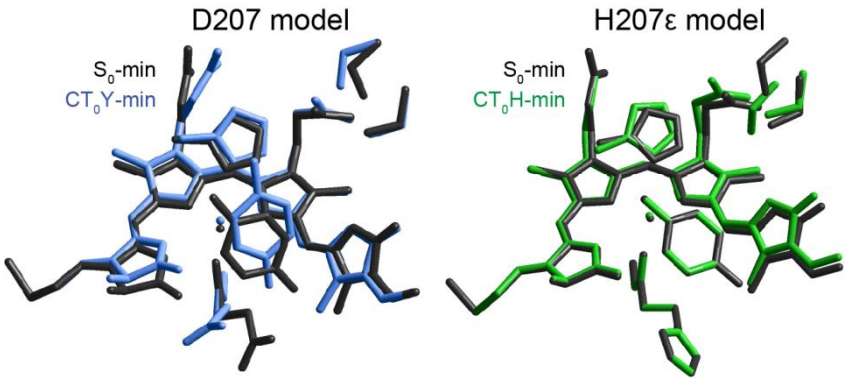

Figure 3.44. Active-site cluster models D207 and H207ε at optimized geometries.

The radical pair can undergo the backward charge transfer: either the recovery of the ground S_0 state or the transition to the excited S_1 state with different hydrogen-bond interactions (Figure 3.43 A). The recombination of the radical pair, which is a transition either to the S_0 or to the S_1 state, depends on the CT_0-S_0 and CT_0-S_1 energy differences. At the CT_0Y-min geometry, the CT_0Y and S_0 states became degenerate and crossing of these two states was enabled, therefore the recovery of the S_0 state occurred. At the CT_0H-min geometry, the CT_0H state was too high in energy to cross with the S_0 state

which made the recovery of the S_0 state energetically unfavorable, instead of that the CT_0H state could cross with the S_1 state leading to the S_1-state recovery. During the time when radical pair exists in the CT_0H state, the interactions of the neutralized chemical entities may change and the crossing of the CT_0H and S_1 states may result in a different minimum (S_1'-min), where the hydrogen-bonding interactions in the active site differ from the ones at the S_1-min geometry.

Whether the CT state is populated and how the radical pair recombines, either by recovery of the S_0 or the S_1 state, depends on the CT_0 energy at the S_1-min geometry, which in turn depends on energies at the S_0-min geometry (Figure 3.43 A and Table 3.20). For the D207 and H207ε models, the energies of the S_1 and CT_0 states at the S_1-min geometry were very similar to the energies at the S_0-min geometry and the energy gap between these two states increased only by 0.028±0.010 eV in the S_1-min as compared to the S_0-min geometry. Along the reaction coordinate from the S_1-min to the CT_0-min geometry, the energy of the CT_0 state decreased by 1.62±0.17 eV and the energy of the S_1 state increased by 0.37±0.08 eV which resulted in the total decrease of the CT_0-S_1 energy difference by 1.99±0.09 eV. This indicates that at the S_0-min geometry the S_1-CT_0 energy gap should be not larger than 2 eV, thus the CT_0-state energy should be not higher than ~3.7 eV in order to have the CT_0-state energy at CT_0-min not higher than the S_1-state energy at S_1-min. Such energies suggest the radical pair formation if the activation energy is low enough to overcome the barrier between the S_1 and CT_0 states. The radical pair undergoes the S_0-state recovery if CT_0 and S_0 are close in energy at the CT_0-min geometry (0.08 eV at CT_0Y-min), whereas if this gap is big (0.97 eV at CT_0H-min) and rather CT_0 and S_1 are closer in energy (0.78 eV at CT_0H-min), then recovery of the S_1 state occurs. The energies at the CT_0-min can be extrapolated from the energies at the S_0-min, assuming that the stabilization of the CT_0 state and the destabilization of the S_1 state are as computed for the D207 and H207ε models. According to such assumption, if the CT_0 state is energetically close to the S_1 state at the S_0-min geometry, then the S_0-state recovery ($CT_0 \rightarrow S_0$) occurs. However, if the CT_0 state is energetically considerably higher than the S_1 state but not higher than ~3.7 eV, then the transition to the S_1 state ($CT_0 \rightarrow S_1$) with different hydrogen-bonding interactions occurs.

Table 3.20. Ground- and excited-state energies and properties for electron donors Y263 and H260. Values (energy E, transition dipole moment μ as well as X, Y and Z components of the dipole moment **d**) for the Y263 donor in the D207 model and the H260 donor in the H207ε model computed with respect to the state in which the geometry was optimized. E is indicated with respect to the S_0 state at the S_0-min geometry of the same model, whereas μ and **d** are indicated with respect to the particular state in which geometry was optimized. Values were obtained from the XMCQDPT2-SA7-CASSCF(6,5) calculations, where the active space consisted of three occupied (two biliverdin and one H260 or one Y263 MOs) and two unoccupied (biliverdin) MOs.

D207 model

State	S_0-min			S_1-min			CT_0Y-min		
	E (eV)	μ (at. un.)	**d** (debye)	E (eV)	μ (at. un.)	**d** (debye)	E (eV)	μ (at. un.)	**d** (debye)
S_0	0.00		-11.331; -0.038; 24.585	0.10	4.9895		0.42	3.1708	-12.691; -7.848; 19.335
S_1	1.73	4.7723		1.71		-5.280; -0.308; 24.847	2.16	2.4246	-13.771; -9.504; 16.426
S_2	2.81	0.6433		2.65	1.6497		3.09	0.1475	
S_3	3.31	2.1866		3.26	3.8985				
S_4	3.65	0.7996		3.49	4.5409				
CT_0Y	1.80	2.7363	5.461; 1.034; 21.253	1.79	3.3716	5.790; 0.919; 21.879	0.34		2.908; -4.454; 15.858
CT_1Y	3.13	0.3478		3.02	0.6438		1.60	0.9229	
CT_2Y							2.36	4.6913	
CT_3Y							3.21	0.5962	

H207ε model

State	S_0-min		S_1-min			CT_0H-min			S_1'-min		
	E (eV)	μ (at. un.)	E (eV)	μ (at. un.)	**d** (Debye)	E (eV)	μ (at. un.)	**d** (Debye)	E (eV)	μ (at. un.)	**d** (Debye)
S_0	0.00		0.02	5.4344		0.15	0.7210		0.03	5.4524	
S_1	1.72	5.2580	1.60		7.977; -19.673; 18.749	1.90	0.7782	4.905; -19.533; 7.729	1.61		10.193; -19.569; 17.199
S_2	2.68	0.5525	2.38	1.1326		2.83	0.4128		2.43	1.4769	
S_3	3.34	2.1823	3.18	2.8755		3.48	0.2696		3.18	4.2971	
S_4	3.57	0.8381	3.34	5.6730					3.32	4.5592	
CT_0H	2.99	1.3984	2.91	2.0386	9.322; -8.382; 17.971	1.12		5.401; -2.802; 13.562	2.76	1.9714	10.498; -5.862; 17.783
CT_1H	4.43	0.2690	4.24	0.1676		2.50	1.4481		4.06	0.0503	
CT_2H						3.08	4.2831				

3.3.2.3 Charge transfer rates

Excited-state dynamics can be explained by the structure of the active site and the excited-state energies. To evaluate the excited-state dynamics involving different forward and backward charge transfer reactions, rates of these reactions were calculated using the properties of the ground and excited states at the optimized geometries. To calculate the charge transfer rate constants, the adiabatic Marcus theory and the generalized Mulliken-Hush scheme (164-166) were used (Figure 3.45). The rate constant k_{CT} depends on three parameters: the electronic coupling V_{el} of two states, determining the strength of the interaction between the states, the reorganization energy λ of the state from which the transition occurs, and the activation energy $E^{\#}$ of the undergoing charge transfer reaction, which is the energy barrier between the two states:

$$k_{CT} = \frac{2\pi}{\hbar\sqrt{4\pi\ \lambda\ k_b T}} V_{el}^2 \cdot \exp\left(-\frac{E^{\#}}{k_b T}\right)$$

where k_b, $\hbar$, T are Boltzmann constant, reduced Planck constant and standard ambient temperature (298.15 K), respectively.

The activation energy is defined by the crossing of the potential energy surfaces which are considered as possesing the parabolic shapes (Figure 3.45 A). Therefore the size of the activation energy $E^{\#}$ correlates with the energy difference between the two crossing states before the charge transfer reaction (at the S_0-min and S_1-min geometries for reactions $S_1 \rightarrow CT_0$, or at the CT_0-min geometry for reactions $CT_0 \rightarrow S_0/S_1$). The electronic coupling V_{el} was calculated from the dipole moments of the two states and the transition dipole moment between the two states (as described in Methods Section 2.1.6).

The rate of the charge transfer is modulated by the activation energy $E^{\#}$, which decreases the rate, and by the electronic coupling V_{el}, which increases the rate. To illustrate how these two parameters tune the charge transfer rates in the phytochrome models, the logarithm of k_{CT} is shown as a sum of two terms, one depending on V_{el} and λ and another depending on $E^{\#}$ (Figure 3.45 B). For a fast reaction rate, the first term should be large and the second one as small as possible. The competing pathways in the studied models are the forward charge transfer reactions $S_1 \rightarrow CT_0Y$ and $S_1 \rightarrow CT_0H$ with the following backward charge transfer reactions $CT_0Y \rightarrow S_0$ and $CT_0H \rightarrow S_1'$, respectively. For the

$S_1 \rightarrow CT_0Y$ and $CT_0Y \rightarrow S_0$ reactions, the value of $E^{\#}$ is very small (below 0.01 eV), therefore the large rate constants of $4.67 \cdot 10^{12}$ s^{-1} and $1.20 \cdot 10^{12}$ s^{-1}, respectively, are defined by the term depending on V_{el}. For the $S_1 \rightarrow CT_0H$ reaction, both terms, depending on $E^{\#}$ (0.06 eV) and V_{el} (0.44 eV), are larger therefore they compensate each other and the rate constant is large ($9.47 \cdot 10^{13}$ s^{-1}). The rate is even one order of magnitude larger than for the $S_1 \rightarrow CT_0Y$ reaction due to very strong V_{el} between the S_1 and CT_0H states since the H260 and biliverdin MOs participate in the π-π stacking. For the $CT_0H \rightarrow S_1'$ reaction the activation energy $E^{\#}$ is very high (0.55 eV), therefore it decreases the rate constant drastically (until $8.15 \cdot 10^{3}$ s^{-1}). However, if the molecular complex is trapped in the CT_0 minimum and the CT_0 state cannot cross with the S_0 state, it will undergo the charge transfer reaction and the recovery of the S_1 state even if the reaction is slow. At the S_1'-min geometry, in parallel with the radiative decay, the charge transfer reaction again to the CT_0 state such as CT_0H state ($S_1' \rightarrow CT_0H$) may occur. The activation energy $E^{\#}$ of this reaction is low and the electronic coupling V_{el} is high resulting in the large rate constant ($7.97 \cdot 10^{13}$ s^{-1}), similar as for the same reaction from the S_1-min geometry.

The majority of the discussed charge transfer reactions are ultrafast, occurring on the femtosecond-picosecond timescale, which indicates their competition with radiative decay occurring on the nanosecond timescale. The radiative decay from the S_1 to the S_0 state at the S_1-min geometry occurs with the lifetime of 9.10 and 8.02 ns in the D207 and H207ε models, respectively. The experimentally estimated excited-state lifetimes in the phytochromes are shorter, ~0.37 ns (123), indicating that radiationless decay pathways such as charge transfer reactions may take place. The radiative lifetime at the S_1'-min geometry of the H207ε model is the same as at the S_1-min geometry (8.02 ns). The $S_1 \rightarrow CT_0$ reactions, defining the formation of the radical pairs biliverdin-Y263 and biliverdin-H260, occur on the femtosecond timescale (214 fs for the CT_0Y and 10.6 fs for the CT_0H states). The radical pair biliverdin-Y263 undergoes recovery of the S_0 state via the $CT_0Y \rightarrow S_0$ reaction also on the femtosecond timescale (836 fs) which suggests the ultrafast de-excitation of the excited state via the $S_1 \rightarrow CT_0Y \rightarrow S_0$ pathway. The radical pair biliverdin-H260 undergoes the recovery of the S_1 state via the $CT_0H \rightarrow S_1$ reaction, occurring on the microsecond timescale (275 μs). After the S_1 state is recovered, the charge transfer to the CT_0H state is again fast and occurs on the femtosecond timescale

(12.5 fs), competing with the radiative decay occurring on the nanosecond timescale. The computed rates indicate that the charge transfer reactions indeed compete with the radiative decay and may contribute to the de-excitation of the excited state via the radical pair formation as well as to the equilibration of the S_1 and CT_0H states, which might facilitate photoproduct formation.

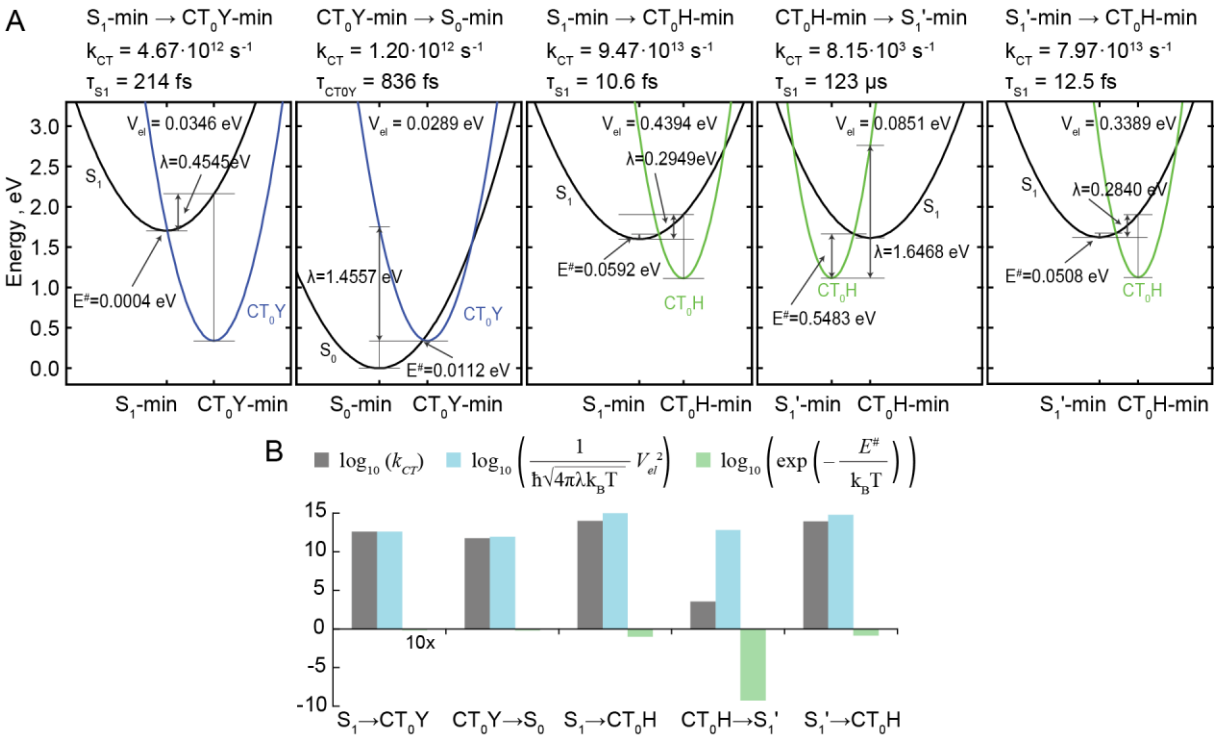

Figure 3.45. Kinetics of the charge transfer reactions. A) Parabolic shapes of potential energy surfaces of crossing states used to determine reaction rates. Charge transfer rate constants and lifetimes ($\tau=(k_{CT})^{-1}$) at particular state are indicated. B) Rate constant composition of the terms depending on electronic coupling V_{el} and activation energy $E^{\#}$. Excited-state energies and properties were taken from Table 3.20. Values were calculated as described in Methods Section 2.1.6 using the active-site cluster models D207 and H207ε.

3.3.3 Tetrapyrrole radical absorption in the near-infrared (NIR) region

The existence of the charge transfer reactions can be characterized by the detection of their intermediates i. e. radical pairs. If the CT states are populated and the radical pairs are formed, it should be possible to probe this spectroscopically. Therefore the absorption spectra were simulated from the computed excitation energies and their oscillator strength. Spectroscopic detection of the biliverdin radical at the radical-pair geometry (CT_0-min) might be possible as a detection of the CT_0-CT_1 and CT_0-CT_2 transitions (Figure 3.46 and Table 3.21) which are at the visible region below 850 nm (above 1.46 eV) and at the near-infrared (NIR) region above 850 nm (below 1.46 eV).

The CT_0-CT_1 transition possesses a relatively low oscillator strength and is at energies of 1.26 eV for the CT_0Y-min and of 1.38 eV for the CT_0H-min geometry, which falls into the NIR spectral region. The CT_0-CT_2 transition has a high oscillator strength and is at energies of 2.02 eV and 1.97 eV for the CT_0Y-min and CT_0H-min geometries, respectively. At the CT_0Y-min geometry, the CT_0Y-CT_3Y transition has a relatively small oscillator strength and is at 2.87 eV. Transitions from the CT_0 state to the S_n states are also present in the spectra: CT_0Y-S_1 is at 1.82 eV and has a moderate oscillator strength, whereas CT_0H-S_2, CT_0H-S_3 and CT_0Y-S_2 are at 1.72, 2.37, 2.75 eV, respectively, and have negligible oscillator strengths. The excited-state energies and their oscillator strengths at the radical pair geometries (CT_0-min) indicate that the charge transfer intermediates might be detected in the visible and NIR region using ultrafast transient absorption spectroscopy.

Table 3.21. XMCQDPT2-SA7-CASSCF(6,5) excitation energies (in eV) and oscillator strengths (in parentheses) of the active-site cluster models at the optimized geometries. Transitions are indicated from the state in which geometry was optimized. CT_n depicts CT_nY, CT_nH and D_n in the D207, H207ε and At-Pr models, respectively.

	S_0-min		S_1-min		S_1'-min	CT_0-min		D_0-min*
State	D207	H207ε	D207	H207ε	H207ε	D207	H207ε	At-Pr
S_0	-	-	-1.61 (0.980)	-1.58 (1.146)	-1.58 (1.151)	0.08 (0.020)	-0.96 (0.012)	
S_1	1.73 (0.967)	1.72 (1.164)	-	-	-	1.82 (0.262)	0.78 (0.012)	
S_2	2.81 (0.028)	2.68 (0.020)	0.94 (0.063)	0.78 (0.024)	0.82 (0.044)	2.75 (0.001)	1.72 (0.007)	
S_3	3.31 (0.388)	3.34 (0.390)	1.56 (0.580)	1.58 (0.319)	1.57 (0.708)		2.37 (0.004)	
S_4	3.65 (0.057)	3.57 (0.062)	1.79 (0.904)	1.74 (1.371)	1.71 (0.872)			
CT_0	1.80 (0.330)	2.99 (0.143)	0.08 (0.023)	1.31 (0.133)	1.15 (0.109)	-	-	-
CT_1	3.13 (0.009)	4.43 (0.008)	1.31 (0.013)	2.63 (0.002)	2.45 (0.000)	1.26 (0.026)	1.38 (0.071)	1.23 (0.085)
CT_2						2.02 (1.087)	1.97 (0.885)	1.98 (1.309)
CT_3						2.87 (0.025)		2.68 (0.085)
CT_4								3.15 (0.144)

*Transitions from D_0 to D_1-D_4 computed with XMCQDPT2-SA5-CASSCF(4,5), containing the tetrapyrrole MOs in the active space.

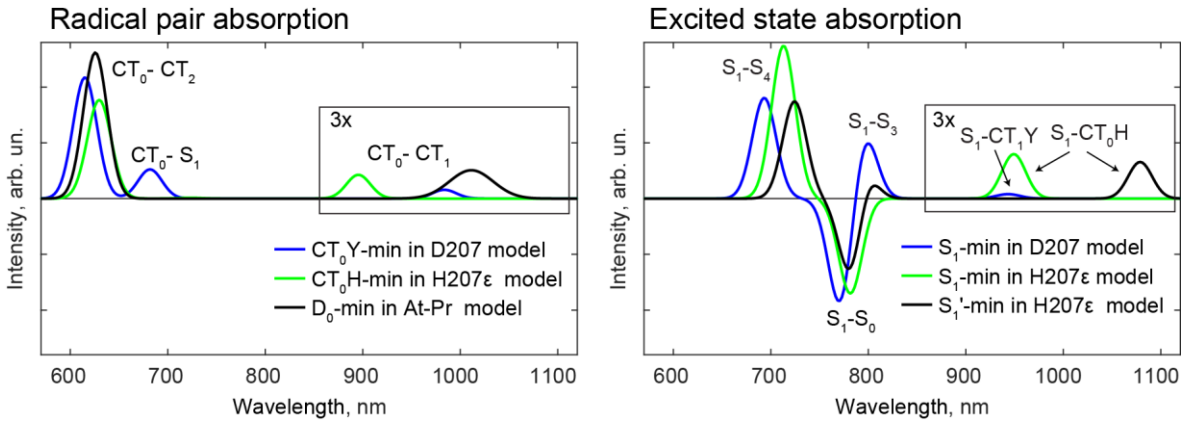

Figure 3.46. Computed absorption spectra of the tetrapyrrole radical (left) and excited tetrapyrrole (right) at the indicated geometries of the active-site cluster models representing bacterial (D207, H207ε models) and plant (At-Pr model) phytochromes. Excited-state energies and oscillator strengths were taken from Table 3.21.

The tetrapyrrole radical could be modelled and its detection predicted also in other phytochromes, containing chromophores other than biliverdin. The absorption spectrum of the phytochromobilin radical, modelled in the active-site cluster model At-Pr, representing plant phytochrome AtPhyB in the Pr state (model composition shown in Section 3.1.5, Figure 3.6), was computed at the D_0-min geometry which was optimized in the duplet state depicting an additional electron added to the protonated tetrapyrrole chromophore. The changes of the bond length in the biliverdin at the D_0-min geometry (Appendix Figure C.21) are similar as at the CT_0-min geometries (Figure 3.40 C), which are mostly on rings B-C and methine bridges between and around them. The D_0-D_1 transition, corresponding to the CT_0-CT_1 transition, has relatively low oscillator strength and is at 1.23 eV, which is in the NIR region (Figure 3.46 and Table 3.21). The D_0-D_2 transition, similar to CT_0-CT_2, has high oscillator strength and is at 1.98 eV. The D_0-D_3 and D_0-D_4 transitions are at 2.68 and 3.15 eV and have relatively low and moderate oscillator strengths, respectively.

The detection of the radical pairs at the CT_0-min or D_0-min geometry might be complicated as the transitions from the CT_0 or D_0 states overlap with the transitions from the S_1 state at the S_1-min and S_1'-min geometries (Table 3.21). The transitions from both CT_0 and S_1 are in the broad range, covering visible and NIR regions, whereas the transitions from the S_0 state as well as emission from the S_1 state are higher than 1.7 eV and does not cover the NIR region. This makes the NIR region an advantageous spectral region as there only the transitions from the S_1 and CT_0 states but not the S_0 state can be

observed. Therefore, this region may be suitable to study the charge transfer processes spectroscopically.

In the NIR region there are different types of excitations from the S_1 state: local excitations of the tetrapyrrole (to the S_n states) and intermolecular excitations to the CT states. The computed spectrum depends on the active-space size in the XMCQDPT2-CASSCF calculations. In the spectra of the D207 and H207ε models computed with the smaller active space, XMCQDPT2-SA7-CASSCF(6,5), only the S_1-CT_1Y and S_1-CT_0H transitions, respectively, are observed in the NIR region (Figure 3.46 and Table 3.21). However, if the active space of the CASSCF calculations is increased to SA9-CASSCF(8,6) and SA13-CASSCF(12,8), in the D207 model the transitions not only to the CT_1Y but also to the CT_0H and S_3 states are obtained in the NIR region (Table 3.22). The blue-shifted S_1-CT_0H transition at the S_1'-min geometry as compared to the S_1-min geometry indicates that the dynamics of the absorption band in the NIR region might be contributed by the S_1 and CT_0 states equilibration as well as by the absorption of different species. Therefore, in order to prove existence of the tetrapyrrole radical in phytochrome photoreceptors, transient absorption spectroscopy should be pursued with a detailed analysis of the species detected in the NIR region.

Table 3.22. XMCQDPT2-CASSCF excitation energies (in eV) and oscillator strengths (in parentheses) of the active-site cluster model D207 at the S_1-min geometry. Transitions from the S_1 state are listed.

State	XMCQDPT2-SA9-CASSCF(8,6)	XMCQDPT2-SA13-CASSCF(12,8)
S_0	1.64 (1.176)	1.64 (1.173)
S_2	0.88 (0.053)	0.87 (0.012)
S_3	1.38 (0.354)	1.32 (0.032)
S_4	1.84 (0.998)	1.55 (0.254)
S_5		1.94 (0.770)
S_6		2.34 (0.345)
S_7		2.44 (0.173)
S_8		2.53 (0.027)
CT_0Y	0.14 (0.017)	0.11 (0.022)
CT_1Y	1.44 (0.352)	1.41 (0.006)
CT_2Y	2.03 (0.018)	2.06 (0.067)
CT_0H	1.25 (0.074)	1.15 (0.017)

3.3.4 Multiple electron donors in different phytochromes

As described above, the electron donor residues in the active site of the phytochromes may take part in the charge transfer reactions leading to fluorescence quenching. The computed charge transfer rates are as such that charge transfer competes with the radiative decay. Therefore mutating the electron donor residues should increase fluorescence lifetime of such a mutant by reducing the excited-state decay via the radiationless decay pathways. The identification of residues acting as electron donors in phytochromes may be employed for rational design of phytochrome-based fluorescent variants.

The phytochrome active site contains multiple tyrosine and histidine residues that might act as potential electron donors, not only the above-described Y263 and H260 (according to the DrBphP numbering which is used in the following text to refer to residues in all computed models if not specified otherwise). The electron donor properties may vary between different phytochromes due to different interactions in the active site and chemical properties of the tetrapyrrole, having different length of the π-conjugated system. For example, plant phytochromes, containing the phytochromobilin chromophore, have a higher S_1-state energy (as shown in Results Part 3.1) and the experimentally measured excited-state lifetime is shorter (117). A study on different active sites was conducted to investigate the plausible electron donors and evaluate their competition with the radiative decay.

The properties of the electron donors were studied in the active-site models of several phytochromes such as bacterial DrBphP in the Pr and Pfr states, PaBphP in the Pfr state and plant AtPhyB in the Pr state. The corresponding models were Dr-Pr, Dr-Pfr, Pa-Pfr and the increased-size At-Pr (as described in Methods Section 2.1.2), in this section referred to the name of At-Pr. These four models were optimized in the ground state to obtain the S_0-min geometry of each model. The models contained the tetrapyrrole adduct and its surrounding residues including the closest tyrosine and histidine residues which potentially could act as electron donors (Figure 3.47). The Dr-Pr, Dr-Pfr and Pa-Pfr models contained four to five tyrosine or histidine residues which were in close proximity to the biliverdin tetrapyrrole. The At-Pr model contained in total eight tyrosine and histidine residues next to the phytochromobilin tetrapyrrole. In order to compute

excitation energies, which is computationally highly demanding for such a large model, three different fragments of the optimized active-site model were cut out: A, B and C (Figure 3.48). The model fragment A is the largest and contains all electron donor residues of the At-Pr model, whereas fragment C is the smallest and its size is comparable to the other models, specifically Dr-Pr, Dr-Pfr and Pa-Pfr.

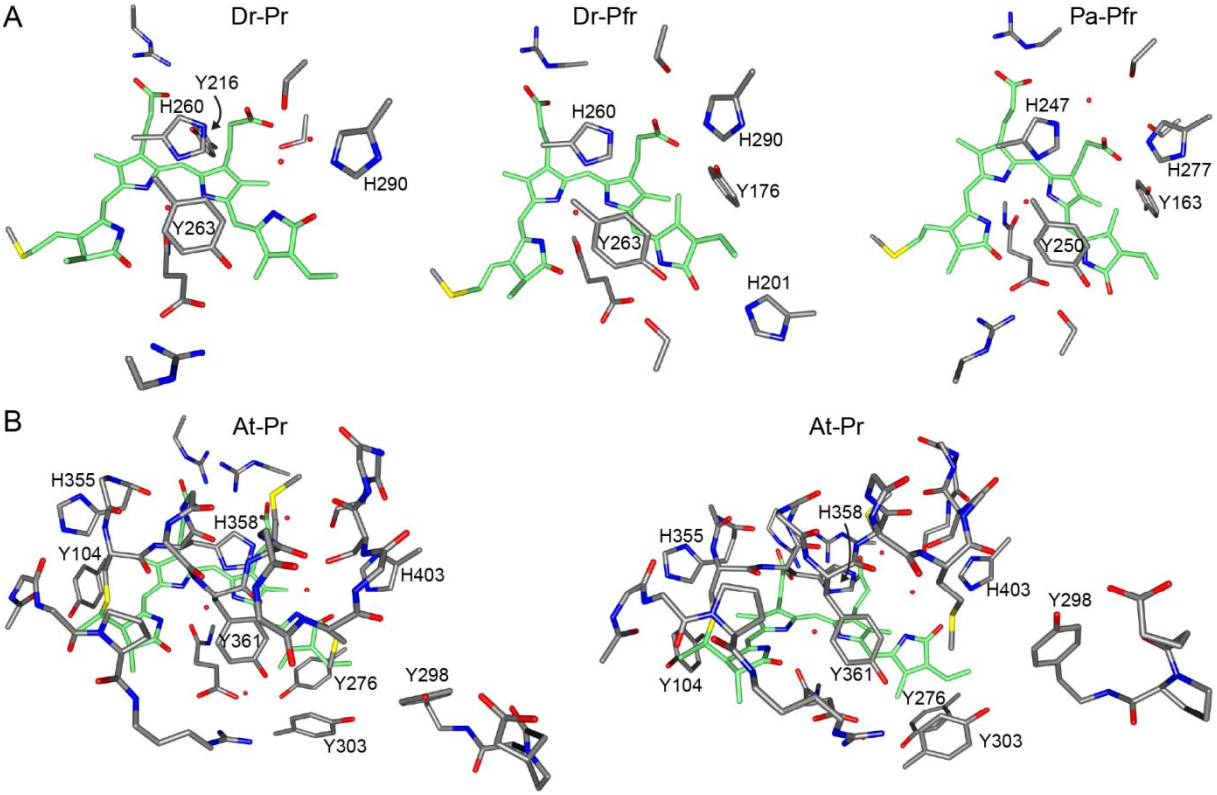

Figure 3.47. Active-site cluster models of bacterial and plant phytochromes. A) Dr-Pr, Dr-Pfr and Pa-Pfr models of bacterial phytochromes (models are the same as in Sections 3.1.5-3.1.6.) B) The At-Pr model of plant phytochrome shown in two orientations (the model is named as the increased-size At-Pr model in Methods Section 2.1.2). Tetrapyrrole is colored in green and surrounding residues including tyrosines and histidines, which potentially can act as electron donors, in grey. Residue numbers are according to the protein sequences.

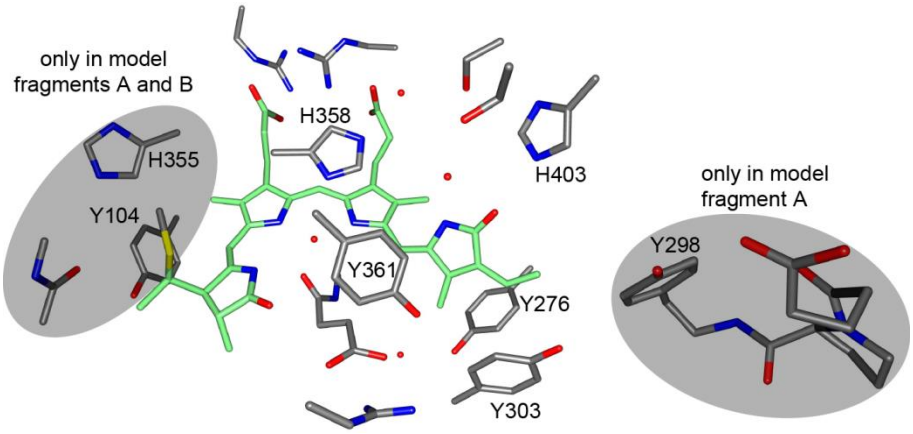

Figure 3.48. Composition of three fragments of the At-Pr active-site model. Residues shown in grey ovals were present only in the indicated model fragments, the rest – in all three model fragments: A, B and C. Tetrapyrrole is colored in green.

To determine energies of the CT states, corresponding to different electron donors in all models, the excited-state energies were calculated using the XMCQDPT2-CASSCF method with an active space, consisting of 5-10 MOs with computed 6-15 states. In previous calculations, described in Section 3.1.2, it was shown that the active space should consist of at least two occupied and two unoccupied MOs of biliverdin to obtain the XMCQDPT2 energies corresponding to the experimental spectra. However, here in addition to the locally excited states of the tetrapyrrole, multiple CT states were needed to be calculated, too. For such an active space, including two occupied and two unoccupied MOs of the tetrapyrrole and multiple unoccupied MOs of the electron donor residues, in the calculations of the current large models more states are needed to compute which is computationally too expensive. In order to get a solution for an active space including as many as possible MOs of the electron donor residues, the active spaces were reduced-size meaning that they consisted of up to nine occupied MOs, including tetrapyrrole and electron donor residues, and only one unoccupied MO of the tetrapyrrole. The calculations with the reduced-size active space enabled to find the CT states corresponding to all tyrosine and histidine residues in the prepared active-site models and indicated that CT state energies do not exceed 4 eV (Figure 3.49 and Table 3.23).

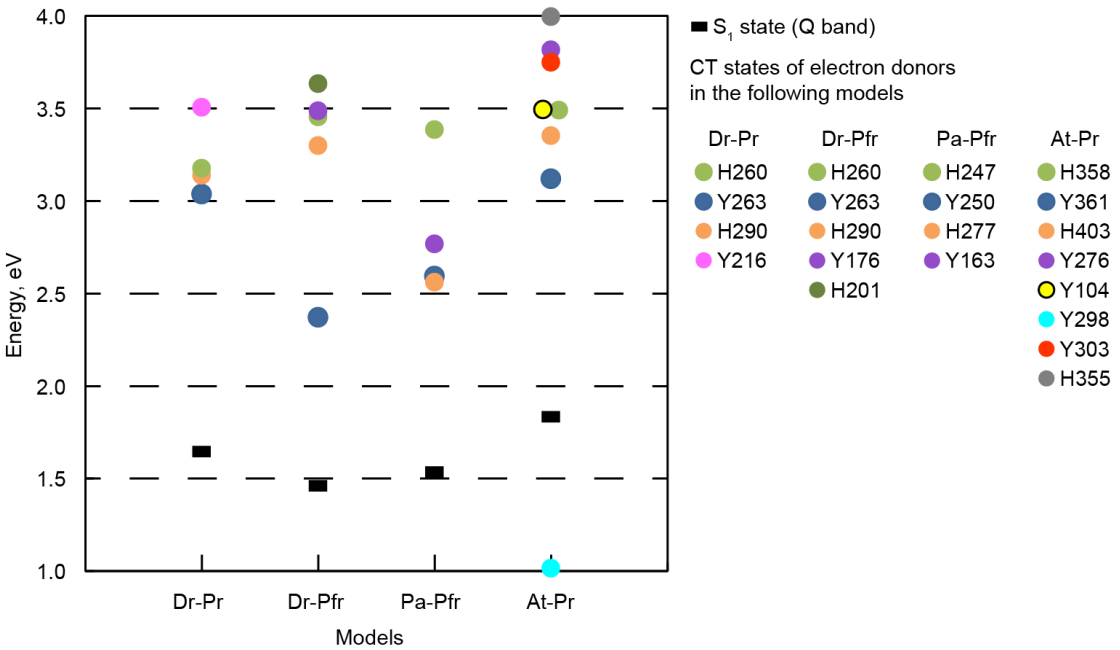

Figure 3.49. Excitation energies of electron donors in phytochrome active-site cluster models at S_0-min geometries. Energies of the S_1 state (black dash), corresponding to the Q band absorption, and CT_0 states (circles), corresponding to different electron donors, are shown with respect to the S_0-state energy of the respective model; values taken from Table 3.23. The numbering of the electron donor residues is according to the protein sequences.

Table 3.23. XMCQDPT2-CASSCF excitation energies E and oscillator strengths *f* (with respect to the ground state) computed with reduced-size active spaces at the S_0-min geometries of the active-site cluster models. Energies shown in colors are for the CT_0 states corresponding to electron donors as shown in Figure 3.49, using the same color coding. For the At-Pr model, three calculations (Table 3.24) on different model fragments (Figure 3.48) were produced. The active-space size of the XMCQDPT2-CASSCF calculations is indicated.

Dr-Pr		Dr-Pfr		Pa-Pfr		At-Pr	
SA8-CASSCF(12,7)		SA10-CASSCF(18,10)		SA8-CASSCF(12,7)		model fragment C SA9-CASSCF(16,9)	
E, eV	*f*	E, eV	*f*	E, eV	*f*	E, eV	*f*
1.64	1.213	1.46	1.103	1.53	0.989	1.83	1.363
2.50	0.336	2.17	0.294	2.29	0.264	2.85	0.297
3.04	0.004	2.37	0.014	2.56	0.000	3.12	0.001
3.14	0.004	2.54	0.060	2.59	0.006	3.32	0.109
3.18	0.092	2.98	0.261	2.77	0.001	3.35	0.010
3.34	0.161	3.30	0.000	2.96	0.317	3.49	0.009
3.51	0.001	3.45	0.022	3.39	0.014	3.75	0.000
		3.49	0.000			3.82	0.001
		3.63	0.000			3.49*	0.005*
		3.72	0.003			4.00*	0.000*
						1.02**	0.000**

* model fragment B, SA10-CASSCF(18,10). ** model fragment A; SA9-CASSCF(8,6).

Table 3.24. XMCQDPT2-CASSCF excitation energies E and oscillator strengths *f* (with respect to the ground state) of different fragments of the At-Pr active-site cluster model at the S_0-min geometry. Energies shown in colors are for the CT_0 states, corresponding to Y104 (yellow), Y276 (purple), Y298 (cyan), Y303 (red), H355 (grey), H358 (green), Y361(blue), H403 (orange) electron donors. Composition of each model fragment is shown in Figure 3.48. H358, Y361 and H403 correspond to H260, Y263 and H290 in DrBphP. The active-space size of the XMCQDPT2-CASSCF calculations is indicated.

fragment A		fragment B		fragment C	
SA9-CASSCF(8,6)		SA10-CASSCF(18,10)		SA9-CASSCF(16,9)	
E, eV	*f*	E, eV	*f*	E, eV	*f*
1.02	0.000	1.85	1.328	1.83	1.363
1.80	1.364	2.92	0.223	2.85	0.297
2.24	0.000	2.99	0.093	3.12	0.001
2.84	0.013	3.26	0.002	3.32	0.109
2.96	0.000	3.47	0.072	3.35	0.010
3.25	0.518	3.49	0.005	3.49	0.009
3.51	0.270	3.53	0.002	3.75	0.000
4.08	0.113	3.68	0.004	3.82	0.001
		4.00	0.000		

The excited-state calculations with the reduced-size active space are less accurate than the above-described calculations used to characterize the charge transfer reactions (Section 3.3.2). To evaluate the accuracy of the calculations with the reduced-size active

space, the excited-state energies were compared to the calculations with different active spaces, especially those that contained two unoccupied MOs in the active space. The calculations with the reduced-size active space resulted in reduced energies of the S_n states corresponding to the Q and Soret bands in comparison to the calculations with the active space containing two unoccupied MOs such as SA7-CASSCF(6,5), which reproduced the experimental spectral signatures of the Q and Soret bands as was shown in Section 3.1.5, Table 3.3. The excitation energies of the S_n states corresponding to the Q and Soret bands differed in these calculations by 0.14-0.16 eV and 0.65-0.82 eV, respectively. However, the CT-state energies were increased in the calculations with the reduced-size active space (Table 3.23) in comparison to the calculations with the active space containing two unoccupied MOs (Table 3.25). Among all four models, the energy difference for the CT states corresponding to the Y263 and H290 electron donors was 0.17-0.28 eV and 0.19-0.30 eV, respectively. In the Dr-Pr model, the energies of the CT states corresponding to H260, Y263 and H290 were higher in the calculations with the reduced-size active space by -0.01-0.06 eV, 0.10-0.25 eV and 0.11-0.29 eV, respectively, as compared to the calculations with various active spaces containing two unoccupied MOs (Table 3.26).

Table 3.25. XMCQDPT2-SA9-CASSCF(8,6) excitation energies E and oscillator strengths *f* (with respect to the ground state) of the active-site cluster models at S_0-min geometries. Energies shown in colors are for the CT states, corresponding to Y263(blue) and H290 (orange) electron donors according to the numbering in DrBphP. The active-space size of the XMCQDPT2-CASSCF calculations is indicated.

Dr-Pr		Dr-Pfr		Pa-Pfr		At-Pr*	
E, eV	*f*	E, eV	*f*	E, eV	*f*	E, eV	*f*
1.60	1.065	1.50	1.001	1.49	0.804	1.80	1.221
2.48	0.010	2.09	0.022	2.14	0.087	2.57	0.017
2.80	0.003	2.38	0.012	2.37	0.001	2.86	0.024
2.84	0.209	2.64	0.233	2.38	0.007	3.01	0.005
2.88	0.152	3.00	0.000	2.61	1.020	3.26	0.665
3.42	0.073	3.38	0.009	3.08	0.218	3.64	0.004
4.08	0.001	3.39	0.079	3.56	0.001	3.98	0.005
4.10	0.009	4.28	0.000	3.59	0.000	4.09	0.001

* - energies computed for model fragment C.

For the excited-state calculations of the At-Pr model, three fragments of this model were used as shown in Figure 3.48. The energy calculations with the reduced-size active space varied in the three model fragments: by 0.14 eV and 0.18 eV for the CT states corresponding to Y263 and H290, respectively, whereas only by 0.02 eV for the CT state

corresponding to H260 (Table 3.24). These results show that the calculations with the reduced-size active space result in decreased energies for the S_n states, which correspond to the local excitations (up to 0.16 eV for the Q band), and increased energies for the CT states, especially corresponding to the Y263 and H290 electron donors (up to 0.30 eV). However the calculations with the reduced-size active space are comparable with the calculations with the larger active spaces and may be thus used to predict the electron donors based on the energies of the particular CT states.

Table 3.26. XMCQDPT2-CASSCF excitation energies E and oscillator strengths *f* (with respect to the ground state) computed with active space containing one or two unoccupied MOs for the Dr-Pr model at the S_0-min geometry. Energies shown in colors are for the CT states, corresponding to Y216 (pink), H260 (green), Y263 (blue), H290 (orange) electron donors. The higher energy indicated with the same color for the same calculation represents the CT_1 state. The active-space size of the XMCQDPT2-CASSCF calculations is indicated.

SA8-CASSCF(12,7)		SA6-CASSCF(6,5)		SA9-CASSCF(12,8)		SA10-CASSCF(12,8)		SA11-CASSCF(12,8)	
E, eV	*f*	E, eV	*f*	E, eV	*f*	E, eV	*f*	E, eV	*f*
1.64	1.213	1.76	1.078	1.68	1.170	1.66	1.183	1.61	1.154
2.50	0.336	2.57	0.032	2.72	0.090	2.63	0.062	2.55	0.060
3.04	0.004	3.00	0.016	2.89	0.004	2.94	0.003	2.87	0.004
3.14	0.004	3.08	0.371	3.03	0.004	2.99	0.037	2.92	0.076
3.18	0.092	4.25	0.001	3.12	0.090	3.04	0.199	2.96	0.240
3.34	0.161			3.24	0.147	3.19	0.070	3.15	0.057
3.51	0.001			3.59	0.102	3.50	0.107	3.41	0.110
				4.39	0.001	4.29	0.008	4.01	0.033
						4.30	0.005	4.21	0.001
								4.23	0.007

SA12-CASSCF(12,8)		SA13-CASSCF(12,8)		SA13-CASSCF(14,9)		SA14-CASSCF(14,9)		SA15-CASSCF(14,9)	
E, eV	*f*	E, eV	*f*	E, eV	*f*	E, eV	*f*	E, eV	*f*
1.60	1.156	1.55	1.111	1.61	1.194	1.57	1.138	1.56	1.125
2.55	0.062	2.53	0.085	2.56	0.057	2.56	0.081	2.56	0.084
2.85	0.004	2.79	0.004	2.67	0.035	2.68	0.021	2.68	0.021
2.91	0.032	2.85	0.018	2.90	0.052	2.86	0.031	2.86	0.019
2.97	0.304	2.92	0.259	2.98	0.008	2.94	0.005	2.93	0.004
3.19	0.052	3.14	0.046	3.04	0.361	3.00	0.286	3.01	0.308
3.38	0.114	3.45	0.210	3.17	0.057	3.12	0.064	3.18	0.050
3.97	0.028	3.82	0.006	3.46	0.078	3.45	0.166	3.45	0.183
4.21	0.001	4.02	0.091	3.83	0.078	3.80	0.049	3.81	0.098
4.22	0.008	4.14	0.001	4.02	0.137	3.82	0.045	3.81	0.011
4.58	0.004	4.14	0.006	4.23	0.001	3.99	0.196	4.00	0.179
		4.53	0.001	4.25	0.005	4.19	0.001	4.20	0.001
						4.21	0.012	4.22	0.011
								4.55	0.001

The energies of the CT states, corresponding to the electron donors in the computed models of bacterial and plant phytochromes, do not exceed 4.0 eV in the calculations with the reduced-size active space which with the larger active space could be up to 3.7 eV. For the charge transfer to happen, the energy gap between the S_1 and CT states at the S_0-state geometry should be not larger than ~2 eV, assuming significant radical pair stabilization as discussed in Subsection 3.3.2.2. Therefore, the charge transfer reactions of the electron transfer coupled to proton transfer including a significant radical pair stabilization may occur with such electron donors which have CT-state energy not higher than ~3.7 eV and ~3.9 eV for bacterial and plant phytochromes, respectively. The excited-state calculations suggest that several residues may potentially act as electron donors if the electronic coupling V_{el} of the S_1 and CT_0 states meet the criteria for a fast charge transfer process.

A fast charge transfer rate is ensured by a low energy of the CT state and a strong electronic coupling V_{el}. The hypothetical charge transfer rate was computed for all potential electron donors assuming that changes of the potential energy surface along the charge transfer coordinate include the electron transfer coupled to proton transfer similar as described for the electron donors Y263 and H260 in Subsection 3.3.2.2. To undergo such a charge transfer reaction, a proton acceptor such as a negatively charged aspartate, glutamate or propionate should be located in close proximity to the electron donor in order to stabilize the radical pair. In case there is no proton acceptor next to the electron donor interacting with it directly or via a hydrogen-bonding network, the radical pair would be stabilized less due to the absence of the proton transfer. This results in an increased activation energy $E^{\#}$ and reduced charge transfer rate k_{CT}. The maximal rates presented in the following paragraph were estimated assuming that the radical pair undergoes stabilization during the electron transfer coupled to proton transfer as described in Subsection 3.3.2.2. For the energy calculations the results obtained with the reduced-size active space (Tables 3.23 and 3.24) were used; the correction of the CT-state energies was done by decreasing it by 0.2 eV, taking into consideration the increased CT-state energies by up to 0.3 eV when computed with the reduced-size active spaces as described above. For every electron donor in each model it was assumed that an energy gap between the S_1 and CT_0 states increases by 0.028 eV in the S_1-min as compared to the S_0-min geometry. It was also assumed that the energy of the CT_0 state decreases by

1.62 eV and the energy of the S_1 state increases by 0.37 eV along the reaction coordinate from the S_1-min to the CT_0-min geometry. The computed activation energies are 0.02-0.33 eV (Table 3.27) and indicate energetically possible charge transfer.

Table 3.27. **Energies and charge transfer rate properties.** S_0-CT_0 energies, activation energies $E^{\#}$, electronic couplings V_{el} and charge transfer rate constants k_{CT} were obtained from the XMCQDPT2-CASSCF calculations of the active-site cluster models at S_0-min geometries. Energies shown in colors are for the computed CT states with respect to the S_0 state as shown in Tables 3.23 and 3.24, color coding is the same as in Figure 3.49. For the At-Pr model, the model fragment C was used if not indicated otherwise. The numbering of the electron donor residues is according to the protein sequences.

Dr-Pr XMCQDPT2-SA8-CASSCF(12,7)					Dr-Pfr XMCQDPT2-SA10-CASSCF(18,10)				
	CT_0, eV	$E^{\#}$, eV	V_{el}, meV	k_{CT}, s^{-1}		CT_0, eV	$E^{\#}$, eV	V_{el}, meV	k_{CT}, s^{-1}
Y263	3.04	0.07	61.3	$1.1 \cdot 10^{12}$	Y263	2.37	0.02	90.6	$1.65 \cdot 10^{13}$
H290	3.14	0.09	82.9	$1.06 \cdot 10^{12}$	H290	3.30	0.17	13.7	$1.21 \cdot 10^{9}$
H260	3.18	0.09	686.9	$5.57 \cdot 10^{13}$	H260	3.45	0.23	186.3	$2.31 \cdot 10^{10}$
Y216	3.51	0.18	28.7	$3.96 \cdot 10^{9}$	Y176	3.49	0.24	25.1	$2.32 \cdot 10^{8}$
					H201	3.63	0.33	7.1	$5.64 \cdot 10^{5}$

Pa-Pfr XMCQPDT2-SA8-CASSCF(12,7)					At-Pr (model fragment C) XMCQDPT2-SA9-CASSCF(16,9)				
	CT_0, eV	$E^{\#}$, eV	V_{el}, meV	k_{CT}, s^{-1}		CT_0, eV	$E^{\#}$, eV	V_{el}, meV	k_{CT}, s^{-1}
H277	2.56	0.03	1.6	$3.67 \cdot 10^{9}$	Y358	3.12/3.26*	0.05/0.07*	58.7/34.9*	$1.79 \cdot 10^{12}$/$3.22 \cdot 10^{11}$*
Y250	2.59	0.03	67.8	$5.96 \cdot 10^{12}$	H403	3.35/3.53*	0.09/0.12*	12.9/18.8*	$2.17 \cdot 10^{10}$/$1.21 \cdot 10^{10}$*
Y163	2.77	0.05	22.2	$3.26 \cdot 10^{11}$	H361	3.49/3.47*	0.12/0.11*	333/330*	$4.82 \cdot 10^{12}$/$6.14 \cdot 10^{12}$*
H247	3.39	0.25	105	$2.49 \cdot 10^{9}$	Y303	3.75	0.19	8.58	$1.69 \cdot 10^{8}$
					Y276	3.82	0.22	42.6	$1.45 \cdot 10^{9}$
					Y104	3.49*	0.12*	54.6*	$1.42 \cdot 10^{11}$*
					H355	4.00*	0.31*	7.62*	$1.34 \cdot 10^{6}$*
					Y298	1.02**	0.03**	0.21**	$6.30 \cdot 10^{7}$**

* model fragment B computed with XMCQDPT2-SA10-CASSCF(18,10). ** model fragment A computed with XMCQDPT2-SA9-CASSCF(8,6).

For the estimation of the electron transfer rate, the strength of the electronic coupling V_{el} was calculated for each electron donor in the models. The electronic coupling V_{el} was calculated between the S_1 and CT_0 states, but the energies and the excited-state properties of the S_0-min geometries were used as they are similar to those obtained at the geometry optimized in the S_1 state. For the majority of the donors, the electronic coupling was above 20 meV (Table 3.27), which corresponds to a strong electronic coupling resulting in fast charge transfer if the energies are favorable. The histidine H260 has the largest

electronic coupling in all models, whereas H290 in all models except Dr-Pr, H201 in Dr-Pfr, as well as Y303, H355 and Y298 in At-Pr models had electronic couplings smaller than 20 meV (DrBphP numbering).

The estimated activation energies $E^{\#}$ and electronic couplings V_{el} were used to compute the charge transfer rates k_{CT}. The results indicate relatively large charge transfer reaction rates for the majority of the computed electron donors, with the respective S_1-state lifetimes on the picosecond and femtosecond timescales. However, the rates including electron donors Y176 for the Dr-Pfr model and Y298, Y303, H355 for the At-Pr model are on the nanosecond timescale while the rate including H201 for the Dr-Pfr model is on the microsecond timescale. H260 and Y263 are predicted to be efficient electron donors in all studied models.

As charge transfer rates depend on the excited-state energies, activation energies $E^{\#}$ and electronic couplings V_{el}, these properties were compared for the highly conserved H260, Y263, H290 (DrBphP numbering) residues among all four models. Excited-state energies for the respective three CT states and the corresponding $E^{\#}$ as well as strong V_{el} are in line with the fast electron transfer in all four models. The largest V_{el} in all models is for the H260 electron donor, especially in the Pr-state models, because this residue is located above the tetrapyrrole and allows the π-π stacking. The Y263 donor also has large V_{el} in all models and relatively low energies of the CT state in the Pfr-state models, which results in larger charge transfer rate constants in the Pfr-state models as compared to the Pr-state models. H290 has a large V_{el} only in the Dr-Pr model but has still a relatively large charge transfer rate constant in all models. The fastest rates are predicted for H260/H361 in Dr-Pr/At-Pr and Y263/Y250 in Dr-Pfr/Pa-Pfr, indicating the importance of these two conserved residues for the charge transfer reactions in the Pr- and Pfr-state phytochromes.

The experimentally estimated excited-state lifetime in phytochromes are on the picosecond timescale (117), indicating that charge transfer reactions on the same or faster timescale can compete with radiative decay. The calculated rates based on the estimated energies suggest that the highly conserved H260, Y263, H290 residues may act as electron donors in all computed phytochromes. Additionally, Y216 in Pr-state DrBphP, Y163 in

Pfr-state PaBphP as well as Y276 and Y104 in Pr-state AtPhyB are predicted to act as electron donors as well. The identified electron donors can be mutated in order to abolish charge transfer pathways and increase the fluorescence quantum yield of the engineered phytochrome-based markers. Alternatively, a negatively charged residue, located next to the electron donor and acting as a proton acceptor from the electron donor, can be mutated.

3.3.5 Molecular dynamics of models with mutated electron donors

3.3.5.1 Proteins considered in the molecular dynamics study

In order to make suggestions for the design of phytochrome-based markers with increased fluorescence, MD simulations of the models with mutated potential electron donors were performed for two templates with different absorption maxima: red-absorbing IFP2.0 (in Pr form) (142) and far-red-absorbing PaBphP (in Pfr form) (40) (Table 3.28). Two templates have different advantages as IFP2.0 is small in size, and PaBphP has the Pfr state as a dark-adapted state. Although IFP2.0 is relatively small as it consists only of the CBD domain, its spectrum does not show the farthest red shift. PaBphP possesses a far-red-shifted spectrum since it is in the Pfr state, but for that both the CBD and PHY domains are needed. The PHY domain is necessary to stabilize the interactions between the highly conserved aspartate and biliverdin ring D and to ensure the red-shifted spectrum (as described in Results Part 3.1). The advantage of each template is connected to particular challenges due to possible unstable interactions in the active site: opening of the active site which is not stabilized by the PHY domain in the IFP2.0 mutants, or disruptions of the aspartate–biliverdin ring D or the CBD–PHY interactions in the PaBphP mutants. Single and multiple mutations of possible electron donors (the residue numbering in the following section is according to the specific protein sequence) were done to simulate protein models with increased fluorescence by abolishing the charge transfer pathways.

Tyrosine and histidine residues close to the biliverdin in the active site (Figure 3.50) were mutated to residues which cannot act as electron donors: phenylalanine, glutamine, serine, threonine, arginine or lysine. Arginine or lysine were introduced instead of the tyrosine interacting with the negatively charged PropB (Y216 in IFP2.0 and Y203 in PaBphP) or

instead of the histidine H277 interacting with the negatively charged PropC in the Pfr-state PaBphP mutants. Other amino acids were introduced instead of all tyrosine residues indicated in Table 3.28 or instead of histidines H260 and H290 in the IFP2.0 and H247 in the PaBphP mutants. Models of the double and triple mutants of the IFP2.0 template included Y263F-H290Q and Y263F-H290Q-H260Q mutations. The sextuple mutants contained Y198F, Y216F, H260Q, Y263F, H290Q and Y176Q or Y176F mutation.

Table 3.28. Construction of phytochrome-based protein models with increased fluorescence by mutating electron donors which contribute to fluorescence quenching.

Template	IFP 2.0*	wild-type PaBphP
Excitation max.	~ 700 nm, Pr-state spectrum	~ 750 nm, Pfr-state spectrum
Composition	CBD domain	CBD-PHY domains
Advantage	small	Long excitation wavelength
Challenges	"open" active site	Unstable CBD↔PHY and Asp↔ring D
Mutation type	Single, double, triple, sextuple	Single
Electron donors	Y176, Y198, Y216, H260, Y263, H290	Y163, Y185, Y190, Y203, H247, Y250, H277
Single mutations	Y176F/Q, Y198F/Q/T, Y216F/Q/R/S, H260Q, Y263F/Q/T, H290Q	Y163F/Q, Y185F/Q, Y190F, Y203F/R, H247Q, Y250F/Q, H277R/K
Nr of models	18	12

* - engineered from the wild-type DrBphP phytochrome (142)

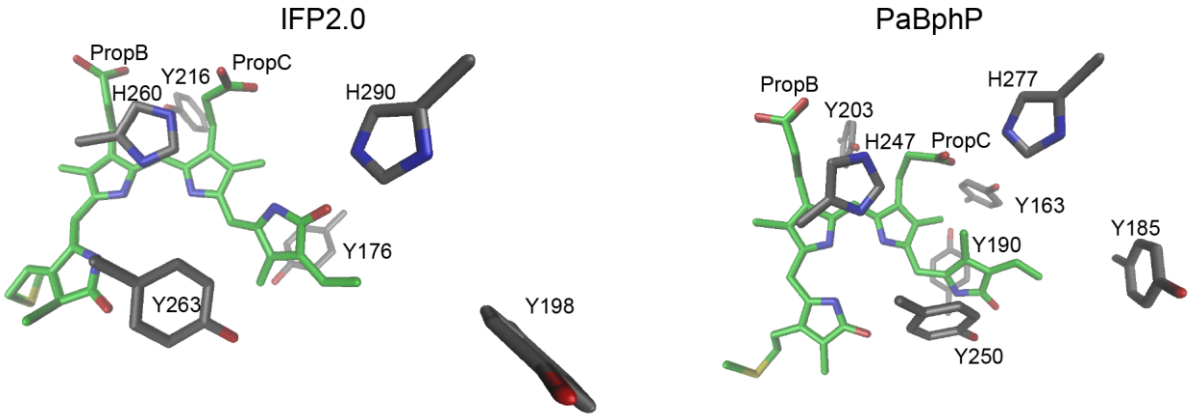

Figure 3.50. Electron donors in phytochrome models IFP2.0 and PaBphP. The numbering is according to the protein sequence.

MD simulations of 100 ns were performed for both template models, IFP2.0 and PaBphP, and each prepared mutant model. In the IFP2.0 model and in most of its mutant models, the measured RMSDs for all non-hydrogen atoms in the protein and its backbone were increasing during the initial 30 ns (Figure 3.51) Therefore, the initial 30 ns were considered as part of the equilibration phase and were thus not used for further

analysis for all models. In the PaBphP model, the RMSDs increased during the initial 30 ns, however for some PaBphP mutant models the RMSDs were changing during the entire 100 ns trajectory (Figure 3.52), indicating that mutations in the active site may lead to some changes in the protein dynamics and structure. The MD trajectories of the remaining 70 ns of the simulation for every model were used for further analysis.

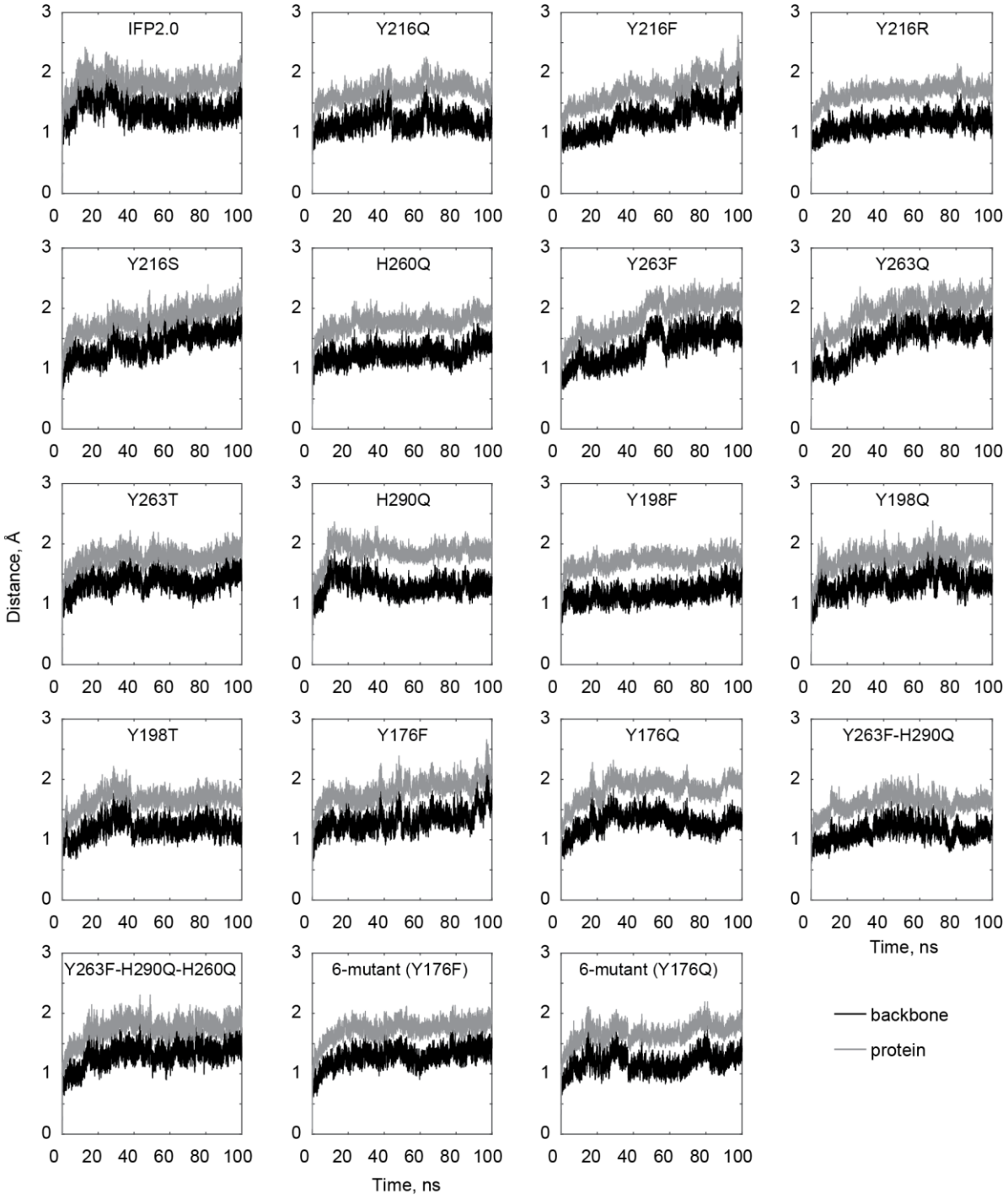

Figure 3.51. RMSDs for the non-hydrogen atoms of the protein and its backbone over time in IFP2.0. and its mutant models. Sextuple mutants contain Y198F, Y216F, H260Q, Y263F, H290Q and Y176Q or Y176F mutation. The numbering is according to the protein sequence.

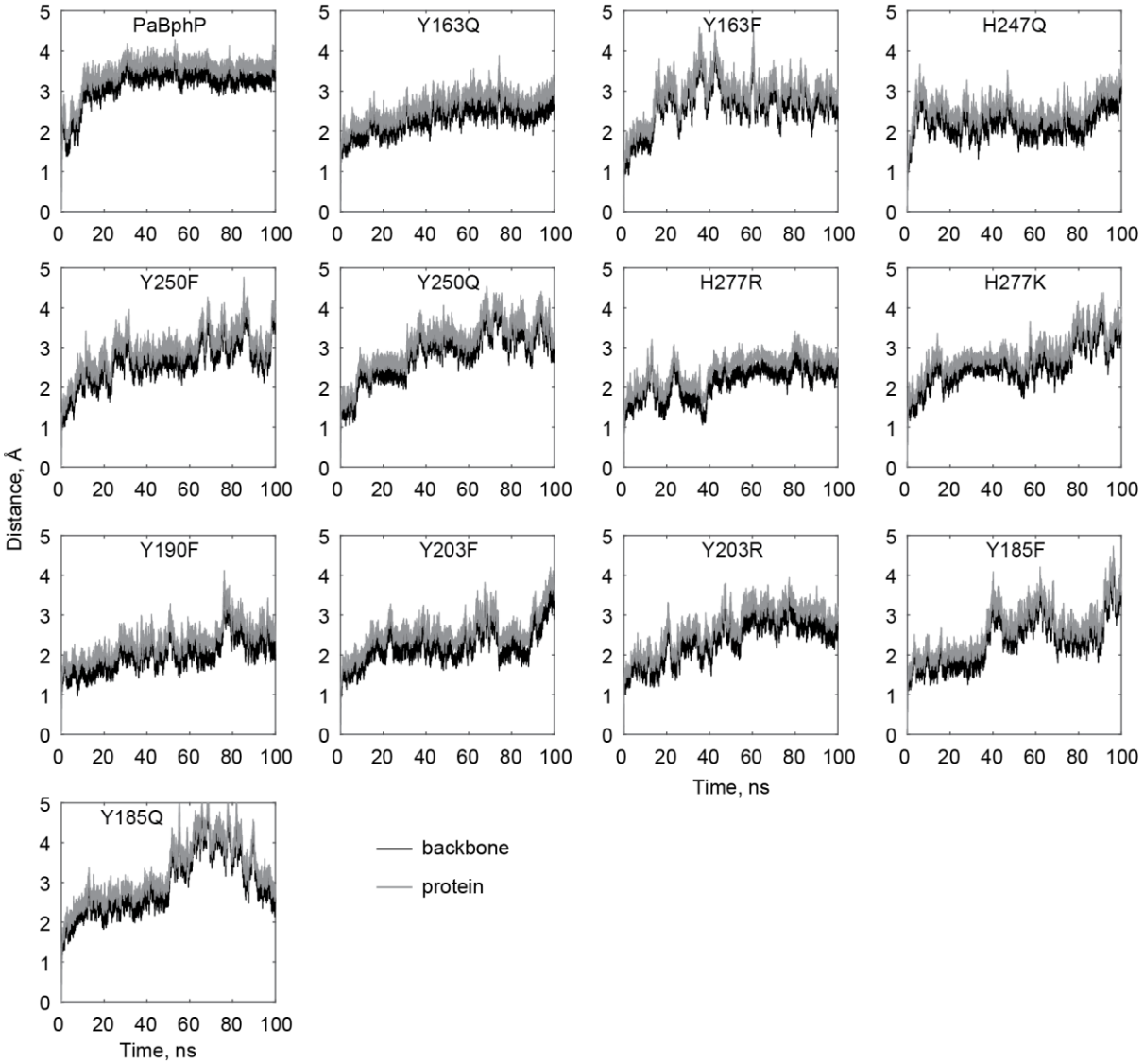

Figure 3.52. RMSD for the non-hydrogen atoms of the protein and its backbone over time in PaBphP and its mutant models. The numbering is according to the protein sequence.

The trajectories of the IFP2.0, PaBphP and their mutant models were visually inspected and analytically analyzed. Since the IFP2.0 model consist only of the CBD domain and its active site is solvent-exposed and not stabilized by the PHY domain, bulk water entered between Y263 and T207 as it was described in Section 3.1.7 and was already reported by Field and co-workers (180). In the PaBphP model, the PHY domain stabilizes the active site and therefore entering of water molecules into the active site was not observed. The distances in the active site of the IFP2.0, PaBphP and their mutant models, as well as the planarity of the biliverdin were analyzed as described in the following subsections. In particular, distances between an electron donor or a mutated residue and other residues interacting with them were investigated.

3.3.5.2 Active-site interactions in the IFP 2.0 protein and its mutants

Several types of distances were measured in the active site of the simulated IFP2.0 model (Figure 3.53): distances characterizing direct hydrogen bonds or hydrogen bonds via water molecules, distances between close residues which do not interact via hydrogen bonds, and distances between the biliverdin (ring A or D) and residues of the above-located α-helix. The distances characterizing the hydrogen bonds were as follows: between biliverdin ring D and H290, between the propionate (PropC or PropB) and H260, S272, S274, Y216, or between Y176 and T207. Y263 and Y198 residues are solvent-exposed and do not interact with other protein residues via hydrogen bonds, therefore the position of these residues in the active site was estimated by measuring the distances between Y263 and T207 or between Y198 and biliverdin ring D, M267, R172. The distances ring A-M259 and ring D-M267 indicated that there was no water entering between biliverdin and the above-located α-helix. Distributions of the hydrogen bonds had small bandwidths (first six distances in Figure 3.53 B), whereas distributions of other distances had large bandwidths (next four distances in Figure 3.53 B) or showed even two populations (last two distances in Figure 3.53 B).

Deviations of the interactions in the active site of the IFP 2.0 model from its X-ray crystal structure (142) were evaluated (Figure 3.53 C). The maximum value of the distribution of a particular measured distance was compared to the distance in the crystal structure. The distances were grouped to represent the distances corresponding to the hydrogen bonds (distributions with small bandwidth), distances representing proximity of the neighboring residues (distributions with larger bandwidth) and distances representing the biliverdin-α-helix interactions (distributions with larger bandwidth and even two populations). The distribution maxima of the distances in the IFP2.0 model had deviations from the crystal-structure distances of 1.0 Å and 1.5 Å for the small bandwidth distributions of the hydrogen bonds between PropC and S274, and between Y216 and PropB, respectively, and of 1.1 Å, 1.7 Å and 1.8 Å for the large bandwidth distributions of weak interactions between biliverdin ring A and M259, between Y263 and T207, and between Y198 and biliverdin ring D, respectively. The distribution maxima of other distances in IFP2.0 deviated less than 0.5 Å from the crystal structure.

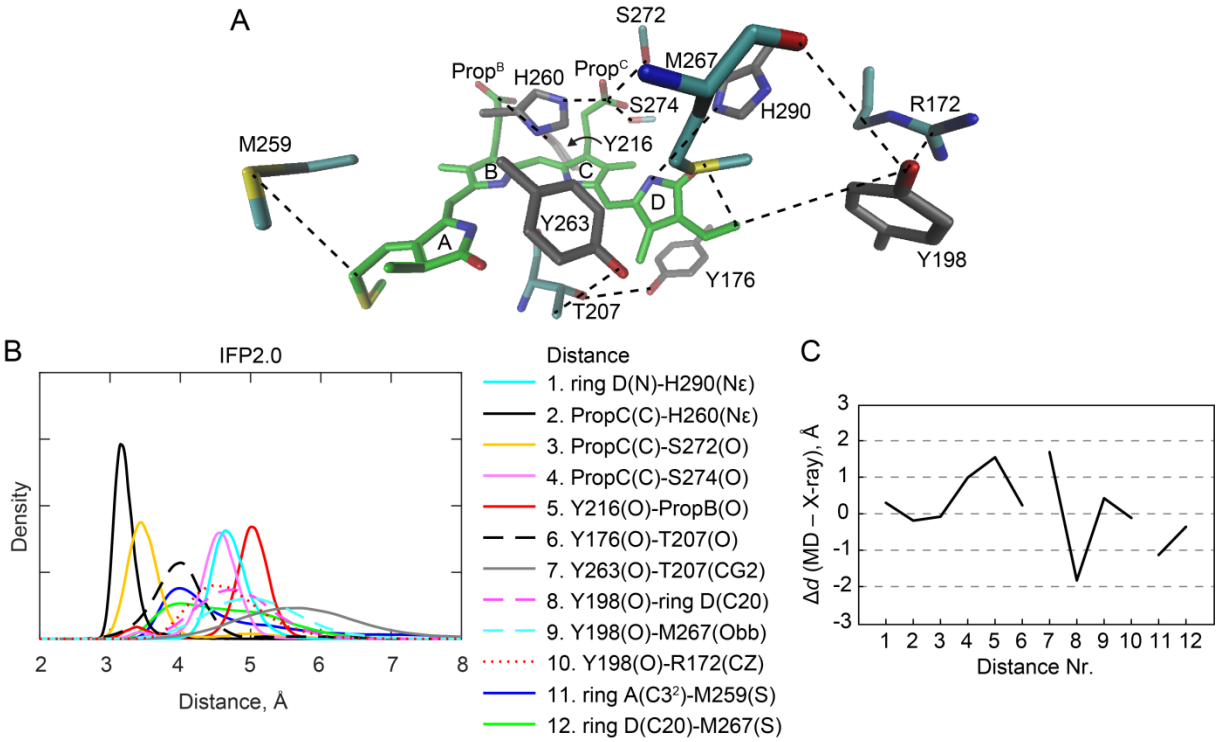

Figure 3.53. Distances in the active site of the IFP2.0 model. A) Measured distances between non-hydrogen atoms. B) Distributions of all measured distances over the last 70 ns of 100 ns MD simulation. C) Differences (Δd) between the distribution maxima of the distances in the IFP2.0 model (MD) and the distances in the X-ray crystal structure of IFP2.0 (X-ray).

In the simulated IFP2.0 mutant models, the same distances in the active site were analyzed and distributions were plotted as discussed for the IFP 2.0 model (Figure 3.54). In case of the mutated residues, the distances were measured to the specific atoms of all residues of a certain type: HZ of Phe, N of Gln, O of Ser, CZ of Arg, O of Thr but CG2 of Thr198 (atom names are shown in Appendix A). To make the analysis of the active-site interactions more comprehensive, the distribution maximum of every measured distance in the IFP2.0 mutant models was compared to the distance in the crystal structure of the IFP2.0 protein (Figure 3.55), similarly as described above for the IFP 2.0 model. This enables the comparison of the active-site dynamics in mutant models with dynamics in the IFP2.0 model as well. The mutant models with distribution maxima deviating less than 2 Å from the crystal-structure distances or from the distribution maxima in the IFP2.0 model were considered as models with stable interactions. For every electron donor at least one tested mutation resulted in a model with stable interactions: Y176Q, Y198F, Y216F, Y263F/Q/T, H260Q, H290Q (Table 3.29). Multiple mutations such as double (Y263F-H290Q), triple (Y263F-H290Q-H260Q) and sextuple (Y263F-H290Q-H260Q-Y198F-Y216F-Y176Q) also resulted in models with stable interactions.

Based on the analysis of te discussed mutants, in most cases histidine can be mutated to glutamine and tyrosine can be mutated to phenylalanine. Mutations of tyrosine Y176 to glutamine resulted in a more stable active site. Mutations of for the solvent-exposed Y263 to phenylalanine, glutamine or threonine resulted in a similar active-site stability as in the template model. This analysis also shows that stable interactions in the active site can be present also in models with multiple mutations.

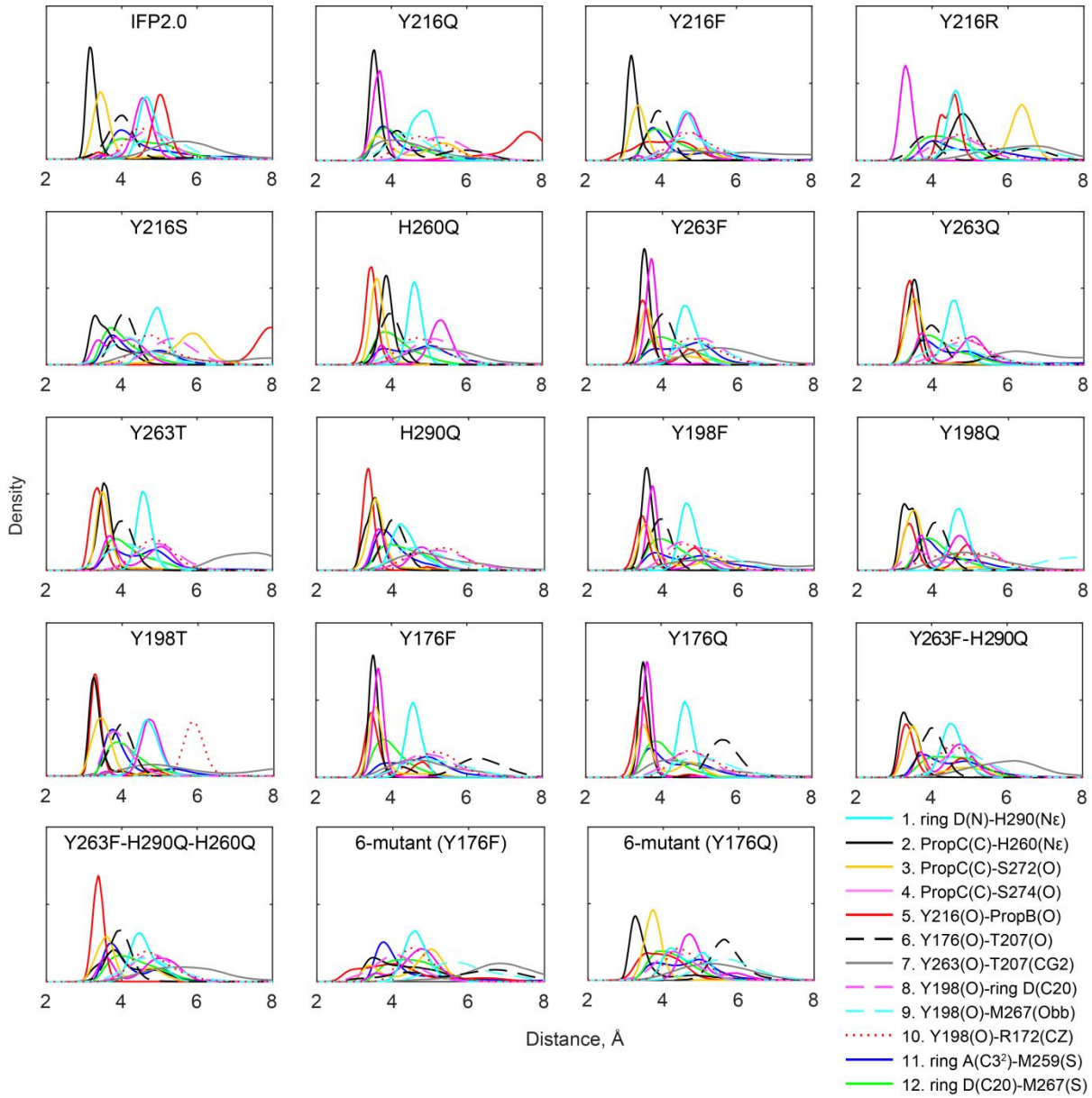

Figure 3.54. Distance distributions in the active site of IFP2.0 and its mutant models measured over the last 70 ns of 100 ns MD simulation. Sextuple mutants contain Y198F, Y216F, H260Q, Y263F, H290Q and Y176Q or Y176F mutation. In case of mutated residues, the distances were measured to the specific atoms of all residues of a certain type: HZ of Phe, N of Gln, O of Ser, CZ of Arg, O of Thr but CG2 of Thr198, as shown in Appendix A.

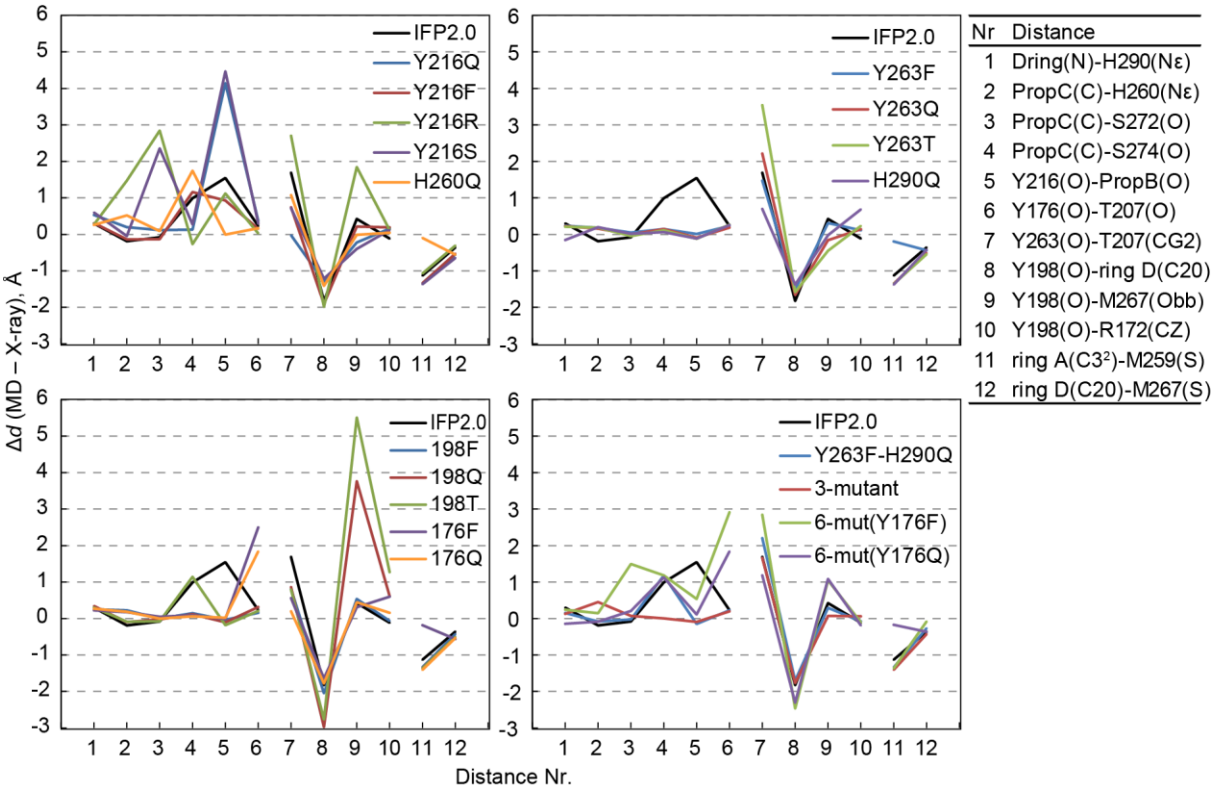

Figure 3.55. Distances in the active site of IFP2.0 and its mutants models. Differences(Δd) between the distribution maxima of the distances in IFP2.0 or its mutant models (MD) and the distances in the X-ray crystal structure of IFP2.0 (X-ray). Triple mutant "3-mutant" contains H260Q, Y263F, H290Q mutations, sextuple mutants contains Y198F, Y216F, H260Q, Y263F, H290Q and Y176F or Y176Q mutations in "6-mut(Y176F)" and "6-mut(Y176Q)" models, respectively. In case of mutated residues, the distances were measured to the specific atoms of all residues of a certain type: HZ of Phe, N of Gln, O of Ser, CZ of Arg, O of Thr but CG2 of Thr198, as shown in Appendix A.

Table 3.29. IFP2.0 mutant models with stable interactions in the active site. The numbering is according to the protein sequence.

Residue	Mutation
Y176	Q
Y198	F
Y216	F
Y263	F/Q/T
H260	Q
H290	Q

3.3.5.3 Active-site interactions in the PaBphP protein and its mutants

The distances in the active site of the simulated PaBphP and its mutant models were analyzed similarly as in IFP2.0 and its mutant models. Several types of distances were measured in the PaBphP model (Figure 3.56): distances characterizing direct hydrogen bonds or hydrogen bonds via water molecules and distances between neighboring residues. The direct hydrogen bonds included interactions between the conserved aspartate D194 and ring D, S459 or R453, between Y250 and S459, which are important

for the spectral red shift and CBD-PHY domains interactions, and between PropC and H277, Y163 or S275. The distributions of these distances had small bandwidth (first seven distances in Figure 3.56 B). The distance characterizing a hydrogen bond via water molecules was between PropC and H247, while the Y190-Y163 distance was representing a distance between these neighboring residues. The distributions of these two distances had larger bandwidths (next two distances in Figure 3.56 B). Other distances between neighboring residues were Q188-ring D and Y203-PropB (last two distances in Figure 3.56 B). These two distributions were multimodal, the first with two peaks and the second one with three peaks.

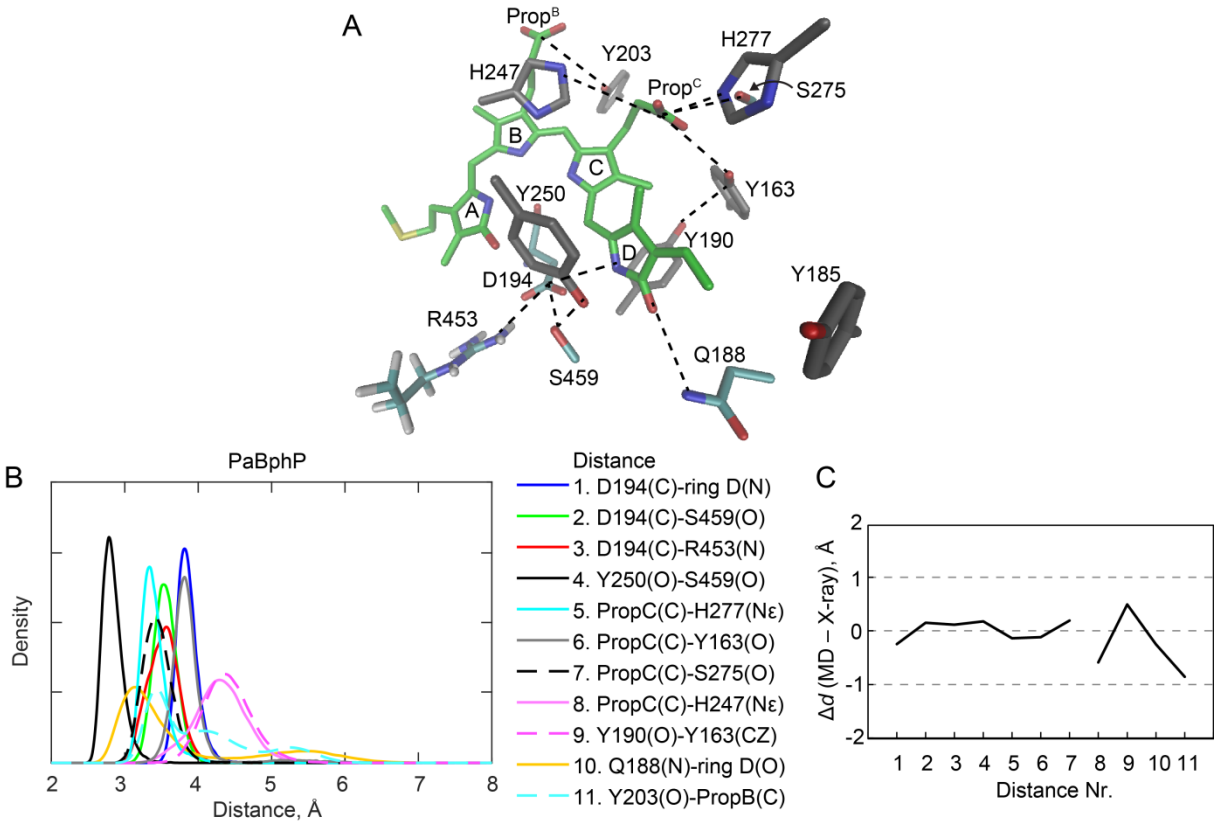

Figure 3.56. Distances in the active site of the PaBphP model. A) Measured distances between non-hydrogen atoms. B) Distributions of all measured distances over the last 70 ns of 100 ns MD simulation. C) Differences (Δd) between the distribution maxima of the distances in PaBphP model (MD) and the distances in the X-ray crystal structure of PaBphP (X-ray). The numbering is according to the protein sequence.

Deviations of the interactions in the active site of the PaBphP model from its X-ray crystal structure (40) were evaluated (Figure 3.56 C). The maximum value of the distribution of a particular measured distance in the simulated model was compared to the distance in the crystal structure. The two groups of distributions were analyzed: with small bandwidths and with larger bandwidths or even multimodal distributions. In the

simulated PaBphP model, the distribution maxima of measured distances are very similar to the crystal-structure distances and do not deviate more than 0.9 Å. The largest deviations were found for the distances of the second group, distributions with larger bandwidths or multimodal distributions.

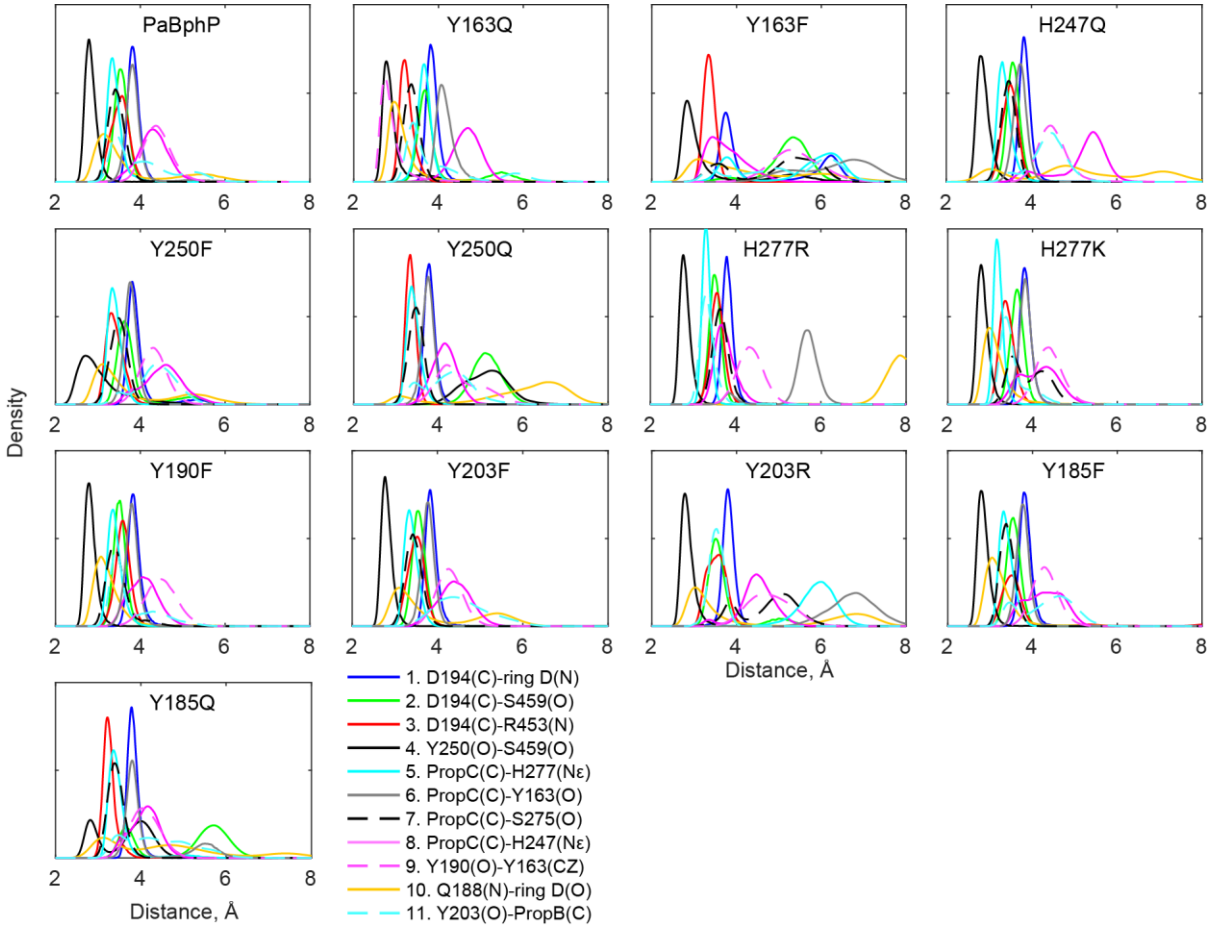

Figure 3.57. Distance distributions in the active site of PaBphP and its mutant models measured over the last 70 ns of 100 ns MD simulation. In case of mutated residues, the distances were measured to the specific atoms of all residues of a certain type: HZ of Phe and N of Gln, Lys or Arg as shown in Appendix A. The numbering is according to the protein sequence.

In the simulated PaBphP mutant models, the same distances in the active site were analyzed and distributions were plotted and grouped the same way as for the wild-type model (Figure 3.57). In case of the mutated residues, the distances were measured to the specific atoms of all residues of a certain type: HZ of Phe and N of Gln, Lys or Arg (atom names are shown in Appendix A). The distribution maximum of every measured distance in the PaBphP mutant models was compared to the distance in the crystal structure of PaBphP (Figure 3.58), similarly as described above for the PaBphP model. The mutant models with distribution maxima deviating less than 2 Å from the crystal-structure distances or from the distribution maxima in the PaBphP model were

considered as models with stable interactions. For every electron donor one tested mutation resulted in a model with stable interactions: Y163Q, Y185F, Y190F, Y203F, H247Q, Y250F, H277K (Table 3.29).

Similarly to the IFP2.0 mutants, tyrosine mutations to phenylalanine in PaBphP resulted in more stable active-site interactions than mutations to other residues. However, for the Y163 residue, mutation to glutamine resulted in a more stable active site than the mutation to phenylalanine. The histidine H247 mutation to glutamine and the histidine H277 mutation to lysine resulted also in stable active-site interactions.

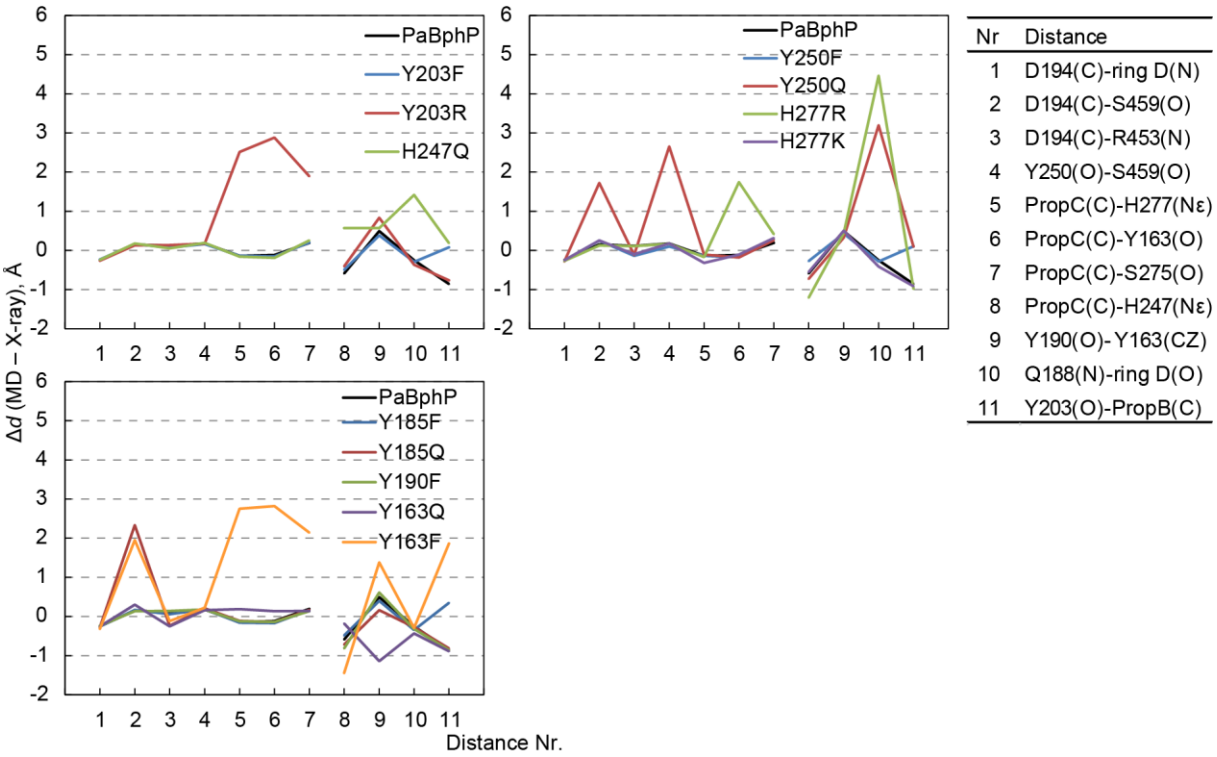

Figure 3.58. Distances in the active site of PaBphP and its mutants models. Differences (Δd) between the distribution maxima of the distances in PaBphP or its mutant models (MD) and the distances in the X-ray crystal structure of PaBphP (X-ray). In case of mutated residues, the distances were measured to the specific atoms of all residues of a certain type: HZ of Phe and N of Gln, Lys or Arg) as shown in Appendix A. The numbering is according to the protein sequence.

Table 3.29. PaBphP mutant models with stable interactions in the active site. The numbering is according to the protein sequence.

Residue	Mutation
Y163	Q
Y190	F
Y185	F
Y203	F
Y250	F
H247	Q
H277	K

3.3.5.4 Chromophore dynamics in IFP 2.0, PaBphP and their mutants

Chromophore dynamics have an influence on the fluorescence properties of the protein: a more planar chromophore leads to a larger fluorescence quantum yield due to larger oscillator strength and a thus larger fluorescence rate constant (181, 182). Based on MD simulations, Field and co-workers proposed that in IFP2.0 as well as in other DrBphP fluorescent variants, the enhancement of fluorescent properties is likely due to improved planarity of the chromophore, especially between ring A and B (180). To study how this observation correlates with the dynamics of the models analyzed in this section, the dihedral angles between adjacent rings of biliverdin were determined in IFP2.0, PaBphP and their mutant models (Figure 3.59 and Appendix Figures C.22-C.23). In total six dihedral angles were analyzed: a pair of two dihedral angles for each methine bridge, between rings A and B, rings B and C, as well as rings C and D. The distributions of all dihedral angles had small bandwidths corresponding to a rather rigid structure of the biliverdin. It was analyzed how much the distribution maximum deviates from the value of zero degrees: the larger was the deviation the less planar was the biliverdin. The deviations of every measured dihedral angle were compared between the template (IFP2.0 or PaBphP) and its mutant models by plotting the difference ($\Delta\chi$) of how much the distribution maximum of a dihedral angle deviated from the 0-degree value in mutant and template models (Figure 3.59). Therefore, a negative $\Delta\chi$ value in the plot corresponds to a smaller deviation of the distribution maximum from the 0-degree value in the mutant model compared to the template model and indicates a more planar biliverdin geometry in the mutant model. The dihedral angles in the MD simulations depend on the force field parameters, facilitating a rather planar structure of the biliverdin. Since in this study the same parameters were used for all template and mutant protein models, it was assumed that differences in the dihedral angle distributions originate from variations in the active-site interactions.

In the IFP2.0 mutant models the majority of the dihedral angles deviated from the 0-degree value less than in the IFP2.0 model, therefore biliverdin was more planar in the mutant models (Figure 3.59, left panel). Dihedral angles between ring A and B are more planar in the mutant models than in the IFP2.0 model, except the dihedral AB1 which is insignificantly larger in the Y216R mutant than in the IFP2.0 model. In the Y216R and

Y216S mutant models, the dihedral angle BC2 deviated from the 0-degree value more than in the IFP2.0 model (by more than 5 degrees). The larger deviation of this dihedral angle correlated with the unstable PropC-S272 interactions in these two mutants, suggesting that the loss of these interactions together with changes of other interactions might induce the biliverdin flexibility and less planar structure between rings B and C. The sum of the six distribution maxima differences between mutant and template models had a negative value for all IFP2.0 mutant models (Figure 3.59, right panel) indicating that distribution maxima deviated from the 0-degree value less in the mutant models than in the IFP2.0 model and overall planarity of the biliverdin geometry is larger in the mutant models than in the IF2.0 model.

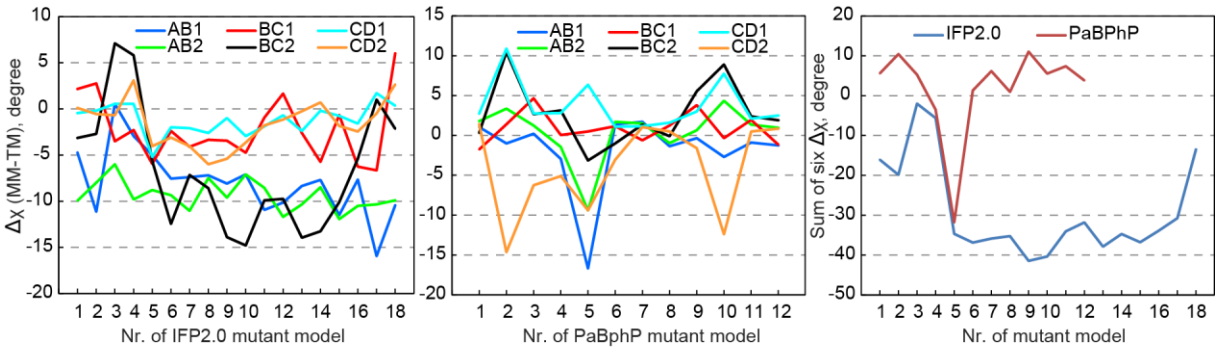

Nr.	IFP2.0 mutant
1	Y216Q
2	Y216F
3	Y216R
4	Y216S
5	H260Q
6	Y263F
7	Y263Q
8	Y263T
9	H290Q

Nr.	IFP2.0 mutant
10	Y198F
11	Y198Q
12	Y198T
13	Y176F
14	Y176Q
15	Y263F-H290Q
16	3-mutant
17	6-mutant (Y176F)
18	6-mutant (Y176Q)

Nr.	PaBphP mutant
1	Y163Q
2	Y163F
3	H247Q
4	Y250F
5	Y250Q
6	H277R
7	H277K
8	Y190F
9	Y203F
10	Y203R
11	Y185F
12	Y185Q

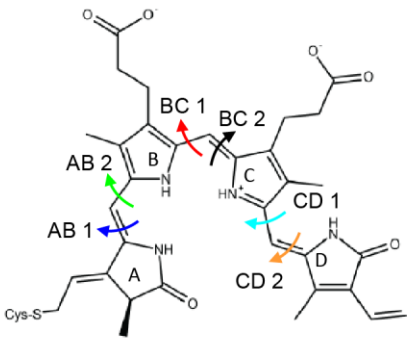

Figure 3.59. Dihedral angles (χ) in IFP2.0 and PaBphP and their mutant models. Differences (Δχ) between distribution maxima (its deviation from the 0-degree value) of dihedral angles in mutant models (MM) and in the template model (TM) of IFP2.0 (left) and PaBphP (middle). Δχ>0 indicates that the distribution maximum of χ deviates from the 0-degree value more in the mutant than in the template model. The sum of the six distribution maxima differences (corresponding to AB1, AB2, BC1, BC2, CD1, CD2 dihedral angles) between mutant and template models (right). The triple mutant "3-mutant"contains H260Q, Y263F, H290Q, sextuple mutants contain Y198F, Y216F, H260Q, Y263F, H290Q and Y176F or Y176Q in "6-mutant(Y176F)" and "6-mutat(Y176Q)" models, respectively. Arrows indicate rotations around central bonds of the specified dihedral angles in the chromophore. All dihedral angles were measured by defining atoms N-C-C-C except dihedral angles CD1 in IFP2.0 and CD1 and CD2 in PaBphP, which were defined by atoms N-C-C-H. Distributions of all dihedral angles are shown in Appendix Figures C.22-C.23.

A similar analysis of the biliverdin dihedral angles was done in the PaBphP and its mutant models (Figure 3.59, middle panel). In most of the PaBphP mutant models the dihedral angles AB1 and CD2 deviated from the 0-degree value less than the respective dihedrals in the PaBphP model. Conversely, the dihedral angles BC1, BC2 and CD1 deviated from the 0-degree value in most mutant models more than in the PaBphP model. The dihedral angle AB2 in some mutant models varied more (but not more than by two degrees except two models) in some less from the 0-degree value than the same angle in the PaBphP model. This analysis indicated that in most of the mutant models the biliverdin planarity between rings A and B increased or remained similar and between rings B and C decreased as compared to the biliverdin planarity in the template model. The largest deviations of the dihedral angles were observed for the mutant models T250Q, Y163F and Y203R. In the Y250Q mutant model, most of the dihedral angles deviated from the 0-degree value less than in the PaBphP model and resulted in a more planar biliverdin geometry. However in the Y163F and Y203R mutant models, the dihedral angles BC2 and CD1 deviated more and CD2 deviated less from the 0-degree value than in the PaBphP models and resulted in less planar biliverdin geometry. These three mutants had more deviating distributions of the active-site distances as compared to the PaBphP model. Reduced biliverdin planarity between rings B and C in Y163F and Y203R mutants correlated with the loss of the PropC-Y163 interaction. The sum of the six distribution maxima differences between mutant and template models had a positive value in most mutant models except the Y250F/Q mutant models, indicating that the majority of the PaBphP mutants have an overall less planar tetrapyrrole.

Altogether, the dihedral angle analysis suggests that the overall planarity of the biliverdin is increased in the IFP2.0 mutant models, whereas in the majority of the PaBphP mutant models it is decreased. The loss of some interactions in the active site, such as between PropC and serine or tyrosine, might lead to changes in the hydrogen-bonding interactions resulting in decreased planarity between rings B and C and reduce the overall biliverdin planarity which might result in lower fluorescence quantum yield. In the majority of the IFP2.0 and PaBphP mutants, the dihedral angles AB1 and AB2 deviated from the 0-degree value more or similarly as in the respective template models. The differences of the AB1 and AB2 dihedral angles between template and mutant models suggested an

increased biliverdin planarity between rings A and B in the mutant models, especially the mutants of IFP2.0. The obtained results of the biliverdin dihedral angle analysis indicate that fluorescence is expected to be increased in the studied mutant models of IFP2.0 and slightly increased or of similar extend in the studied mutant models of PaBphP.

4 Discussion

The aim of this thesis was to elucidate the molecular mechanisms of spectral tuning and excited-state decay in phytochrome photoreceptors. The spectral red shift of the Pfr-state phytochrome was discovered to be induced by the interactions between a linear tetrapyrrole chromophore and a protein residue. It was determined how the red-shifting interactions depend on dynamics of other interactions in the active site. The molecular mechanism of the tetrapyrrole deprotonation in the active site and consequent spectral blue shift was investigated and suggested as an explanation for the Q-band blue shoulder in the Pr-state absorption spectrum. For the first time electron donors and the respective charge transfer states were characterized in phytochromes. The pathways of the electron transfer coupled to proton transfer and their role for the excited-state decay are discussed. Moreover, the contributions of the electron donor residues to the fluorescence quenching and Lumi-R photoproduct formation are predicted and thus the strategies to improve phytochrome-based molecular tools are suggested.

4.1 Spectral tuning in phytochromes

4.1.1 Tetrapyrrole interactions causing the red shift of the Pfr state spectrum in phytochromes

The quantum chemical calculations of the phytochrome active-site cluster models enabled to uncover the molecular origin of the spectral tuning between phytochrome Pr and Pfr states. The spectral properties of both states were computed using the highly accurate and efficient state-of-the-art multi-configurational multi-reference XMCQDPT2 method (161). This method has already been applied to compute excited-state energies of other photoreceptors such as rhodopsin, BLUF, cryptochrome, DNA (6-4) photolyase (183-186) but has never been used for phytochrome calculations. So far, the excited-state properties of phytochromes and their tetrapyrrole chromophores were mostly computed (67, 68, 87, 88, 103, 105-107) with the widely-used TD-DFT method (187, 188), which is a single-electron excitation method. Therefore, the latter method cannot model multielectron excitations, in addition to its major limitation, namely its underestimation of the charge transfer state energies (189, 190). It was reported that the Q band in the

computed TD-DFT spectra of linear tetrapyrroles is contributed by a single-electron excitation HOMO-LUMO, whereas the higher-energy Soret band, computations of which are usually not discussed in the literature, is comprised of multiple states with high oscillator strengths (68, 107). However, the herein computed XMCQDPT2 spectra indicate that the Soret band includes multielectron excitations. The computed XMCQDPT2 spectra of the active-site models, representing phytochromes in the Pr and Pfr state, are in good agreement with the experimental spectra (30, 33, 41). The spectral red shift in the Pfr state was computed for both the Q and Soret bands. Furthermore, computed spectra of the plant phytochrome (AtPhyB) models are blue-shifted with respect to the bacterial phytochrome (DrBphP, PaBphP) models, in a similar way as it was observed in experimentally obtained spectra (14, 30, 33, 41). The spectral red shift of the Pfr state was computed for the first time. In addition to the calculations with the highly accurate XMCQDPT2 method, the shift was also computed with the TD-DFT and CIS methods. Although the latter methods result in blue-shifted spectra similarly as presented in the literature (87, 103, 104, 106), they might also be used to evaluate the spectral shifts of the Q band.

The spectral properties of phytochromes originate from the absorption of their linear tetrapyrrole chromophore, which undergoes double-bond isomerization and is present in different configurations of the C15=C16 double bond in the Pr and Pfr states. In the tetrapyrrole calculations without protein environment, the spectra of the isomers differ by not more than 0.04 eV for the biliverdin and 0.06 eV for the phytochromobilin tetrapyrroles. In contrast, the experimental absorption spectra between the Pr and Pfr states of the phytochrome proteins differ by 0.12 eV (30, 33, 41). These findings indicate that the chromophore isomerization from 15Z to 15E does not induce the significant red shift. In previous computational studies, it was also demonstrated that the chromophore isomerization is not sufficient to obtain the spectral shift observed in the Pfr-state phytochromes (104, 105, 108). It is expected that the chromophore interactions with the active site are important for the spectral properties. The QM/MM calculations of the Pr-state DrBphP phytochrome CBD domain reproduce the experimental spectrum but with a slight blue shift (of at least 0.1 eV) (106), whereas there are no such calculations for the Pfr-state phytochrome in the literature. In this thesis, the interactions in the active site

were characterized by the quantum mechanical (QM) cluster models that are significantly larger than the QM part of the QM/MM calculations, which usually contains only the chromophore. The representation of the active-site interactions by the cluster models enabled the reproduction of spectral properties of the phytochrome proteins.

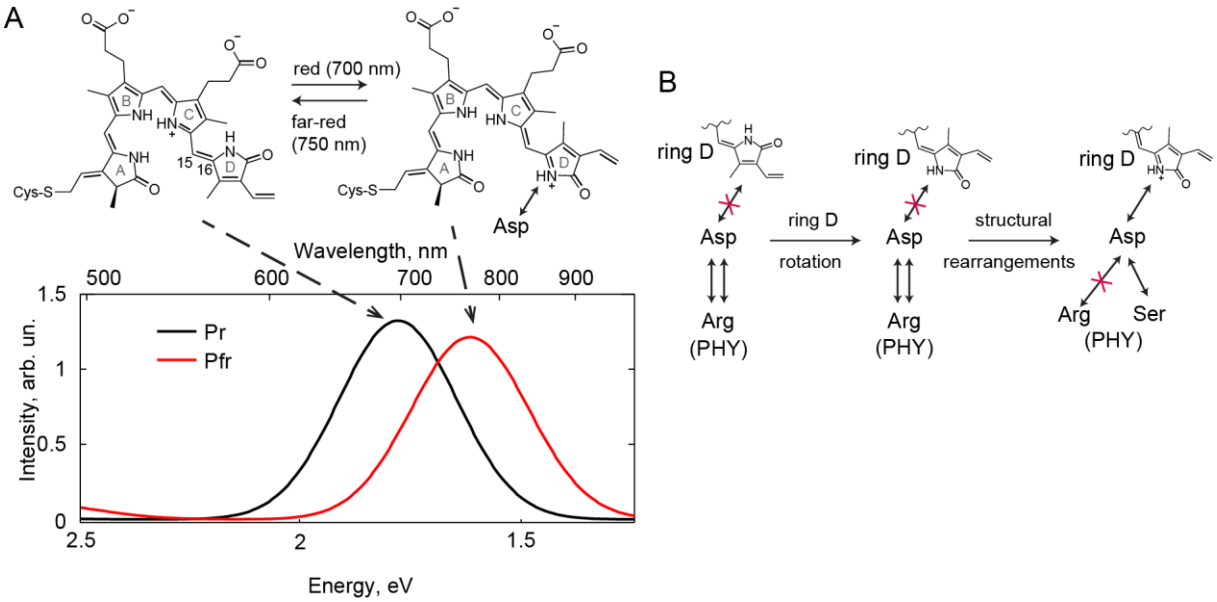

Figure 4.1. Molecular mechanism of the spectral red shift in the phytochrome Pfr state. A) Tetrapyrrole resonance structures leading to Pr and Pfr state spectra. The structure with the positive charge on ring D is promoted by its interactions with the highly conserved aspartate (D207 in DrBphP) B) Role of the PHY domain tongue: aspartate-arginine interactions in the Pr state prevent premature formation of the red-shifting aspartate-ring D interactions.

The results demonstrated that the spectral shift between the Pr and Pfr states is induced by different interactions in the active site, which are enabled by different tetrapyrrole chromophore isomers. In the Pr state the tetrapyrrole ring D interacts with the conserved histidine H290 (according to DrBphP sequence) (12, 32, 45), whereas in the Pfr state the rotated ring D interacts with the highly conserved aspartate D207 (47, 48). This specific Pfr-state interaction of the NH group of ring D with the negatively charged carboxylate of the aspartate changes the tetrapyrrole geometry and charge distribution such that the resonance structure with the positive charge on ring D contributes more than in the Pr state. The larger contribution of this resonance structure leads to the red shift in the Pfr state (Figure 4.1). The results indicate that upon the double-bond isomerization and red-shifting bond formation the positive charge from rings A-B-C is partially shifted to ring D. The changes of the tetrapyrrole geometry in the Pfr state indicate that the conjugation of the tetrapyrrole π-electron system increases, especially between rings C and

D, a finding which is consistent with an NMR study performed on a cyanobacterial phytochrome in the Pr and Pfr states (191). The anionic carboxylate of the aspartate stabilizes the positive charge on ring D. Therefore, the changes of the tetrapyrrole geometry would not take place and the spectral red shift would be absent without the aspartate-ring D hydrogen bond formation. Moreover, mutagenesis studies showed that a point mutation of this conserved aspartate such as D207A results in a complete loss of the red-shifted Pfr-state spectrum, and it was suggested that the aspartate is crucial for the Pfr state formation (30, 37, 40). However, the formation of the functional signaling Pfr state in the D207A mutant cannot be excluded based only on absorption spectroscopy. The results obtained herein indicate that the significant spectral red shift should not occur even if the signaling Pfr state forms in this mutant. Thus without the aspartate D207 presence in the protein, the Pfr state cannot be detected spectroscopically. In summary, this thesis demonstrates that the tetrapyrrole ring D-aspartate interactions in the Pfr-state phytochrome induce changes in the tetrapyrrole electronic structure that result in the spectral red shift.

The distance representing the red-shifting hydrogen bond between the highly conserved aspartate D207 and ring D in the Pfr-state cluster models is short, whereas in the X-ray crystal structures (38, 40) used to prepare these models, the respective distances are slightly longer (as shown in Section 3.1.8, Figure 3.18). However, the higher resolution (2.55 Å) X-ray crystal structure of the bathy PaBphP phytochrome (100) shows shorter D207-ring D distance which is rather similar to the distance in the computed models. The higher resolution structures of the Pfr-state phytochromes might help to uncover more exact distances including the red-shifting hydrogen bond. The MD simulations of the Pfr-state phytochromes in this thesis and in the literature (192) showed a stable formation of this hydrogen bond. The hydrogen-deuterium exchange experiments also indicate the presence of a strong hydrogen bond between D207 and ring D in phytochrome (179). These observations together with the presented results are hinting at the presence of the hydrogen bond between the aspartate and ring D in the Pfr-state phytochromes and its role in the red shift of the spectrum.

To address the active-site dynamics in the phytochrome Pr and Pfr states and how it influences the stability of the red-shifting ring D-aspartate interaction, an MD study was

performed. Since the phytochrome active site contains two titratable groups (histidines H260 and H290 according to the DrBphP sequence), it was investigated how their protonation states influence the stability of the active-site interactions. It was observed that H260 should be neutral (Nε-H) and H290 should be protonated when simulated using the CHARMM force field in order to preserve crystal-structure interactions in the active site of the CBD-PHY domain models with bound protonated tetrapyrrole. Otherwise, the interactions with the pyrrole water molecule, the Pr-state D207-Y263 interactions, the Pfr-state PropC-H290 interactions or other interactions become destabilized. However, when the protein was simulated using the AMBER force field, these interactions were not reported to be destabilized with neutral H290 (192). It is possible that MD simulations of phytochromes using the CHARMM and AMBER force fields are different due to different force field parameters i. e. charges and force constants. The H290 protonation state significantly affected the active-site dynamics but the effect on the computed spectra of the active-site cluster models was not significant. In addition to the histidines protonation state effects, the MD simulations also showed that the presence of the PHY domain stabilizes the active site, since interactions were more flexible in the models consisting only of the CBD domain.

Although the chromophore double-bond isomerization occurs on the picosecond timescale, the Pfr-state signal appears only on the millisecond timescale (115, 117) indicating that the formation of the ring D-aspartate interactions does not occur immediately after the double-bond isomerization and the ring D rotation. The MD simulations presented in this thesis illustrate that the aspartate-ring D hydrogen bond does not form directly after the tetrapyrrole isomerization and the ring D rotation, at least not during 80 ns of the simulation. This indicates that other structural changes are necessary to induce the formation of the red-shifting bond. Removing the conserved aspartate-arginine interactions by truncation of the PHY domain in the simulated model facilitated partial formation of the aspartate-ring D bond and enhanced other interactions typical for the Pfr state such as PropC-H290 and a flip of tyrosine Y176 from ring D to PropC. This suggests that the conserved aspartate (CBD) - arginine (PHY) interactions, present in the Pr state, might disable aspartate interactions with ring D before other structural changes happen. In the recent MD study it was shown that, upon the force-

probe simulation of the phytochrome model with rotated ring D, the aspartate-arginine interactions are weakened, since these residues interact only via one hydrogen bond and two new hydrogen bonds are formed: aspartate-ring D (NH group) and arginine-ring D (CO group) (192). Such a structure was proposed to represent the Lumi-R photoproduct (192), which is observed in the transient absorption spectra with a maximum at a slightly higher wavelength than the Q-band maximum of the Pr-state phytochrome (47, 122). These observation are in line with the following hypothesis that is based on the presented MD simulation results: in order to form the red-shifting aspartate-ring D hydrogen bond the conserved aspartate-arginine interactions should become destabilized.

The simulations demonstrated that the aspartate-ring D interactions are stable under the presence of aspartate interactions with the highly conserved serine of the PHY-domain tongue, hinting at the crucial role of the serine in stabilizing the aspartate-ring D interactions (Section 3.1.8). This correlates with the UV/visible spectroscopy experiments showing that the Pfr-state formation is restricted by mutations of the aspartate or serine as well as in the truncated phytochrome, which lacks the PHY domain (37, 40). Therefore, the MD study illustrates the importance of the active-site dynamics, including the CBD-PHY domain interactions, for the phytochrome photoswitching function. It also demonstrates that the formation of the red-shifting aspartate-ring D hydrogen bond is highly dependent on other active-site interactions such as aspartate-serine.

The understanding of how spectral red shift of the Pfr-state phytochrome is formed opens up opportunities to create molecular tools with the red-shifted spectrum. The significance of the aspartate-tetrapyrrole hydrogen bond stabilization for the shift formation suggests that either the PHY domain should remain in the engineered tools or a CBD domain should be modified to mimic the stabilization of the aspartate interactions in the Pfr state provided by the tongue of the PHY domain. However, it is possible that the Pfr-state stability is limited by the tetrapyrrole isomerization. Therefore, further studies on Pfr state stabilization and on controlling the double-bond isomerization in tetrapyrroles should be performed.

4.1.2 Tetrapyrrole deprotonation causing the blue shoulder of the Q band in the Pr state

In Pr state phytochromes, the absorption spectrum features a blue shoulder of the Q band (Figure 4.2 A). The shoulder was shown to be sensitive to changes such as pH and temperature (62, 65, 66, 69, 92). Decreased intensity of the Q band at high pH was interpreted as tetrapyrrole deprotonation (66, 69), whereas computations of deprotonated tetrapyrrole predicted its blue shift (67, 68). Therefore, in this thesis the tetrapyrrole deprotonation in the phytochrome active site was studied to obtain insights into its contribution to the Q band absorption.

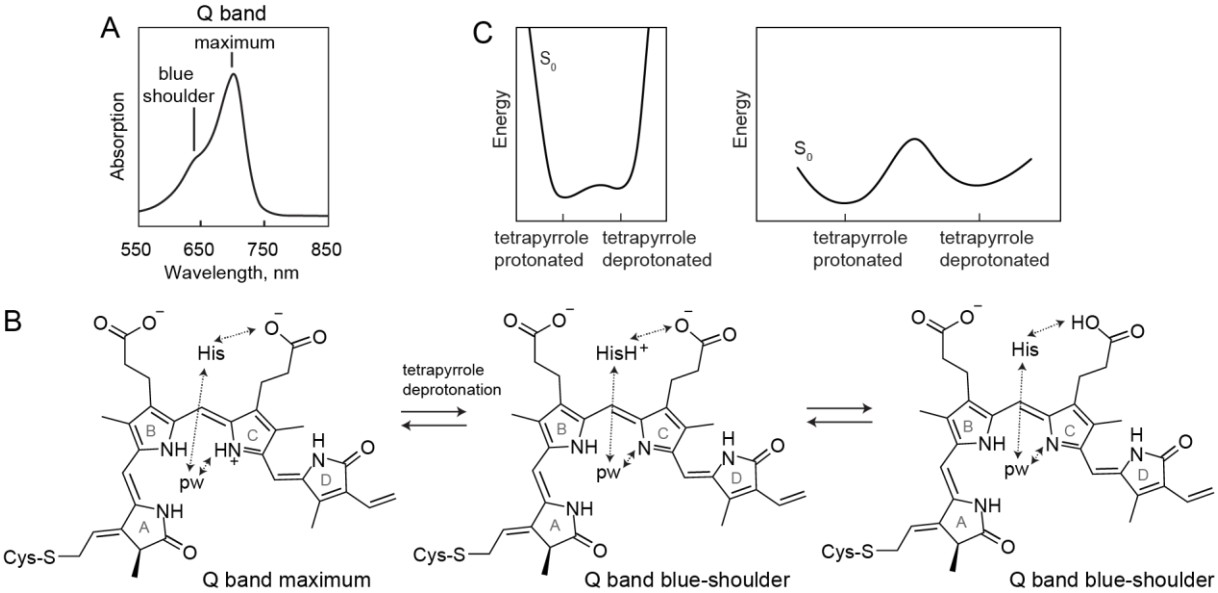

Figure 4.2. Tetrapyrrole deprotonation in the phytochrome Pr state leads to absorption at the Q-band blue shoulder. A) Q band in the absorption spectrum of the Pr-state DrBphP phytochrome (adapted from Wagner et al. (30)). B) Molecular mechanism of the tetrapyrrole ring C deprotonation by the pyrrole water (pw) molecule and the highly conserved histidine (H260 in DrBphP) C) Proton transfer results in a transition between two ground states (right) or in a ground state splitting into a double-well potential (left).

Quantum chemical calculations presented in this thesis illustrate energetics of a possible mechanism of the tetrapyrrole deprotonation in phytochromes. The tetrapyrrole may donate its proton to a highly conserved histidine H260 via the pyrrole water molecule (Figure 4.2 B). The pyrrole ring of the histidine is located above the tetrapyrrole and is stacked with the tetrapyrrole rings B and C, especially ring C (32). Both ring B and ring C are hydrogen-bonded with the pyrrole water molecule (32), and resonance Raman spectroscopy indicates that the deprotonation occurs either at ring B or C (61). Computed absolute energies for the tetrapyrroles deprotonated at ring B and C are similar, which –

together with experimental observations – suggests that similar energies might be expected for both ring B and ring C deprotonation. The herein presented results on the tetrapyrrole intrinsic properties demonstrated that tetrapyrrole deprotonation at any of the rings induces a blue shift of the tetrapyrrole excitation spectrum which is consistent with tetrapyrrole calculations present in the literature (67, 68). In this thesis, the deprotonation of ring C was computed for the active-site cluster models, demonstrating that the biliverdin deprotonation (at ring C) leads to a spectral blue shift that was similar to previously discussed tetrapyrrole calculations. The computed blue shift might be assigned to the blue shoulder of the Q band in the Pr-state phytochrome spectrum (Figure 4.2 A-B). Therefore, the spectral signature of the Q band with its blue shoulder is interpreted as a sign of the presence of a phytochrome with protonated and neutral tetrapyrrole in the ground state.

In the literature, there is no agreement on the origin of the specific shape of the phytochrome's Q band, in particular the blue shoulder of the Q band. In numerous studies, the shoulder was interpreted as evidence for the heterogeneity of the ground state in phytochromes (74-76), which in some studies was pointed at being related to different protonation states of the tetrapyrrole (66, 69). However, one study suggests that the blue shoulder originates from the 0-2 vibronic absorption of the tetrapyrrole (73). The pH titrations of phytochromes (from pH ~6 to ~9-11) combined with UV/visible spectroscopy demonstrated that at higher pH the intensity of the Q band with its blue shoulder decreases and the ratio between the blue-shoulder intensity and the Q-band maximum intensity increases (62, 65, 66). The observed decrease of the Q band intensity was assigned to tetrapyrrole deprotonation (62, 65, 66), which would correspond to the decreased oscillator strength of the deprotonated tetrapyrrole as compared to the protonated tetrapyrrole. However, the assignment conflicts with the computations presented in this thesis and in the literature (67, 68), which show that the neutral deprotonated tetrapyrrole has a blue-shifted computed spectrum. Furthermore, the observed increase of the ratio between the blue-shoulder intensity and the Q-band maximum intensity at higher pH is not explained in the literature. Based on the results presented in this thesis, a pH-increase might induce the proton transfer from tetrapyrrole to H260 and result in a higher contribution of the phytochrome form with the neutral

tetrapyrrole. However, the reason for the Q-band intensity decrease at higher pH remains unclear. Recently, a study on phytochrome Cph1 from *Synechocystis* PCC6803 has demonstrated that at higher pH both the Q band and its shoulder blue-shifts, which the authors assigned to tetrapyrrole deprotonation (69). However, the observation contradicts previous findings on the same (69) and other phytochrome proteins (62, 65, 66) for which no blue shifts were observed. The reason for the different results in this phytochrome is unclear. Therefore, more investigations on the pH-dependent spectral properties and molecular structures of phytochromes are required.

The absolute energies of the active-site cluster models with protonated and neutral biliverdin were compared. The ground-state energy, computed with the PBE0 method, was lower in the model with protonated biliverdin by 0.67 kcal/mol. Such a low energy difference hints at the possibility that the phytochrome with both protonated and neutral biliverdin might be present in the ground state, whereas protonated biliverdin is expected to be more abundant. The energy similarity of both models indicates that there might be indeed a transition between two minima in the ground state, with protonated and neutral biliverdin, if the energy barrier between two states is low enough, or that there might be a ground state splitting in a double-well potential (Figure 4.2 C). The calculations demonstrated that the tetrapyrrole deprotonation at ring C induces changes of the bond length alternations, single bonds elongate and double bonds shorten. The similar effect, in particular C=C, C-C and C-N stretches, were reported as a signature of the 0-2 vibronic transition in phytochrome (73). The ratio between intensity of the Q band maximum and its shoulder does not change drastically upon pH titration (62, 65, 66). These observations indicate that a proton between tetrapyrrole and histidine is shared, which corresponds to a double-well potential.

How the proton transfer from tetrapyrrole ring C to H260 influences the active-site dynamics was investigated by the MD study. So far, the MD studies addressing protein dynamics in the Pr and Pfr state, deciphering solution X-ray scattering data and structural changes during photoactivation were performed by simulating phytochrome with protonated tetrapyrrole (34, 35, 170, 192, 193). In the study addressing the relation between biliverdin planarity and phytochrome fluorescence, the simulations with both protonated and neutral (deprotonated at ring B) biliverdin were carried out on the CBD

domain variants and indicated no major differences in their dynamics (180). The force field parameters for the biliverdin deprotonated at ring C, which were used in this thesis, were prepared based on the parameters of the protonated tetrapyrrole by changing only the atomic charges without reparametrizing the force constants. The dynamics of the CBD domain with protonated and deprotonated tetrapyrrole at ring C are similar, especially regarding the accessibility of the pyrrole water region by bulk water, which agrees with the results published on CBD domain variants with protonated and deprotonated (at ring B) biliverdin (180). However, the dynamics of the CBD-PHY domains showed that the stability of the active-site interactions might depend on the charge distribution on neutral tetrapyrrole. The most sensitive interactions were associated with the Y263 residue: its interactions with D207 were weakened but became stronger with biliverdin ring D and R466 upon the biliverdin deprotonation at ring C. However, results with particular parameters of the atomic charges suggest no significant differences in the hydrogen-bonding network with protonated and neutral (deprotonated at ring C) biliverdin in the Pr-state CBD and CBD-PHY domains. A change of the protonation states of H260 or H290 in the protein model might disturb interactions more significantly. Therefore, these results indicate that the Pr-state phytochrome existence with bound protonated and neutral biliverdin in the ground state would result in a similar hydrogen-bonding network in the active site.

In contrast to the Pr-state phytochrome, the simulations of the Pfr-state phytochrome with deprotonated biliverdin show less conservation of the interactions in the active site and induce disruption of typical Pfr-state hydrogen bonds such as the interactions of PropC and of the conserved serine of the PHY-domain tongue. The lower stability of the hydrogen-bonding network in the Pfr-state models during MD simulations hints at the possibility of the tetrapyrrole deprotonation being involved in thermal conversion of the Pfr state back into the Pr state. However, how this may be involved together with the keto-enol tautomerization of ring D, which has been proposed as controlling the thermal conversion (179), should be further studied. Interestingly, the quantum-chemical calculations presented in this thesis suggest that the proton transfer from tetrapyrrole rings A-B-C is less likely to occur in the Pfr state as compared to the Pr state because of the charge re-distribution on protonated tetrapyrrole in the Pr and Pfr states (as described

in Section 3.1.6). In the Pfr-state phytochrome, the positive charge is shifted to ring D, therefore the proton on ring C is less acidic and cannot be transferred to H260 as easily as in the Pr state. The signature of the proton transfer between tetrapyrrole and histidine is observed as a Q-band blue shoulder in the Pr-state phytochrome spectrum. However, this process may also lead to low efficiency of the phytochrome photoswitching since it was predicted that double-bond isomerization is less favorable in neutral tetrapyrrole as compared to protonated tetrapyrrole (86, 87).

Additionally, phytochromes may also undergo (de)protonation reactions involving tetrapyrrole in the excited state. Based on transient absorption and fluorescence data, Kennis and co-workers suggested the ESPT (excited state proton transfer), in particular a proton transfer from the protonated tetrapyrrole to the backbone carbonyl group oxygen of the conserved aspartate (122). However, carbonyl protonation is energetically unfavorable. The herein presented XMCQDPT2 calculations indicate that the proton transfer from tetrapyrrole to H260 via the pyrrole water molecule may happen in the excited state. This is suggested by the lower S_1-state energy (by 1.63 kcal/mol) in the active-site model with neutral biliverdin as compared to the model with protonated biliverdin. According to the calculations, the biliverdin deprotonation in the excited state should result in an emission spectrum blue-shifted by ~0.2 eV. In the emission spectrum of the engineered phytochrome-based GAF-FP protein, no change of the Q band shape upon pH increase was observed but its intensity decreased, however the excitation spectrum of this protein also showed only the Q-band intensity decrease but not the change of its shape (92). Therefore, it is not clear how the shape change of the emission band correlates with the shape change of the absorption band upon pH titrations. To better understand how the tetrapyrrole (de)protonation in the phytochrome active site influences the Q-band shape in the absorption and emission spectra as well as the excited-state dynamics, further experiments in different conditions should be performed. Interestingly, the Stokes shifts are predicted to be larger for the neutral biliverdin as compared to the protonated one, which can be employed for engineering fluorescent markers with a large excitation-emission difference to overcome the current limitation of phytochrome-based markers (23).

4.2 Excited-state decay contributed by charge transfer state reactions

4.2.1 Charge transfer states, their evolution and detection

The herein presented quantum chemical calculations show that the low-lying excited states in phytochromes include not only locally excited states of the tetrapyrrole but also the CT states, which are dark states and are not visible in the absorption spectrum. The excited states were computed with the XMCQDPT2 method (161) which was also used to calculate the CT states in other photoactive systems and showed that the energies are in agreement with experimental observations (184-186). This indicates a similar accuracy of the CT-state energies in phytochromes. Although the CT states do not contribute to the absorption spectrum, they influence the excited-state dynamics in phytochromes. Population of the CT states enables the charge transfer reactions that are electron transfer coupled to proton transfer and involve the electron donor residues tyrosine and histidine, which are characterized here for the first time in phytochromes.

Histidine H260 and tyrosine Y263 (according to the numbering in DrBphP) are highly conserved across the phytochrome photoreceptor family (46). They were shown to act as electron donors while the protonated tetrapyrrole acts as a good electron acceptor (Figure 4.3 A). The computed charge transfer reactions in phytochrome are the electron transfer from the electron donor residue to the excited tetrapyrrole, coupled with the proton transfer from the electron donor to a nearby-located anionic proton acceptor, such as the highly conserved aspartate D207 next to tyrosine Y263 or PropC next to histidine H260. The formed radical pair tetrapyrrole-tyrosine or tetrapyrrole-histidine is energetically stabilized and can undergo back charge transfer which is the recovery of either the ground (S_0) state or the locally excited (S_1) state (Figure 4.3 B). The charge transfer reactions leading to the ground-state recovery correspond to the internal conversion reactions, which are non-productive reactions and do not lead to the photoproduct formation. Optimization of the tetrapyrrole-H260 radical pair in the computed model led to changes of the hydrogen-bonding network in the active site, such as the weakening of the PropC interactions with serines. Thereby this resulted in new hydrogen-bond interactions in the S_1 state after its recovery. Therefore, the charge transfer reactions leading to the S_1-state recovery may participate in an equilibration of the CT and S_1 states, which may potentially lead to the Lumi-R photoproduct formation.

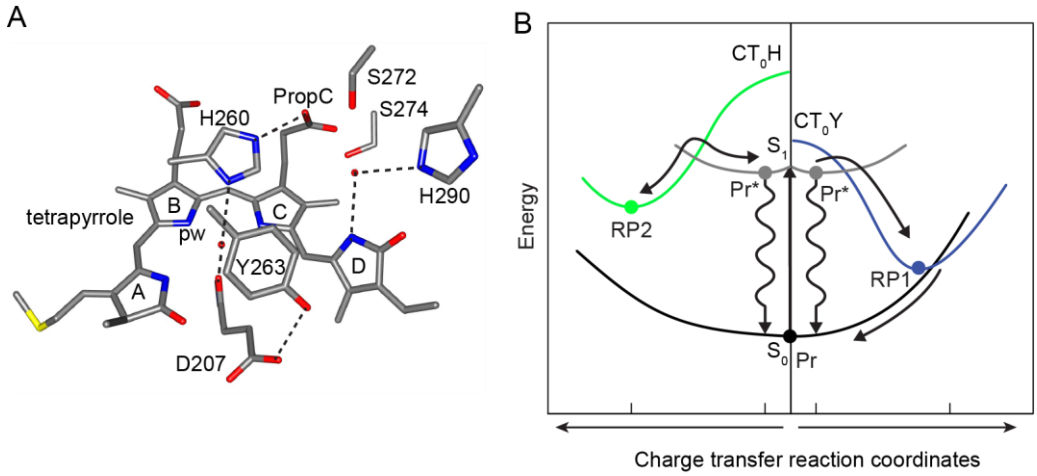

Figure 4.3. Charge transfer in phytochrome photoreceptors. A) Active site including H260 and Y263 donors (in DrBphP phytochrome). B) Charge transfer reactions, including Y263 and H260 electron donors with respective CT_0Y and CT_0H states. The resulting radical pairs (RP1 and RP2) lead to the ground(S_0)- or excited(S_1)-state recovery, respectively.

The evolution of the CT state, either recovery of the S_0 or the S_1 state, depends on the excited-state energies in the Franck-Condon region, which is the S_0-min geometry. In the computed DrBphP models, the CT_0Y state, which involves Y263 as electron donor, is close in energy to the S_1 state, whereas the CT_0H state, which involves H260 as electron donor, is ~1 eV higher. The stabilization in the CT_0Y or CT_0H state due to electron transfer coupled to proton transfer reduces the CT-state energies by a similar value. Therefore, at the respective optimized radical-pair geometries, the CT_0Y state is close in energy to the S_0 state, whereas the CT_0H state is significantly higher. Thence, the tetrapyrrole-Y263 radical pair undergoes the S_0-state recovery and the tetrapyrrole-H260 radical pair undergoes the S_1-state recovery. The small energy barrier for the S_0-state recovery from the tetrapyrrole-Y263 radical pair facilitates fast kinetics of this reaction. The energy barrier for the S_1-state recovery from the tetrapyrrole-H260 radical pair is larger, but since the system is trapped in the CT-state minimum, it undergoes this reaction even though with slower kinetics. This suggests that by tuning the CT-state energy at the ground-state geometry, in particular the S_1-CT_0 energy difference, it is possible to influence the evolution of the radical pair.

According to the calculated rates, the charge transfer reactions are ultrafast. Therefore, it can be predicted that the charge transfer reactions take place in phytochromes and compete with other excited-state energy dissipation pathways. The predicted fast kinetics of the radical pair formation and the ground-state recombination is ensured by low energy

barriers and high electronic couplings. In ultrafast transient absorption spectroscopy it was detected that there are intermediates forming on the femtosecond-picosecond timescale (47, 120-122, 124, 125). This is the same timescale as for the computed charge transfer reactions producing the radical pair intermediates, which suggests that they might be related to the experimentally observed excited-state dynamics. The computed excited-state energies indicate that radical pairs should absorb in the Q band region (CT_0-CT_2, CT_0-S_1 transitions) and in the near-infrared (NIR) region (CT_0-CT_1 transition), however the latter is usually not measured for phytochromes. A broad absorption band in the NIR region, which decays simultaneously as the band of the stimulated emission and the ground-state bleach, was observed in plant phytochrome and was assigned to the excited-state absorption (118). According to the calculations, the absorption of the radical pairs in the NIR region is indeed similar in energy to the excited-state absorption (S_1-CT_0H, S_1-CT_0Y, S_1-S_n transitions). In order to detect the radical pairs and characterize the charge transfer states experimentally, a complex analysis of the time-resolved absorption spectra should be pursued, taking into account multiple radical pair species. Analysis of the absorption in the NIR region should be less complicated than in the Q band region, where the absorption difference is contributed by the ground-state bleach and stimulated emission.

4.2.2 Effects of charge transfer pathways on fluorescence and Lumi-R photoproduct formation

The effects of the charge transfer reactions are observed experimentally by manipulating residues which take part in these reactions. Since charge transfer competes with fluorescence, photoproduct formation and other radiationless decay reactions, blocking the charge transfer pathway by mutating electron donor or proton acceptor leads to an extended excited-state lifetime and higher fluorescence quantum yield. Indeed the point mutations of the tyrosine (Y263F, Y263H, Y263S; according to the DrBphP numbering) and aspartate (D207H, D207A) residues in different phytochromes were shown to increase the fluorescence quantum yield and excited-state lifetime (30, 125, 128, 140). Calculations showed that the D207H mutation results in an increased CT_0Y energy which indicates a higher activation energy for the biliverdin-Y263 radical pair formation if the reorganization energy remains similar. Increased activation energy results in a slower rate

of the charge transfer reaction. Therefore, in the D207H mutant, the internal conversion via the S_0-state recovery from the CT_0Y state should be diminished and the S_1-state recovery should be more probable. Calculations on the models representing bacterial and plant phytochromes in the Pr and/or Pfr state indicate that multiple tyrosine and histidine residues in close proximity to the tetrapyrrole chromophore, also including the residues specific for each phytochrome protein in addition to the highly conserved H260 and Y263, might act as electron donors and block fluorescence by facilitating ultrafast charge transfer reactions. Other aromatic residues such as tyrosine Y276 in AtPhyB (corresponding to Y176 in DrBphP), are here suggested to act as electron donors, which is consistent with experimental observations showing that mutations of this tyrosine in plant and cyanobacterial phytochromes lead to increased fluorescence quantum yield (126, 127).

Experimental studies on bacterial phytochromes demonstrated that excited-state lifetime and quantum yield of the Lumi-R photoproduct formation increase in D_2O buffer as compared to H_2O buffer, which indicates that the excited-state decay rate is limited by proton-transfer processes (122, 128). Increased excited-state lifetime in the D207A mutant and the truncated CBD construct was explained by a reduced rate of ESPT (proton transfer from the tetrapyrrole to the backbone carbonyl group of D207) due to perturbation of the hydrogen-bonding network around the tetrapyrrole (128). However, the proposed ESPT mechanism does not provide an explanation why Lumi-R formation is increased in D_2O experiments but decreased in the D207A mutant and truncated CBD construct. It is unknown how the kinetic isotope effect influences the double-bond isomerization reaction, but experimental observations (128) hint at a dependence of the Lumi-R formation on proton-transfer including processes. Based on the computations, it might be concluded that the newly-found charge transfer reactions including electron donors may contribute to the ground-state recovery, i. e. internal conversion. An increased Lumi-R formation might indicate that the charge transfer reactions leading to internal conversion are slower; therefore, the excited state decays less through this channel but more through radiative decay and radiationless decay including the photoproduct formation. However, to clarify these pathways and how they contribute to the excited-state decay and Lumi-R formation, more experimental studies in D_2O and

extensive spectra analysis, especially in the NIR region where the radical pair-absorption is predicted, are required.

Experimental observations indicate that the charge transfer pathways might be important for the Lumi-R photoproduct formation. Mutants such as Y263F, D207H, D207A (according DrBphP sequence), in which the charge transfer is reduced, does not only show an increase of the excited-state lifetime but also a decrease of the Lumi-R quantum yield (123, 125, 128, 140). Therefore, this suggests that charge transfer reactions might be required for the Lumi-R formation. It was observed that the positive signal in the NIR region, where excited-state absorption is predicted, and the negative signal in the Q-band region, mostly contributed by ground-state bleach and stimulated emission, decay simultaneously (118). This suggests that the S_1 state and the species absorbing in the NIR region have the same lifetime. The calculations predict that the radical pair absorption contributes in the NIR region which, together with the experimental observations, suggests that the radical pairs do not exist longer than the S_1 excited state. This hints at an equilibrium between the CT and S_1 states which may indeed be present in phytochromes and may lead to the Lumi-R formation. This raises the question why charge transfer reactions are needed to proceed the double-bond isomerization. It might be that the change of the hydrogen-bonding network in the active site, required for the ring D rotation (117), is induced by charge transfer reactions which may result in a lowering of the energy barrier of the isomerization (Figure 4.4 A). The calculations demonstrated weaker hydrogen bonds in the radical pair geometries due to charge neutralization and even a change of interactions in the biliverdin-H260 radical pair; these interactions were preserved after the S_1-state recovery. Charge transfer reactions including multiple electron donors may induce changes of different hydrogen bonds. However, which electron donors are contributing to the phytochrome internal conversion and Lumi-R formation and how charge transfer states influence excited-state dynamics, should be further studied extensively in different mutants, in which electron donor or proton acceptors are manipulated.

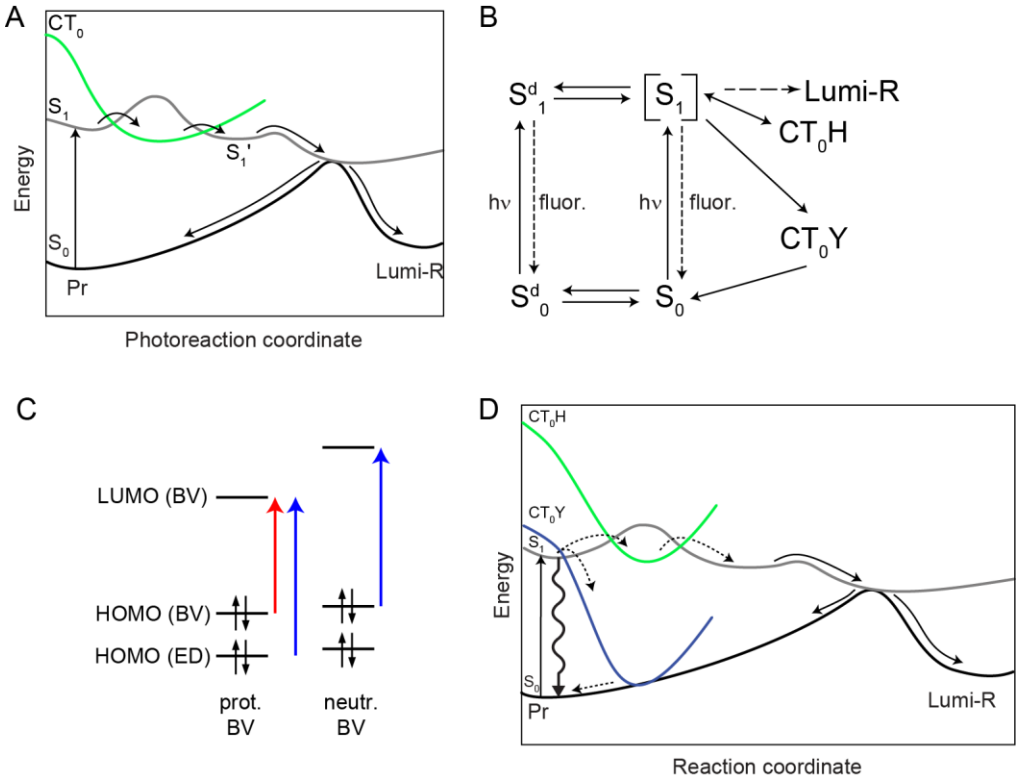

Figure 4.4. Charge transfer in phytochrome photoreceptors. A) CT states reduce the S_1-state barrier of the double bond isomerization. B) Scheme of the ground-state and excited-state reactions in phytochromes: the tetrapyrrole deprotonation in the ground and excited states (S^d_0, S^d_1) and charge transfer including states which equilibrate with the S_1 state (S_1 state with different variations of hydrogen-bonding interactions) or recover the S_0 state. C) Excitations at wavelengths corresponding to the Q band maximum (red) and its blue shoulder (blue) in the phytochrome with protonated and neutral tetrapyrrole. Excitations include HOMO and LUMO orbitals of the tetrapyrrole such as biliverdin (BV) and an electron donor (ED). D) Charge transfer reactions (dashed arrows) which contribute to internal conversion and Lumi-R photoproduct formation.

4.2.3 Excited-state decay contributed by the tetrapyrrole deprotonation and charge transfer states

The quantum chemical calculations demonstrated that CT states are present in phytochromes with different tetrapyrrole protonation states: protonated and neutral. The CT-state energies are significantly higher (by ~0.5 eV) in the model with neutral tetrapyrrole (deprotonated at ring C) in comparison to the model with protonated tetrapyrrole because the neutral tetrapyrrole is a worse electron acceptor. Based on the energy difference between the S_1 and CT_0 states in the Franck-Condon region, the activation energy of the charge transfer reactions is expected to be higher in the model with neutral biliverdin leading to slower rates. Therefore, it is expected that the charge transfer reactions will include rather the protonated tetrapyrrole as an electron acceptor. The S_1-state recovery from the CT state, which might result in an equilibration between

these states, thus leads to facilitation of the protonated tetrapyrrole in the excited state rather than of the neutral tetrapyrrole (Figure 4.4 B). Such reduction of the neutral tetrapyrrole fraction, by producing radical pairs and equilibrating the S_1 and CT states, might be useful for the photoproduct formation. The reason is that double-bond isomerization occurs in protonated tetrapyrrole since it has a lower energy barrier than in neutral tetrapyrrole (104). Thence, blocking the charge transfer reactions may increase the amount of the neutral tetrapyrrole, which might lead to an increase of internal conversion and a decrease of the Lumi-R formation.

In addition to higher barrier of the double-bond isomerization(86, 87) and presumably slower charge transfer rates in the active site containing neutral tetrapyrrole, the computed radiative lifetime is shorter in the model with neutral biliverdin (deprotonated at ring C) than in the model with protonated biliverdin. Therefore, the herein presented results suggest that fluorescence quantum yield might be increased not only by blocking the charge transfer reactions but also by stabilizing neutral tetrapyrrole in the active site.

The presented results suggest an explanation for the decreased Lumi-R quantum yield in phytochrome mutants, in which an electron donor or a proton acceptor is mutated. In such mutants the charge transfer is reduced and the equilibration of the CT and S_1 states might thus be reduced. This may lead to an increased formation of neutral tetrapyrrole, resulting in internal conversion rather than isomerization, to a larger barrier of the protonated tetrapyrrole's double-bond isomerization due to unchanged hydrogen bonds, or to both. The experimental observations hint at a complex excited-state dynamics in phytochromes. Spectroscopy experiments demonstrated that phytochrome excitation with different wavelengths, at around the Q-band maximum and at its blue shoulder, results in different excited-state dynamics (70, 121, 194, 195). Based on the herein presented calculations, it is proposed that different kinetics might be influenced by the direct excitation of the neutral tetrapyrrole-containing phytochrome resulting in different populations of phytochrome with protonated and neutral tetrapyrrole in the excited-state (Figure 4.4 C). Alternatively, excitation with a wavelength at the blue shoulder may also lead to a direct CT-state excitation and its immediate population which results in faster radical pair formation. Therefore, the wavelength-dependent kinetics in phytochromes

should be interpreted with caution and analyzed with taking into consideration both: the tetrapyrrole deprotonation and the charge transfer including electron donors.

Further investigations should be performed in order to clarify which electron donor-dependent charge transfer reactions contribute to the phytochrome internal conversion and which to the Lumi-R formation on the potential energy surface (Figure 4.4 D), how they contribute to reduced tetrapyrrole deprotonation, and how the tetrapyrrole deprotonation influences the reduced formation of Lumi-R. The mechanisms presented in this thesis will enable extended analyses of phytochrome kinetics in excitation wavelength- and pH-dependent studies and a more detailed understanding of the excited-state decay in phytochromes. Increasing the Lumi-R quantum yield by manipulating these pathways might be beneficial for the engineering of phytochrome-based optogenetic tools, whereas removing internal conversion pathways is beneficial for engineering fluorescent markers. However, large amounts of internal conversion pathways, leading to low yields of photoproduct formation, are crucial to maintain the phytochrome's biological function, which is not an immediate light-response but regulation of gene expression under durable light conditions (130). Additionally, internal conversion photoprotects the protein.

4.2.4 Electron donor mutations increasing fluorescence

Electron donors take part in the charge transfer reactions, which contribute to fluorescence quenching, therefore blocking of such reactions by mutating the electron donor or proton acceptor residues might be used to increase the fluorescence quantum yield and engineer fluorescent markers. The MD simulations demonstrated that there might be electron donor mutations, which do not significantly disturb the hydrogen-bonding network in the mutated phytochrome variants. Mutations of at least six potential electron donors were tested in IFP2.0, an engineered variant of DrBphP phytochrome with increased fluorescence (142), and PaBphP, a bathy phytochrome, which has a Pfr-state spectrum (40). The analysis of dihedral angles between pyrrole rings during the simulation time was performed similarly as suggested by Field and co-workers (180). The analysis indicated that the mutation-introduced changes of the hydrogen-bonding network around the tetrapyrrole such as disruption of PropC-serine or PropC-tyrosine correlate with the increased tetrapyrrole flexibility and reduced its planarity resulting in lower

fluorescence. Regarding mutations to phenylalanine, glutamine, serine and other residues, the ones preserving the most stable active-site interactions were the tyrosine mutations to phenylalanine and histidine mutations to glutamine. An exception was one tyrosine electron donor (Y176 according to the DrBphP numbering) whose mutation to glutamine resulted in a more stable active site. The tested mutations such as Y176Q, Y198F, Y216F, Y263/Q/T, H260, H290Q in IFP2.0 and Y163Q, Y190F, Y185F, Y203F, Y250F, H247Q, H277K in PaBphP suggest increased fluorescence and stable active-site interactions. Therefore, they may be introduced experimentally to test the predicted role of the electron donors in reducing the excited-state lifetime. Multiple electron donor mutations in IFP2.0 based on the MD results are predicted to preserve a hydrogen-bonding network in the active site that is similar to the IFP2.0 template, therefore this variant can be further mutated to increase fluorescence quantum yield. The specific electron donor mutation suggested in this thesis may be employed in order to improve fluorescence properties of rationally-designed phytochrome-based molecular tools.

5 Conclusions and Outlook

This computational study provides insights into molecular mechanisms of spectral tuning and excited-state energy dissipation pathways in phytochrome photoreceptors. The origin of the Pfr-state spectral red shift and the link between its formation and protein conformation switch was explained. The mechanism of the tetrapyrrole deprotonation in the phytochrome active site was suggested as a probable cause of the Q-band blue shoulder in the Pr-state absorption spectrum. It was shown that intramolecular or intermolecular transfer of the positive charge induces changes in tetrapyrrole geometry and its spectrum: shift of the positive charge from rings A-B-C to ring D induces a red shift, and intermolecular proton transfer from tetrapyrrole induces a blue shift. For the first time electron donors were identified in phytochromes. The electron donors take part in intermolecular photoinduced charge transfer which may contribute to photoproduct Lumi-R formation and internal conversion, which quenches fluorescence. These insights might be applied to further phytochrome studies and in rational design of phytochrome-based molecular tools such as fluorescent markers or optogenetic tools by tuning their absorption and emission properties as well as quantum yields.

Quantum chemical calculations of the active-site cluster models of bacterial and plant phytochromes in the Pr and Pfr states performed with the highly accurate XMCQDPT2 method reproduce experimental spectra. The Pfr state spectrum was computed for the first time which allowed uncovering the hydrogen bond between tetrapyrrole ring D and the highly conserved aspartate as an origin of the red-shifted spectrum. This study underlined the significance of the chromophore-protein interactions in the spectral tuning of phytochrome photoreceptors. Furthermore, the MD simulations indicated that after the tetrapyrrole ring D rotation, other structural changes, including the change of the interactions of the PHY domain tongue, should occur in order to enable the formation of the red-shifting hydrogen bond. This study is an initial step in uncovering how the spectral tuning is coupled to structural phytochrome rearrangements in order to maintain photoreceptor's functionality. This study suggests that the red-shifting aspartate-ring D hydrogen bond should be stabilized to preserve the red-shifted Pfr-state spectrum which can be employed in engineered molecular tools.

The spectral blue shift in the Pr-state phytochrome was demonstrated after proton transfer from tetrapyrrole to a conserved histidine (H260 in DrBphP) via the structurally conserved pyrrole water molecule. Hydrogen-bonding network showed similar dynamics in the Pr-state phytochrome with neutral and protonated tetrapyrrole. Here it is proposed that a phytochrome with neutral tetrapyrrole might contribute to the absorption at the Q-band blue shoulder in the Pr-state spectrum, the origin of which has been a point of debate in the literature. Additionally, such proton transfer may occur in the excited state and presumably might contribute to fluorescence quenching and reduced formation of the Lumi-R photoproduct. The herein presented tetrapyrrole (de)protonation mechanism will contribute to the assignment of phytochrome spectral signatures and to the analysis of excited-state dynamics.

This study shows for the first time that charge transfer states may contribute to the excited-state decay in phytochromes. Multiple tyrosine and histidine residues were identified as electron donors taking part in electron transfer coupled to proton transfer and resulting in the formation of radical pairs (tetrapyrrole-electron donor) which might be detected in the near-infrared region. Therefore, the detection window in spectroscopy experiments should be extended and the following analysis should contain more variables, i.e. species in order to characterize the complex processes in phytochromes. The formed radical pairs undergo backward charge transfer reactions resulting in the recovery of the ground state, which contributes to fluorescence quenching, or in the equilibration of the CT state with the excited state, which might contribute to the Lumi-R photoproduct formation. These findings lay the basis for further phytochrome studies which might provide a detailed mechanism how charge transfer reactions regulate the chromophore double-bond isomerization and phytochrome photoswitching.

Based on the herein presented MD study, the mutations of the electron donors with blocked charge transfer pathways and potentially increased fluorescence quantum yield are suggested and may be used for further improvements of fluorescence markers. Therefore, in addition to mechanistic insights about phytochrome photoreceptors, this comprehensive computational study also provides some indications facilitating the improvement of phytochrome-based molecular tools.

References

1. Van der Horst MA, Hellingwerf KJ. Photoreceptor proteins, "star actors of modern times": A review of the functional dynamics in the structure of representative members of six different photoreceptor families. Accounts Chem Res. 2004;37(1):13-20.
2. O'Banion CP, Lawrence DS. Optogenetics: A Primer for Chemists. Chembiochem. 2018;19(12):1201-16.
3. Kottke T, Xie A, Larsen DS, Hoff WD. Photoreceptors Take Charge: Emerging Principles for Light Sensing. Annu Rev Biophys. 2018.
4. Ortiz-Guerrero JM, Polanco MC, Murillo FJ, Padmanabhan S, Elias-Arnanz M. Light-dependent gene regulation by a coenzyme B-12-based photoreceptor. Proceedings of the National Academy of Sciences of the United States of America. 2011;108(18):7565-70.
5. Kutta RJ, Hardman SJO, Johannissen LO, Bellina B, Messiha HL, Ortiz-Guerrero JM, et al. The photochemical mechanism of a B-12-dependent photoreceptor protein. Nature communications. 2015;6.
6. Jost M, Fernandez-Zapata J, Polanco MC, Ortiz-Guerrero JM, Chen PYT, Kang G, et al. Structural basis for gene regulation by a B-12-dependent photoreceptor. Nature. 2015;526(7574):536-U167.
7. Wilson A, Punginelli C, Gall A, Bonetti C, Alexandre M, Routaboul JM, et al. A photoactive carotenoid protein acting as light intensity sensor. Proceedings of the National Academy of Sciences of the United States of America. 2008;105(33):12075-80.
8. Gong J, Yuan Y, Ward A, Kang L, Zhang B, Wu Z, et al. The C. elegans Taste Receptor Homolog LITE-1 Is a Photoreceptor. Cell. 2016;167(5):1252-63 e10.
9. Rizzini L, Favory JJ, Cloix C, Faggionato D, O'Hara A, Kaiserli E, et al. Perception of UV-B by the Arabidopsis UVR8 Protein. Science. 2011;332(6025):103-6.
10. Christie JM, Arvai AS, Baxter KJ, Heilmann M, Pratt AJ, O'Hara A, et al. Plant UVR8 Photoreceptor Senses UV-B by Tryptophan-Mediated Disruption of Cross-Dimer Salt Bridges. Science. 2012;335(6075):1492-6.
11. Mathes T, Heilmann M, Pandit A, Zhu JY, Ravensbergen J, Kloz M, et al. Proton-Coupled Electron Transfer Constitutes the Photoactivation Mechanism of the Plant Photoreceptor UVR8. J Am Chem Soc. 2015;137(25):8113-20.
12. Rockwell NC, Lagarias JC. A brief history of phytochromes. Chemphyschem : a European journal of chemical physics and physical chemistry. 2010;11(6):1172-80.
13. Karniol B, Wagner JR, Walker JM, Vierstra RD. Phylogenetic analysis of the phytochrome superfamily reveals distinct microbial subfamilies of photoreceptors. The Biochemical journal. 2005;392(Pt 1):103-16.
14. Auldridge ME, Forest KT. Bacterial phytochromes: more than meets the light. Critical reviews in biochemistry and molecular biology. 2011;46(1):67-88.
15. Rockwell NC, Lagarias JC. Phytochrome diversification in cyanobacteria and eukaryotic algae. Current opinion in plant biology. 2017;37:87-93.
16. Smith H. Phytochromes and light signal perception by plants--an emerging synthesis. Nature. 2000;407(6804):585-91.
17. Hughes J. Phytochrome cytoplasmic signaling. Annu Rev Plant Biol. 2013;64:377-402.

18. Jung JH, Domijan M, Klose C, Biswas S, Ezer D, Gao M, et al. Phytochromes function as thermosensors in Arabidopsis. Science. 2016;354(6314):886-9.
19. Giraud E, Fardoux L, Fourrier N, Hannibal L, Genty B, Bouyer P, et al. Bacteriophytochrome controls photosystem synthesis in anoxygenic bacteria. Nature. 2002;417(6885):202-5.
20. Tasler R, Moises T, Frankenberg-Dinkel N. Biochemical and spectroscopic characterization of the bacterial phytochrome of Pseudomonas aeruginosa. Febs J. 2005;272(8):1927-36.
21. Starostzik C, Marwan W. A Photoreceptor with Characteristics of Phytochrome Triggers Sporulation in the True Slime-Mold Physarum-Polycephalum. FEBS letters. 1995;370(1-2):146-8.
22. Tester M, Morris C. The Penetration of Light through Soil. Plant Cell and Environment. 1987;10(4):281-6.
23. Chernov KG, Redchuk TA, Omelina ES, Verkhushaa VV. Near-Infrared Fluorescent Proteins, Biosensors, and Optogenetic Tools Engineered from Phytochromes. Chem Rev. 2017;117(9):6423-46.
24. Shu X, Royant A, Lin MZ, Aguilera TA, Lev-Ram V, Steinbach PA, et al. Mammalian expression of infrared fluorescent proteins engineered from a bacterial phytochrome. Science. 2009;324(5928):804-7.
25. Shcherbakova DM, Verkhusha VV. Near-infrared fluorescent proteins for multicolor in vivo imaging. Nature methods. 2013;10(8):751-4.
26. Kaberniuk AA, Shemetov AA, Verkhusha VV. A bacterial phytochrome-based optogenetic system controllable with near-infrared light. Nature methods. 2016;13(7):591-+.
27. Adrian M, Nijenhuis W, Hoogstraaten RI, Willems J, Kapitein LC. A Phytochrome-Derived Photoswitch for Intracellular Transport. Acs Synth Biol. 2017;6(7):1248-56.
28. Moglich A, Moffat K. Engineered photoreceptors as novel optogenetic tools. Photoch Photobio Sci. 2010;9(10):1286-300.
29. Gu Z, Zhao MX, Sheng YW, Bentolila LA, Tang Y. Detection of Mercury Ion by Infrared Fluorescent Protein and Its Hydrogel-Based Paper Assay. Anal Chem. 2011;83(6):2324-9.
30. Wagner JR, Zhang J, von Stetten D, Gunther M, Murgida DH, Mroginski MA, et al. Mutational analysis of Deinococcus radiodurans bacteriophytochrome reveals key amino acids necessary for the photochromicity and proton exchange cycle of phytochromes. The Journal of biological chemistry. 2008;283(18):12212-26.
31. Rockwell NC, Su YS, Lagarias JC. Phytochrome structure and signaling mechanisms. Annu Rev Plant Biol. 2006;57:837-58.
32. Wagner JR, Brunzelle JS, Forest KT, Vierstra RD. A light-sensing knot revealed by the structure of the chromophore-binding domain of phytochrome. Nature. 2005;438(7066):325-31.
33. Burgie ES, Bussell AN, Walker JM, Dubiel K, Vierstra RD. Crystal structure of the photosensing module from a red/far-red light-absorbing plant phytochrome. Proceedings of the National Academy of Sciences of the United States of America. 2014;111(28):10179-84.

34. Takala H, Bjorling A, Berntsson O, Lehtivuori H, Niebling S, Hoernke M, et al. Signal amplification and transduction in phytochrome photosensors. Nature. 2014;509(7499):245-8.
35. Bjorling A, Berntsson O, Takala H, Gallagher KD, Patel H, Gustavsson E, et al. Ubiquitous Structural Signaling in Bacterial Phytochromes. J Phys Chem Lett. 2015;6(17):3379-83.
36. Bjorling A, Berntsson O, Lehtivuori H, Takala H, Hughes AJ, Panman M, et al. Structural photoactivation of a full-length bacterial phytochrome. Sci Adv. 2016;2(8):e1600920.
37. Burgie ES, Wang T, Bussell AN, Walker JM, Li H, Vierstra RD. Crystallographic and electron microscopic analyses of a bacterial phytochrome reveal local and global rearrangements during photoconversion. The Journal of biological chemistry. 2014;289(35):24573-87.
38. Burgie ES, Zhang J, Vierstra RD. Crystal Structure of Deinococcus Phytochrome in the Photoactivated State Reveals a Cascade of Structural Rearrangements during Photoconversion. Structure. 2016;24(3):448-57.
39. Wagner JR, Zhang J, Brunzelle JS, Vierstra RD, Forest KT. High resolution structure of Deinococcus bacteriophytochrome yields new insights into phytochrome architecture and evolution. The Journal of biological chemistry. 2007;282(16):12298-309.
40. Yang X, Kuk J, Moffat K. Crystal structure of Pseudomonas aeruginosa bacteriophytochrome: photoconversion and signal transduction. Proceedings of the National Academy of Sciences of the United States of America. 2008;105(38):14715-20.
41. Yang X, Kuk J, Moffat K. Conformational differences between the Pfr and Pr states in Pseudomonas aeruginosa bacteriophytochrome. Proceedings of the National Academy of Sciences of the United States of America. 2009;106(37):15639-44.
42. Essen LO, Mailliet J, Hughes J. The structure of a complete phytochrome sensory module in the Pr ground state. Proceedings of the National Academy of Sciences of the United States of America. 2008;105(38):14709-14.
43. Bellini D, Papiz MZ. Structure of a bacteriophytochrome and light-stimulated protomer swapping with a gene repressor. Structure. 2012;20(8):1436-46.
44. Davis SJ, Vener AV, Vierstra RD. Bacteriophytochromes: phytochrome-like photoreceptors from nonphotosynthetic eubacteria. Science. 1999;286(5449):2517-20.
45. Burgie ES, Vierstra RD. Phytochromes: An Atomic Perspective on Photoactivation and Signaling. The Plant cell. 2014;26(12):4568-83.
46. Rockwell NC, Duanmu D, Martin SS, Bachy C, Price DC, Bhattacharya D, et al. Eukaryotic algal phytochromes span the visible spectrum. Proceedings of the National Academy of Sciences of the United States of America. 2014;111(10):3871-6.
47. Mathes T, Ravensbergen J, Kloz M, Gleichmann T, Gallagher KD, Woitowich NC, et al. Femto- to Microsecond Photodynarnics of an Unusual Bacteriophytochrome. J Phys Chem Lett. 2015;6(2):239-43.
48. Yang X, Stojkovic EA, Kuk J, Moffat K. Crystal structure of the chromophore binding domain of an unusual bacteriophytochrome, RpBphP3, reveals residues that modulate photoconversion. Proceedings of the National Academy of Sciences of the United States of America. 2007;104(30):12571-6.
49. Anders K, Daminelli-Widany G, Mroginski MA, von Stetten D, Essen LO. Structure of the cyanobacterial phytochrome 2 photosensor implies a tryptophan switch for phytochrome signaling. The Journal of biological chemistry. 2013;288(50):35714-25.

50. Song PS. The electronic spectroscopy of photoreceptors (other than rhodopsin). In Photochemical and Photobiological reviews, Ed: Kendric C Smith, Plenum press, New York. 1983:77-140.
51. Ghosh S, Yu CL, Ferraro DJ, Sudha S, Pal SK, Schaefer WF, et al. Blue protein with red fluorescence. Proceedings of the National Academy of Sciences of the United States of America. 2016;113(41):11513-8.
52. Inomata K, Hammam MA, Kinoshita H, Murata Y, Khawn H, Noack S, et al. Sterically locked synthetic bilin derivatives and phytochrome Agp1 from Agrobacterium tumefaciens form photoinsensitive Pr- and Pfr-like adducts. The Journal of biological chemistry. 2005;280(26):24491-7.
53. Lamparter T. Evolution of cyanobacterial and plant phytochromes. FEBS letters. 2004;573(1-3):1-5.
54. Nagano S, Scheerer P, Zubow K, Michael N, Inomata K, Lamparter T, et al. The Crystal Structures of the N-terminal Photosensory Core Module of Agrobacterium Phytochrome Agp1 as Parallel and Anti-parallel Dimers. Journal of Biological Chemistry. 2016;291(39):20674-91.
55. Rockwell NC, Ohlendorf R, Moglich A. Cyanobacteriochromes in full color and three dimensions. Proceedings of the National Academy of Sciences of the United States of America. 2013;110(3):806-7.
56. Fushimi K, Nakajima T, Aono Y, Yamamoto T, Ni Ni W, Ikeuchi M, et al. Photoconversion and Fluorescence Properties of a Red/Green-Type Cyanobacteriochrome AM1_C0023g2 That Binds Not Only Phycocyanobilin But Also Biliverdin. Front Microbiol. 2016;7:588.
57. Hardman SJ, Hauck AF, Clark IP, Heyes DJ, Scrutton NS. Comprehensive analysis of the green-to-blue photoconversion of full-length Cyanobacteriochrome Tlr0924. Biophys J. 2014;107(9):2195-203.
58. Burgie ES, Walker JM, Phillips GN, Jr., Vierstra RD. A photo-labile thioether linkage to phycoviolobilin provides the foundation for the blue/green photocycles in DXCF-cyanobacteriochromes. Structure. 2013;21(1):88-97.
59. Narikawa R, Nakajima T, Aono Y, Fushimi K, Enomoto G, Ni Ni W, et al. A biliverdin-binding cyanobacteriochrome from the chlorophyll d-bearing cyanobacterium Acaryochloris marina. Scientific reports. 2015;5:7950.
60. Wiltbank LB, Kehoe DM. Two Cyanobacterial Photoreceptors Regulate Photosynthetic Light Harvesting by Sensing Teal, Green, Yellow, and Red Light. MBio. 2016;7(1):e02130-15.
61. Borucki B, von Stetten D, Seibeck S, Lamparter T, Michael N, Mroginski MA, et al. Light-induced proton release of phytochrome is coupled to the transient deprotonation of the tetrapyrrole chromophore. The Journal of biological chemistry. 2005;280(40):34358-64.
62. von Stetten D, Seibeck S, Michael N, Scheerer P, Mroginski MA, Murgida DH, et al. Highly conserved residues Asp-197 and His-250 in Agp1 phytochrome control the proton affinity of the chromophore and Pfr formation. The Journal of biological chemistry. 2007;282(3):2116-23.
63. Scheerer P, Michael N, Park JH, Nagano S, Choe HW, Inomata K, et al. Light-induced conformational changes of the chromophore and the protein in phytochromes: bacterial phytochromes as model systems. Chemphyschem : a European journal of chemical physics and physical chemistry. 2010;11(6):1090-105.

64. Edlund P, Takala H, Claesson E, Henry L, Dods R, Lehtivuori H, et al. The room temperature crystal structure of a bacterial phytochrome determined by serial femtosecond crystallography. Scientific reports. 2016;6:35279.
65. Zienicke B, Molina I, Glenz R, Singer P, Ehmer D, Escobar FV, et al. Unusual spectral properties of bacteriophytochrome Agp2 result from a deprotonation of the chromophore in the red-absorbing form Pr. The Journal of biological chemistry. 2013;288(44):31738-51.
66. Velazquez Escobar F, Lang C, Takiden A, Schneider C, Balke J, Hughes J, et al. Protonation-Dependent Structural Heterogeneity in the Chromophore Binding Site of Cyanobacterial Phytochrome Cph1. The journal of physical chemistry B. 2017;121(1):47-57.
67. Borg OA, Durbeej B. Relative ground and excited-state pK(a) values of phytochromobilin in the photoactivation of phytochrome: A computational study. Journal of Physical Chemistry B. 2007;111(39):11554-65.
68. Matute RA, Contreras R, Perez-Hernandez G, Gonzalez L. The chromophore structure of the cyanobacterial phytochrome Cph1 as predicted by time-dependent density functional theory. The journal of physical chemistry B. 2008;112(51):16253-6.
69. Kirpich JS, Mix LT, Martin SS, Rockwell NC, Lagarias JC, Larsen DS. Protonation Heterogeneity Modulates the Ultrafast Photocycle Initiation Dynamics of Phytochrome Cph1. J Phys Chem Lett. 2018;9(12):3454-62.
70. Kim PW, Rockwell NC, Martin SS, Lagarias JC, Larsen DS. Dynamic inhomogeneity in the photodynamics of cyanobacterial phytochrome Cph1. Biochemistry. 2014;53(17):2818-26.
71. Ulijasz AT, Vierstra RD. Phytochrome structure and photochemistry: recent advances toward a complete molecular picture. Current opinion in plant biology. 2011;14(5):498-506.
72. Rockwell NC, Martin SS, Lagarias JC. Identification of Cyanobacteriochromes Detecting Far-Red Light. Biochemistry. 2016;55(28):3907-19.
73. Spillane KM, Dasgupta J, Lagarias JC, Mathies RA. Homogeneity of phytochrome Cph1 vibronic absorption revealed by resonance Raman intensity analysis. J Am Chem Soc. 2009;131(39):13946-8.
74. Nieder JB, Brecht M, Bittl R. Dynamic intracomplex heterogeneity of phytochrome. J Am Chem Soc. 2009;131(1):69-71.
75. Schmidt P, Gensch T, Remberg A, Gartner W, Braslavsky SE, Schaffner K. The complexity of the P-r to P-fr phototransformation kinetics is an intrinsic property of native phytochrome. Photochem Photobiol. 1998;68(5):754-61.
76. von Stetten D, Gunther M, Scheerer P, Murgida DH, Mroginski MA, Krauss N, et al. Chromophore heterogeneity and photoconversion in phytochrome crystals and solution studied by resonance Raman spectroscopy. Angew Chem Int Ed Engl. 2008;47(25):4753-5.
77. Falk H. The Chemistry of Linear Oligopyrroles and Bile pigments. Springer, Wien, New York. 1989.
78. Fodor SPA, Lagarias JC, Mathies RA. Resonance Raman-Spectra of the Pr-Form of Phytochrome. Photochem Photobiol. 1988;48(2):129-36.
79. Siebert F, Grimm R, Rudiger W, Schmidt G, Scheer H. Infrared-Spectroscopy of Phytochrome and Model Pigments. European Journal of Biochemistry. 1990;194(3):921-8.

80. Matysik J, Hildebrandt P, Schlamann W, Braslavsky SE, Schaffner K. Fourier-transform resonance Raman spectroscopy of intermediates of the phytochrome photocycle. Biochemistry. 1995;34(33):10497-507.
81. Foerstendorf H, Mummert E, Schafer E, Scheer H, Siebert F. Fourier-transform infrared spectroscopy of phytochrome: difference spectra of the intermediates of the photoreactions. Biochemistry. 1996;35(33):10793-9.
82. Kneip C, Hildebrandt P, Schlamann W, Braslavsky SE, Mark F, Schaffner K. Protonation state and structural changes of the tetrapyrrole chromophore during the Pr --> Pfr phototransformation of phytochrome: a resonance Raman spectroscopic study. Biochemistry. 1999;38(46):15185-92.
83. Velazquez Escobar F, Hildebrandt T, Utesch T, Schmitt FJ, Seuffert I, Michael N, et al. Structural parameters controlling the fluorescence properties of phytochromes. Biochemistry. 2014;53(1):20-9.
84. Ulijasz AT, Cornilescu G, von Stetten D, Kaminski S, Mroginski MA, Zhang J, et al. Characterization of two thermostable cyanobacterial phytochromes reveals global movements in the chromophore-binding domain during photoconversion. The Journal of biological chemistry. 2008;283(30):21251-66.
85. Strauss HM, Hughes J, Schmieder P. Heteronuclear solution-state NMR studies of the chromophore in cyanobacterial phytochrome Cph1. Biochemistry. 2005;44(23):8244-50.
86. Durbeej B, Borg OA, Eriksson LA. Computational evidence in favor of a protonated chromophore in the photoactivation of phytochrome. Chemical Physics Letters. 2005;416(1-3):83-8.
87. Strambi A, Durbeej B. Initial excited-state relaxation of the bilin chromophores of phytochromes: a computational study. Photochemical & photobiological sciences : Official journal of the European Photochemistry Association and the European Society for Photobiology. 2011;10(4):569-79.
88. Durbeej B. On the primary event of phytochrome: quantum chemical comparison of photoreactions at C4, C10 and C15. Physical chemistry chemical physics : PCCP. 2009;11(9):1354-61.
89. Durbeej B. A computational perspective on the photochemistry of photosensory proteins: phytochromes and Anabaena sensory rhodopsin. In: Quantum Simulations of Materials and Biological Systems, Ed: Jun Zeng, Rui-Qin Zhang and Herbert R Treutlein, Springer Netherlands. 2012:169-94.
90. Borg OA, Durbeej B. Which factors determine the acidity of the phytochromobilin chromophore of plant phytochrome? Physical chemistry chemical physics : PCCP. 2008;10(18):2528-37.
91. Singer P, Worner S, Lamparter T, Diller R. Spectroscopic Investigation on the Primary Photoreaction of Bathy Phytochrome Agp2-Pr of Agrobacterium fabrum: Isomerization in a pH-dependent H-bond Network. Chemphyschem : a European journal of chemical physics and physical chemistry. 2016;17(9):1288-97.
92. Rumyantsev KA, Shcherbakova DM, Zakharova NI, Emelyanov AV, Turoverov KK, Verkhusha VV. Minimal domain of bacterial phytochrome required for chromophore binding and fluorescence. Scientific reports. 2015;5:18348.
93. Li F, Burgie ES, Yu T, Heroux A, Schatz GC, Vierstra RD, et al. X-ray radiation induces deprotonation of the bilin chromophore in crystalline D. radiodurans phytochrome. J Am Chem Soc. 2015;137(8):2792-5.

94. Thummler F, Rudiger W. Models for the Photoreversibility of Phytochrome - Z,E Isomerization of Chromopeptides from Phycocyanin and Phytochrome. Tetrahedron. 1983;39(11):1943-51.
95. Fodor SP, Lagarias JC, Mathies RA. Resonance Raman analysis of the Pr and Pfr forms of phytochrome. Biochemistry. 1990;29(50):11141-6.
96. Andel F, 3rd, Murphy JT, Haas JA, McDowell MT, van der Hoef I, Lugtenburg J, et al. Probing the photoreaction mechanism of phytochrome through analysis of resonance Raman vibrational spectra of recombinant analogues. Biochemistry. 2000;39(10):2667-76.
97. Rudiger W, Thummler F, Cmiel E, Schneider S. Chromophore structure of the physiologically active form (P(fr)) of phytochrome. Proceedings of the National Academy of Sciences of the United States of America. 1983;80(20):6244-8.
98. Thummler F, Rudiger W, Cmiel E, Schneider S. Chromopeptides from Phytochrome and Phycocyanin - Nmr-Studies of the Pfr and Pr Chromophore of Phytochrome and E,Z Isomeric Chromophores of Phycocyanin. Z Naturforsch C. 1983;38(5-6):359-68.
99. Rudiger W, Thummler F. Phytochrome, the Visual Pigment of Plants. Angewandte Chemie-International Edition in English. 1991;30(10):1216-28.
100. Yang X, Ren Z, Kuk J, Moffat K. Temperature-scan cryocrystallography reveals reaction intermediates in bacteriophytochrome. Nature. 2011;479(7373):428-32.
101. Song C, Psakis G, Lang C, Mailliet J, Gartner W, Hughes J, et al. Two ground state isoforms and a chromophore D-ring photoflip triggering extensive intramolecular changes in a canonical phytochrome. Proceedings of the National Academy of Sciences of the United States of America. 2011;108(10):3842-7.
102. Ulijasz AT, Cornilescu G, Cornilescu CC, Zhang J, Rivera M, Markley JL, et al. Structural basis for the photoconversion of a phytochrome to the activated Pfr form. Nature. 2010;463(7278):250-4.
103. Falklöf O, Durbeej B. Red-light absorption and fluorescence of phytochrome chromophores: A comparative theoretical study. Chemical Physics. 2013;425:19-28.
104. Durbeej B, Eriksson LA. Protein-bound chromophores astaxanthin and phytochromobilin: excited state quantum chemical studies. Physical chemistry chemical physics : PCCP. 2006;8(35):4053-71.
105. Durbeej B, Anders Borg O, Eriksson LA. Phytochromobilin C15-Z,syn? C15-E,anti isomerization: concerted or stepwise? Physical Chemistry Chemical Physics. 2004;6(21):5066.
106. Falklof O, Durbeej B. Modeling of phytochrome absorption spectra. Journal of computational chemistry. 2013;34(16):1363-74.
107. Matute RA, Contreras R, Gonzalez L. Time-Dependent DFT on Phytochrome Chromophores: A Way to the Right Conformer. J Phys Chem Lett. 2010;1(4):796-801.
108. Hasegawa J, Isshiki M, Fujimoto K, Nakatsuji H. Structure of phytochromobilin in the P-r and P-fr forms: SAC-CI theoretical study. Chemical Physics Letters. 2005;410(1-3):90-3.
109. Cornilescu G, Ulijasz AT, Cornilescu CC, Markley JL, Vierstra RD. Solution structure of a cyanobacterial phytochrome GAF domain in the red-light-absorbing ground state. J Mol Biol. 2008;383(2):403-13.

110. Goller AH, Strehlow D, Hermann G. The excited-state chemistry of phycocyanobilin: a semiempirical study. Chemphyschem : a European journal of chemical physics and physical chemistry. 2005;6(7):1259-68.
111. Eilfeld P, Rudiger W. Absorption-Spectra of Phytochrome Intermediates. Z Naturforsch C. 1985;40(1-2):109-14.
112. Eilfeld P, Eilfeld P, Vogel J, Maurer R. Evidence for a Sequential Pathway from Pr to Pfr of the Phototransformation of 124-Kda Oat Phytochrome. Photochem Photobiol. 1987;45(6):825-30.
113. Bjorling SC, Zhang CF, Farrens DL, Song PS, Kliger DS. Time-Resolved Circular-Dichroism of Native Oat Phytochrome Photointermediates. J Am Chem Soc. 1992;114(12):4581-8.
114. Andel F, Lagarias JC, Mathies RA. Resonance Raman analysis of chromophore structure in the lumi-R photoproduct of phytochrome. Biochemistry. 1996;35(50):15997-6008.
115. van Thor JJ, Borucki B, Crielaard W, Otto H, Lamparter T, Hughes J, et al. Light-induced proton release and proton uptake reactions in the cyanobacterial phytochrome Cph1. Biochemistry. 2001;40(38):11460-71.
116. Altoe P, Climent T, De Fusco GC, Stenta M, Bottoni A, Serrano-Andres L, et al. Deciphering Intrinsic Deactivation/Isomerization Routes in a Phytochrome Chromophore Model. Journal of Physical Chemistry B. 2009;113(45):15067-73.
117. Ihalainen JA, Takala H, Lehtivuori H. Fast Photochemistry of Prototypical Phytochromes-A Species vs. Subunit Specific Comparison. Frontiers in molecular biosciences. 2015;2:75.
118. Andel F, Hasson KC, Gai F, Anfinrud PA, Mathies RA. Femtosecond time-resolved spectroscopy of the primary photochemistry of phytochrome. Biospectroscopy. 1997;3(6):421-33.
119. Kandori H, Yoshihara K, Tokutomi S. Primary Process of Phytochrome - Initial Step of Photomorphogenesis in Green Plants. J Am Chem Soc. 1992;114(27):10958-9.
120. Dasgupta J, Frontiera RR, Taylor KC, Lagarias JC, Mathies RA. Ultrafast excited-state isomerization in phytochrome revealed by femtosecond stimulated Raman spectroscopy. Proceedings of the National Academy of Sciences of the United States of America. 2009;106(6):1784-9.
121. Heyne K, Herbst J, Stehlik D, Esteban B, Lamparter T, Hughes J, et al. Ultrafast dynamics of phytochrome from the cyanobacterium Synechocystis, reconstituted with phycocyanobilin and phycoerythrobilin. Biophys J. 2002;82(2):1004-16.
122. Toh KC, Stojkovic EA, van Stokkum IHM, Moffat K, Kennis JTM. Proton-transfer and hydrogen-bond interactions determine fluorescence quantum yield and photochemical efficiency of bacteriophytochrome. Proceedings of the National Academy of Sciences of the United States of America. 2010;107(20):9170-5.
123. Lehtivuori H, Rissanen I, Takala H, Bamford J, Tkachenko NV, Ihalainen JA. Fluorescence Properties of the Chromophore-Binding Domain of Bacteriophytochrome from Deinococcus radiodurans. Journal of Physical Chemistry B. 2013;117(38):11049-57.
124. Kim PW, Rockwell NC, Freer LH, Chang CW, Martin SS, Lagarias JC, et al. Unraveling the Primary Isomerization Dynamics in Cyanobacterial Phytochrome Cph1 with Multipulse Manipulations. J Phys Chem Lett. 2013;4(16):2605-9.

125. Sineshchekov V, Mailliet J, Psakis G, Feilke K, Kopycki J, Zeidler M, et al. Tyrosine 263 in Cyanobacterial Phytochrome Cph1 Optimizes Photochemistry at the prelumi-R -> lumi-R Step. Photochem Photobiol. 2014;90(4):786-95.
126. Fischer AJ, Lagarias JC. Harnessing phytochrome's glowing potential. Proceedings of the National Academy of Sciences of the United States of America. 2004;101(50):17334-9.
127. Fischer AJ, Rockwell NC, Jang AY, Ernst LA, Waggoner AS, Duan Y, et al. Multiple roles of a conserved GAF domain tyrosine residue in cyanobacterial and plant phytochromes. Biochemistry. 2005;44(46):15203-15.
128. Toh KC, Stojkovic EA, van Stokkum IHM, Moffat K, Kennis JTM. Fluorescence quantum yield and photochemistry of bacteriophytochrome constructs. Physical Chemistry Chemical Physics. 2011;13(25):11985-97.
129. Takala H, Lehtivuori HK, Berntsson O, Hughes A, Nanekar R, Niebling S, et al. On the (un)coupling of the chromophore, tongue interactions, and overall conformation in a bacterial phytochrome. The Journal of biological chemistry. 2018;293(21):8161-72.
130. Buhrke D, Kuhlmann U, Michael N, Hildebrandt P. The Photoconversion of Phytochrome Includes an Unproductive Shunt Reaction Pathway. Chemphyschem : a European journal of chemical physics and physical chemistry. 2018;19(5):566-70.
131. Kim PW, Rockwell NC, Martin SS, Lagarias JC, Larsen DS. Heterogeneous photodynamics of the pfr state in the cyanobacterial phytochrome Cph1. Biochemistry. 2014;53(28):4601-11.
132. Shcherbakova DM, Baloban M, Verkhusha VV. Near-infrared fluorescent proteins engineered from bacterial phytochromes. Current opinion in chemical biology. 2015;27:52-63.
133. Auldridge ME, Satyshur KA, Anstrom DM, Forest KT. Structure-guided engineering enhances a phytochrome-based infrared fluorescent protein. The Journal of biological chemistry. 2012;287(10):7000-9.
134. Piatkevich KD, Subach FV, Verkhusha VV. Engineering of bacterial phytochromes for near-infrared imaging, sensing, and light-control in mammals. Chemical Society reviews. 2013;42(8):3441-52.
135. Ziegler T, Moglich A. Photoreceptor engineering. Frontiers in molecular biosciences. 2015;2:30.
136. Yao J, Kaberniuk AA, Li L, Shcherbakova DM, Zhang R, Wang L, et al. Multiscale photoacoustic tomography using reversibly switchable bacterial phytochrome as a near-infrared photochromic probe. Nature methods. 2016;13(1):67-73.
137. Dortay H, Mark J, Wagener A, Zhang E, Grotzinger C, Hildebrandt P, et al. Dual-wavelength photoacoustic imaging of a photoswitchable reporter protein. Proc Spie. 2016;9708.
138. Mark J, Dortay H, Wagener A, Zhang E, Buchmann J, Grotzinger C, et al. Dual-wavelength 3D photoacoustic imaging of mammalian cells using a photoswitchable phytochrome reporter protein. Commun Phys. 2018;1.
139. Li L, Shemetov AA, Baloban M, Hu P, Zhu L, Shcherbakova DM, et al. Small near-infrared photochromic protein for photoacoustic multi-contrast imaging and detection of protein interactions in vivo. Nature communications. 2018;9(1):2734.
140. Lehtivuori H, Bhattacharya S, Angenent-Mari NM, Satyshur KA, Forest KT. Removal of Chromophore-Proximal Polar Atoms Decreases Water Content and

Increases Fluorescence in a Near Infrared Phytofluor. Frontiers in molecular biosciences. 2015;2:65.
141. Shcherbakova DM, Baloban M, Pletnev S, Malashkevich VN, Xiao H, Dauter Z, et al. Molecular Basis of Spectral Diversity in Near-Infrared Phytochrome-Based Fluorescent Proteins. Chem Biol. 2015;22(11):1540-51.
142. Yu D, Gustafson WC, Han C, Lafaye C, Noirclerc-Savoye M, Ge WP, et al. An improved monomeric infrared fluorescent protein for neuronal and tumour brain imaging. Nature communications. 2014;5.
143. Gasser C, Taiber S, Yeh CM, Wittig CH, Hegemann P, Ryu S, et al. Engineering of a red-light-activated human cAMP/cGMP-specific phosphodiesterase. Proceedings of the National Academy of Sciences of the United States of America. 2014;111(24):8803-8.
144. Reichhart E, Ingles-Prieto A, Tichy AM, McKenzie C, Janovjak H. A Phytochrome Sensory Domain Permits Receptor Activation by Red Light. Angew Chem Int Edit. 2016;55(21):6339-42.
145. Tchekanda E, Sivanesan D, Michnick SW. An infrared reporter to detect spatiotemporal dynamics of protein-protein interactions. Nature methods. 2014;11(6):641-+.
146. Chen MH, Li W, Zhang ZP, Liu SY, Zhang XW, Zhang XE, et al. Novel near-infrared BiFC systems from a bacterial phytochrome for imaging protein interactions and drug evaluation under physiological conditions. Biomaterials. 2015;48:97-107.
147. Zlobovskaya OA, Sergeeva TF, Shirmanova MV, Dudenkova VV, Sharonov GV, Zagaynova EV, et al. Genetically encoded far-red fluorescent sensors for caspase-3 activity. Biotechniques. 2016;60(2):62-8.
148. Pandey N, Nobles CL, Zechiedrich L, Maresso AW, Silberg JJ. Combining Random Gene Fission and Rational Gene Fusion To Discover Near-Infrared Fluorescent Protein Fragments That Report on Protein-Protein Interactions. Acs Synth Biol. 2015;4(5):615-24.
149. To TL, Piggott BJ, Makhijani K, Yu D, Jan YN, Shu X. Rationally designed fluorogenic protease reporter visualizes spatiotemporal dynamics of apoptosis in vivo. Proceedings of the National Academy of Sciences of the United States of America. 2015;112(11):3338-43.
150. Vuillet L, Kojadinovic M, Zappa S, Jaubert M, Adriano JM, Fardoux J, et al. Evolution of a bacteriophytochrome from light to redox sensor. EMBO J. 2007;26(14):3322-31.
151. HyperChem(TM) Professional 7.51 H, Inc., 1115 NW 4th Street, Gainesville, Florida 32601, USA.
152. https://www.chemcraftprog.com C-gsfvoqcc.
153. Granovsky AA. Firefly version 8.2.0. http://classicchemmsusu/gran/firefly/indexhtml.
154. Schmidt MW, Baldridge KK, Boatz JA, Elbert ST, Gordon MS, Jensen JH, et al. General Atomic and Molecular Electronic-Structure System. Journal of computational chemistry. 1993;14(11):1347-63.
155. Gaussian 09 RA, Frisch MJ et al. Gaussian, Inc., Wallingford CT. 2016.
156. MATLAB and Statistics Toolbox Release 2017a The MathWorks I, Natick, Massachusetts, United States.

157. Grimme S, Antony J, Ehrlich S, Krieg H. A consistent and accurate ab initio parametrization of density functional dispersion correction (DFT-D) for the 94 elements H-Pu. Journal of Chemical Physics. 2010;132(15).
158. Woon DE, Dunning TH. Gaussian-Basis Sets for Use in Correlated Molecular Calculations .5. Core-Valence Basis-Sets for Boron through Neon. Journal of Chemical Physics. 1995;103(11):4572-85.
159. Lee CT, Yang WT, Parr RG. Development of the Colle-Salvetti Correlation-Energy Formula into a Functional of the Electron-Density. Phys Rev B. 1988;37(2):785-9.
160. Becke AD. Density-Functional Thermochemistry .3. The Role of Exact Exchange. Journal of Chemical Physics. 1993;98(7):5648-52.
161. Granovsky AA. Extended multi-configuration quasi-degenerate perturbation theory: the new approach to multi-state multi-reference perturbation theory. The Journal of chemical physics. 2011;134(21):214113.
162. Yanai T, Tew DP, Handy NC. A new hybrid exchange-correlation functional using the Coulomb-attenuating method (CAM-B3LYP). Chemical Physics Letters. 2004;393(1-3):51-7.
163. Foresman JB, Headgordon M, Pople JA, Frisch MJ. Toward a Systematic Molecular-Orbital Theory for Excited-States. J Phys Chem-Us. 1992;96(1):135-49.
164. Marcus RA. On the Theory of Oxidation-Reduction Reactions Involving Electron Transfer .1. Journal of Chemical Physics. 1956;24(5):966-78.
165. Marcus RA. Electron transfer reactions in chemistry - Theory and experiment. J Electroanal Chem. 1997;438(1-2):251-9.
166. Hsu CP. The Electronic Couplings in Electron Transfer and Excitation Energy Transfer. Accounts Chem Res. 2009;42(4):509-18.
167. Humphrey W, Dalke A, Schulten K. VMD: Visual molecular dynamics. J Mol Graph Model. 1996;14(1):33-8.
168. Phillips JC, Braun R, Wang W, Gumbart J, Tajkhorshid E, Villa E, et al. Scalable molecular dynamics with NAMD. Journal of computational chemistry. 2005;26(16):1781-802.
169. Centre. JS. JURECA: Modular supercomputer at Jülich Supercomputing Centre. Journal of large-scale research facilities, . 2018;4, A132. http://dx.doi.org/10.17815/jlsrf-4-121-1.
170. Kaminski S, Daminelli G, Mroginski MA. Molecular Dynamics Simulations of the Chromophore Binding Site of Deinococcus radiodurans Bacteriophytochrome Using New Force Field Parameters for the Phytochromobilin Chromophore. Journal of Physical Chemistry B. 2009;113(4):945-58.
171. Kaminski S. Theoretical studies on structural, dynamicand spectroscopic properties ofphytochrome photoreceptors. Doctoral Thesis. Technische Universität Berlin. 2010.
172. Jorgensen WL, Chandrasekhar J, Madura JD, Impey RW, Klein ML. Comparison of Simple Potential Functions for Simulating Liquid Water. Journal of Chemical Physics. 1983;79(2):926-35.
173. Feller SE, Zhang YH, Pastor RW, Brooks BR. Constant-Pressure Molecular-Dynamics Simulation - the Langevin Piston Method. Journal of Chemical Physics. 1995;103(11):4613-21.
174. Martyna GJ, Tobias DJ, Klein ML. Constant-Pressure Molecular-Dynamics Algorithms. Journal of Chemical Physics. 1994;101(5):4177-89.

175. Maximowitsch E. Unravelling the mechanism of fluorescence quenching in phytochrome photoreceptors. Master Thesis. Ruprecht-Karls-Universität Heidelberg. 2015.
176. Song C, Essen LO, Gartner W, Hughes J, Matysik J. Solid-State NMR Spectroscopic Study of Chromophore-Protein Interactions in the Pr Ground State of Plant Phytochrome A. Mol Plant. 2012;5(3):698-715.
177. Song C, Rohmer T, Tiersch M, Zaanen J, Hughes J, Matysik J. Solid-State NMR Spectroscopy to Probe Photoactivation in Canonical Phytochromes. Photochem Photobiol. 2013;89(2):259-73.
178. Takiden A, Velazquez-Escobar F, Dragelj J, Woelke AL, Knapp EW, Piwowarski P, et al. Structural and Vibrational Characterization of the Chromophore Binding Site of Bacterial Phytochrome Agp1. Photochem Photobiol. 2017;93(3):713-23.
179. Velazquez Escobar F, Piwowarski P, Salewski J, Michael N, Fernandez Lopez M, Rupp A, et al. A protonation-coupled feedback mechanism controls the signalling process in bathy phytochromes. Nat Chem. 2015;7(5):423-30.
180. Feliks M, Lafaye C, Shu X, Royant A, Field M. Structural Determinants of Improved Fluorescence in a Family of Bacteriophytochrome-Based Infrared Fluorescent Proteins: Insights from Continuum Electrostatic Calculations and Molecular Dynamics Simulations. Biochemistry. 2016;55(31):4263-74.
181. Nijegorodov NI, Downey WS. The Influence of Planarity and Rigidity on the Absorption and Fluorescence Parameters and Intersystem Crossing Rate-Constant in Aromatic-Molecules. J Phys Chem-Us. 1994;98(22):5639-43.
182. Nijegorodov NI, Downey WS. The influence of symmetrical substitution on fluorescence parameters and the intersystem crossing rate constant in aromatic molecules. Spectrochim Acta A. 1995;51(13):2335-46.
183. Luk HL, Melaccio F, Rinaldi S, Gozem S, Olivucci M. Molecular bases for the selection of the chromophore of animal rhodopsins. Proceedings of the National Academy of Sciences of the United States of America. 2015;112(50):15297-302.
184. Udvarhelyi A, Domratcheva T. Photoreaction in BLUF receptors: proton-coupled electron transfer in the flavin-Gln-Tyr system. Photochem Photobiol. 2011;87(3):554-63.
185. Solov'yov IA, Domratcheva T, Moughal Shahi AR, Schulten K. Decrypting cryptochrome: revealing the molecular identity of the photoactivation reaction. J Am Chem Soc. 2012;134(43):18046-52.
186. Domratcheva T. Neutral histidine and photoinduced electron transfer in DNA photolyases. J Am Chem Soc. 2011;133(45):18172-82.
187. Runge E, Gross EKU. Density-Functional Theory for Time-Dependent Systems. Phys Rev Lett. 1984;52(12):997-1000.
188. Marques MAL, Gross EKU. Time-dependent density functional theory. Annu Rev Phys Chem. 2004;55:427-55.
189. Tozer DJ, Amos RD, Handy NC, Roos BO, Serrano-Andres L. Does density functional theory contribute to the understanding of excited states of unsaturated organic compounds? Mol Phys. 1999;97(7):859-68.
190. Dreuw A, Head-Gordon M. Failure of time-dependent density functional theory for long-range charge-transfer excited states: the zincbacteriochlorin-bacteriochlorin and bacteriochlorophyll-spheroidene complexes. J Am Chem Soc. 2004;126(12):4007-16.
191. Rohmer T, Lang C, Hughes J, Essen LO, Gartner W, Matysik J. Light-induced chromophore activity and signal transduction in phytochromes observed by 13C and 15N

magic-angle spinning NMR. Proceedings of the National Academy of Sciences of the United States of America. 2008;105(40):15229-34.
192. Ihalainen JA, Gustavsson E, Schroeder L, Donnini S, Lehtivuori H, Isaksson L, et al. Chromophore-Protein Interplay during the Phytochrome Photocycle Revealed by Step-Scan FTIR Spectroscopy. J Am Chem Soc. 2018;140(39):12396-404.
193. Kaminski S, Mroginski MA. Molecular dynamics of phycocyanobilin binding bacteriophytochromes: a detailed study of structural and dynamic properties. The journal of physical chemistry B. 2010;114(50):16677-86.
194. Muller MG, Lindner I, Martin I, Gartner W, Holzwarth AR. Femtosecond kinetics of photoconversion of the higher plant photoreceptor phytochrome carrying native and modified chromophores. Biophys J. 2008;94(11):4370-82.
195. Fitzpatrick AE, Lincoln CN, van Wilderen LJ, van Thor JJ. Pump-dump-probe and pump-repump-probe ultrafast spectroscopy resolves cross section of an early ground state intermediate and stimulated emission in the photoreactions of the Pr ground state of the cyanobacterial phytochrome Cph1. The journal of physical chemistry B. 2012;116(3):1077-88.

Appendix

A. Amino acids and tetrapyrrole atom names

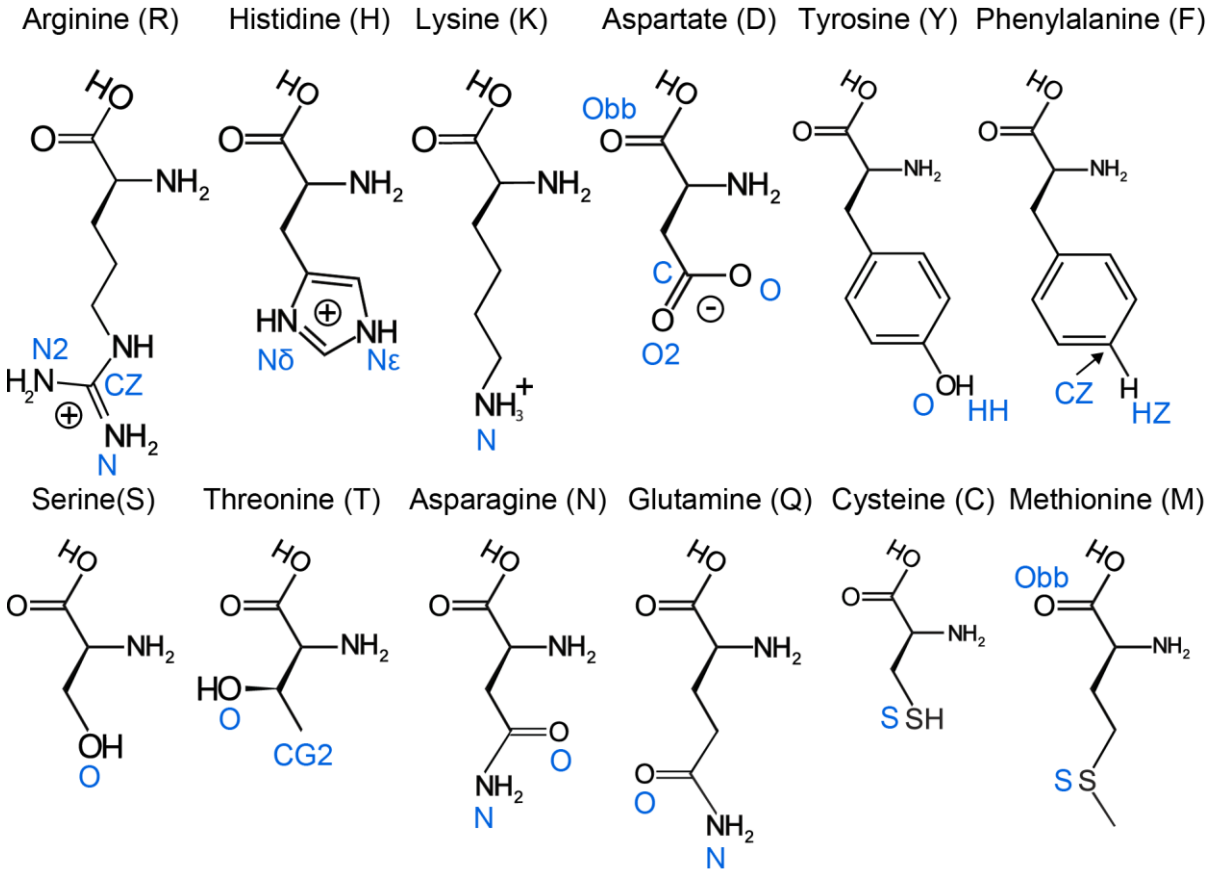

Figure A.1. Atoms names in amino acids. Atoms of the carboxyl group in aspartate or propionate (PropB, PropC) are named O or O2 as well as atoms of arginine are named N or N2 depending on which atoms forms a hydrogen bond. Atom "O" or atom "N" is the main atom forming a hydrogen bond. For the conserved aspartate in the Pfr state models, atom "O" is the atom forming the hydrogen bonds with ring D and serine of the PHY domain.

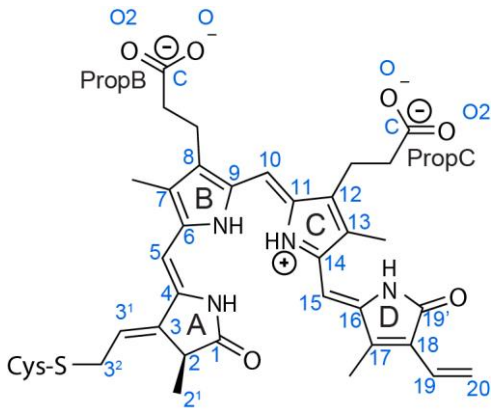

Figure A.2. Tetrapyrrole atom names. N and O atoms of four pyrrole rings in tetrapyrrole are named with indicating a ring next to the atom or as an subscript e.g. ring D (N), ND or N^D. Numbers for the C atoms in tetrapyrrole are indicated.

B. Supplementary tables

Table B.1. Bond lengths (Å) and dihedral angles (degree) of biliverdin extracted from X-ray crystal structures (2o9c, 5c5k, 3c2w,4our, 4our) and optimized in Cartesian Coordinates.

Bond/ Dih. angle	15Z-BV^{Dr}	15E-BV^{Dr}	15E-BV^{Pa}	15Z-PΦB	15E-PΦB
S-C3^{2}	1.8295	1.8315	1.8104	1.8351	1.8346
C3^{2}-C3^{1}	1.4862	1.4860	1.5350	1.5209	1.5208
C3^{1}-C3	1.3464	1.3463	1.4913	1.5379	1.5388
C3-C4	1.4663	1.4665	1.4636	1.5160	1.5167
C4-C5	1.3721	1.3727	1.3661	1.3630	1.3630
C5-C6	1.4203	1.4209	1.4288	1.4270	1.4274
C6-C7	1.4171	1.4176	1.4143	1.4135	1.4150
C7-C8	1.3989	1.3994	1.4044	1.4004	1.4011
C8-C9	1.4211	1.4201	1.4189	1.4200	1.4201
C9-C10	1.3910	1.3927	1.4029	1.3919	1.3946
C10-C11	1.3968	1.3979	1.3908	1.3957	1.3974
C11-C12	1.4166	1.4165	1.4244	1.4173	1.4175
C12-C13	1.4037	1.4037	1.3991	1.4026	1.4040
C13-C14	1.4170	1.4167	1.4244	1.4177	1.4177
C14-C15	1.4301	1.4287	1.4226	1.4295	1.4265
C15-C16	1.3673	1.3707	1.3736	1.3679	1.3711
C16-C17	1.4660	1.4671	1.4649	1.4661	1.4657
C17-C18	1.3655	1.3668	1.3672	1.3657	1.3670
C18-C19	1.4458	1.4443	1.4434	1.4458	1.4443
C19-C20	1.3434	1.3442	1.3447	1.3434	1.3443
C18-C19'	1.4975	1.4968	1.4997	1.4970	1.4983
C1-N^{A}	1.3837	1.3848	1.4031	1.3858	1.3854
C4-N^{A}	1.3803	1.3816	1.3941	1.3696	1.3728
C6-N^{B}	1.3754	1.3732	1.3666	1.3731	1.3690
C9-N^{B}	1.3973	1.3966	1.3872	1.3970	1.3962
C11-N^{C}	1.3935	1.3932	1.3896	1.3938	1.3927
C14-N^{C}	1.3715	1.3715	1.3678	1.3718	1.3722
C16-N^{D}	1.3715	1.3752	1.3717	1.3714	1.3744
C19'-N^{D}	1.3977	1.3894	1.3900	1.3985	1.3884
C1-O^{A}	1.2095	1.2104	1.2169	1.2092	1.2114
C19'-O^{D}	1.2081	1.2093	1.2084	1.2079	1.2094
N^{A}-H	1.0108	1.0109	1.0130	1.0112	1.0113
N^{B}-H	1.0161	1.0109	1.0153	1.0157	1.0147
N^{C}-H	1.0132	1.0137	1.0122	1.0133	1.0139
N^{D}-H	1.0104	1.0129	1.0153	1.0105	1.0142
C3-C4-C5-C6	-173.8	-173.5	-169.2	-175.5	-176.1
C4-C5-C6-C7	-166.5	-167.6	-172.2	-163.2	-164.9
C8-C9-C10-C11	168.7	167.1	169.1	170.2	168.6
C9-C10-C11-C12	163.4	159.6	158.7	162.6	157.2
C13-C14-C15-C16	34.0	38.1	35.9	33.2	36.4
C14-C15-C16-C17	-176.6	15.9	16.7	-175.3	15.9

Table B.2. XMCQDPT2-SA7-CASSCF(6,5) excited-state energies and HOMO, LUMO energies computed with PBE0 of the active-site cluster models. Five main models (shown in Figure 3.6) contain neutral (Nε-H) histidines. Some additional models contain neutral (Nδ-H) or protonated H290 (according to the DrBphP numbering, all indicated in parentheses as δ or H, respectively. Models without (w/) D207 or H290 prepared from five main models containing neutral (Nε-H) histidines as described in Sections 2.1.2-2.1.3.

Model	XMCQDPT2	ε(HOMO)	ε(LUMO)	Δε(HOMO-LUMO)
Dr-Pr	1.78	-0.1816	-0.0961	0.0855
Dr-Pfr	1.62	-0.1258	-0.0471	0.0787
Pa-Pfr	1.67	-0.1873	-0.1081	0.0792
At-Pr	1.97	-0.2535	-0.1611	0.0924
At-Pfr	1.70	-0.1729	-0.0870	0.0859
Dr-Pr(H)	1.77	-0.2400	-0.1528	0.0872
Dr-Pr(δ)	1.76	-0.1711	-0.0861	0.0850
Dr-Pfr(H)	1.56	-0.1816	-0.1035	0.0781
Pa-Pfr(H)	1.62	-0.2418	-0.1629	0.0789
At-Pr(H)	2.06	-0.3066	-0.2141	0.0925
Dr-Pr w/o D207	1.77	-0.2460	-0.1601	0.0859
Dr-Pfr w/o D207	1.70	-0.2038	-0.1213	0.0825
Pa-Pfr w/o D207	1.75	-0.2710	-0.1906	0.0804
At-Pr w/o D207	1.93	-0.3196	-0.2262	0.0934
At-Pfr w/o D207	1.92	-0.2526	-0.1636	0.0890
Dr-Pr w/o H290	1.79	-0.1729	-0.0878	0.0851
At-Pr w/o H290	1.95	-0.2475	-0.1553	0.0922

Table B.3. Bond lengths (Å) of biliverdin in the active-site cluster models with neutral (Nε-H) histidines: five main models (wild-type) and models without (w/o) D207. Five main models are shown in Figure 3.6. Models without (w/) D207 or H290 prepared from five main models containing neutral (Nε-H) histidines as described in Sections 2.1.2-2.1.3.

Bond	Wild-type models					Models w/o D207				
	Dr-Pr	Dr-Pfr	Pa-Pfr	At-Pr	At-Pfr	Dr-Pr	Dr-Pfr	Pa-Pfr	At-Pr	At-Pfr
S-C3^2	1.827	1.838	1.818	1.844	1.843	1.826	1.833	1.812	1.843	1.843
C3^2-C3^1	1.491	1.490	1.545	1.523	1.522	1.490	1.490	1.548	1.522	1.843
C3^1-C3	1.343	1.343	1.497	1.539	1.530	1.344	1.344	1.494	1.540	1.533
C3-C4	1.480	1.480	1.469	1.522	1.522	1.478	1.478	1.461	1.519	1.520
C4-C5	1.362	1.365	1.368	1.367	1.363	1.361	1.366	1.368	1.362	1.361
C5-C6	1.427	1.432	1.432	1.424	1.426	1.429	1.429	1.426	1.427	1.426
C6-C7	1.419	1.414	1.418	1.437	1.425	1.421	1.418	1.421	1.434	1.428
C7-C8	1.392	1.401	1.400	1.385	1.389	1.393	1.397	1.399	1.382	1.385
C8-C9	1.423	1.416	1.419	1.437	1.427	1.423	1.422	1.418	1.437	1.434
C9-C10	1.401	1.403	1.408	1.385	1.398	1.399	1.395	1.403	1.383	1.388
C10-C11	1.387	1.383	1.382	1.399	1.390	1.388	1.390	1.382	1.400	1.398
C11-C12	1.439	1.438	1.440	1.424	1.435	1.436	1.431	1.438	1.422	1.429
C12-C13	1.392	1.389	1.385	1.400	1.391	1.393	1.394	1.388	1.402	1.397
C13-C14	1.432	1.437	1.441	1.423	1.433	1.429	1.426	1.434	1.417	1.423
C14-C15	1.434	1.419	1.419	1.445	1.425	1.435	1.431	1.426	1.444	1.435
C15-C16	1.366	1.376	1.375	1.359	1.375	1.367	1.365	1.364	1.357	1.368
C16-C17	1.470	1.469	1.466	1.464	1.473	1.469	1.460	1.456	1.461	1.466
C17-C18	1.361	1.363	1.367	1.367	1.364	1.361	1.371	1.372	1.367	1.368
C18-C19	1.446	1.447	1.444	1.449	1.445	1.447	1.448	1.443	1.447	1.447
C19-C20	1.342	1.343	1.344	1.342	1.344	1.343	1.343	1.341	1.343	1.343
C18-C19'	1.492	1.493	1.494	1.489	1.502	1.496	1.483	1.480	1.494	1.492
C1-N^A	1.370	1.369	1.384	1.385	1.382	1.362	1.367	1.375	1.374	1.377
C4-N^A	1.379	1.373	1.380	1.358	1.361	1.392	1.375	1.387	1.364	1.365
C6-N^B	1.361	1.368	1.362	1.352	1.354	1.361	1.365	1.363	1.352	1.353
C9-N^B	1.385	1.386	1.379	1.388	1.383	1.385	1.387	1.377	1.389	1.386
C11-N^C	1.382	1.380	1.377	1.374	1.378	1.383	1.379	1.379	1.376	1.379
C14-N^C	1.354	1.354	1.346	1.355	1.353	1.356	1.352	1.341	1.357	1.354
C16-N^D	1.373	1.370	1.368	1.386	1.366	1.372	1.391	1.402	1.383	1.378
C19'-N^D	1.385	1.373	1.384	1.379	1.380	1.383	1.379	1.405	1.377	1.386
C1-O^A	1.216	1.213	1.221	1.210	1.208	1.227	1.217	1.240	1.221	1.214
C19'-O^D	1.217	1.224	1.216	1.220	1.214	1.216	1.223	1.216	1.217	1.212
N^A-H	1.043	1.038	1.036	1.039	1.034	1.046	1.039	1.034	1.042	1.030
N^B-H	1.023	1.027	1.029	1.024	1.028	1.020	1.026	1.027	1.026	1.027
N^C-H	1.033	1.037	1.036	1.028	1.038	1.030	1.038	1.040	1.023	1.036
N^D-H	1.034	1.067	1.031	1.007	1.048	1.041	1.006	1.014	1.012	1.008

Table B.4. Mulliken charges of biliverdin in the active-site cluster models with neutral (Nε-H) histidines. Five main models are shown in Figure 3.6.

Atoms	Dr-Pr	Dr-Pfr	Pa-Pfr	At-Pr	At-Pfr
rings ABC	0.257	0.198	0.259	0.167	0.118
ring D	0.002	0.083	0.070	0.113	0.162
N^A	-0.401	-0.372	-0.420	-0.367	-0.378
N^B	-0.373	-0.396	-0.380	-0.365	-0.363
N^C	-0.347	-0.356	-0.347	-0.343	-0.349
N^D	-0.434	-0.418	-0.392	-0.367	-0.403

C. Supplementary figures

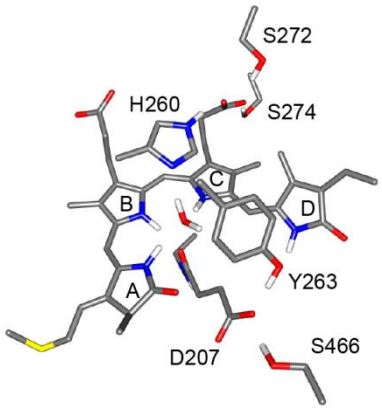

Figure C.1. Active-site cluster model of DrBphP, where biliverdin is as in Pfr state but aspartate D207 does not form a hydrogen bond with ring D. However, D207 forms a hydrogen bond with tyrosine Y263. In the model only hydrogen atoms, bound to the N and O atoms are shown. The first excited-state energy, computed with XMCQDPT2-SA7-CASSCF(6,5) is 1.68 eV. The model includes protonated biliverdin, anionic D207 and neutral (Nε-H) H260 and was prepared as Dr-Pfr model (as described in Section 2.1.2 with an exception that at the starting coordinates the H atom of the OH group in Y263 was positioned to face D207 instead of S466. Geometry optimization and XMCQDPT2 calculations were done as for the Dr-Pfr model, described in Section 2.1.3 and Section 2.1.4, respectively.

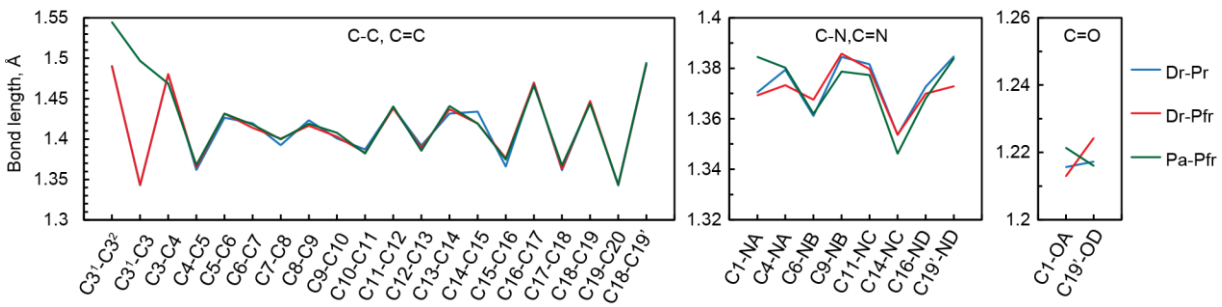

Figure C.2. Bond lengths of biliverdin in the active-site cluster models with neutral (Nε-H) histidines. The three main models are shown in Figure 3.6. Values are taken from Table B.3.

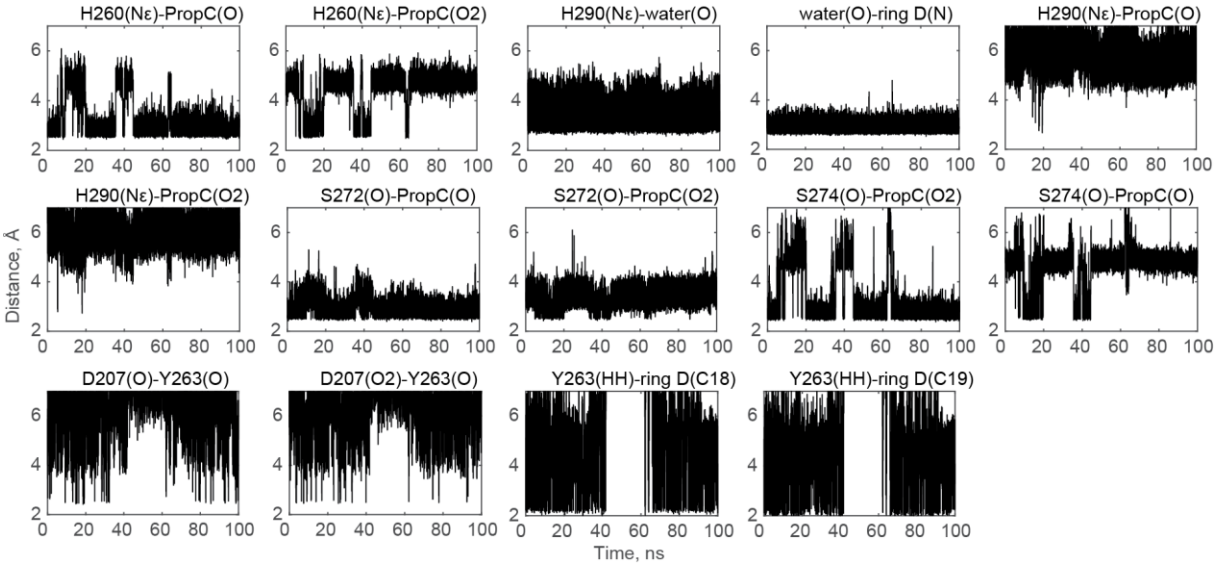

Figure C.3. Distances in the Dr-Pr-CBD model with protonated biliverdin and neutral (Nε-H) H260 and H290 during MD simulation.

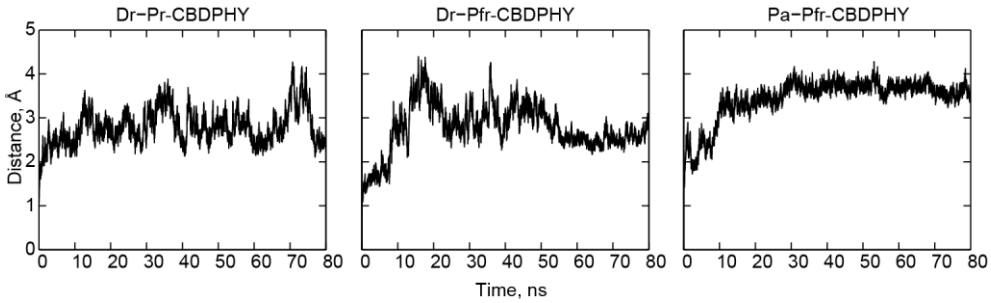

Figure C.4. RMSDs for the non-hydrogen atoms of Dr-Pr, Dr-Pfr, Pa-Pfr models comprised of CBD-PHY domains with protonated biliverdin, neutral (Nε-H) H260 and protonated H290 during MD simulation. Hydrogens were excluded in all RMSDs.

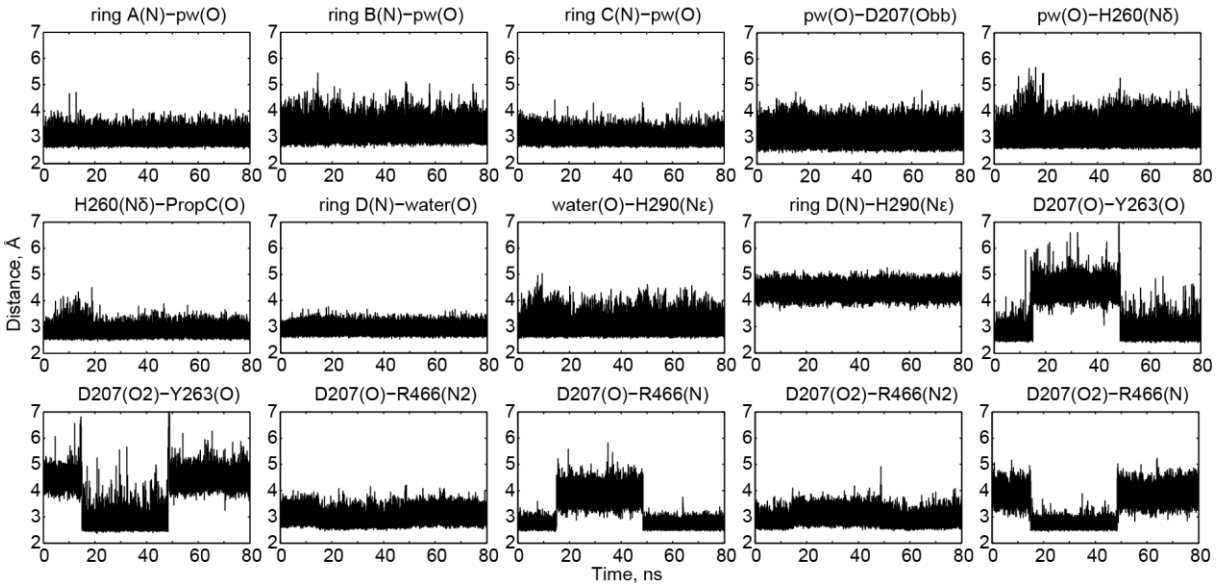

Figure C.5. Distances in the Dr-Pr-CBDPHY model with protonated biliverdin, neutral (Nε-H) H260 and protonated H290 during MD simulation.

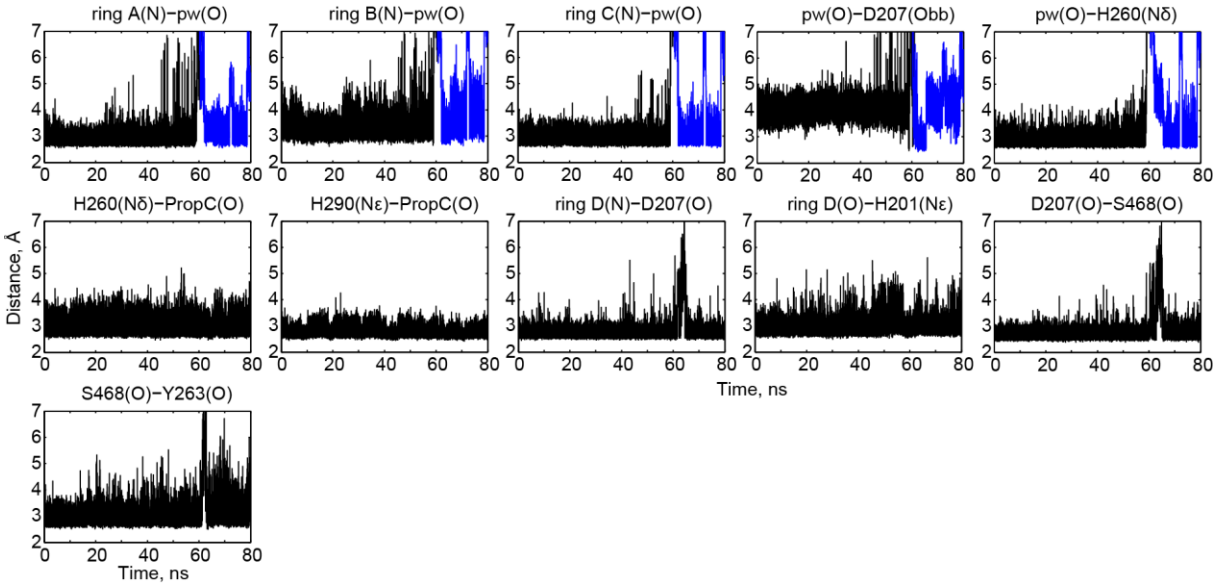

Figure C.6. Distances in the Dr-Pfr-CBDPHY model with protonated biliverdin, neutral (Nε-H) H260 and protonated H290 during MD simulation.

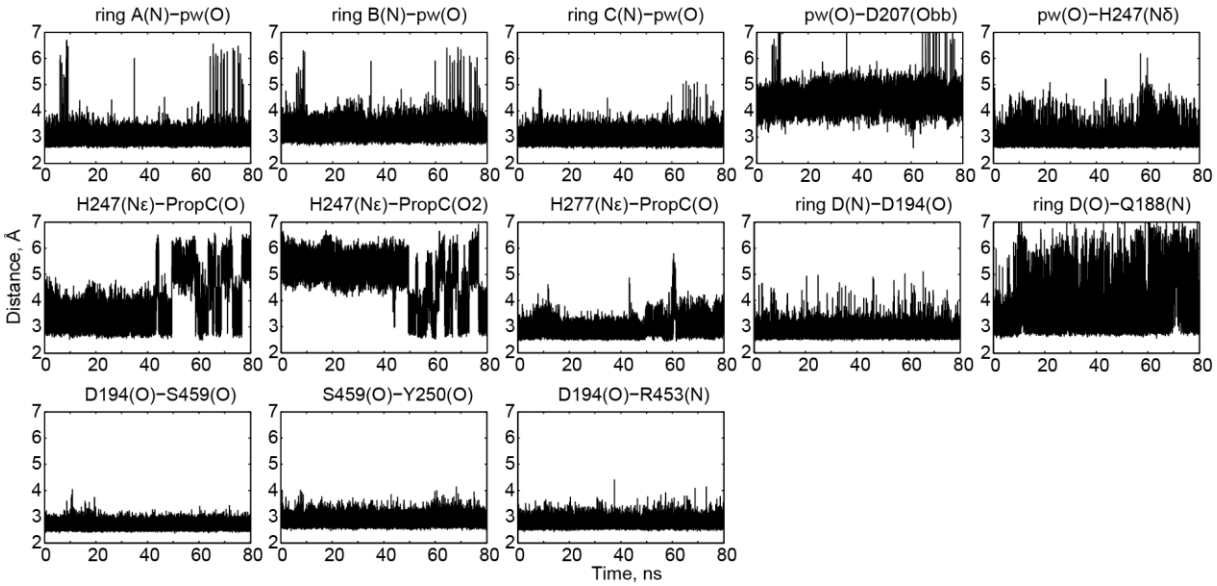

Figure C.7. Distances in the Pa-Pfr-CBDPHY model with protonated biliverdin, neutral (Nε-H) H260 and protonated H290 during MD simulation.

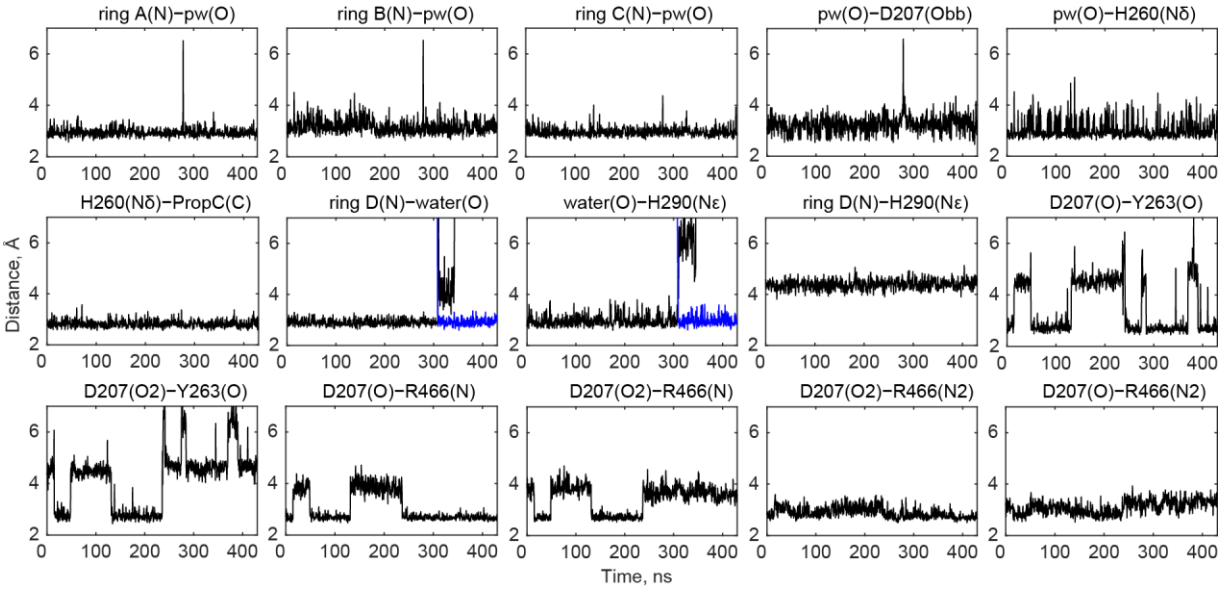

Figure C.8. Distances in the Dr-Pr-CBDPHY model with protonated biliverdin, neutral (Nε-H) H260 and protonated H290 during MD simulation. The model name in Section 3.2 is DrPr-protBV-(εP).

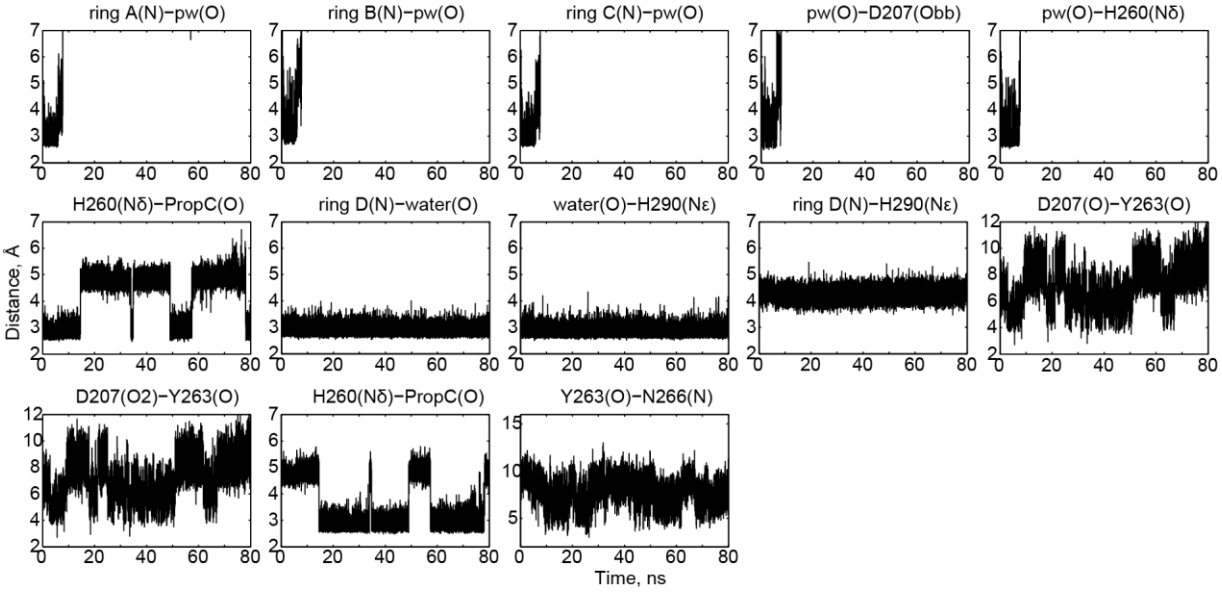

Figure C.9. Distances in the Dr-Pr-CBD model with protonated biliverdin, neutral (Nε-H) H260 and protonated H290 during MD simulation.

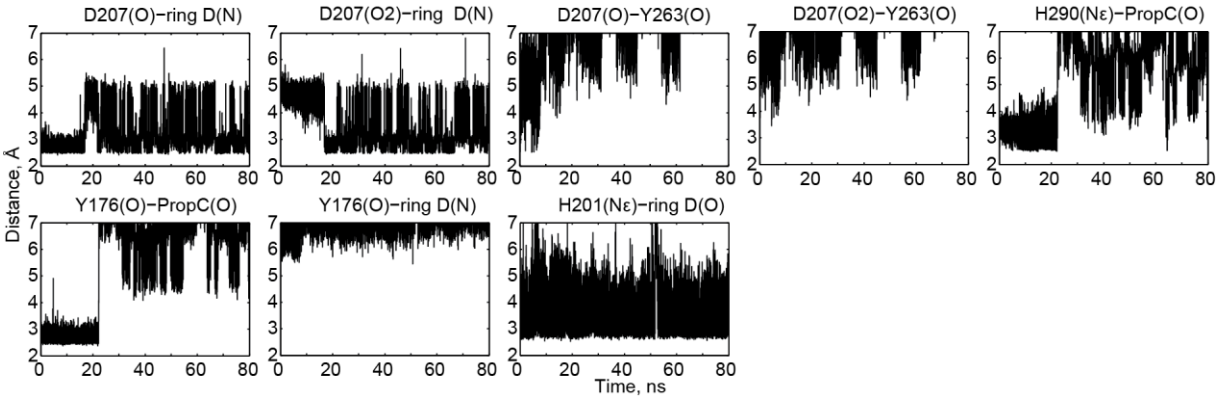

Figure C.10. Distances in the Dr-Pfr-CBD model with protonated biliverdin, neutral (Nε-H) H260 and protonated H290 during MD simulation.

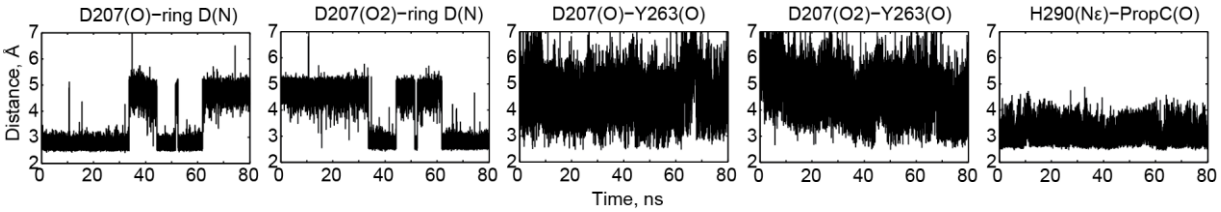

Figure C.11. Distances in the Pa-Pfr-CBD model with protonated biliverdin, neutral (Nε-H) H260 and protonated H290 during MD simulation.

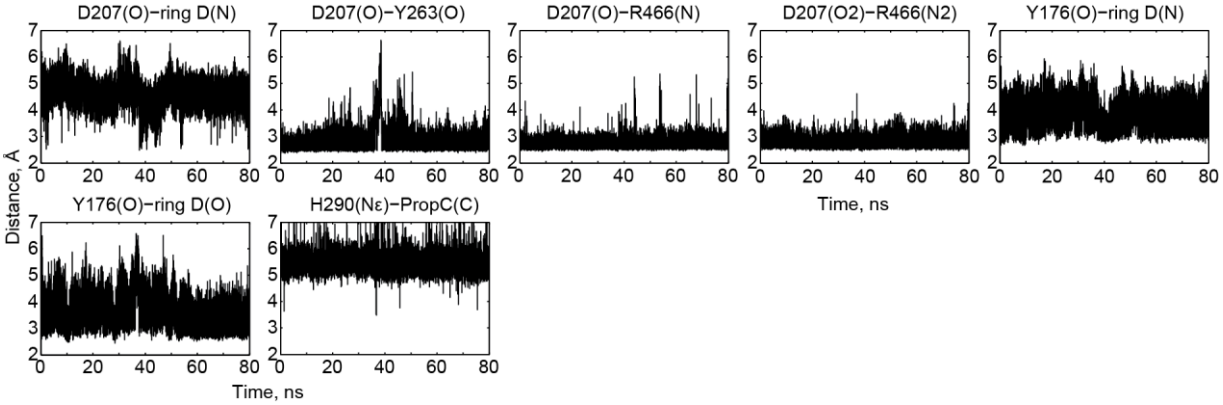

Figure C.12. Distances in the 15E-CBD(Pr)-PHY(Pr) model of DrBphP protein with protonated 15E-biliverdin, neutral (Nε-H) H260 and protonated H290 during MD simulation.

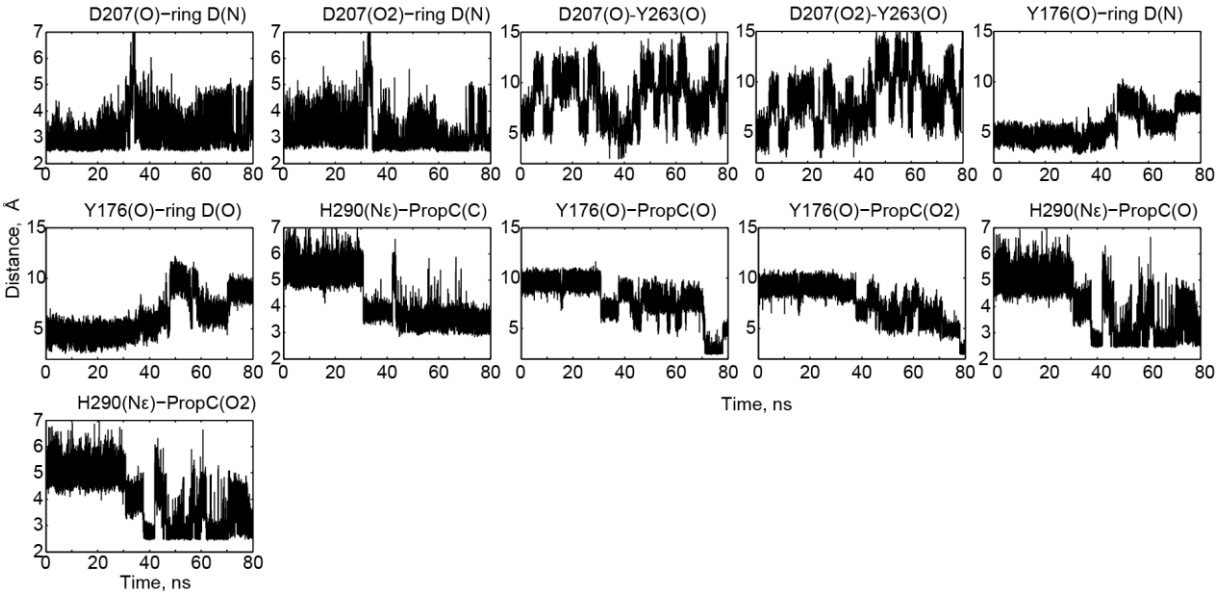

Figure C.13. Distances in the 15E-CBD(Pr) model of DrBphP protein with protonated 15E-biliverdin, neutral (Nε-H) H260 and protonated H290 during MD simulation.

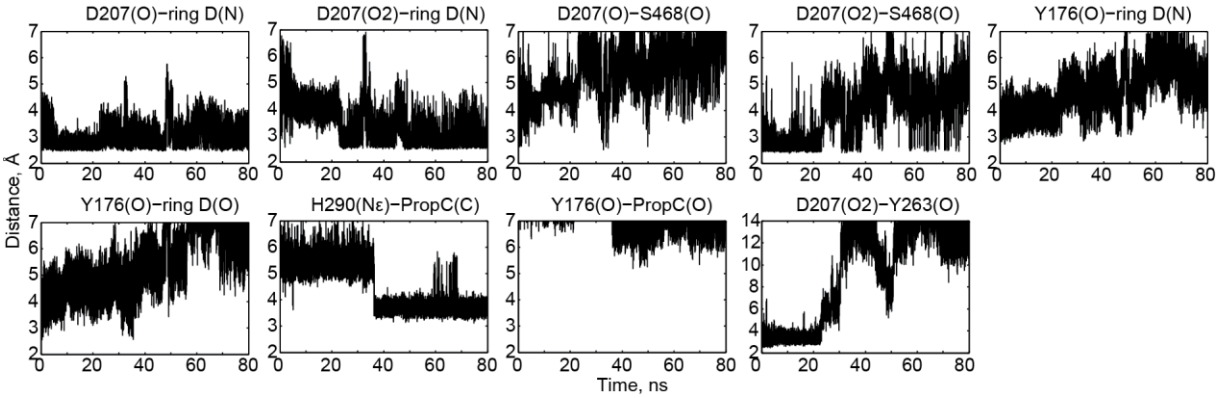

Figure C.14. Distances in the 15E-CBD(Pr)-PHY(Pfr) model of DrBphP protein with protonated 15E-biliverdin, neutral (Nε-H) H260 and protonated H290 during MD simulation.

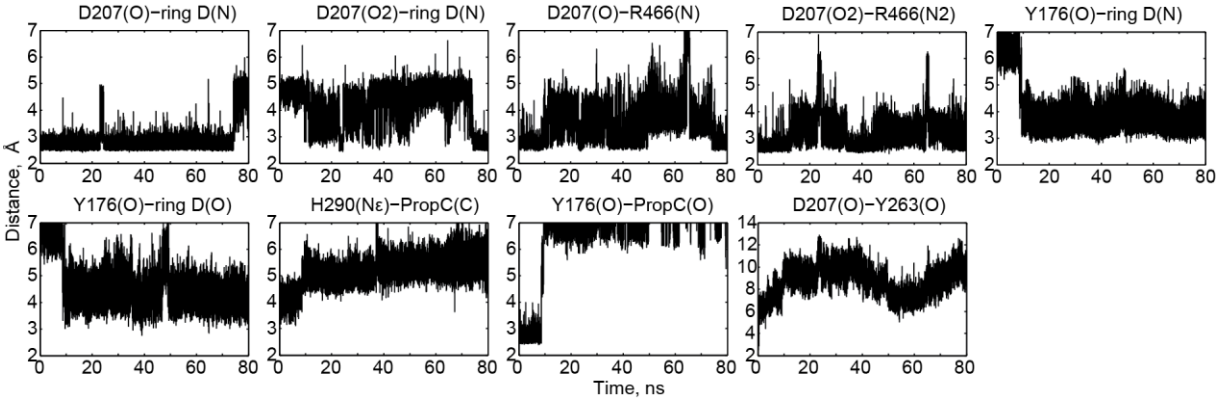

Figure C.15. Distances in the CBD(Pfr)-PHY(Pr) model of DrBphP protein with protonated biliverdin, neutral (Nε-H) H260 and protonated H290 during MD simulation.

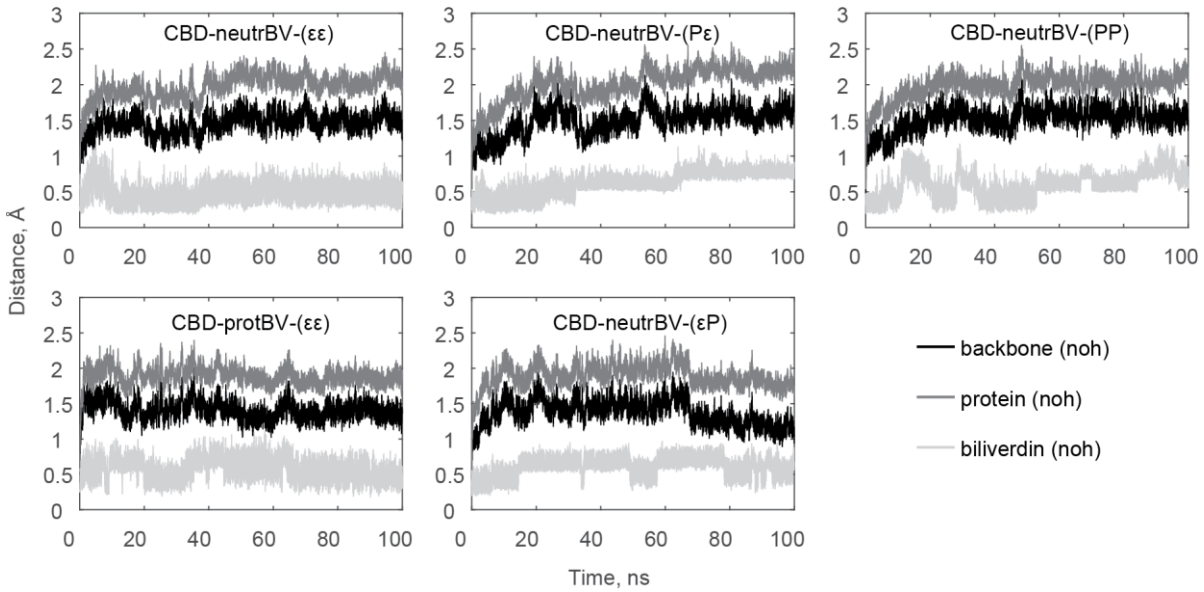

Figure C.16. RMSD for the non-hydrogen atoms of protein backbone, protein, and biliverdin in CBD models of DrBphP phytochrome in Pr state during MD simulations. Models with different protonation state of biliverdin, H260 and H290. Hydrogens were excluded in all RMSDs.

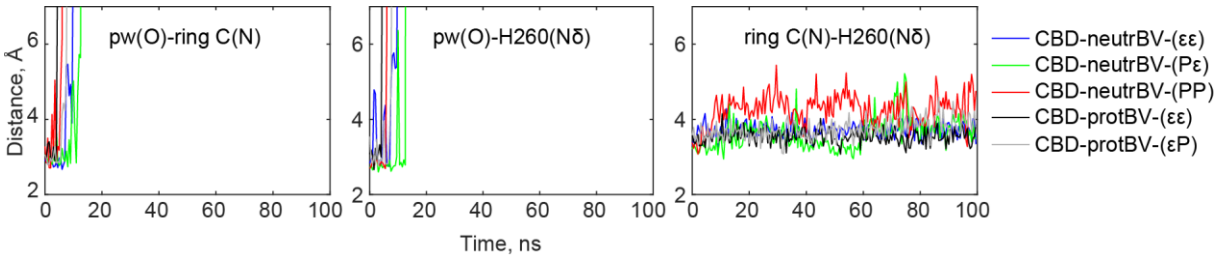

Figure C.17. Hydrogen bonds between H260 and biliverdin ring C via the pyrrole water in CBD models of DrBphP phytochrome in Pr state during MD simulations. The pyrrole water (pw), serving as a bridge for the ring C-H260 interactions, is exchanged by bulk water after 5-15 ns; here only the interactions with an initial pw molecule are shown.

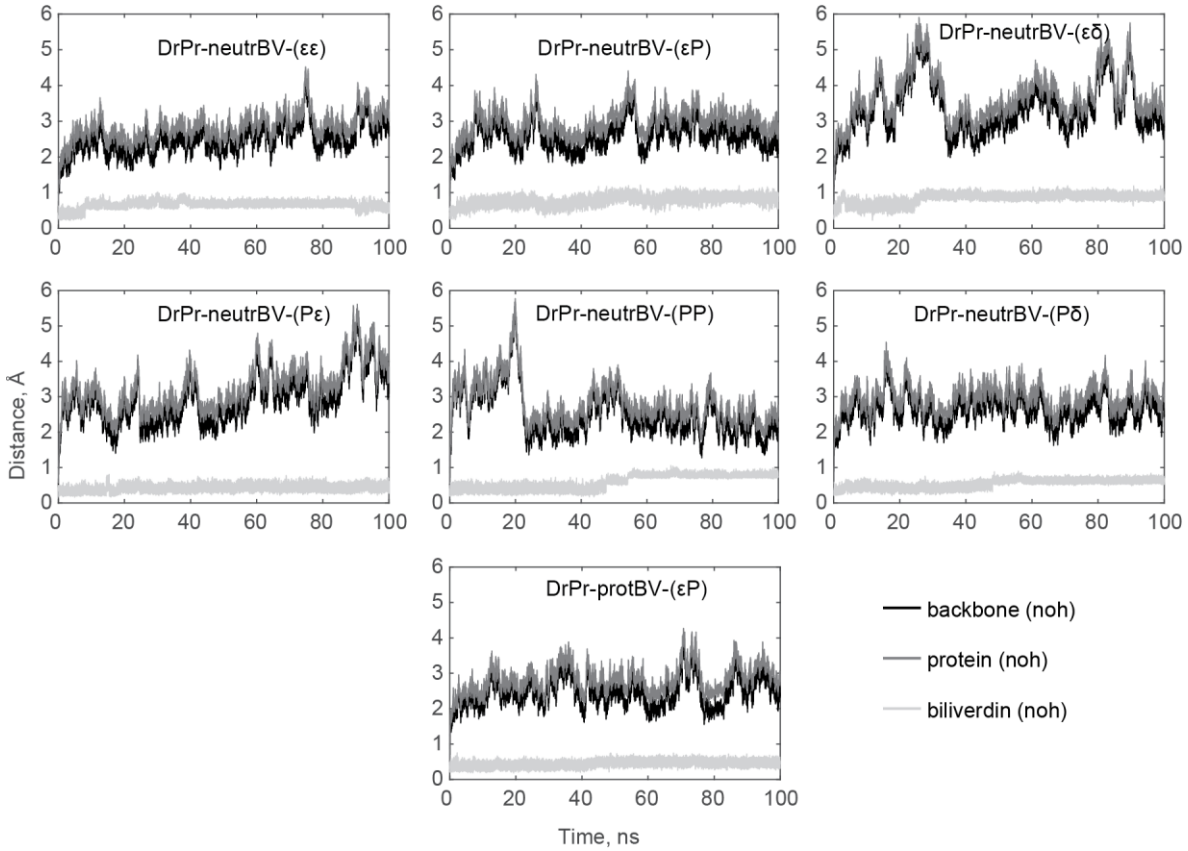

Figure C.18. RMSD for the non-hydrogen atoms of protein backbone, protein, and biliverdin in DrPr models of DrBphP phytochrome in Pr state consisting of CBD-PHY domains during MD simulation. Models with different protonation state of biliverdin, H260 and H290. Hydrogens were excluded in all RMSDs.

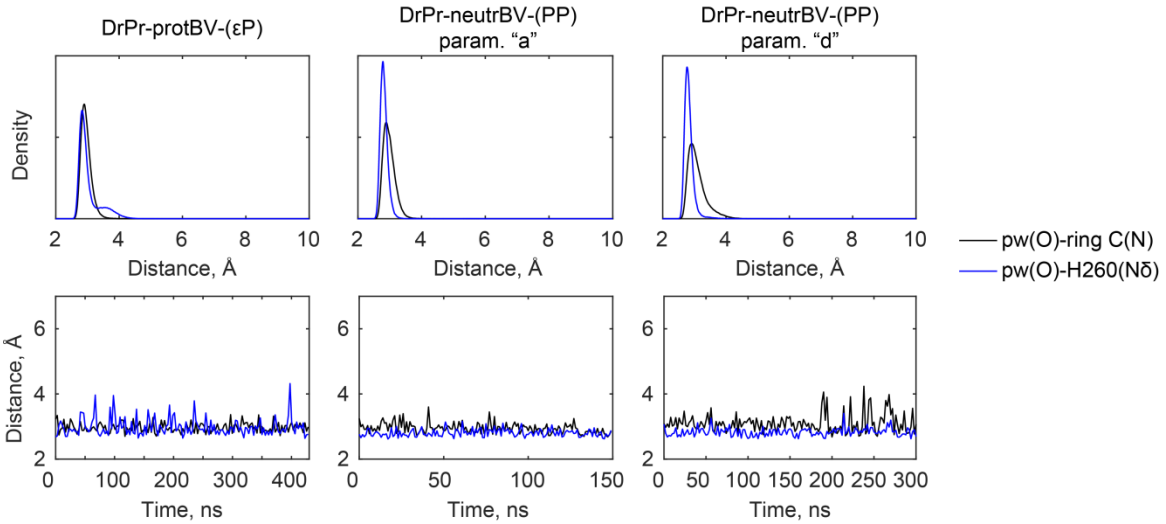

Figure C.19. Interactions between biliverdin ring C and H260 in DrPr models consisting of CBD-PHY domains with protonated or neutral (deprotonated at ring C) biliverdin. Distributions of the bonds from the last 400, 120 ns or 270 ns of the 430, 150 or 300 ns MD simulation, respectively. Force field parameters set "a" or "d" were used for neutral biliverdin.

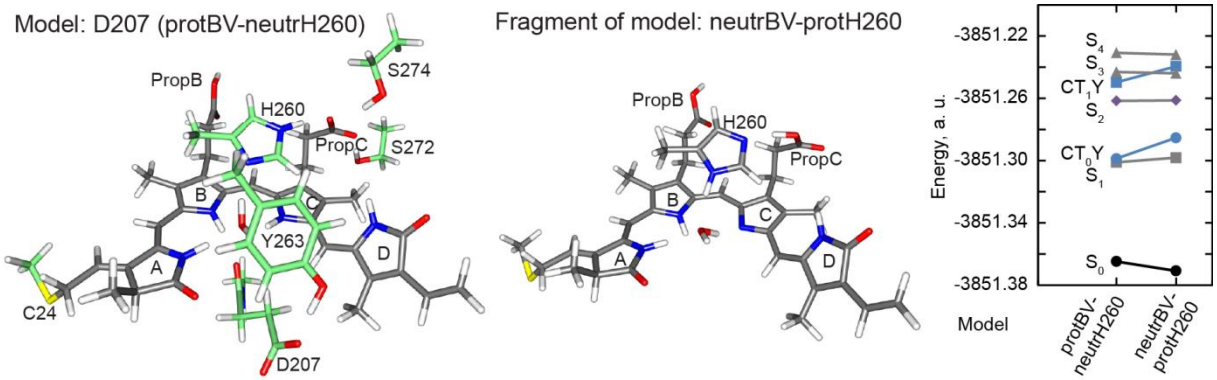

Figure C.20. Tuning of the CT-state energy by deprotonating biliverdin. Tetrapyrrole bond distances in the ground and excited states. Excited-state energies in the models computed with XMCQDPT2-SA7-CASSCF(6,5), where four MOs of biliverdin and one MO of Y263 are present in the active space.

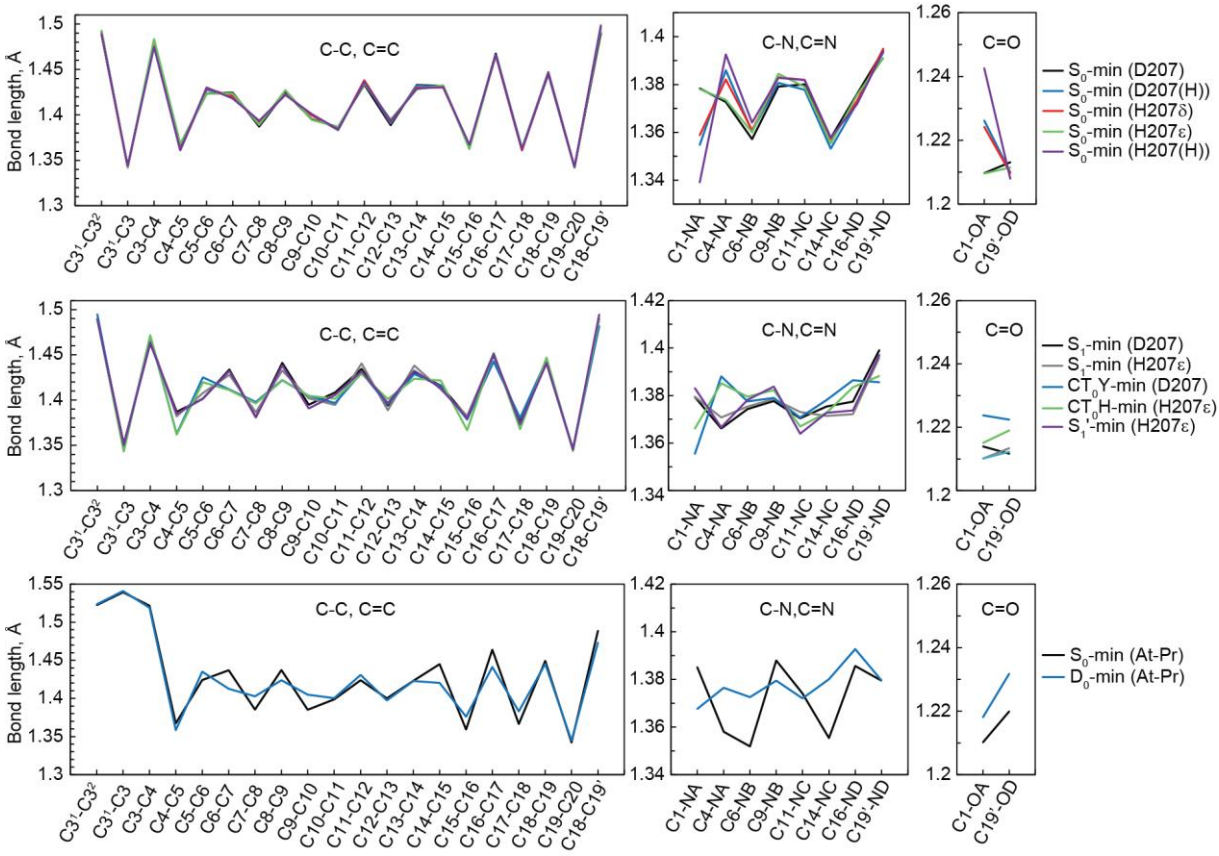

Figure C.21. Tetrapyrrole bond distances in the ground and excited states. Bond lengths at the optimized geometries of reduced-size active site models representing DrBphP in Pr state (top and middle panels) and of At-Pr model representing AtPhyB in Pr state (bottom panel).

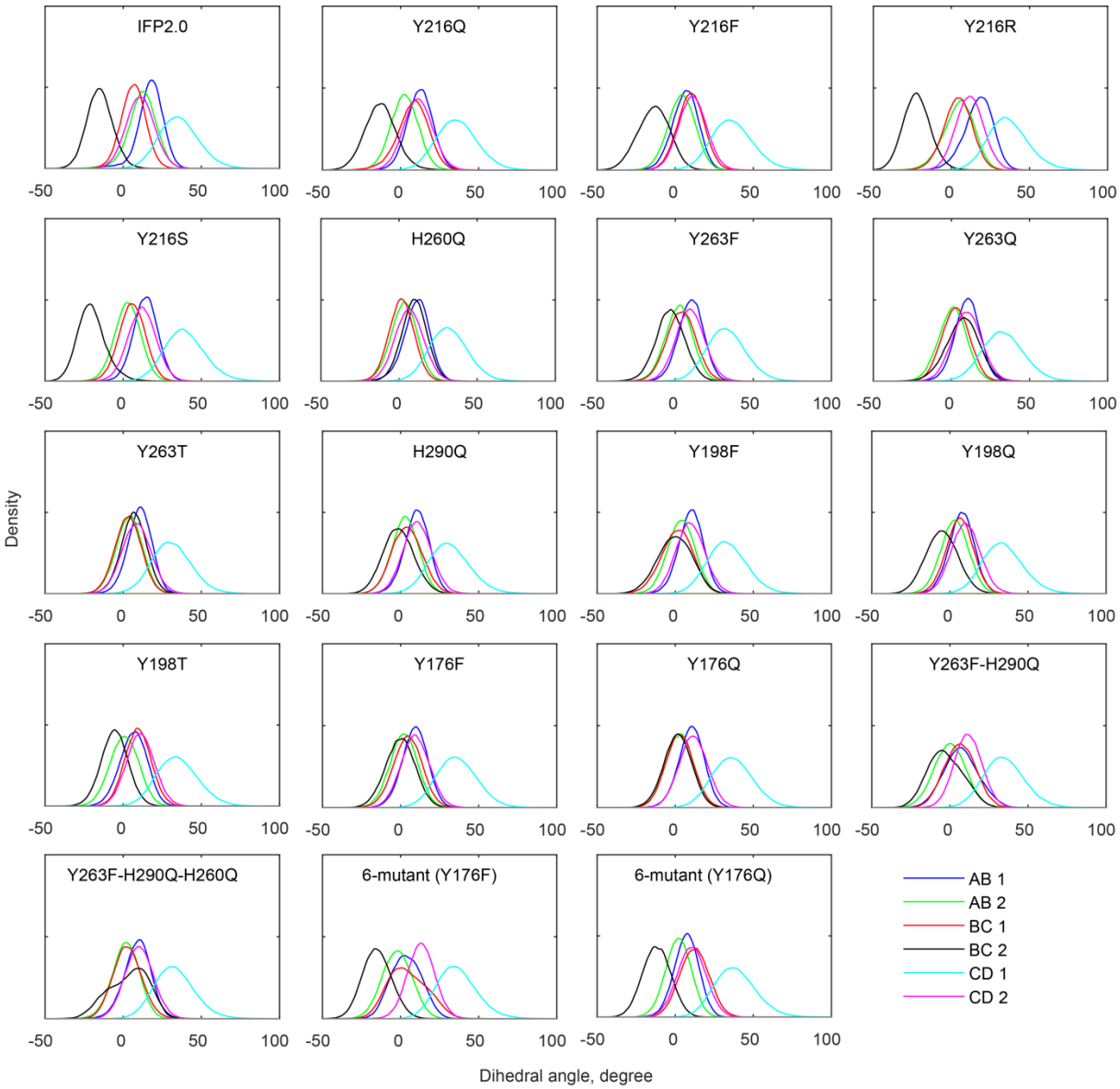

Figure C.22. Dihedral angles in the biliverdin in IFP2.0 and its mutant models. Distributions of all measured angles over the last 70 ns of MD simulation. Sextuple mutants contain Y198F, Y216F, H260Q, Y263F, H290Q and Y176Q or Y176F mutation. Dihedral angles between rings A and B (angles AB1, AB2), rings B and C (angles BC1, BC2), rings C and D (angles CD1, CD2) as shown in Figure 3.59 were measured by defining atoms N-C-C-C, except CD1 angle which was measured by defining atoms N-C-C-H.

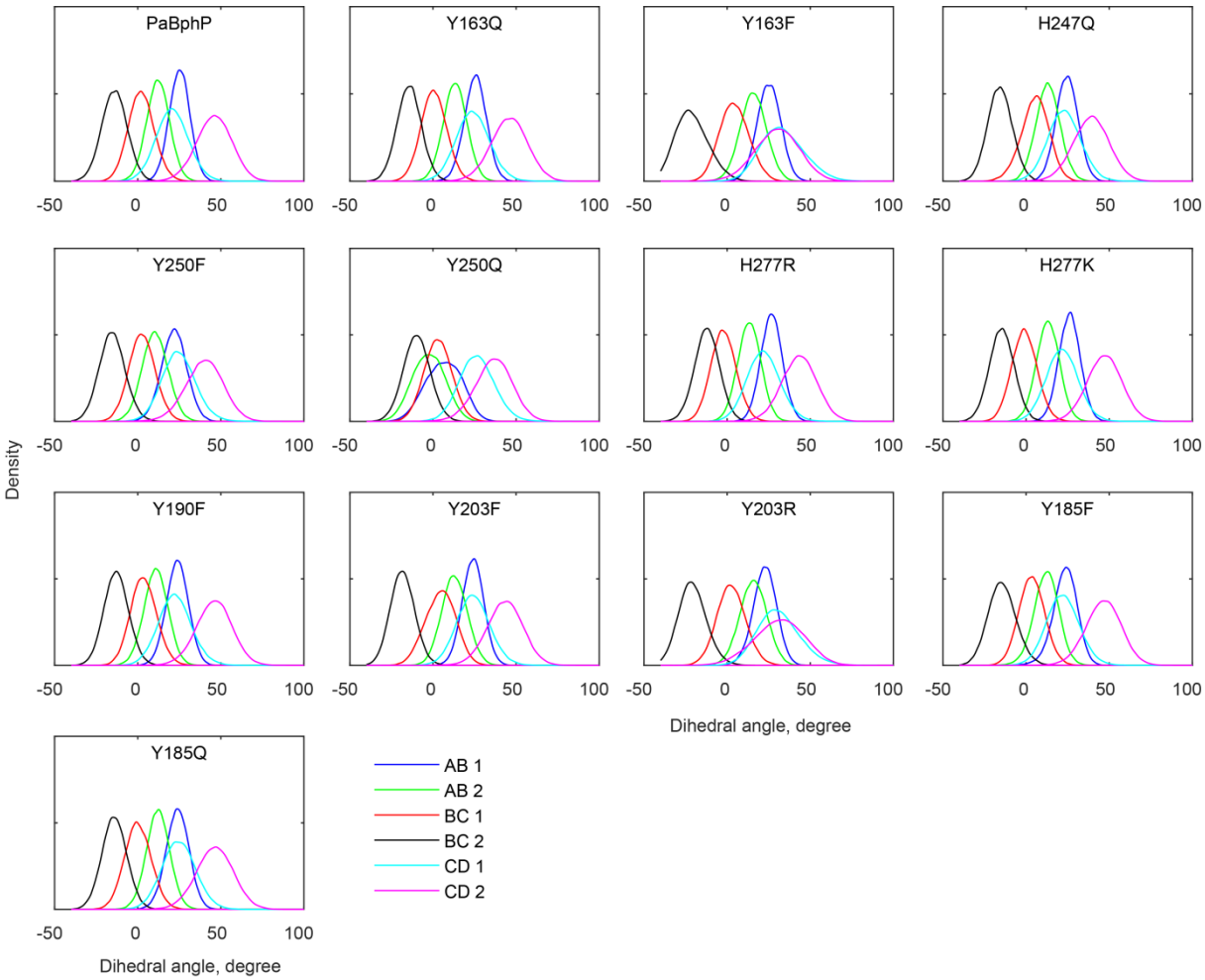

Figure C.23. Dihedral angles in the biliverdin in PaBphP and its mutant models. Distributions of all measured angles over the last 70 ns of MD simulation. Dihedral angles between rings A and B (angles AB1, AB2), rings B and C (angles BC1, BC2), rings C and D (angles CD1, CD2) as shown in Figure 3.59 were measured by defining atoms N-C-C-C, except CD1 and CD2 angles which were measured by defining atoms N-C-C-H.

D. Abbreviations

At	*Arabidopsis thaliana*
a. u.	atomic units
BphP	bacterial phytochrome
BV	biliverdin
CASSCF	complete-active-space self-consistent-field
CBD	chromophore binding domain
CD	circular dichroism
CIS	configuration interaction singles
CT	charge transfer
d	distance
D	doublet
DFT	density functional theory
Dr	*Deinococcus radiodurans*
E#	activation energy
EM	electron microscopy
ESPT	electron transfer coupled to proton transfer
ET	electron transfer
FC	Franck-Condon
FF	force field
GGA	generalized gradient approximation
HF	Hartree-Fock
k_{CT}	charge transfer rate
MD	molecular dynamics
MM	mutant model
MO	molecular orbital
n/a	not applicable
NIR	near-infrared
Pa	*Pseudomonas aeruginosa*
PCB	phycocyanobilin
PDB	protein data bank
PES	potential energy surface
Pfr	protein-far-red
PHY	phytochrome-specific
PhyB	phytochrome B
Pr	protein-red
PropB	propionate bound to ring B
PropC	propionate bound to ring C
PΦB	phytochromobilin
pw	pyrrole water
QM	quantum mechanics
QM/MM	quantum mechanics/ molecular mechanics
RMSD	root-mean-square deviation
Rp	*Rhodopseudomonas palustris*
S	singlet

SA	state-averaged
TD-DFT	time-dependent density functional theory
TM	template model
V_{el}	electronic coupling
w/o	without
XMCQDPT2	extended multi-configuration quasi-degenerate perturbation theory to the 2nd order
λ	reorganization energy
τ_{rad}	radiative lifetime
χ	dihedral angle

Amino acids in one and three letter code

alanine	Ala	A
arginine	Arg	R
asparagine	Asn	N
aspartate	Asp	D
cysteine	Cys	C
glutamate	Glu	E
glutamine	Gln	Q
glycine	Gly	G
histidine	His	H
isoleucine	Ile	I
leucine	Leu	L
lysine	Lys	K
methionine	Met	M
phenylalanine	Phe	F
proline	Pro	P
serine	Ser	S
threonine	Thr	T
tryptophan	Trp	W
tyrosine	Tyr	Y
valine	Val	V